Amorphous Mirror Coatings for Ultra-High Precision Interferometry

Martin Joseph Hart

School of Physics and Astronomy

College of Science and Engineering

University of Glasgow

Presented as a Thesis for The Degree of

Doctor of Philosophy

Supervised by Dr. Ian MacLaren and Prof. Sheila Rowan

May 2017

Abstract

The dominant noise source in aLIGO is Brownian thermal noise, due to mechanical losses in the atomic structure of the amorphous titania doped tantala end test-mass mirror coatings. This thesis investigates the structural source of these losses.

The effect of titania doping and thermal annealing upon the atomic structure of amorphous tantalum pentoxide coating preparations are studied using advanced electron diffraction techniques. Significant differences between the coating atomic structures have been identified for the first time in detail.

The tantala based coatings studied have been demonstrated as better described by a heterogeneous phase separated model, rather than the continuous random network model for covalently bonded amorphous metal-oxides.

The short-range ordering (SRO) of the coating atomic structures was investigated using pair-distribution function analyses, with an upper limit found to be ~4 Å. Correlations spanned ~9 Å, and have been related to model structures; between 4 - 5 Å, correlations were identified as signatures for 3D structural ordering.

Fluctuation Electron Microscopy (FEM) was employed to investigate the MRO of the coating atomic structures. A novel approach to FEM was developed by the author during this PhD, in which the structural variance was computed using normalised cross-correlation coefficients. This made absolute intensity irrelevant, with the shape and the spatial distribution of the diffracted intensity taking precedence. The method is insensitive to poor SNR, illumination conditions, slight differences in experimental facility, and slight thickness variations in the samples.

Virtual Dark-Field (VDF) imaging was adapted to amorphous structures in novel ways for the first time in this thesis. Simultaneous representation of the FEM data in real and reciprocal space, spatially resolved the structures responsible for the FEM signal. Correlation analyses were performed between VDF images of the structural ordering that relate to specific atom-pair correlations, including the use of novel annular variance images. The images and correlations clearly highlight the heterogeneous ordering and phase separation within the structures.

Mechanisms responsible for the coating mechanical losses have been proposed, relating to the MRO, tensile-stress, as well as its reduction by titanium doping.

Declaration

This thesis is an account and record of research carried out at the Institute for Gravitational Research and the Materials and Condensed Matter Physics Group, School of Physics and Astronomy at the University of Glasgow, between October 2012 and May 2017. The work described herein is my own, except where specific reference is made to the work of others. The contents of this dissertation are original and have not been submitted in whole or in part for consideration for any other degree or qualification in this, or any other university.

Martin Joseph Hart

August 2017

Some of the results from the amorphous Ta_2O_5 medium-range order investigations of chapter 4, section 4.1.1 have been previously published in the following publication:

Medium range structural order in amorphous tantala spatially resolved with changes to atomic structure by thermal annealing

Hart MJ, Bassiri R, Borisenko KB, Véron M, Rauch EF, *et al*. J Non Cryst Solids. 2016 Apr;438:10–7.

External examiner: Dr. Alex Eggeman
Internal examiner: Dr. Damien McGrouther
Convenor: Professor Ken Strain

Contents

List of Publications

The author has contributed to experimental work in all the following publications.

1. Hart MJ, Bassiri R, Borisenko KB, Véron M, Rauch EF, Martin IW, et al. Medium range structural order in amorphous tantala spatially resolved with changes to atomic structure by thermal annealing. J Non Cryst Solids. 2016 Apr;438:10–7.

2. Bassiri R, Hart M, Byer RL, Borisenko KB, Evans K, Fejer MM, et al. Investigating the medium range order in amorphous Ta2O5 coatings. J Phys Conf Ser. 2014 Jun 11;522(1):12043.

3. Bassiri R, Liou F, Abernathy MR, Lin AC, Kim N, Mehta A, et al. Order within disorder: The atomic structure of ion-beam sputtered amorphous tantala (a-Ta2O5). APL Mater. 2015 Mar;3(3):36103.

4. Bassiri R, Abernathy MRMR, Liou F, Mehta A, Gustafson EKEK, Hart MJ, et al. Order, disorder and mixing: The atomic structure of amorphous mixtures of titania and tantala. J Non Cryst Solids. 2016;438:59–66.

5. Bassiri R, Abernathy MR, Borisenko KB, Byer RL, Evans K, Fejer MM, et al. Investigating the atomic structure and properties of Ta2O5 coatings. In: Optical Interference Coatings. Washington, D.C.: OSA; 2013. p. PMB.9.

6. Granata M, Craig K, Cagnoli G, Carcy C, Cunningham W, Degallaix J, et al. Cryogenic measurements of mechanical loss of high-reflectivity coating and estimation of thermal noise. Opt Lett. 2013;38(24):5268–71.

7. Craig K, Martin IW, Murray PG, Robie R, Steinlechner J, Bell A, et al. Amorphous hafnia-based coatings for cryogenic gravitational wave detectors. 2016;1–10.

8. MacLaren I, Nord M, Ross A, Krajnak M, Hart M, Doye A, et al. Pixelated STEM detectors: opportunities and challenges. In: European Microscopy Congress 2016: Proceedings. Weinheim, Germany: Wiley-VCH Verlag GmbH & Co. KGaA; 2016. p. 663–4.

Acknowledgements

This thesis is dedicated to my family, in acknowledgement of their unending support through the hardest of times. Thank you, Alicia, Joe, Brian, Allison and Gerard. The Harts.

I would like to thank Prof. Jim Hough for offering me the opportunity to do this work, and his subsequent efforts in securing funding for the position. Many thanks go to Dr. Riccardo Bassiri for his continued support, advice and discussions on the structures of the materials studied in this thesis. Thanks also go to Dr Ian MacLaren for the setting-up and driving of the electron microscope in the collection of electron diffraction data for the PDF work, and likewise to Dr Magnus Nord for his work in collecting the FEM datasets on the Medipix detector. Special thanks go to Dr Stavros Nicolopolous of NanoMEGAS who organized a demonstration of the ASTAR system at the University of Grenoble, in which opportunity was taken to collect scanning diffraction data of samples studied in this thesis, without which this thesis would be have been possible; equal thanks go to DR Edgar Rauch and Prof Muriel Veron for the data collection during this demonstration. Appreciation is also extended to Dr Konstantin Borisenko for his valuable input on the FEM work.

A special mention of appreciation goes to Dr Sam McFadzean, Colin How and William Smith for their technical expertise in solving many of the problems I faced along the way.

A final note of appreciation is FOR the LIGO collaboration. It is an honor to have been a part of the project, and to be associated with one of the greatest scientific discoveries of our times.

Preface

Chapter 1 is a brief overview of the sources and nature of gravitational waves, their detection, and limits to detector sensitivity. Discussion of Brownian thermal noise is given with respect to the amorphous mirror coatings.

Chapter 2 describes the methods used in this thesis for atomic structure investigations. It covers the transmission electron microscope and its modes of operation, sample preparation for TEM, and a description of the pair distribution function (PDF) and fluctuation electron microscopy (FEM) techniques employed.

Chapter 3 encompasses the electron diffraction based PDF analysis of the various titania doped and heat-treated amorphous mirror coating preparations, with data taken at Glasgow University in experiments setup by Dr Ian MacLaren.

Chapter 4 contains the FEM studies of the structures. The technique was introduced to the author by Dr Riccardo Bassiri, whom began experiments with it, and Dr Ian MacLaren. Data for the un-doped and 14% titania doped samples were collected in an optically coupled setup at the University of Grenoble, by Dr Edgar Rauch and Prof. Muriel Veron, and was organised as a hardware demonstration by Dr Stavros Nicolopolous of NanoMEGAS. The remaining data were recorded using a Medipix direct electron counting setup at the University of Glasgow and collected be Dr Magnus Nord.

1. The dawn of Gravitational Wave Astronomy & the next steps in improving detector sensitivity

1.1 Introduction

On September 14, 2015, a new window of observation opened upon the Universe; a brand-new astronomy, one which through gravitational radiation allows the Universe to be 'heard', and not just seen, as by the traditional astronomy of electro-magnetic radiation. The two detectors of the advanced Laser Interferometer Gravitational-Wave Observatory (aLIGO) simultaneously observed a transient gravitational-wave signal, shown in Figure 1.

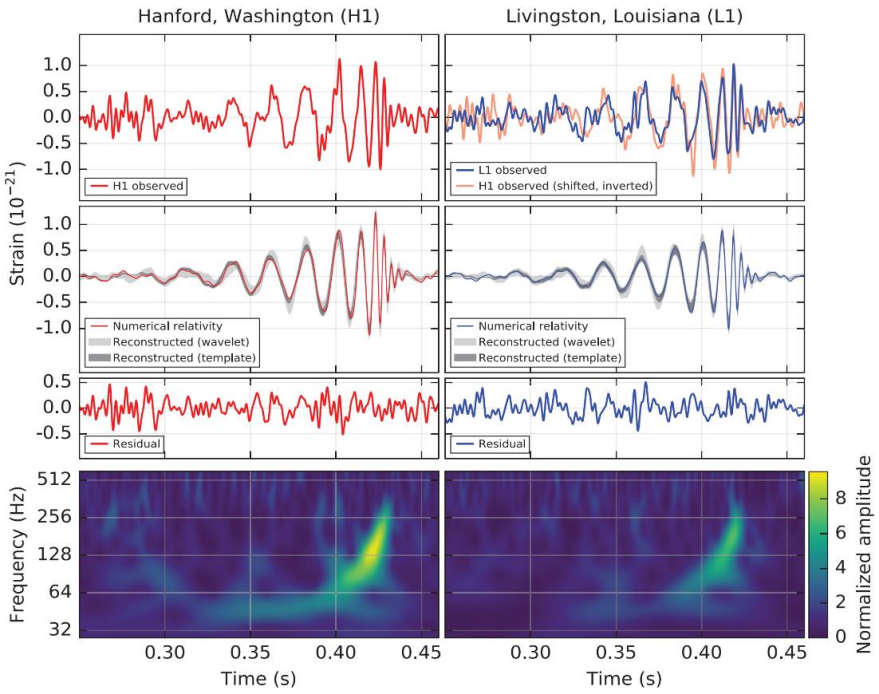

Figure 1-1: Detection signal of GW150914, the first direct detection of gravitational waves and the first direct observation of binary black hole merger (1).

It matched the waveform predicted by general relativity for the inspiral and merger of a binary black hole pair and the ringdown of the resulting single black hole. This was the first direct detection of gravitational waves and the first observation of a binary black hole merger(1).

This chapter will briefly discuss the nature of gravitational waves, the instrumentation employed in their detection, and finally, the various sources of noise which are a limit to detector sensitivity.

1.2 The nature of gravitational waves

Albert Einstein's 1916 publication of The General Theory of Relativity (GR) predicted that gravitational waves travelling at the speed of light are generated in the medium of space-time because of the asymmetric acceleration of mass(2). Gravitational radiation is quadrupolar at lowest order, as the conservation of mass and momentum precludes the existence of monopole and dipole radiation respectively(3); the waves are a superposition of two polarisations, h_+ and $h_\times$ which are offset by 45°.

As a gravitational wave propagates, a strain, h, is induced in the space-time medium transverse to its direction of propagation, differentially changing the distance between two points in which the respective orthogonal components are simultaneously expanded and contracted. An illustration of the geometrical distortion caused by a gravitational wave passing through a ring of test particles normal to the page is shown in Figure 1-2.

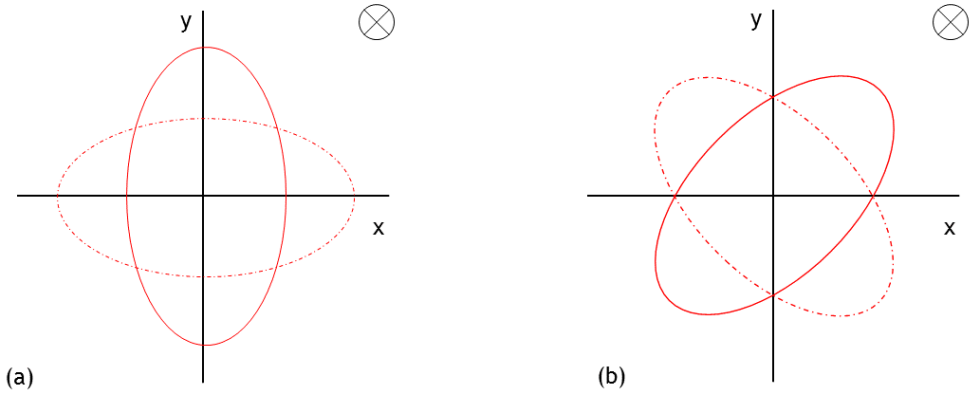

Figure 1-2: Effect of a passing gravitation wave on a ring of test particles. Positive x & y axes analogous to arms of aLIGO interferometer. (a) & (b) are the two transverse polarisations detectable in aLIGO.

The amplitude of the induced strain, h, caused by gravitational waves, detected by a gravitational wave interferometer is defined as,

$$h = \frac{2\Delta L}{L} \tag{1.1}$$

where L represents the distance between two test particles, and ΔL is the change in that distance induced by a passing gravitational wave.

This deceptively simple property underpins the principal operation of interferometric gravitational wave detectors; however, in consideration of the strain amplitudes expected from the most violent of astrophysical sources to be around one millionth the diameter of a proton(4), a sense of the grand scale of the precision engineering and measurement involved in detecting these waves is apparent. A useful review of the physics of ground-based gravitational wave detectors is given by Saulson(5).

1.3 Sources of gravitational waves

The following section shall briefly discuss the types of astrophysical events that are expected to generate gravitational waves. An in-depth overview of gravitational wave sources is given by Cutler & Thorne(6). The main sources are classified into three types: transient sources, continuous sources and the stochastic background.

Astrophysical events which generate a short burst of gravitational waves fall into the category of transient sources and occur on timescales between milliseconds and minutes. Examples of this type of source are compact binary coalescences and supernovae. A compact binary for example may be two neutron stars, a neutron star and a black hole, or two black holes. The first direct detection of gravitational waves was generated by a black hole binary system, in which the signal was confirmed to correspond to their inspiral, merger and subsequent ringdown; the signal swept up in frequency from 35 to 250 Hz with a peak gravitational-wave strain of $h = 1.0 \times 10^{-21}$ at a luminosity source distance of 410 Mpc(1). A core collapse supernovae on the other hand is expected to generate a strain of the order of $h = 1.0 \times 10^{-21}$ at a source distance of 10 kpc(7).

Examples of continuous sources include pulsars and X-ray binaries. A pulsar (supernovae remnant) is a rapidly spinning magnetised neutron star that beams huge jets of radiation from its poles. Observation of the orbital decay of the pulsar/neutron star binary discovered in 1974(8) won Hulse & Taylor the 1993 Nobel Prize in Physics for the first indirect evidence for the existence of gravitational waves. An estimate for the gravitational wave strain generated by the shortest period, binary neutron star inspiral at a distance of ~10 kpc, has been reported as $h \approx 4 \times 10^{-22}$ by Kip Thorne(9); at a frequency of $f \approx 5 \times 10^{-3}$ Hz, it is however well below the sensitivity range in aLIGO.

X-ray binaries consist of a neutron star and normal star from which it accretes mass, increasing in angular momentum until it reaches a point of instability, where the mass is accelerated asymmetrically, generating gravitational waves of strain in the region of $h = 1.0 \times 10^{-27}$, as reported by Wagoner(10).

Stochastic gravitational waves are a relic from the early evolution of the universe. Akin to the Cosmic Microwave Background (CMB), regarded as the remnant light left over from the Big Bang, stochastic gravitational waves are thought to be the remnant signals from many independent events that have combined to form a cosmic gravitational wave background. If indeed from the Big Bang, they will contain information about the origin and history of the Universe(11).

1.4 Interferometric gravitational wave detectors

The search for gravitational waves began many decades ago, initially using aluminium bars in which resonant modes were expected to be excited by the passing of a gravitational wave of sufficient amplitude(12), however the limited frequency range and sensitivity was orders of magnitude lower than the stringent requirements now known for detection. A comprehensive review of such resonant-mass detectors is given by Ju & Zhao(13).

Long base-line laser interferometric gravitational wave detectors are the most sensitive displacement detection devices ever created, and are the only experimentally proven devices capable of detecting a gravitational wave signature(1). They are based upon Michelson type interferometers in which an input laser beam is split in two, travelling in orthogonal paths, where the beams are reflected and recombine to create an interference pattern, which is then detected using a photodetector. A simplified schematic of a Michelson interferometer is shown in Figure 1-3.

A passing gravitational wave will cause one arm of the interferometer to contract while the other extends, resulting in a variation of the interference pattern at the photodetector. The initial setup is such that the arm lengths of the detector have a π phase difference, so that the interference pattern is centered close to a dark fringe, and is thus sensitive to increases in intensity. The nature of the possible events responsible for a detected signal are determined through cross-correlation of the signal with a library of modelled signals using known astrophysics.

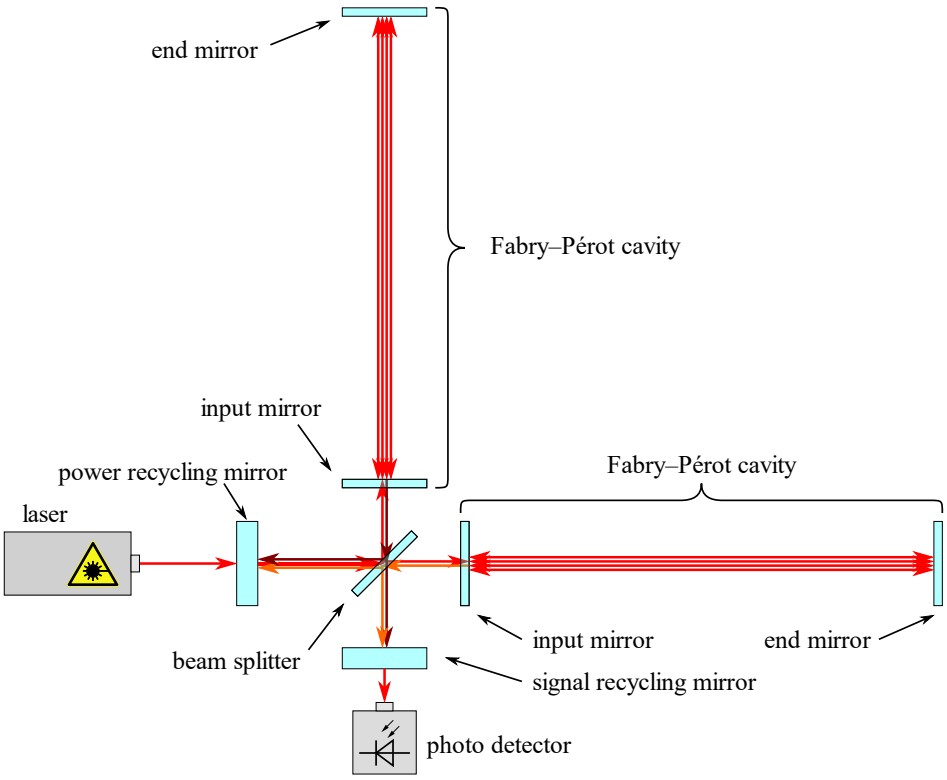

Figure 1-3: A simplified schematic of a Michelson interferometer(14).

The most advanced detector of this type is aLIGO in the USA, made famous by the recent detection; aLIGO consists of two 4km long arm length interferometers with 40 Kg ultra-pure fused silica end test masses (ETMs). One is based in Hanford, Washington, and the other in Livingstone, Louisiana, with a sensitivity range spanning ~ 10 Hz to 2 kHz(1). The end test masses, hung from four stage pendulum suspensions, with the final stage pendulum incorporating fused silica fibres, are coated with a highly reflective dielectric mirror stack of alternating pairs of high refractive index titanium cation doped tantalum pentoxide (Ti:Ta_2O_5) and low index silica (SiO_2)(15). The layer configuration maximises the reflectivity, *R*, at the operational laser frequency, as per the Fresnel condition for an arbitrary polarisation incident normal to the mirror surface,

$$R = \left(\frac{n_1 \cos\theta_i - n_2 \cos\theta_t}{n_1 \cos\theta_i + n_2 \cos\theta_t}\right) \tag{1.2}$$

where $n_1, \theta_i, n_2, \theta_t$ represent the refractive indices for the different layers, and the angles for the incident and transmitted beams respectively. There are a range of technologies employed in aLIGO, enhancing the simple Michelson setup to achieve greater sensitivity.

These include Fabry-Perot cavities to increase the optical path length(16), and include power and signal recycling techniques to increase the power stored in the arm cavities, and enhance the detected signal size(17).

Other detectors include GEO600 in Germany which provided much of the technology that enabled aLIGO to make its recent detection(18), TAMA in Japan(19), the soon to be operational advanced VIRGO(20) in Italy, the currently under construction cryogenically operated KAGRA in Japan(21) and INDIGO in India(22).

These detectors when operating simultaneously will enable triangulation of the signal sources, and thus enable EM-radiation based follow up studies to be conducted. There are also future detectors in the pipeline such as the Einstein telescope (ET)(23) and the proposed space based LISA mission, for which a successful technology test mission was recently flown(24).

1.5 Limits to detector sensitivity

Owing to the miniscule amplitude of gravitational waves, most of the effort in constructing an effective ground based detector, and improving its sensitivity, is spent on the mitigation of sources of noise at frequencies similar to that of the expected GW signals. These noise sources in many cases can be thought of as effectively modulating the phase of the laser beam, masking phase changes that are induced by a gravitational wave. Figure 1-4 is a plot of the total noise budget calculated for aLIGO, showing the strain sensitivity limits as a function of frequency. The major sources of noise are described below.

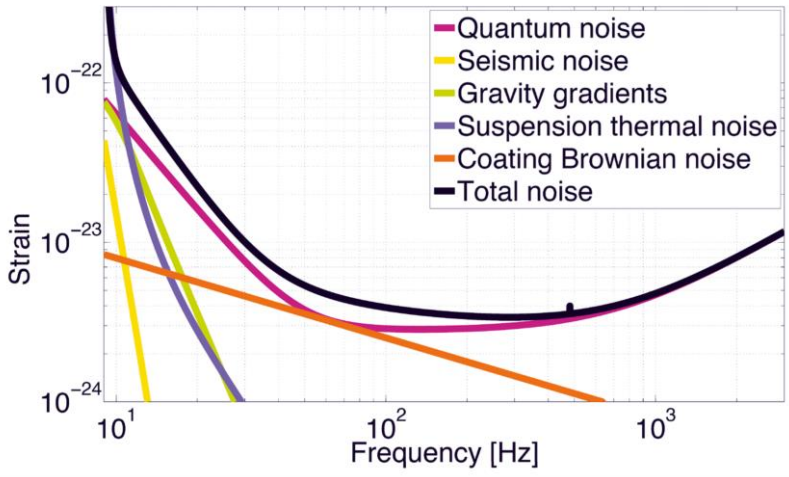

Figure 1-4: The significant noise sources affecting the sensitivity of aLIGO(25).

1.5.1 Gravitational gradient noise

Gravitational gradient noise (Newtonian noise) arises from fluctuations in the local gravitational field, and can cause significant displacement noise of the test masses below 20 Hz; this is due to the inability of shielding the interferometer from gravitational fields, and sets an effective lower limit on the low frequency sensitivity of earth based detectors.

Fluctuating gravitational fields in the local vicinity of the detector can be due to the motion of mass such as passing cars, pedestrian footfall, airplanes *etc.*; density fluctuations of the surrounding earth and air are the culprits, with a major contribution from the impact of ocean waves, which are efficiently transmitted through the earth's crust. However, this noise is not a limiting source in aLIGO, but is expected to become so in future ground based detectors(5,26).

1.5.2 Seismic noise

Seismic noise is due to the continual motion of the ground, and if unmitigated, induces displacements of the test masses in the micron range. This major limit to sensitivity has been overcome in aLIGO by suspending the test masses from complex multiple-stage seismic isolation systems. The systems are comprised of a combination of passive and active systems which provide a broadband seismic attenuation.

Seismic isolation is achieved using stiff springs connected to seismometers, which monitor all six degrees of freedom, where the seismometer signals are driven to zero via a feedback control to a system of actuators. The detector additionally includes an out of vacuum hydraulic actuator for the attenuation of large low frequency motion in the millimetre range(26,27).

1.5.3 Quantum noise

As illustrated in Figure 1-4, quantum noise is the limiting noise source over most frequencies in the aLIGO detection band. There are two mechanisms which contribute to quantum noise: photon shot noise and radiation pressure noise. Photon shot noise arises because photons in a laser beam follow a Poisson distribution; they are not equally distributed in time and so any laser beam detected by a photodiode will cause the output of that photodiode to carry noise. This shot noise is considered as the readout or sensing noise of the interferometer.

Radiation pressure noise on the other hand manifests as a fluctuation of the position of the mirror surface due to the transfer of fluctuating momenta from the photons to the mirror. This radiation pressure noise is a form of back-action noise from the actual process of measurement(26,28). Mitigation of these effects are realised through the various technological enhancements of the Michelson interferometer described previously, and are described by Hammond *et. al.*(27).

1.5.4 Thermal noise

Thermal noise is a limiting source in detector sensitivity for aLIGO between ~10 Hz and 1 kHz; the detectors most sensitive region of operational bandwidth, and primarily affects the test masses, their mirror coatings and suspensions(27). Thermal noise is a result of mechanical dissipation through internal friction, and the effects of statistical temperature fluctuations in the materials which make up these systems.

Thermal noise from mechanical dissipation is currently understood to arise from the energy lost by the movement of atoms ($\frac{1}{2}k_BT$ per degree of freedom) about their equilibrium positions at finite temperature, and is also referred to as Brownian noise, after Robert Brown's 1827 observations of the irregular motion of pollen grains suspended in water(29), and Einstein's later theoretical derivation of the phenomenon(30).

Statistical temperature fluctuations, on the other hand, can couple through properties of the material such as local expansion and refractive index, and are collectively referred to as thermo-optic noise(31). The most significant source of thermal noise, however, is attributed to Brownian noise, an important source of which was shown to originate from the amorphous tantala mirror coatings applied to the test masses in initial LIGO.

This level was reduced in aLIGO through titania doping of the tantala within the coatings(32,33). Brownian thermal noise is consequential not only for aLIGO, but for all ultra-high precision experiments which utilise optical metrology, and is covered in greater detail below.

1.5.5 Brownian thermal noise and mechanical dissipation

Brownian thermal noise, due to mechanical dissipation within the atomic structure of the end test mass mirror (ETM) coatings, constitute the dominant source of thermal noise in aLIGO(33), and mitigation of this noise is a primary goal of the next stage in detector upgrades.

Moreover, it is the amorphous titania doped tantala ($Ti:Ta_2O_5$) layers of the dielectric multi-layer stack that are the largest contributor to this noise source(33).

As such, this thesis aims to shed some light on possible mechanisms responsible for the observed macroscopic mechanical dissipation at the atomic level, by investigating the atomic structure of various preparations of $Ti:Ta_2O_5$, and where possible, relating any observed differences in structures, to the differences observed in the mechanical loss spectra measured for that same variety of coating preparations.

When these loss mechanisms are identified, the ad hoc nature of mirror coating selection, and the trial and error approach of finding coatings with the desired properties will give way to atomically engineered structures of the desired functionality.

Mechanical loss/dissipation, describes the observed macroscopic average of the effects of internal friction, and are understood to be a proxy measure for Brownian thermal noise. The quantification of internal friction and its contribution to the noise budget in aLIGO is described below.

Investigations into Brownian noise paved the way for the development of the Fluctuation-Dissipation theorem, originally formulated by Nyquist in 1928(34), and later proven by Callen & Welton in 1951(35).

The theorem is a general result of statistical thermodynamics and quantifies the magnitude and frequency of thermal fluctuations in a dissipative system, related to the system's mechanical impedance (internal friction), $Z(f)$, in response to an applied force.

Following Martin & Reid(36), the power spectral density, $S_f(f)$, of the fluctuating thermal force on a mechanical system is given by,

$$S_f(f) = 4k_B \mathrm{T}\Re\{Z(f)\} \tag{1.3}$$

where $Z(f)$ is defined as,

$$Z(f) = \frac{F(f)}{v(f)} \tag{1.4}$$

for a force $F(f)$ applied to the system resulting in motion with a velocity of amplitude $v(f)$. This assumes that significant external sources of damping are mitigated. In the current context, the theorem is more commonly written in terms of the power spectral density of the fluctuating motion of the system $S_x(f)$,

$$S_x(f) = \frac{4k_B \mathrm{T}\Re\{Y(f)\}}{4\pi f^2} \tag{1.5}$$

where $Y(f)$, the mechanical admittance of the system, is the reciprocal of the mechanical impedance.

Internal friction is a consequence of a materials anelasticity which is a description of a materials delayed strain response to an applied stress(37,38). Application of an oscillating stress σ can be expressed as,

$$\sigma = \sigma_0 e^{i2\pi ft} \tag{1.6}$$

where σ_0 is the stress amplitude, and *f* is the frequency of the applied oscillation. As there is a linear relationship between stress and strain, the resulting strain *ε* will also be periodic with the same angular frequency, but have a phase lag *φ* with respect to the stress,

$$\varepsilon = \varepsilon_0 e^{i(2\pi ft - \varphi)} \tag{1.7}$$

This phase lag is known as the mechanical loss angle due to internal friction and can result from internal properties of the material which are a function of internal stresses(38), signs of which are searched for in the current atomic structure investigations. The mechanical loss angle is equivalently defined by the measured dissipation of mechanical energy in a material, and is the basis for the experimentally derived values for mechanical loss of the coating preparations investigated in this thesis.

For a mechanical system oscillating at a resonant frequency f_0, the loss angle is defined by,

$$\varphi(f_0) = \frac{E_{lost\ per\ cycle}}{2\pi E_{stored}} = \frac{\Delta f}{f_0} \tag{1.8}$$

where E_{stored}, is the total energy stored in the oscillating system, $E_{lost\ per\ cycle}$ is the energy dissipated during each oscillation and Δf is a measured resonance peak at FWHM.

With external sources of damping minimised, the mechanical loss is measured using a ring-down technique in which a resonant mode of a sample is excited and the exponential decay of the amplitude is recorded, with the mechanical loss $\varphi(f_0)$ related to the amplitude of decay, $\mathrm{A}(t)$ by,

$$\mathrm{A}(t) = A_0 e^{-\frac{2\pi\varphi(f_0)f_0 t}{2}} \tag{1.9}$$

where A_0 is the initial excitation amplitude and f_0 is the frequency of the resonant mode excited. The intrinsic coating loss $\varphi(f_0)_{coating}$ is then obtained from(39),

$$\varphi(f_0)_{coating} = \frac{E_s}{E_c}(\varphi(f_0)_{coated} - \varphi(f_0)_{substrate}) - \varphi(f_0)_{coating\ thermoelastic} \tag{1.10}$$

where $\varphi(f_0)_{coated}$ is the measured loss of the coated sample, $\varphi(f_0)_{substrate}$ is the measured loss of a nominally identical uncoated substrate, and E_s and E_c are the elastic energies stored in the substrate and coating respectively.

The coating thermoelastic loss $\varphi(f_0)_{coating\ thermoelastic}$ can be calculated using the formulas derived by Fejer *et. al.*(40), and is associated with the irreversible flow of heat driven by temperature gradients in the coating.

The above procedure for the quantification of internal friction in mirror coating applies to both coatings on cantilevers, and to coatings on discs/cylinders(41).

However, it should be noted that in calculation of Brownian thermal noise, there is an underlying assumption that the amorphous structures of the mirror coatings are homogeneous and isotropic; over what length scale this assumption is valid is unknown.

A fully comprehensive mathematical treatment of the Brownian thermal noise with respect to the Fluctuation-Dissipation Theorem summarised here, as well as all other known sources of thermal noise and their relation to mechanical loss, can be found in the reference text 'Optical Coatings and Thermal Noise in Precision Measurement'(36).

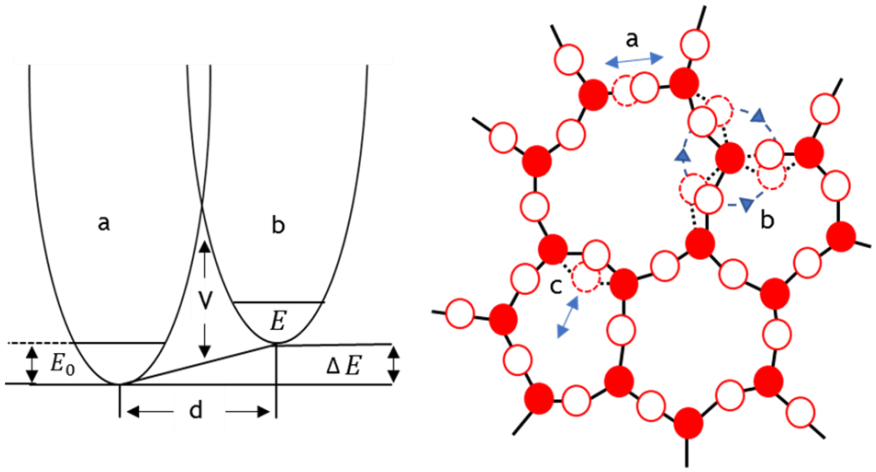

Figure 1-5 Double well potential for an atom with two meta-stable states, and a small energy barrier between them, highlighted for the bond flipping mechanism in amorphous silica.

The current structural interpretation of the Brownian thermal noise that results from internal friction is based upon the motion of a particle in a double well potential, described by Hunklinger (42) for the case of silica, and is sketched in Figure 1-5.

In figure 1-5 (left), the double well potential model describes two metastable states of oxygen, with a small energy barrier between them, in which mechanical dissipation results from thermally activated transitions of oxygen between these states.

Possible transitions are shown in Figure 1-5 (right), include motions parallel or perpendicular to the bond direction (A & c), or small angle rotations of the SiO_4 tetrahedra (b).

The following section briefly discusses material structure, specifically the nature of amorphous materials, their challenging physics and technological importance.

1.6 Amorphous materials

The material structures studied in this thesis are amorphous in nature, glass-like, in that they do not possess the periodic long-range atomic ordering inherent to crystalline structures. Whilst the term 'glass' is conventionally reserved for amorphous structures that have been formed in a 'quench from the melt', it is used interchangeably with the general 'amorphous solid' term for brevity.

A perfect crystal can be described in its entirety by the translational symmetry of its unit cell, whilst the description of an amorphous structure has historically been limited to its short-range chemical order, common to its crystalline counterpart, but without the translational symmetry.

A 'perfect' amorphous structure may be described as homogeneous and isotropic close to the scale of its short-range chemical order; and similarly, in a perfect crystal, 'defects' constitute departures from structural homogeneity.

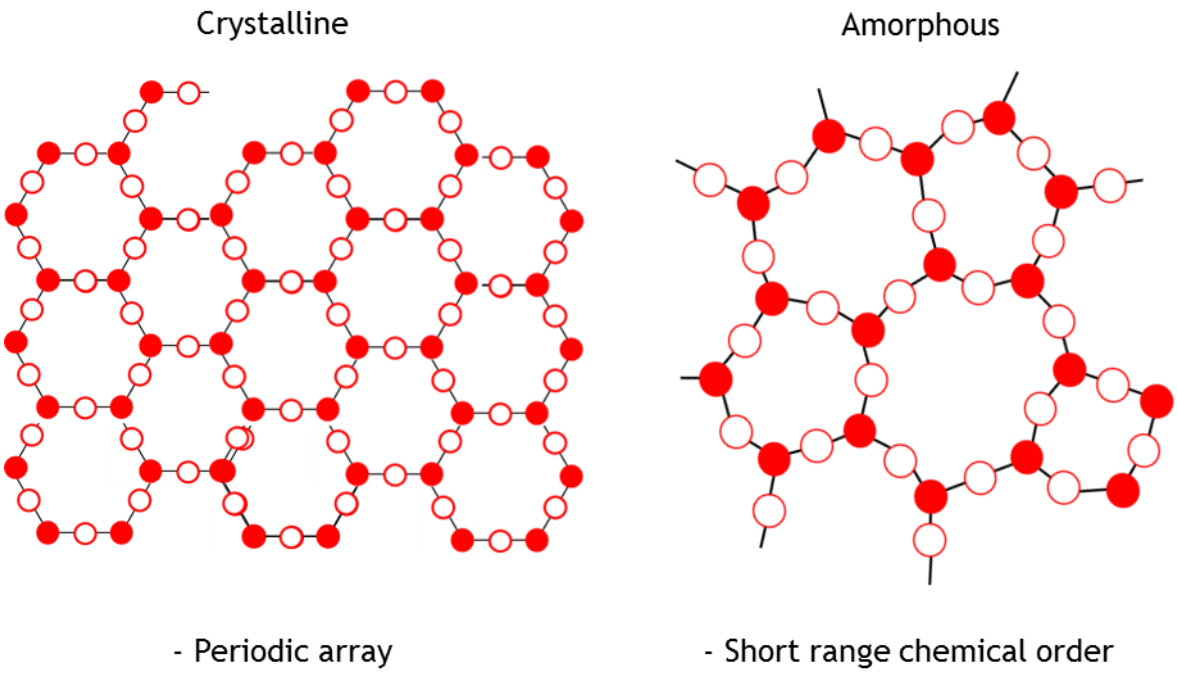

Figure 1-6 Atomic arrangements in (left) a periodic crystalline solid, and (right) the disordered structure of an amorphous solid.

These are the two idealized extremes of structural order in materials and are sketched 2-dimensionally in Figure 1-6 for crystalline (left) and amorphous (right) materials; however, a spectrum of intermediate phases usually exists in solids, encompassing various contributions from both extremes.

At the center of this spectrum is the 'polycrystalline' phase of matter that describes the structure of most inorganic solids found in nature, and very loosely can be thought of as a maximally disordered crystal; conversely, a maximally ordered glass may be thought of in this context, if one considers it to consist of nano-crystallite components that are strained or distorted to the extent that structural measurements are sensitive only to its short-range order (SRO).

However, whilst the concept of a perfect crystal structure poses no difficulty, the notion of a perfect amorphous structure does. A glass must be, by definition, heterogeneous at some length scale, and thus a 'perfect' glass may be regarded as one in which structural heterogeneity is minimal at the shortest possible scales whilst remaining amorphous.

The atomic structure of glass, and nano-structured materials in general, remains a major challenge for condensed matter physics in understanding their structure/property relationships, in comparison to crystalline materials which through their periodicity and symmetries facilitate analytical approaches to their structure/property relations. It is essential that accurate structural models are developed for amorphous materials to facilitate a materials-by-design approach for novel structures with the desired properties.

Zallen (43) discussed three models for non-crystalline solids, particular to metal-oxides, and thus relevant to the materials studied in this thesis: the continuous random network model (CRN), first introduced by Zachariasen(44), describing a predominantly covalently bonded structure, exemplified by silica and in which stoichiometry is fulfilled by its SiO_4 primary structural unit (PSU); modified continuous random networks (MCRN) such as in silicate alloys and the tantala based alloys studied in this work, in which metal atom ionic bonds disrupt and modify the covalently bonded CRN, and stoichiometry on average is met at different length scales with less well defined PSUs; and random closed packed (RCP) structures, composed entirely of positive and negative ions, which may include transmission metal-oxides such as hafnia, zirconia and yttria (45).

Lucovsky(46) developed a classification scheme for these amorphous morphologies based upon Pauling's empirical definition of bond iconicity(47), as being proportional to the difference in electronegativity between the bonded elements.

Although bonding in a structure is never completely ionic or covalent, the classification states that a CRN is one in which the bond ionicity is less than ~ 47% and oxygen is typically 2-coordinated, for a MCRN structure the bond ionicity ranges between 47% and 67% with oxygen coordination typically increasing up to 3; RCP structures are defined by a bond iconicity greater than ~67% and where 4-coordinated oxygens are typical.

Oxygen coordination in amorphous metal-oxides increases monotonically with increasing bond ionicity, and the potential complexity of the structures increase with increasing cation oxidation number. Ultra-stable glasses are typically those in which either covalent or ionic bonding dominates within the structure as in silica, the archetypal stable glass(48).

Other relevant models include the paracrystallite theory of glass in which crystallites ≥ 1 nm are dispersed throughout an amorphous network of the three types discussed above(49), or a paracrystalline model which may have more similarity with a fine grained polycrystalline structure composed of highly strained or distorted grains.

Amorphous materials have many beneficial and technologically important properties that separate them from their crystalline counterparts. Consider SiO_2, the main component of regular window glass; both silica and quartz, amorphous and crystalline forms of SiO_2, have similar optical properties due to their identical short-range chemical order, that in conjunction with their large optical band gap (>3eV) facilitates their suitability for this application. However, it is economically unfeasible, if not impossible to make single crystal quartz windows to the same scale and homogeneity as is achieved with silica.

Furthermore, specific aspects of the amorphous structure, such as isotropy make the optical transmission independent of incidence angle. Then there is the disorder itself; the directional bonding in the covalent CRN structure of silica makes it extremely mechanically stable, like a 3D jigsaw, with the rigid SiO_4 tetrahedral arrangements preventing cooperative movement of the atoms in response to applied forces.

The effect is most appreciable from thermal expansion coefficient measurements, in which silica is orders of magnitude lower than quartz.

This arrangement effectively localizes the vibrational states of the structure, attenuating its thermal conductivity, an important property of window glass in that it insulates interiors from external temperature gradients.

Harnessing these properties of glass revolutionized the telecommunication industry with the large-scale production of low loss optical fibers. The utility of amorphous materials extends well beyond their optical applications.

Metallic glasses share the strength of their crystalline forms but are less susceptible to deformation and fatigue, a result of their disorder, making them superior structural materials; low density polymeric glasses such as polystyrene that form a class of lightweight structural materials; amorphous semiconductors that have revolutionized the electronics industry, through large-scale deposition of homogeneous electronically active material, and miniaturization of components due to their superior dielectric properties; amorphous solar cells that utilize their isotropy; high resistance magnetic glasses in high power electrical transformers and data storage applications. The list goes on and continues to grow.

Glass is ubiquitous in nature, and can be found in forms ranging from ‘perfectly’ amorphous to the limits of polycrystallinity. The range of structures arise from the geological timescales over which they form, and reflects their morphological dependence upon thermal history, and their far from equilibrium nature.

Examples include igneous rock, formed through the solidification of magma, which when formed above the surface, cools quickly, forming very fine grained crystalline inclusions such as in basalt; when the cooling is much more rapid, obsidian may be formed which is much closer to the idea of a ‘perfect’ glass.

When formed below the surface, cooling and solidification occurs over much longer timescales, and coarse polycrystalline structures form, as in the case of granite. The message here is that when given enough time for the solid state of matter to form from lower density phases, its final form will be in its lowest energy configuration, the crystalline phase.

Thus, amorphous structures are described as far from equilibrium structures that reach the solid state out with the timescales required to settle in their lowest energy configuration. Conversely, this phase transition can occur in the opposite direction when enough energy is applied to the system.

Over millions of years, deep within the earth's crust, amorphous carbon (coal) subjected to enormous pressure and temperature transforms into the archetypal perfect crystalline structure, diamond. Mimicking nature, modern large-scale glass production, including window glass and metallic glasses, are made by a rapid quench from the melt.

However, many of the most technologically important materials utilized in the electronics industry, and for high precision optics, require highly uniform depositions at the nano-scale.

Thin-film deposition technologies developed for this requirement include evaporative methods such as molecular-beam epitaxy (MBE) and electron-beam evaporation, gas-phase chemical processes including chemical vapor deposition (CVD) and thermal oxidation, liquid-phase chemical processes such as electroplating and spray pyrolysis, and glow-discharge processes such as sputtering which include magnetron sputtering, reactive ion plating and ion beam sputtering (IBS).

The common theme between these techniques is that the phase change to the solid amorphous structure occurs practically instantaneously at relatively low temperatures, like an instantaneous quench from the melt, preventing crystallization and resulting in a structure closest to the idealized 'perfect' amorphous solid of a frozen liquid. A comprehensive review of the techniques mentioned, and many more can be found in the reference text by Seshan(50).

The materials studied in this thesis were deposited using IBS processes which produce films of the highest density, best substrate adhesion, and superior optical properties(50).

It is the only technique currently available that can produce optical coatings to the scale and tolerances required for the aLIGO Ti:Ta_2O_5/SiO_2 multi-layer ETM mirror coatings. Tolerances include <0.5 nm amplitude deviations from flatness over a 160 mm central region of the 340 mm diameter mirrors, absorption losses less the 0.5 ppm and scattering losses <2 ppm(51).

IBS involves the acceleration of ions such as argon, to a target material, which when struck with sufficient energy, the ion momentum is transferred and atoms are ejected from the target surface, which then coat the substrate.

The target may be monatomic, an alloy, single crystal or polycrystalline; the sputtering chamber may also include an injected reactive species such as oxygen if a metal-oxide thin film is the desired result of sputtering a pure metal target.

A basic schematic of the process is shown in Figure 1-7 highlighting the simultaneous coating of two substrates as required in aLIGO for maximal cavity equivalency of the two interferometer arms; the closer view of the sputtering also indicates the possibility for impurities in the target making their way to the substrate, and the possibility of sputtering clusters of atoms as the beam etches away the surface.

The substrates are rotated in a dual planetary setup; each of the substrates rotate independently of the rotating base plate they are attached to, which helps to achieve a uniform and homogeneous coating by avoiding any preferential deposition by the system.

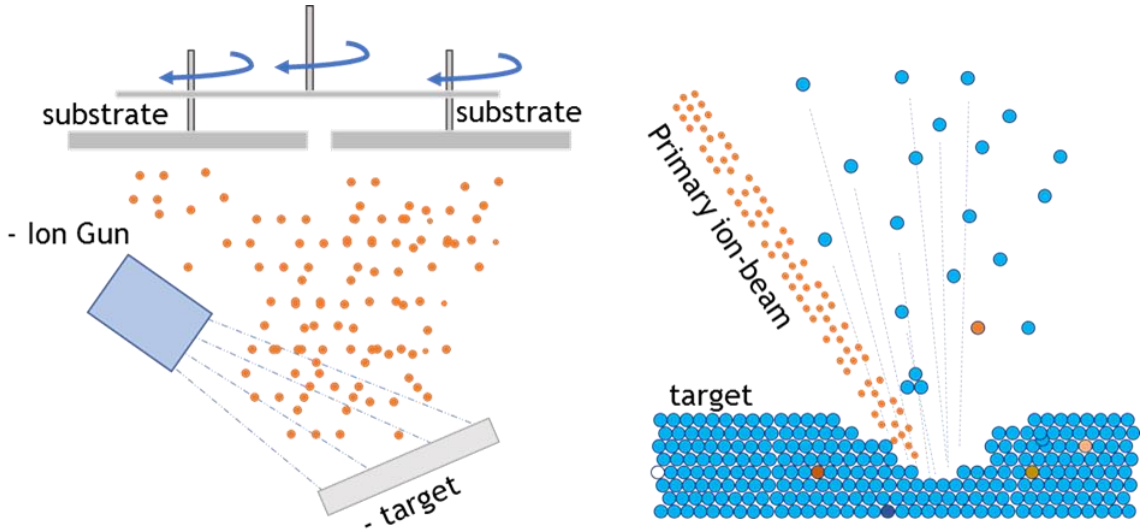

Figure 1-7 Schematic of the Ion beam sputtering setup for aLIGO which utilises dual planetary motion of the substrates to improve deposition homogeneity. The close-up of the sputtering target highlights the posiibility of non-uniform deposition of impurity atoms, or small ordered regions ablated from the surface.

The energy dependence of sputtering can be generalized to four regimes, with incident ion energy ranging from close to the binding energy to several MeV. The low energy regime spans a few eV to ~50 eV and results in very little sputtering. knock-on energy regime, ~40–1000 eV, is energetic enough to eject up to ~10 atoms per, and depending upon, each individual collision sequence.

The collision-cascade regime occurs with incident ion energies between ~1-50 keV, and can break all bonds in a spherical region near the site of impact, generating higher yields than in the knock-on regime. Last is the high energy regime, >50 keV, in which ion implantation of the target occurs, and little sputtering results as the energy is deposited far from the surface.

The structure of amorphous materials has historically been investigated through scattering experiments, with sensitivity only to their short-range order (SRO), employing probes such as electrons(52–57), neutrons (58–63) and X-rays(64–68).

With the growing interest in structural investigations of amorphous materials, because of their increasing technological importance, large variations were found in their macroscopic properties that could not be explained by their very similar short-range structural measurements, and thus motivated the development of techniques to study structural order at intermediate scales.

Indeed, medium-range-order (MRO) has been shown to exist in glasses, through improved scattering techniques using electrons (69–76), neutrons(77–81), and X-rays(72,82–84). However, it is still notoriously difficult to invert these data into structural models of the amorphous structures, as many different atomic configurations can be described by the same data.

The unique ability in electron microscopy, to probe structures down to the atomic scale, is its most attractive quality; it is however a destructive technique, and a specimen cannot be used in subsequent complementary experiments. This is because electrons have an extremely short mean-free-path for interacting everts, such that samples must be prepared for electron transparency, in the tens of nanometer range; these aspects will be discussed further in Chapter 2.

The same is not true for neutron and X-ray scattering experiments; they do not require intricate specimen preparation, and can probe bulk, unprocessed sample materials without damaging them. This is a plus point for these techniques, it is however more of a requirement than a choice, and more so in neutron scattering.

The scattering cross sections for neutron and X-rays are many orders of magnitude lower than that of electrons, and they therefore require a thicker specimen to obtain useful signals; the concept of cross-sections shall be covered in Chapter 2.

Furthermore, neutrons (predominantly) and X-rays allow probing of the atomic nuclei at accessible energies, as they do not participate in the Coulomb interaction as electrons do. It comes down to picking the right tool for the job, depending on what information you want, and what interactions take place in the measurement.

Regardless, the future of amorphous structure determination and its relation to macroscopic properties lies in computational modelling, utilizing various experimental measurements of SRO and MRO as constraints on the modelled structures.

The modelling is performed with classical approaches in molecular dynamics (MD) simulations, and utilizes quantum mechanical constraints obtained through density functional theory (DFT). Remarkable success has already been achieved using these approaches for silica in relating its structure/property relationships(78,85–96).

1.7 Discussion & Summary

The recent detection of gravitational waves by aLIGO(1) has opened a new window of observation upon the Universe, indeed a new era of astronomy is born which can impart knowledge of the beginnings and workings of the Universe that is not possible with EM based astronomy.

Furthermore, long baseline interferometric methods have proved an effective means for this new astronomy, and the drive now is toward improved sensitivity and international detector collaboration.

The research presented herein represents the effective collaboration between the fields of gravitational wave detection and condensed matter physics. These efforts attempt to improve detector sensitivity through understanding the link between atomistic structure and macroscopic mechanical dissipation in amorphous materials, with the end goal of enabling the creation of lower noise mirror coatings by design.

The following chapters will explain the techniques used to probe the amorphous structures of the mirror coatings, the results of the experiments, and any new insight thereby obtained.

2. Methods for atomic structure investigations

2.1 Introduction

Modern methods for the elucidation of atomic structure are predominantly based upon scattering of an incident probe beam with the atomic structure of the material in question, specifically, diffraction is the scattering process of an incident probes wavefront modulation upon encountering an object.

Probes commonly employed in this approach are electrons, X-ray photons and neutrons; however, the choice of probe primarily depends upon the experimental facilities available and what information the interaction of that probe with the structure will relay. In all cases, features of the atomic structure (objects) that impede the incident wavefront are encoded in the modulated wavefront.

Whilst the similarity of these methods lies in the geometrical theory of diffraction(97), dissimilarities arise from the cross sections for elastic and inelastic scattering which describe how that probe interacts with the specimen(98), and shall be explained further in the following sections.

Their common basis, the atomic scattering factor, is a measure of the scattering amplitude of the probe incident radiation by an isolated atom, obtained through a Fourier transform of the atom's spatial density distribution pertaining to that interaction. For a spherically symmetric distribution, the atomic scattering factor, $f(q)$, is defined as

$$f(q) = \int \rho(r) e^{iqr} d^3r \tag{2-1}$$

where $\rho(r)$ is the spatial density of the scatterer in its centre of mass frame,

$$q = |\boldsymbol{q}| = \frac{4\pi \sin\theta}{\lambda} \tag{2-2}$$

q is the magnitude of the scattering vector (momentum transfer), θ is the scattering semi-angle, and λ is the wavelength of the probe. These expressions shall be explained in greater detail in the coming sections, but for now serve to illustrate the mathematical equivalence of the basic scattering process, irrespective of the probing radiation.

X-rays are scattered by the electron shells of the atoms, invisible to the positive atomic nuclei(99), meaning that $\rho(r)$ in equation (2-1) is the electron charge density around the nucleus; electrons on the other hand are scattered by the electrostatic potential of the atomic nuclei and electron shells(100), thus $\rho(r)$ in equation (2-1) represents the potential distribution of the atom.

Neutron scattering arises from the interaction with the delta-function potential of nuclear forces(101), in this case $\rho(r)$ in equation (2-1) represents the spatial density distribution of the nucleus. As $f(q)$ is a Fourier transform of a density distribution, those with greater extension in real-space are attenuated more strongly with increasing q; the electron scattering factor therefore falls off faster than that for X-rays, and as the Fourier transform of a point in real space is a constant in reciprocal space, the neutron scattering factor is effectively independent of q.

Neutrons strictly have two scattering interactions with nuclei, nuclear as described, and magnetic which has an extended spatial density in comparison with associated q dependence. The atomic scattering factor and its relation to cross sections shall be covered in greater detail in the proceeding sections.

Electron diffraction in the transmission electron microscope is the method used for atomic structure investigations in this thesis. It offers the greatest possibility for coherent scattering (scattered electrons waves with a phase relationship) within the specimen, with ratios of scattered intensity, $1:10^{6}:10^{-2}$ for X-rays, electrons and neutrons respectively(98). It is also possible to form probes <<1nm diameter with electrons, allowing differences in short range order to be determined between nano-volumes of the material, as well as determine longer range correlations; this unique ability is what sets electron probe experiments apart from other available methods, and highlights its importance.

Conversely, with X-rays and neutrons, much larger volumes are probed (a limitation of their longer wavelengths), giving an average picture of the local environment, insensitive to variations of the local atomic structure. Additionally, electron diffraction is the most efficient method for the collection huge volumes of diffraction data due to the vastly greater speed of acquisition in comparison to the other methods.

As the development of the electron microscope was pursued to exceed the resolution available from optical microscopes, some basic principles of optical imaging are covered in the following section which are fundamental to imaging and diffraction in the electron microscope.

2.2 Imaging & the limits of resolution: Abbe's theory

Due to diffraction and interference, it is impossible to achieve perfect focus in an optical system that utilises the wave properties of particles(102). Diffraction results when an incident wavefront encounters an object, which includes the edge of a lens, or any superimposed aperture.

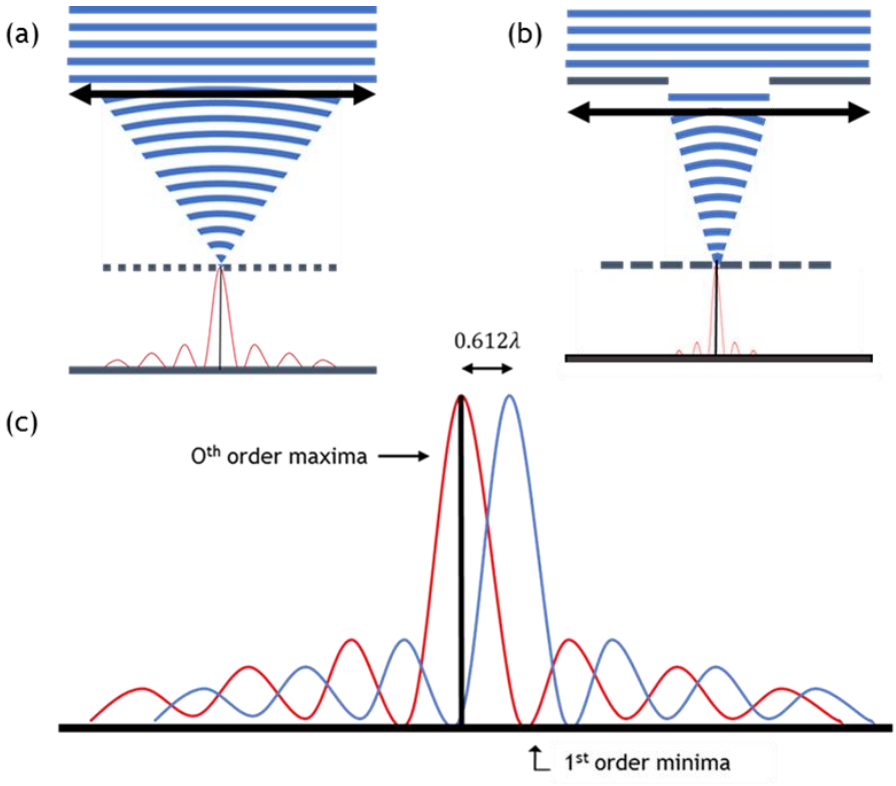

Figure 2-1 Diffraction of an incident wavefront from a large (a) and small aperture (b). Criteria for the resolution of two distinct points: must be separated at least by the distance between the 0th order maxima and the first minima (c).

The diffraction of a point-source plane-wave encountering a circular aperture is sketched two dimensionally in Figure 2-1, for both a large (a) and small (b) aperture, highlighting the modulation of the incident wavefront.

Focussing a point light source with a circular lens, does not result in a perfect dot, instead an Airy disc is formed which is composed of concentric circles that radially diminish in intensity.

The profile of the Airy disc and its dependence upon aperture size is sketched in the bottom of Figures 2-1(a,b); the on-axis maxima is the 0^{th} order diffracted ray, with the n^{th} higher order maxima located exactly at where the constructive interference of waves differ in path length by n-wavelengths; the minima are due to the interference of waves that are out of phase.

In Figure 2-1(c) the limits of resolution are shown to occur when two points are separated by the distance between the 0^{th} order maxima and the first minima; resolution is the empirically described capability of discriminating between two points which will appear as a single point if the object is just below the available resolution.

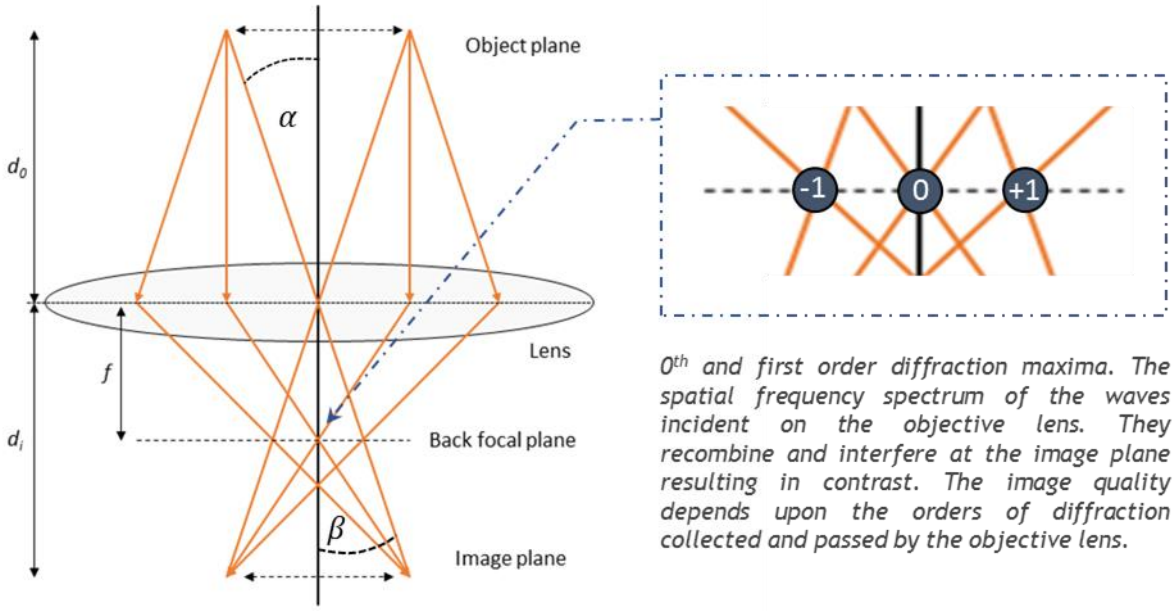

Figure 2-2 A schematic exemplifying Abbe's theory of image formation.

Ernest Abbe developed the theory of image formation for the light microscope in 1873 based upon observations of the diffraction phenomena just discussed, correcting the false assumption that lens quality was the limiting factor in the resolving power of a microscope(103).

Image formation in the Abbe theory progresses in two stages and is sketched in Figure 2-2: The object scatters the incident light by diffraction, and an angular distribution of these diffracted rays are collected by the objective lens which focusses them onto the back focal plane.

This is the diffraction pattern of the object, containing all the available information about the object that can appear in the image; it is mathematically equivalent to a 2D Fourier transform of the object, a decomposition into its constituent spatial frequency components, their binning and distribution in reciprocal space.

The diffracted rays propagate beyond the back focal plane to the image plane, where they interfere to form an inverted image of the object; this is mathematically equivalent to an inverse Fourier transform of the diffraction pattern from reciprocal space (defined at the back focal plane) to real space.

The simplified depiction of the imaging process in Figure 2-2 represents diffracted beams from two points of a periodic object, non-periodic objects are treated in the same way; the only difference is that the scattering in reciprocal space is continuous in contrast to the discrete localisation of diffraction maxima from a periodic object.

Three important distances are defined in Figure 2-2, the separation of the object plane and the lens (d_0), the distance from the lens to the image plane (d_i), and the lens to back focal plane separation (f, the focal length). These are the principal planes of a lens, and their relation is given by Newton's lens equation:

$$\frac{1}{f} = \frac{1}{d_0} + \frac{1}{d_i} \tag{2-3}$$

Newton's lens equation is also used to define the magnification of a convex lens,

$$M = \frac{d_i}{d_0} \approx \frac{\beta}{\alpha} \tag{2-4}$$

which is also, in the small angle approximation (<10 mrads), equal to the ratio of the collection angles of the lens subtended at the object (β) and the image (α), such that in Figure 2-2 the magnification is unity.

Following Abbe's imaging theory, the mathematical description of resolution in a perfect optical system is given by Abbe's equation:

$$r = \frac{0.612\lambda}{n \sin \alpha} \tag{2-5}$$

where r is the minimum resolvable distance between two points, λ is the wavelength of the incident light, n is the index of refraction of the media and α is the semi-angle subtended by the lens at its focal point, with $n \sin \alpha$ commonly expressed as NA (numerical aperture), which is further defined in Figure 2-3. This means that in optical microscopy, the best resolution achievable is in the region of 300 nm.

Abbe's theory importantly shows that diffraction is the foundation of image formation in the microscope, specifically, it shows that image formation requires at the minimum two diffraction orders passed through the objective, as it is fundamentally an interference phenomenon.

Furthermore, it shows that image resolution can be improved by operating at shorter wavelengths or with a larger NA, which enables the acceptance of higher order diffraction by the objective lens, with additional higher orders providing higher detail in the image (large separations in reciprocal space means small separations in real space).

Any modification of the diffraction pattern therefore directly affects the image, opening the concept of image spatial filtering; in fact, all lenses are effectively low-pass spatial filters as an infinite aperture would be required to pass all orders of the diffracted light.

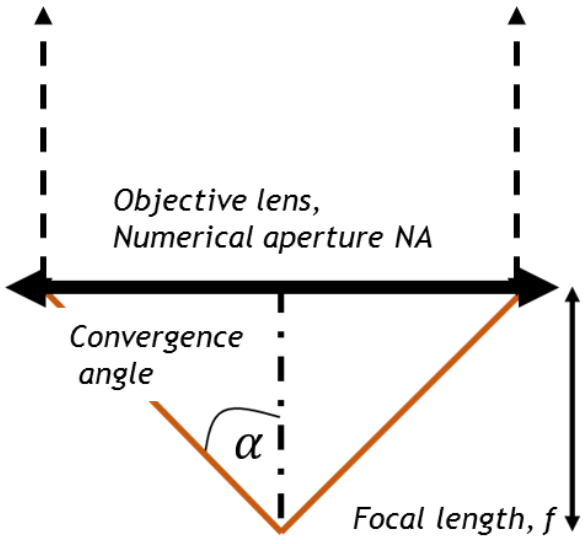

Figure 2-3 The diffraction limited imaging resolution of any wave-optical apparatus at its focal point f, for radiation of wavelength λ, is proportional to the size of its numerical aperture and and convergence angle, α.

Abbe's equation thus describes the diffraction limited resolution of an optical microscope in the absence of distortions and aberrations; if any distortions or aberrations are present, the practical limit of resolution will be limited by them.

2.3 From photons to electrons

Abbe's equation enables calculation of the diffraction limited resolution in the TEM also. To do so, the wavelength of the electron must be determined through the de Broglie equation. in the non-relativistic regime, the electron wavelength λ_e, is related to its momentum p,

$$\lambda_e = \frac{h}{p} = \frac{h}{\sqrt{2m_0 eV}} \tag{2-6}$$

The momentum is derived from the potential difference through which the electrons are accelerated, *V*, *h* is Planck's constant, m_0 is the rest mass of the electron and *e* is the charge of the electron. Modern transmission electron microscopes (TEMs) operate between 60-300 keV, resulting in electrons being accelerated to a significant fraction of the speed of light, and therefore a relativistic correction to Equation 2-6 is required to accurately determine λ_e,

$$\lambda_{e,rel} = \frac{h}{\sqrt{2m_0 eV\left(1 + \frac{eV}{2m_0 c^2}\right)}} \tag{2-7}$$

where $\lambda_{e,rel}$ is the relativistically corrected wavelength, and *c* is the speed of light. A TEM operating at 200 keV, as in this work, will therefore operate at a wavelength of 2.51 pm, theoretically better than atomic resolution. Substituting into Abbe's equation, the theoretical diffraction limited resolution r_{th}, in the absence of aberrations approximates to

$$r_{th} = 1.22\frac{\lambda_{e,rel}}{\beta} \tag{2-8}$$

where the collection angle β, is used here specifically as it depends upon the size of the lens or limiting aperture in use, as can be seen in Figure 2-2, and α is exclusively reserved for the description of convergence angles, defined as the electrons angle of incidence upon the specimen. The angle θ is reserved for all scattering controlled by the specimen.

In practice, picometer resolution is not achieved due to aberrations and limiting factors of the TEM, such as electrical and mechanical stabilities; however, spatial resolution in the TEM is fundamentally limited by spherical aberration of the probe forming lens.

Spherical aberration results when lens behaviour differs for off-axis rays; electrons further from the axis encounter stronger excitation and converge before electrons that are transmitted closer to the axis.

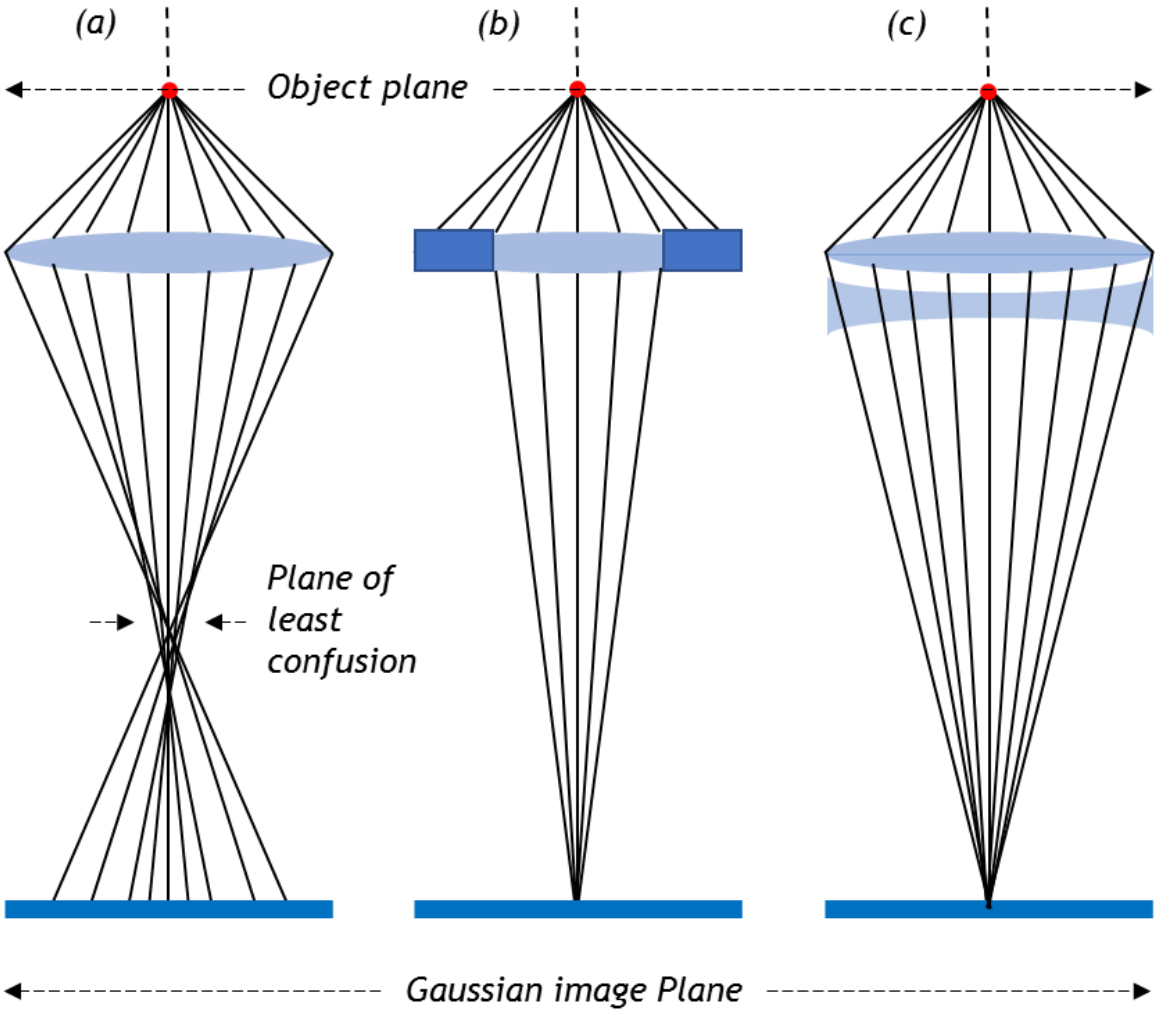

Figure 2-4 The effect of spherical aberration on image formation in the (S)TEM. (a) Incident electrons are focussed from a point in the object plane. The field behaviour of the lens has a radial dependence, and beams further from the axis are deflected with greater force, resulting in different foci for different spatial frequencies, and diminished image resolution. The plane of least confusion is the point on the axis where the smallest image is formed, least affect by the aberration. (b) By inserting a limiting aperture, the image can be brought to focus by blocking higher order diffraction at the expense of resolution and contrast. (c) A (S)TEM with a C_s corrector, approximated here with a convex lens, introduces an equal and opposite spherical aberration to cancel the effects and bring all the spatial frequencies to focus at the same point.

This results in a point object being imaged as a disk of finite size in the Gaussian image plane, similar to Figure 2-1(a), limiting the ability to magnify detail as the imaging process degrades it. The aberration is sketched in Figure 2-4(a), in which the plane of least confusion describes the position on the axis where the smallest image of the object is formed, and the radius of the spherically aberrated disc is given by:

$$r_{sph} = C_s \beta^3 \tag{2-9}$$

where C_s is a constant with dimensions of length called the spherical aberration coefficient, and is specific for a particular lens.

The practical resolution available is conventionally obtained by summing this expression in quadrature with the theoretical resolution limit given by Abbe,

$$r = \sqrt{{r_{th}}^2 + {r_{sph}}^2} \tag{2-10}$$

As both terms are approximate, it can be written as

$$r(\beta) \approx \left[\left(\frac{\lambda}{\beta}\right)^2 + (C_s \beta^3)^2\right]^{1/2} \tag{2-11}$$

The two terms vary differently with the aperture collection angle, so setting the differential of $r(\beta)$ with respect to β equal to zero, a compromise is found:

$$\frac{\lambda^2}{\beta^3} \approx C_s^2 \beta^5 \tag{2-12}$$

An optimum expression for the collection angle is then,

$$\beta_{opt} = A \frac{\lambda^{1/4}}{C_s^{1/4}} \tag{2-13}$$

where A is a numerical factor of the order unity. Substituting into Equation 2-11, a minimum value of $r(\beta)$ is obtained,

$$r_{min} = B(C_s \lambda^3)^{1/4} \tag{2-14}$$

where *B* is again a numerical factor of the order unity, and in which all other aberrations are corrected or negligible, gives the practical resolution of the TEM.

In Figure 2-4 (b) it is shown that by inserting an aperture, the effects of spherical aberration can be reduced by eliminating electrons far from the axis, allowing all the electrons to reach a common focal point.

Correcting spherical aberration in this manner is however far from satisfactory, as insertion of an aperture reduces the numerical aperture of the lens, resulting in reduced spatial resolution.

However, in recent decades, huge advances have been made in the aberration correction of TEMs; spherical aberration correctors have been developed that introduce negative aberrations which effectively cancel out the positive spherical aberrations of the probe forming lens using complex arrangements of multi-pole lenses.

The effect of its correction is shown in Figure 2-4 (c), where the complex multi-pole lens arrangement is approximated by a convex lens with the required lens field profile, reducing the value of C_s.

Following these advances, sub-angstrom level resolution is now routinely achieved, as is picometer precision in the measurement of atom positions(104).

2.3.1 Scattering & diffraction

Electrons are low mass, negatively charged particles which are easily deflected by passing close to other electrons or positive atomic nuclei. These electrostatic interactions cause the scattering of the electrons and are fundamental to all electron microscopy.

In the electron microscope, the high kinetic energy electrons interact with the specimen in many ways, producing a wealth of signals resulting from those interactions, and are summarised in Figure 2-5.

The back scattered signals displayed above the specimen in Figure 2-5 are of relevance in scanning electron microscopy (SEM) and are not utilised in this work; it is the forward scattered signals that are important in TEM and utilised for the structure investigations in this thesis.

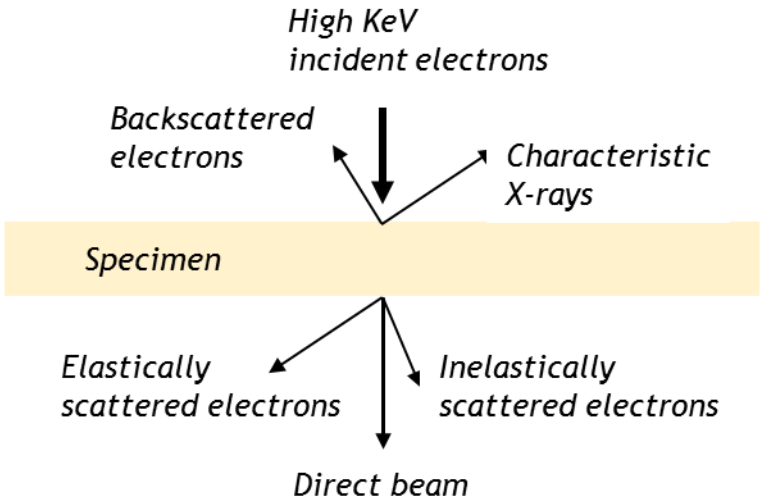

Figure 2-5 The import signals generated and collected in (S)TEM.

However, many of these signals are the basis for analytical electron microscopy (AEM)(105) and can give chemical information about the specimen studied, using for instance X-ray energy-dispersive spectrometry (XEDS), or electron energy-loss spectrometry (EELS).

These interactions can be broadly classified into two processes that describe their production, elastic and inelastic scattering, in which both processes may be further classified coherent (in phase) or incoherent (no phase relation). Williams and Carter(106) define the angular distribution of these processes as follows.

Elastic scattering is strongly peaked in the forward direction and generally occurs in the range ~ 1-10°; at higher angles, >~10°, elastic scattering becomes more incoherent. Inelastic scattering is generally incoherent and occurs at very low angles, <~1°(106). Diffraction is the special case of coherent elastic scattering in which interference phenomena are observed, and forms the basis of this work.

The probability of an electron interacting with an atom is determined by an interaction cross section, which depends on parameters such as the kinetic energy of the electron and the type of scattering atom.

Extending the interaction to a typical specimen, additional factors such as thickness, density, structural order and electron incidence angle become important; however, to appreciate the effects of these parameters, it is easier to first consider the physics involved in the scattering cross section for a single isolated atom.

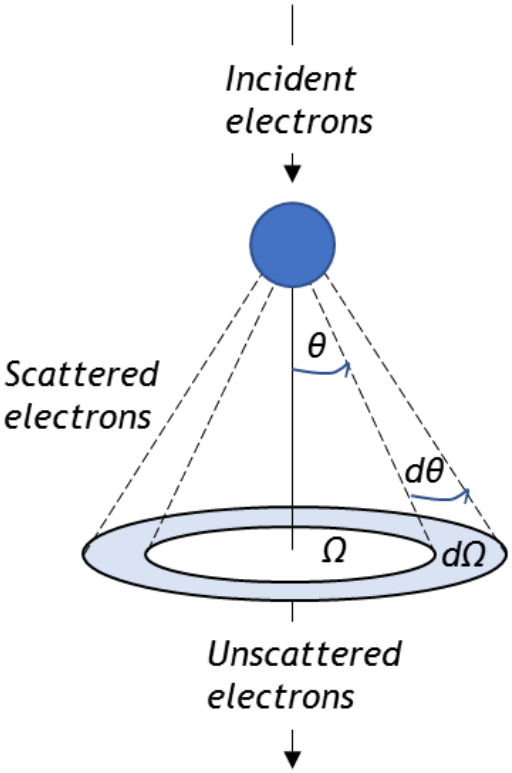

Figure 2-6 The differential cross section is simply a measure of the angular dependence of scattering for a specifc process.

Helpfully, the following analogy by Rudolf Peierls describes the concept of a cross section well, wherein 'disintegration' means inelastic,

"For example, if I throw a ball at a glass window one square foot in area, there may be one chance in ten that the window will break, and nine chances in ten that the ball will just bounce. In the physicist's language, this particular window, for a ball thrown in this particular way, has a "disintegration cross section" of 1/10 square foot and an "elastic cross-section" of 9/10 square foot."

The cross section can be defined by an effective radius of an isolated atom,

$$\sigma_{atom} = \pi r^2 \tag{2-15}$$

where a specific scattering process has a specific r. As sketched in Figure 2-6, of interest is the angular deviation of the incident electron, important for detector positioning amongst other things, and is described by the differential cross section $(d\sigma/d\Omega)$,

$$\Omega = 2\pi(1 - \cos\theta) \tag{2-16}$$

where Ω is a solid angle, and which therefore leads to

$$d\Omega = 2\pi \sin\theta d\theta \tag{2-17}$$

The differential cross section can then be written as,

$$\frac{d\sigma}{d\Omega} = \frac{1}{2\pi \sin\theta}\frac{d\sigma}{d\theta} \tag{2-18}$$

Integrating Equation 2-18 from 0 to π enables determination of the cross section for a given atom for all values of θ in units of area,

$$\sigma_{atom} = \int_0^{\pi} d\sigma = 2\pi \int_0^{\pi} \frac{d\sigma}{d\Omega} \sin\theta d\theta \tag{2-19}$$

indicating that σ decreases as θ increases.

Now considering a specimen that contains *N* atoms/unit volume, the total scattering cross section of the specimen can be defined in units of reciprocal meters by

$$\sigma_{total} = N\sigma_{atom} \tag{2-20}$$

As $N = N_0\rho/A$, where N_0 is Avogadro's number, *A* is the atomic weight of the scattering atoms with density ρ, the total cross section can be written as

$$\sigma_{total} = N\sigma_{atom} = \frac{N_0\sigma_{atom}\rho}{A} \tag{2-21}$$

Which is the total number of scattering events per unit distance that the electron travels through the specimen. The probability of scattering from a specimen of thickness *t* is given by

$$\sigma_{total}t = \frac{N_0\sigma_{atom}(\rho t)}{A} \tag{2-22}$$

where (ρt) is known as the mass-thickness of the specimen. Equation 2-22 in fact contains all of the variables that affect the scattering probability from a real specimen.

By defining the total interaction cross section in terms of inverse length in Equation 2-21, an important new parameter called the mean free path, λ_{mfp}, is defined simply as (not to be confused with wavelength)

$$\lambda_{mfp} = \frac{1}{\sigma_{total}} = \frac{A}{N_0 \sigma_{atom} \rho} \tag{2-23}$$

which has units of length and describes the average distance travelled by an electron before a scattering event.

This important parameter constrains the maximum thickness a specimen can have without undergoing significant plural scattering, ensuring that single-scattering theory is appropriate in the interpretation and analysis of images and data.

Before discussing the coherent elastic scattering of electrons in greater detail in the following section, it is highlighted that the general atomic scattering factor, Equation 2-1 introduced at the beginning of this chapter, is related to the differential elastic cross section by the simple equation:

$$|f(q)|^2 = \frac{d\sigma(q)}{d\Omega} \tag{2-24}$$

2.3.2 Elastic scattering

Elastic scattering can occur in two ways, which both involve the Coulomb force; an electron may interact with the electron cloud and result in a small angular deviation, or penetrate the electron cloud and be scattered through a high angle, due to the attraction of the nucleus. In some cases, the electron may even be completely backscattered.

Elastic scattering, strictly defined, means that there is no change in energy of the scattered electron with respect to the incident electron energy, this is however a convenient simplification; these interactions can and often do involve energy loss of the incident electrons as many electron-electron interactions are inelastic as can be electron-nuclear interactions.

Williams and Carter(107) make this approximation, they do however constrain elastic scattering to a narrow window of ~ 1-10°.

Egerton(108) on the other hand, for convenience, defines scattering to be elastic or inelastic depending upon whether the electrons respond to the field of the nucleus or to its surrounding electrons respectively.

Considering that the nuclear mass exceeds the rest mass of the electron by a factor of 1823 times the scattering atoms mass number, the energy exchange is generally unmeasurable, and thus a fair approximation.

The electron scattering in this work is treated as elastic with the assumption that scattering is predominantly from the nucleus.

Proper treatment of the scattering process requires a wave-optics approach instead of the generalised geometrical description thus far discussed. This picture of electron scattering from a single isolated atom is highlighted in Figure 2-7.

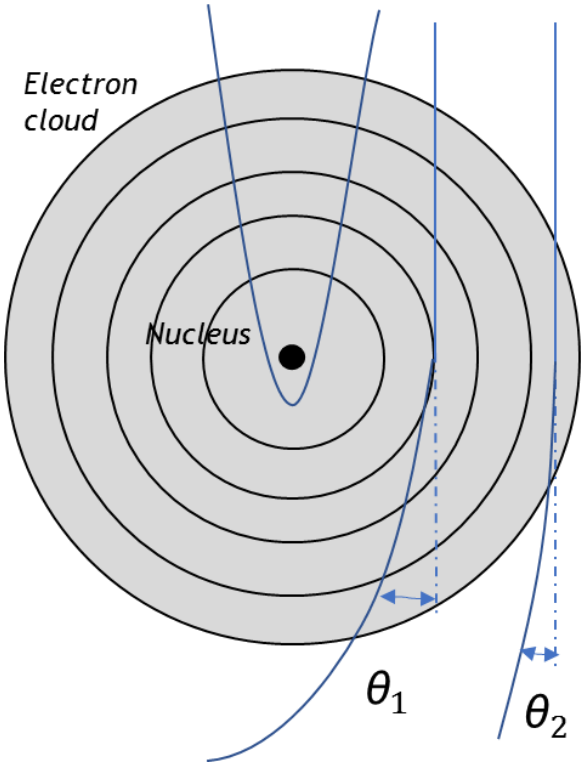

Figure 2-7: Electron scattering from an isolated nucleus.

The two regimes of electron scattering behaviour are incorporated in the Mott-Bethe formulation of the electron scattering factor, in which, the scattering processes are quantified through quantum mechanical calculations of the spherically symmetric projected atomic potentials of single isolated atoms; the treatment of a specimen is based upon a collection of such isolated atoms.

This approach is one of practicality, as presently the computational resources are not readily available to cater for variations in a solids electronic structure due to effect such as bonding. Furthermore, if an atoms valence shell electron is not in the ***s***(*l=0*) angular momentum state, the spherically symmetric potential approximation may not be appropriate.

These approximations incur an error estimate of 5-10% in the accuracy of the projected potentials(109); however, as electron scattering is mainly from the nucleus, and the core and valence electrons effectively act to screen the nuclear charge, the effect is not though to be as significant for high Z atoms(109).

There appears to be no questioning of the spherical symmetry approximation of the nuclear potential, treated here as a point sources, which may be relevant to certain high Z atoms; particularly relevant in this work, where evidence exists that atomic nuclei with a large quadrupole moment as does tantalum, are not necessarily spherically symmetric(110).

The atomic charge distribution of an atom found from a quantum mechanical description of the nucleus and electrons can only be solved analytically for the hydrogen atom; introducing one more electron makes it a many body problem, and requires numerical solution with suitable approximations.

A common approach to its solution is the Hartree-Fock procedure(109) which is a method of calculating the electron wave functions of all the electrons in the atom assuming a central potential, point source model. The total energy of the multi-electron system is minimised through an iterative variational calculus that includes electron-electron, as well as electron-nucleus interactions.

The assumption of a central potential makes the procedure computationally viable, allowing angular integrations to be performed analytically so that only the radial part of the wavefunction needs to be calculated.

Proper treatment of the scattering from high Z atoms require relativistic considerations, the kinetic energy of tantalum inner shell electrons is > 67 keV, so relativistic Hartree-Fock theory is more appropriate. In this formalism, the non-relativistic Schrödinger equation is replaced with the Dirac relativistic wave equation; it has an additional component in the wave equation for each electron and effectively doubles the computational load.

Conventionally, the projected atomic potential is obtained by first calculating the X-ray scattering factors from the electron wavefunctions, then retrieval through the Mott-Bethe formula, which is the electron scattering factor in the first Born approximation (the potential of the scatterer is much smaller than the kinetic energy of the electron), which assumes single scattering and forms the basis of kinematic scattering theory.

The radial distribution of the electron charge $\rho(r)$, calculated from the relativistic Dirac wave equation, is

$$4\pi r^2\rho(r) = \sum_i c_i \left[|Q_i(r)|^2 + |P_i(r)|^2\right] \tag{2-25}$$

where $Q_i(r)$ and $P_i(r)$ are the two components defining each atomic orbital i, of occupancy c_i, with three-dimensional radial coordinate r.

In a spherically symmetric charge distribution, the X-ray scattering factor is defined as

$$f_x(q) = \int r^2\rho(r)\frac{\sin(2\pi qr)}{2\pi qr}dr \tag{2-26}$$

The electron scattering factor, $f_e(q)$, describes the amplitude for single electron scattering by a single atom; the utility of its tabulation in first Born approximation is because it is the three-dimensional Fourier transform of the atomic potential,

$$\begin{aligned} f_e(\boldsymbol{q}) &= \frac{2\pi m_0 e}{h^2}\int V(\boldsymbol{r})e^{2\pi i\boldsymbol{qr}}d^3r \\ &= \frac{1}{2\pi e a_0}\int V(\boldsymbol{r})e^{2\pi i\boldsymbol{qr}}d^3r \end{aligned} \tag{2-27}$$

where $V(\boldsymbol{r})$ is three-dimensional atomic potential, m_0 is the rest mass of the electron, e is the charge on the electron, h is Planck's constant and a_0 is the Bohr radius.

For a spherically symmetric atom, the expression reduces to

$$f_e(q) = \frac{1}{\pi e a_0 q}\int_0^\infty V(r)\sin(2\pi qr)rdr \tag{2-28}$$

The electron and X-ray scattering factors are then simply related by

$$f_e(q) = \frac{2m_0e^2}{h^2}\left(\frac{Z - f_x(q)}{q^2}\right) = \frac{1}{2\pi^2 a_0}\left(\frac{Z - f_x(q)}{q^2}\right) \quad (2\text{-}29)$$

This is the Mott-Bethe formula, which is equivalent to solving Poisson's equation in reciprocal space, and is the convenient method of using the charge distribution to obtain the potential distribution of the atom.

However, due to the singularity at $q = 0$, the formula is substituted by the expression given by Ibers(109)

$$f_e(0) = \frac{4\pi^2 m_0 e^2}{3h^2} Z\langle r^2\rangle = \frac{Z}{3a_0}\langle r^2\rangle \quad (2\text{-}30)$$

$$\langle r^2\rangle = \frac{\int_0^\infty r^2[4\pi r^2\rho(r)]dr}{\int_0^\infty [4\pi r^2\rho(r)]dr} \quad (2\text{-}31)$$

in which $\langle r^2\rangle$ represents the mean squared radius of the atomic electrons.

The most widely referenced tabulation of electron scattering factors for TEM were by Doyle and Turner(111), however there are numerous(109,112,113), and all approximate single electron scattering from a collection of isolated spherically symmetric atoms.

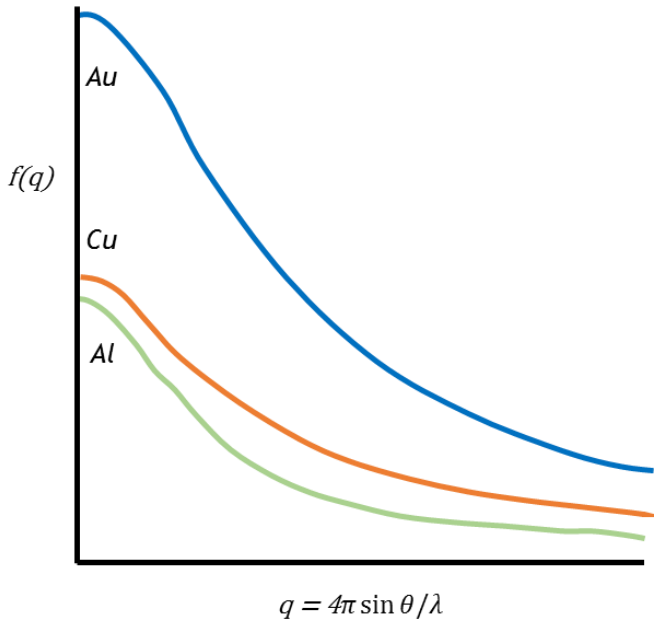

Figure 2-8 An illustration of the Z-dependence of the atomic scattering facter. Simply shows that for higher mass atoms, there is a stronger scattering dependence on q.

Figure 2-8 Highlights how diffraction modifies the angular distribution of scattered electrons from single atoms, such as calculated using the atomic scattering factor of Equation 2-29.

2.3.3 Practical Diffraction

The practical use of diffraction phenomena as discussed is for the elucidation of a materials atomic structure. A typical electron diffraction pattern from an amorphous structure is shown below in Figure 2-9(a); when averaged over a sufficient volume, diffuse rings of varying intensity are produced due to the disordered nature of the structure.

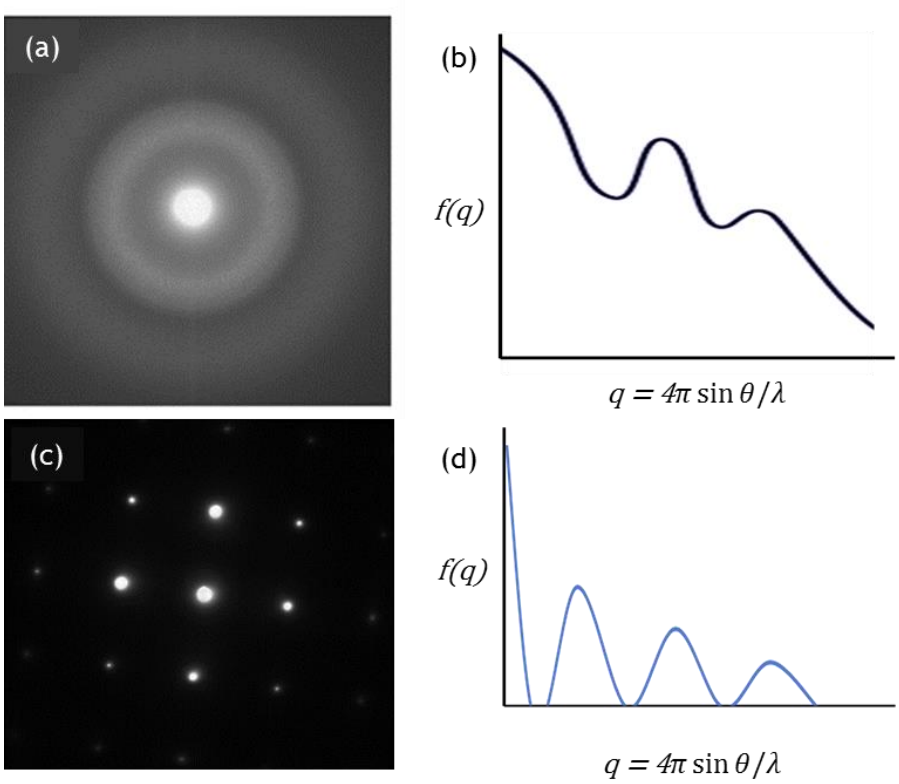

Figure 2-9 (a) typical electron diffraction pattern from an amorphous specimen. (b) Variation in scattering amplutude, indicative of (a). (c) Diffraction from a crystalline specimen, and (d) the variation of scattering amplitude scattering amplitude, indicative of (c), highlighting its greater level of coherence.

The radius of the prominent rings relates to the interatomic spacings of the distributions of nearest neighbouring atoms, from the perspective of an arbitrary atom, and highlights the persistence of chemical short-range molecular ordering and their orientationally diverse distribution.

In Figure 2-9(b), the variation in scattering amplitude, $f(q)$, is shown for the amorphous structure and is equivalent to the radial intensity variation across the diffraction pattern; the peaks occurring at specific angles reflect the SRO, and represent a deviation from the mean amplitude of uncorrelated atoms scattering independently throughout reciprocal space.

This independent coherent scattering is the scattering amplitude calculated for a single atom, plotted in Figure 2-9, and scaled by the number of scattering atoms. Inversion of this data reveals the SRO within the amorphous atomic structure and necessitates a statistical approach, which is the basis of the analysis performed in Chapter 3, and is described in detail in section 2.4.

Diffraction from a crystalline structure and its radial variation in scattering amplitude is shown in Figure 2-9(c) and (d) respectively.

The scattering amplitude of the crystal differs significantly from the case of independently scattering atoms due to the periodicity of its structure, and much more clearly highlights the interference nature of diffraction.

Each of the spots in the diffraction pattern of Figure 2-9(c) represents parallel planes of atoms from which scattered electrons constructively interfere, and are defined by the Miller indices (hkl).

The radial scattering amplitude of the crystal is represented by the well-defined maxima of $f(q)$ in Figure 2-9(d), due to the very well defined and regular interplanar spacings of the structure.

The periodic nature of a crystal enables a much more straight forward inversion of its diffraction data, which is best described by the structure factor $F(\theta)$, and explains the form of the scattered amplitude in Figure 2-9(c).

$F(\theta)$ is the amplitude scattered by a unit cell of the crystal, where the scattering angle θ defines the angle between the incident and scattered electrons. It is defined as the sum of the $f(\theta)$ terms from all i atoms that constitute the unit cell, multiplied by a phase factor.

$$F(\theta) = \sum_{i}^{\infty} f_i \, e^{2\pi i(hx_i + ky_i + lz_i)} \tag{2-32}$$

Equation 2-32, the phase factor, caters for the phase difference between atoms with atomic coordinates $x_i y_i z_i$, scattered from the different parallel atomic planes with the same Miller indices (hkl).

The plane (hkl) is defined such that it cuts the a_1, a_2 and a_3 axes of the unit cell at $1/h$, $1/k$ and $1/l$ respectively, and is demonstrated for a selection of planes in Figure 2-10(a).

Equation 2-32 shows that the scattering depends upon the type of atom $f(\theta)$, its position in the cell $(x_i y_i z_i)$, and the specific atomic planes (hkl), of the structure. Furthermore, specific combinations in the phase factor describe deconstructive interference, resulting in the scattering amplitudes of zero in Figure 2-9(d).

The mathematical relationships that describe the diffraction process are attributed to von Laue, who had shown that diffracted waves are in phase if the path difference between the waves scattered by adjacent points is an integer multiple of the electron wavelength.

The Laue equations are three simultaneous equations that define the conditions for constructive interference in three-dimensions, where the integer multiples of the wavelength are equivalent to the Miller indices of the diffracting planes:

$$a_1(\cos\theta_1 - \cos\theta_2) = h\lambda \tag{2-33}$$

$$a_2(\cos\theta_3 - \cos\theta_4) = k\lambda \tag{2-34}$$

$$a_3(\cos\theta_5 - \cos\theta_6) = l\lambda \tag{2-35}$$

The Laue condition is sketched in Figure 2-11(a) for one-dimension, showing that for two scattering centres, B and C, spaced a distance a apart, the path difference $AB - CD$ is given by Equation 2-33 when the incident beam of wavelength λ makes an angle θ_1 with the scattering centres and is diffracted at an angle θ_2.

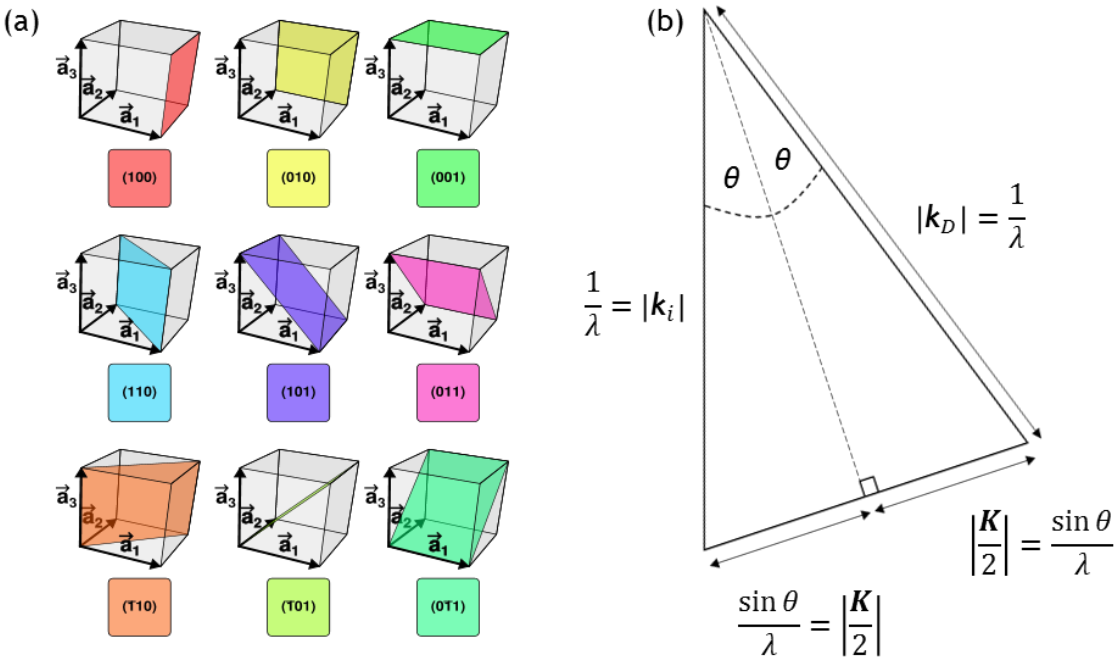

Figure 2-10 (a) An illustration of crystal planes defined by Miller indices(114). (b) Definition of the scattering vector ***K****.*

In Figure 2-11(b), the mathematically equivalent Bragg diffraction is presented in contrast to that of Laue. Whilst its physical interpretation of the process is wrong, it is utilised more often in the TEM because of its simplicity.

The Bragg description formulates diffraction in terms of a reflected plane wave incident at an angle θ to planes of interatomic spacing d, in which the path difference between the reflected planes $AB + BC$ results in constructive interference if it is an integer, n, multiple of the wavelength.

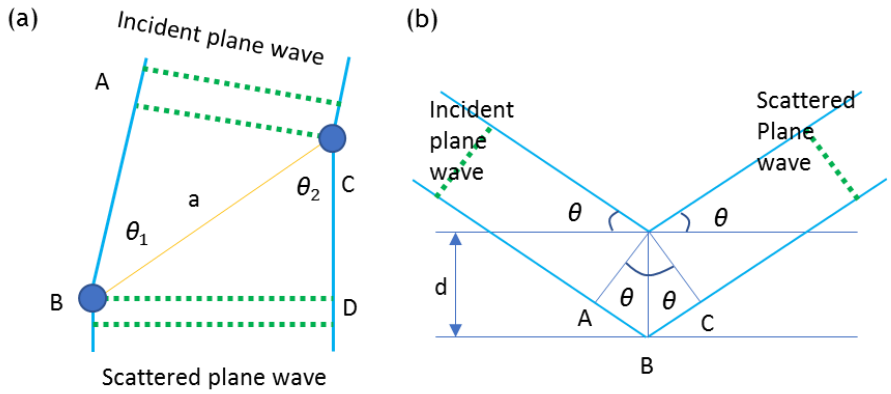

Figure 2-11 (a) The Laue condition, diffraction occurs when the path difference equals $AB - CD$*. (b) The equivalent Bragg condition or diffraction, when the path difference equals* $AB + BC$*.*

Following the definition of the incident ($\boldsymbol{k}_i$) and diffracted ($\boldsymbol{k}_D$) wave propagation vectors shown in Figure 2-10(b), the change in wave vector due to diffraction is,

$$\boldsymbol{K} = \boldsymbol{k}_D - \boldsymbol{k}_i \tag{2-36}$$

Which in the case of elastic scattering is defined as,

$$|\boldsymbol{k}_i| = |\boldsymbol{k}_D| = \frac{1}{\lambda} = |\boldsymbol{k}| \tag{2-37}$$

Expressing the diffraction again in terms of θ, it is written,

$$|\boldsymbol{K}| = \left|\frac{\boldsymbol{q}}{2\pi}\right| = \frac{2\sin\theta}{\lambda} \tag{2-38}$$

The geometrical path difference,

$$AB + BC = 2d\sin\theta \tag{2-39}$$

is the basis of Bragg's law, and when θ equals the Bragg angle θ_B, it becomes

$$n\lambda = 2d\sin\theta_B \tag{2-40}$$

This is Bragg's law; the Bragg angle θ_B, is the most important angle in TEM as it describes the angle at which the electron waves constructively interfere. Therefore, knowing λ, and measuring θ_B, the interplanar spacing of a specimen can be determined. Setting n to 1, it is clear that

$$2\sin\theta_B = \frac{\lambda}{d} = \lambda|\boldsymbol{K}| \tag{2-41}$$

and the important relation is defined,

$$\boldsymbol{K}_B = \frac{1}{d} = \boldsymbol{g} \tag{2-42}$$

where $\boldsymbol{g}$ is often referred to as the diffraction vector, and demonstrates that diffraction at the Bragg angle is equal to the reciprocal of the interatomic spacing of the diffracting planes.

The Laue equations have the solution:

$$\boldsymbol{K} = h\boldsymbol{a}_1^* + k\boldsymbol{a}_2^* + l\boldsymbol{a}_3^* = \boldsymbol{g}_{hkl} \tag{2-43}$$

which is the condition for constructive interference, where $\boldsymbol{a}_1^*$, $\boldsymbol{a}_2^*$, and $\boldsymbol{a}_3^*$ are the unit cell translations in reciprocal space, and the equivalence to the Bragg condition is demonstrated,

$$\frac{2\sin\theta_B}{\lambda} = \frac{1}{d_{hkl}} = |\boldsymbol{g}| = |\boldsymbol{K}_B| \tag{2-44}$$

By measuring the Bragg reflections of a crystalline reference specimen with known interplanar spacings, under identical experimental conditions in which the amorphous specimens are investigated, calibration of the incremental value of the scattering vector modulus δq is obtained, which is attributed to each pixel of the diffraction pattern images,

$$\delta q = \frac{2\pi}{n_{pixels} d} \tag{2-45}$$

The relationship between d_{hkl} and the lattice parameters a_1, a_2 and a_3, is determined geometrically, and depends upon the crystal system; in the case of silicon, its cell in reciprocal space is simple cubic, such that the interplanar spacings are simply obtained by

$$d_{hkl} = \frac{a}{\sqrt{h^2 + k^2 + l^2}} \tag{2-46}$$

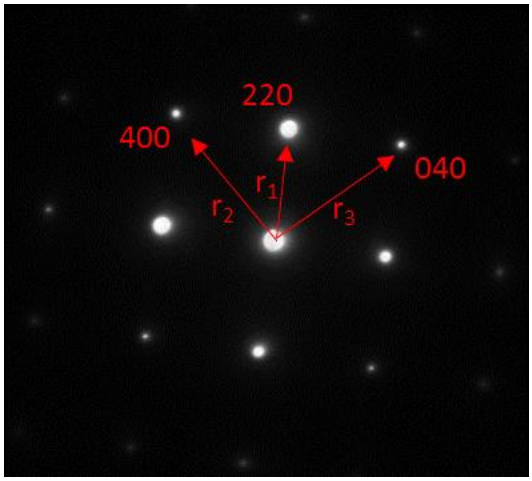

Figure 2-12 Diffraction from silicon [001] zone, and indexing of the Miller indices..

The distances between the indexed planes in Figure 2-12 are in this instance labelled r_1, r_2, r_3, which are measured with respect to the central spot, and are given by,

$$r_1 = \frac{a}{2\sqrt{2}} \; ; \; r_2 = \; r_3 = \frac{a}{4} \tag{2-47}$$

In practice, it is advantageous to average over many equivalent planes as well as many different planes to obtain precision in the value of δq.

The following section shall briefly cover the important processes involving inelastic scattering.

2.3.4 Inelastic scattering

Inelastic scattering is known to have occurred if a measurable loss of energy has been determined in the process; observed at small angles (<20 mrad), through a Coulombic interaction with the electrons surrounding each nucleus, the phenomenon is unavoidable, but is in fact one of the great advantages in TEM.

The main contribution to inelastic scattering beginning below 20 mrad is thermal diffuse scattering or phonon scattering, it is also termed quasi-elastic due to its ubiquity and often negligible effect; at room temperature, losses are around 25 meV. Any losses that may be significant diffraction do not occur before angles of ~ mrad.

Energy losses can be related to chemical, electronic and vibrational properties of the specimen, making the TEM the most versatile and compact nano laboratory in the world. Whilst all the inelastic processes are related to the general topic of electron energy-loss spectrometry (EELS), secondary X-ray signals are also utilised and form the basis of analytical electron microscopy (AEM).

Measurable energy losses are tiny with respect to the average incident beam energy in modern electron microscopes (~100-300 keV); they approach as low as ~10 meV in the most advanced instruments(115,116) enabling the study of vibrational spectra, up to ~ 1 keV in which interactions with inner shell electrons are probed.

EELS is the most important method for the characterisation of inelastic scattering processes in TEM.

The basis of EELS instrumentation is the magnetic prism, in which the electron behaviour is similar to the dispersion of white light in a glass prism, but with additional focussing properties.

The electron prism consists of carefully engineered electromagnetic polepieces which deflect the electron trajectories through a typically 90° angle, which are focussed and eventually dispersed according to their kinetic energies in an energy loss spectrum recorded on a CCD.

The spectrometers are commonly located below the viewing screen, incorporating mm range entrance apertures which control the collection angles and therefore the energy resolution. The instrumentation are varied in design, complexity and implementation, and reviewed by Egerton as well as the physics involved in EELS(108,117–119) .

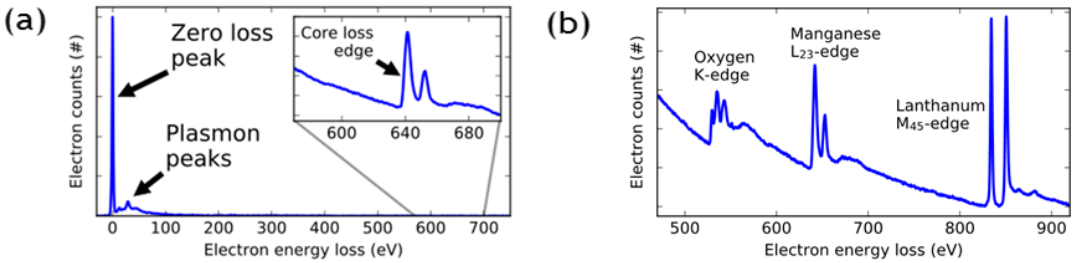

Figure 2-13 By An example of an EELS spectrum(120) (a), with a magnified view of the high energy loss range in (b).

Inelastic scattering can be generalised into processes that generate X-rays, secondary electrons, and processes that result from collective interactions with many electrons or atoms.

The characteristic energy dependencies of these processes are recorded in the EELS spectrum, with a typical example shown in Figure 2-13(a); the spectrum is grouped into two regions called the low-loss and high-loss spectrum and are generally recorded independently for sufficient energy resolution of the individual loss processes.

The low-loss spectrum includes the zero-loss peak, which represents the elastically scattered electrons and inelastic scattered electrons that fall below the energy resolution of the spectrometer, it has a typical width of 0.2 - 3 eV that predominantly reflects the energy distribution of the energy source.

The low-loss region also contains inelastic scattering signals from the valence or conduction band electrons which are the plasmon peaks (~15-25 eV); they are a collective resonance of the valence electrons, caused by the electric field of the incident electron in conjunction with their weak binding to the atom, and enable investigations of a specimen's dielectric properties.

Signals for secondary electron emission are also found in the plasmon peaks (<~50 eV), where the weakly bound electrons are transferred sufficient energy for ejection from the atom.

The cut-off energy for the low-loss spectrum is ~50 eV, after which the high-loss spectrum is defined, which is also known as the core-loss region.

The core-loss region (>50 eV), shown in greater detail with an example in Figure 2-13(b), is named so because this is where sufficient energy is transferred to core-shell electrons that result in inner-shell ionisation; this is the inelastic scattering process responsible for X-ray generation.

The region is characterised by ionisation edges relating to particular electron shells, of specific energies that are a unique identifier of a specific atom, enabling direct elemental identification and imaging of the constituent atomic species in a specimen.

There is no simple relationship between energy-loss and scattering angle; however, for most inelastic collisions, Egerton defines a double-differential cross section in a small angle approximation (<10 mrad) as a function of energy loss(108),

$$\frac{d^2\sigma_i}{d\Omega dE} = \frac{4\gamma^2}{q^2}\frac{R}{E}\frac{df}{dE} = \frac{4a_0^2R^2}{T}\left[\frac{1}{E}\frac{df}{dE}\right]\frac{1}{\theta^2+\theta_E^2} \qquad (2\text{-}48)$$

where $R = 13.6\ \text{eV}$ (the Rydberg energy), df/dE is a differential optical oscillator strength, $T = m_0v_0^2/2$ is a non-relativistic energy of the incident electron, E is the energy loss, and $\theta_E = E/(2\gamma T)$ is the characteristic scattering angle (for an energy loss E).

In θ_E, γ is the relativistic factor (greater than 1), however, γT is still less than the kinetic energy of the incident electron energy E_0.

The energy dependence of inelastic scattering is represented by df/dE, and is a characteristic of the specimen, and highlights the utility of EELS.

The most valuable information extracted from EELS with respect to the work in this thesis are thickness measurements and elemental ratio quantification of the specimens investigated.

Relative thickness measurements are derived from the low-loss region using the log-ratio method(108), which computes the specimen thickness in terms of its inelastic mean path (λ_{imfp}), by measurement of the integrated intensity I_0 of the zero-loss peak relative to integral I_{t} of the whole spectrum.

The Poisson statistics of inelastic scattering,

$$P_n = \frac{1}{n!}\left(\frac{t}{\lambda_{imfp}}\right)^n e^{\frac{-t}{\lambda_{\mathrm{imfp}}}} \tag{2-49}$$

leads to the expression,

$$\frac{t}{\lambda_{imfp}} = \log_e\left(\frac{I_{\mathrm{t}}}{I_0}\right) \tag{2-51}$$

which enables confirmation that analysis performed in the single scattering regime is valid for the specimen studied.

Elemental ratio quantification is achieved by recording the number of electrons that have undergone energy loss through inner-shell ionisation in the high-loss region.

The quantity of each element present in the specimen is proportional to the loss signal characterising it, measured as a cross section $I_{\mathrm{c}}(\beta,\Delta)$, and integrated over an energy range Δ after its core-loss edge, as illustrated in Figure 2-13(a).

Absolute quantification of an elements areal density N, is obtained from the approximate formula,

$$I_{\mathrm{c}}(\beta,\Delta) \approx N\sigma_c I_{\mathrm{c}}(\beta,\Delta) I_{\mathrm{l}}(\beta,\Delta) \tag{2-52}$$

where β is a collection angle of the spectrometer, defined by a limiting aperture, and $I_{\mathrm{l}}(\beta,\Delta)$ is the low-loss intensity integrated up to $E=\Delta$.

A detailed treatment of the signals arising from inelastic scattering processes and their role in analytical electron microscopy can be found in the reference text by Rong(105).

2.4 The (scanning) transmission electron microscope

The conventional transmission electron microscope (TEM) and the scanning transmission electron microscope (STEM) are optically reciprocal systems, as illustrated in Figure 2-14.

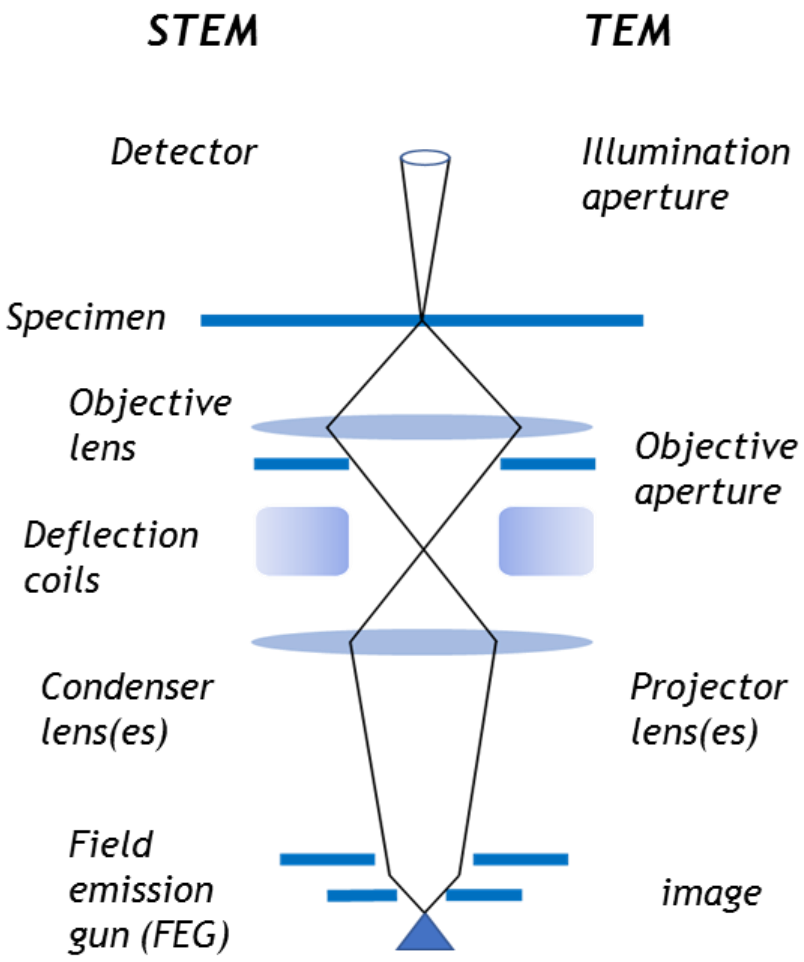

Figure 2-14 The optical reciprocity of TEM/STEM.

The pre-sample optics in the STEM are equivalent to the post-sample optics in conventional TEM; equivalently, the detector plane in STEM plays the same role as the illuminating configuration in TEM.

Imaging in the TEM, in the ideal case, involves illuminating the sample with perfectly coherent plane waves, the post-specimen optics then form a magnified image of the wave transmitted by the sample.

In the optically reciprocal case of imaging with STEM, its electron source is analogous to a single pixel in the final TEM image.

The pre-specimen optics in STEM form a demagnified image of its source at the specimen, which if scanned across the specimen, results in plane wave transmission detected with a photo diode on the optic axis in the far field, and plots the image as a function of probe position.

In both cases, TEM and STEM, the image contrast will be the same, as predicted by the principal of reciprocity, and observed experimentally. Furthermore, the STEM detector, located in the back focal plane, if replaced with a pixelated detector will record a diffraction pattern at each scan position, enabling image reconstruction utilising any desired spatial frequency components or combination thereof.

The column of the (S)TEM is comprised of a series of electromagnetic coils, electromagnetic lenses, and apertures which are operated under high vacuum, that control the direction and rate of the electrons transmitted through the specimen to the detection instrumentation; this behaviour is described by the geometrical optics and scattering physics in the previous sections.

The electromagnetic coils, named shifts, tilts and stigmators, are set during the alignment process, to ensure that the electron beam is symmetrical and centred, as it passes down the optic axis of the column(121).

Electromagnetic lenses consist of copper wire coils inside iron pole pieces; when a current is passed through a coil, the magnetic field generated in the bore of the pole piece converges the electron beam, enabling control over the magnification of the electron beam, images and diffraction patterns.

Apertures in the lenses, usually made from platinum or molybdenum, are primarily used to limit the collection-angle β, of the electrons, and minimise the effects of aberrations.

2.4.1 Electron sources

Electron sources in the TEM come in two varieties: thermionic and field emission sources (FEGs, 'field emission guns'). As the name suggests, thermionic sources produce electrons when they are heated, whereas FEGs produce electrons when a large electric field is applied, between it and an anode.

Thermionic emission operates on the principal that if a material is heated sufficiently, the electrons will gain enough energy to overcome the work function Φ and electron emission will ensue. Thermionic emission is described by Richardson's law which relates the operating temperature T of the source to its current density J,

$$J = AT^2 e^{-\frac{\Phi}{kT}} \tag{2-53}$$

where k is Boltzmann's constant, and A is Richardson's constant $(\mathrm{A/m^2K^2})$ which is specific for a particular material.

Field emission sources operate by the basic principle that an electric field, *E*, increases considerably at sharp points. An applied voltage, *V*, to a spherical point of radius, *r*, gives

$$E = \frac{V}{r} \tag{2-54}$$

The point emitters are made generally from tungsten which are sharpened to an extremely fine tip (<5 nm), and for field emission to occur, the emitter must be operated in ultra-high vacuum to ensure it is free of oxide and contaminants.

In this case, the emitter operates at ambient temperature, and is called a 'cold' FEG.

Cold field emission (CFE) is properly described by Fowler-Nordheim theory, which is the field induced wave mechanical tunnelling of an electron through an exact or triangular barrier.

CFE is characterised by the local current density at the tip, and is given in a generalised form J_K^{GB}, called the kernel current density, and is applicable to any chosen barrier model,

$$J_K^{GB} = \frac{aF_C^2}{\phi}\, e^{\frac{-v_F^{GB} b \phi^{3/2}}{F_C}} \tag{2-55}$$

where $a = e^3/8\pi h_p$ is the first Fowler-Nordheim constant, and the second is $b = (8\pi/3)(2m_e)^{1/2}/eh_p$; ϕ is the local work function, F_C is the barrier field at the tip of the emitter, and v_F^{GB} is the form correction factor for the model barrier, GB, of choice.

An alternative to this is a 'thermal' FEG, or a Schottky gun which operates with the tip at elevated temperature, to keep the surface pristine in a poorer vacuum environment. Figure 2-15 shows a schematic of a field emission electron source.

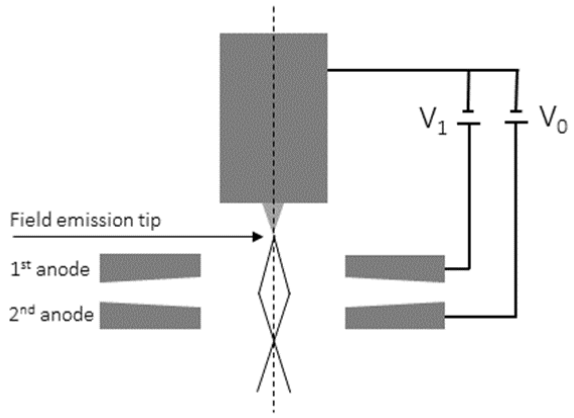

Figure 2-15: Simplified schematic of field emission electron source.

The first anode is positively charged by several kV with respect to the tip, providing the necessary extraction voltage for the electrons to tunnel out of the tip.

The second anode accelerates the electrons to the desired voltage, with the combined fields acting like an electrostatic lens that produce a crossover where the source characteristics are defined.

The relative performance of electron sources are characterised by their brightness and coherency. Brightness β, is the current density per unit solid angle of the source

$$\beta = \frac{i_e}{\pi\left(\frac{d_0}{2}\right)^2 \pi(\alpha_0)^2} = \frac{4i_e}{(\pi d_0 \alpha_0)^2} \tag{2-56}$$

where i_e is the cathode emission current, α_0 is the divergence angle and d_0 is diameter of the source.

Brightness is of utmost importance in STEM and EELS, in which very small convergent probes are used and scanned across the specimen; the more electrons that can be focussed into a small convergent probe, the more information can be extracted from the specimen, and the less exposure time is required for each scan position.

Of course, the possibility of beam damage to the specimen increase with increasing brightness; that however, is its only negative aspect.

The coherency of the electron beam emitted from the source, is categorised by its temporal and spatial coherency.

The temporal coherency, is that defined previously in the conditions for coherent diffraction; waves must have a phase relationship for interference to occur.

If the electron wave packets are all identical, they have the same coherence length, and are defined by

$$\lambda_c = \frac{vh}{\Delta E} \tag{2-57}$$

where ΔE is the energy spread of the beam, v is the velocity of the electron and h is Planck's constant. A highly stable supply of power to the source minimises ΔE and gives the electrons a well-defined wavelength.

In addition to its relevance to diffraction, its importance to EELS can be appreciated from the low-loss energy spectrum shown in Figure 2-14(a).

A smaller ΔE reduces the width of the zero-loss peak, with the improved energy resolution enabling analysis of low energy excitations in that range related to the specimens vibrational and optical properties.

Spatial coherency is related to the size of the source in such that the smaller source, the better its coherence, and implies that perfect spatial coherence is unachievable as all the electrons would need to emanate from the same point at the source.

The distance d_c defines the effective source size for coherent illumination

$$d_c = \frac{\lambda}{2\alpha} \tag{2-58}$$

where the other parameters are as defined previously, and is a general result of Abbe's theory described in Section 2.2.

Calculation of the actual beam size in the following is made for its diameter with respect to its convergence angle, in contrast to the earlier calculated resolution which was in terms of radius and collection angle.

All variables are as described previously, recalling that β in this context is brightness. An initial Gaussian diameter is assumed at the gun d_g,

$$d_g = \frac{2}{\pi}\left(\frac{i}{\beta}\right)^2 \frac{1}{\alpha} \tag{2-59}$$

the disc of minimum confusion arising from spherical aberration has diameter,

$$d_s = 0.5 C_s \alpha^2 \tag{2-60}$$

where previously, the spherical aberration limited resolution referred to the slightly larger disc in the Gaussian image plane. The calculated diameter due to diffraction is,

$$d_d = 1.22 \frac{\lambda}{\alpha} \tag{2-61}$$

These terms are added in quadrature to give the total beam diameter,

$$d_t = \sqrt{{d_g}^2 + {d_s}^2 + {d_d}^2} \tag{2-62}$$

and provides a first order estimate, as contributions are not all Gaussian, and it is assumed that any other aberrations are negligible.

For all applications, a FEG source is the brightest and most coherent available, furthermore, a 'cold' FEG, having the smallest of source sizes offers the most spatially coherent electron beam possible, with an energy spread the smallest available without monochromation(105).

2.4.2 Modes of operation

The two principal modes of operation in TEM are imaging and diffraction, which both can be performed in either the parallel or convergent beam modes of illumination.

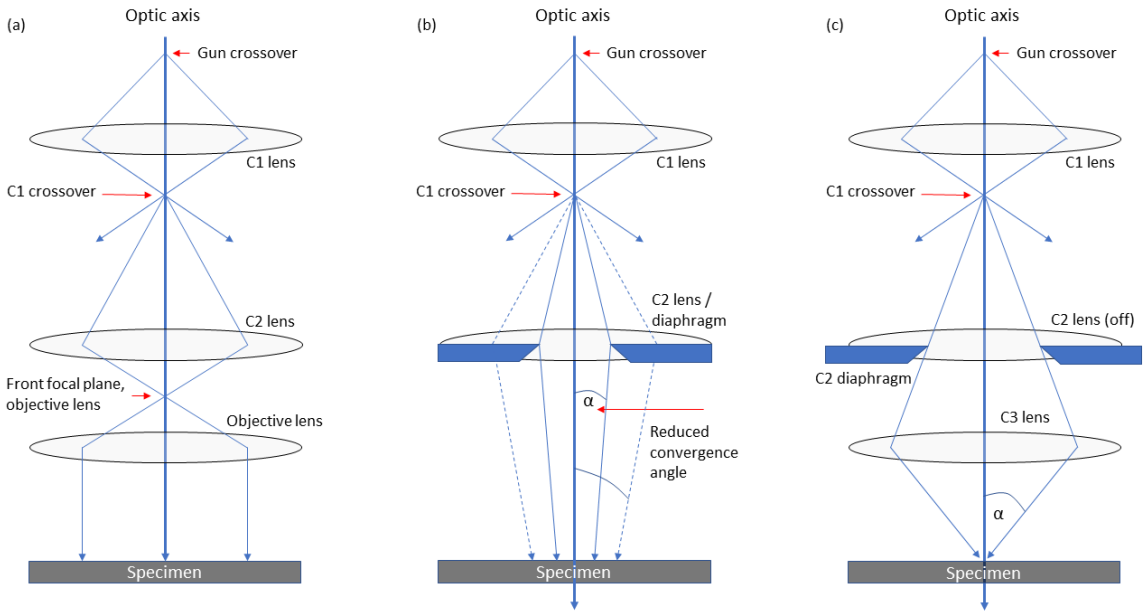

Figure 2-16: Illumination modes in the TEM. (a) parallel, (b) quasi-parallel & (c) convergent.

Figure 2-16 illustrates the differences between the illumination modes. Parallel beam (*a*) is the traditional mode of TEM operation, and is setup as follows.

The first condenser lens (C1) forms a demagnified image of the gun crossover (source), the second condenser lens (C2) is then adjusted to produce a focussed image of the C1 crossover at the front focal plane of the upper objective lens, and the upper objective lens then generates a broad parallel beam (the beam is never truly parallel in practice). The upper objective is also referred to as the C3 lens because of its role in illuminating the specimen.

In practice, the C2 lens is under focussed to fill the viewing screen with the illuminated area of the specimen; increasing the magnification, the C2 lens needs to be strengthened to keep the illuminated area of the specimen filling the viewing screen. This however, results in a reduction of the illuminated area of the specimen, and makes the beam less parallel.

In this mode, the C1 lens operates at one of number of settings prefixed by the manufacturer, so the only option available to compensate for this effect is to insert a C2 aperture, which reduces the convergence angle introduced by the strengthened C2 lens, making the beam more parallel.

This is illustrated in Figure 2-16(b), with the upper objective lens removed for clarity.

To minimise the area of the specimen being illuminated, the C2 lens can be focussed to produce an image of the C1 crossover at the specimen; in practice however, the upper objective lens acts as the third condenser lens and the C2 lens is effectively switched off.

Using C3 in this manner generates the smallest probe size and the largest convergence angles, and defines the convergent beam mode of illumination illustrated in Figure 2-16(c).

Although ideal for studying the diffraction of nano volumes of the specimen, image formation in convergent beam mode destroys the parallelism and contrast.

Convergent beam is the standard illumination mode in STEM, and image formation requires scanning of the probe over the specimen in serial, in contrast to the parallel image acquisition in parallel beam TEM.

2.4.3 Bright-field and Dark-field imaging

Bright-field (BF) imaging describes the generation of images using only the direct, un-diffracted beam, and is achieved in TEM by the insertion of a limiting aperture in the back focal plane of the lower objective lens.

Images in this case result from attenuation of the direct beam by its interaction with the specimen; mass-thickness and diffraction contrast contribute to the formation of the image, and thick and crystalline areas appear with dark contrast.

Dark-field (DF) imaging also uses a limiting aperture, but shifted so that only specific diffracted beams are transmitted and contribute to the image; equivalently, the aperture may remain on axis with the incident beam tilted at an angle.

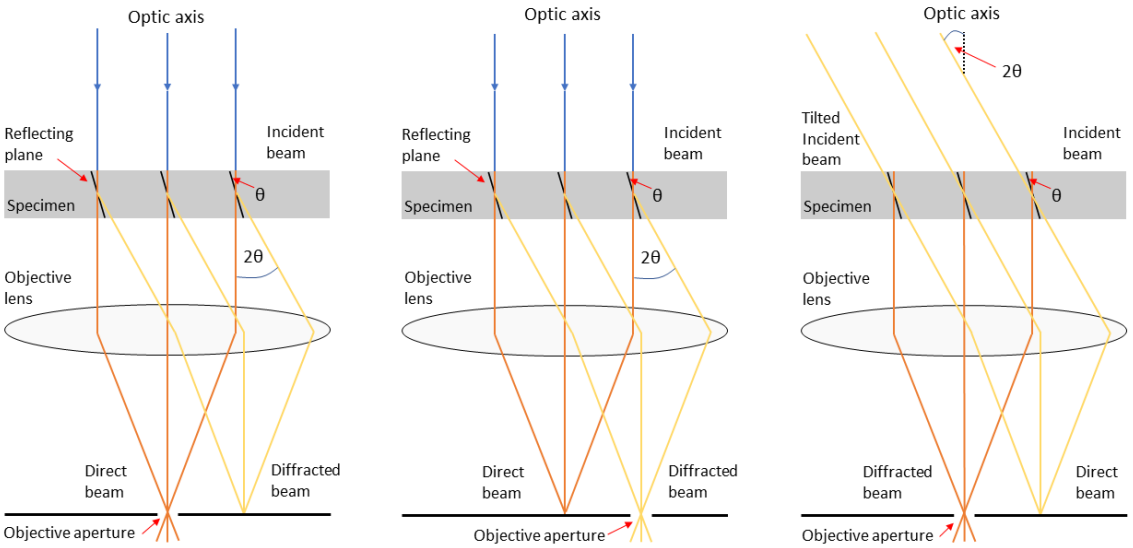

Figure 2-17 Image formation in the (S)TEM. Bright-field images are generated with the direct beam, and dark-field images with the diffracted beam at specific scattering angles.

As the diffracted beams have interacted strongly with the specimen, the dark-field approach is very useful for locating defects in crystal structure, precipitates, or crystalline deposits in amorphous materials.

Figure 2-17 illustrates how the selected beams are used to form images. Of course, the optically reciprocal STEM approach operates on the same principal in its serial acquisition of the images.

2.4.4 Diffraction in the (S)TEM

In parallel beam mode, selected area diffraction (SAD) is performed by the insertion of an aperture into the image plane to select a specific site from which to view the diffraction pattern, and is illustrated in Figure 2-18.

SAD is very useful for the determination of lattice parameters in a crystal, as the diffraction spots are sharply focussed in the diffraction plane, however it is not so useful when the requirement is the study of nano-volumes as parallel beams in TEM have a minimum diameter of ~0.5μm.

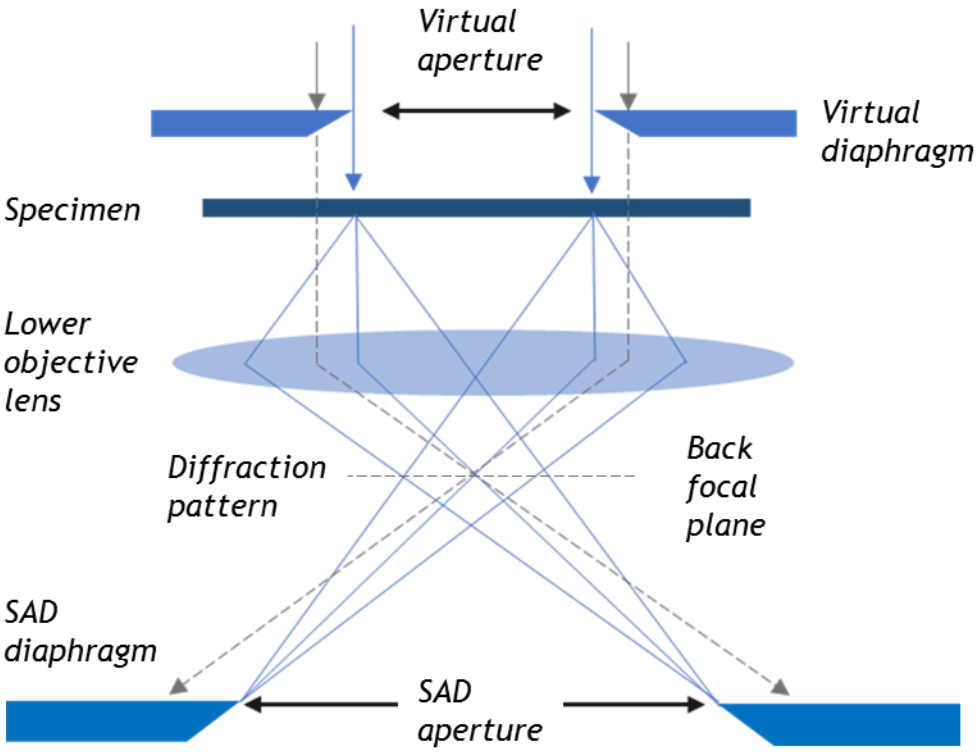

Figure 2-18 Ray diagram showing SADP formation

Convergent beam electron diffraction (CBED), on the other hand, can generate diffraction from sub-nm areas of the specimen.

The resulting diffraction spots from a crystal become arrays of discs in the diffraction plane, the diameter of which increases with increasing convergence angle.

In this work, the convergent beam approach is used for the superior spatial resolution it offers in diffraction, whilst efforts are made to maintain as low a convergence angle as possible to reduce the effect of overlapping diffraction events.

CBED patterns also enable calculation of the beam convergence angle as shown in Figure 2-19. The total convergence angle 2α is proportional to the width of the diffraction discs a,

$$2\alpha = 2\theta_B \frac{a}{b} \tag{2-63}$$

where all variables are as previously defined.

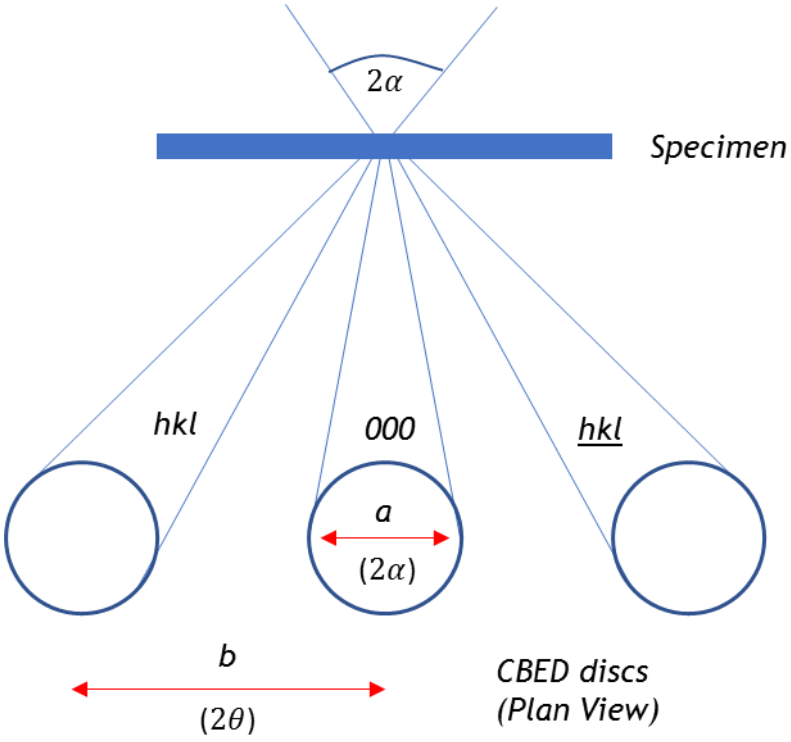

Figure 2-19 Large convergent angle electron diffraction produce discs whose diameter and separation enable calculation of α.

STEM diffraction, obviously, is exclusively CBED. Nanobeam electron diffraction (NBED) is another mode available on some field emission TEMs that utilise a quasi-parallel nanometric probe; it falls somewhere between SAD and CBED, and is generally more parallel than the probes available in CBED, but less than in SAD.

In contrast to SAD, the selection of a specimen area is made with a condenser aperture and the convergence angle of the incident beam in NBD, rather than a selector aperture in the image plane.

The remaining important aspect of diffraction in the (S)TEM in the notion of camera length, L, illustrated in Figure 2-20. It is the parameter that describes the magnification of the diffraction pattern, and is conceptual rather a physical length.

Electrons scattered through an angle 2θ at the specimen are measured on the screen with a separation R between the direct and diffracted beams, and are related by L,

$$\frac{R}{L} = \tan 2\theta \backsim \theta \qquad (2\text{-}64)$$

Equating with the Bragg equation, Equation 2-64, leads to

$$Rd = \lambda L \tag{2-65}$$

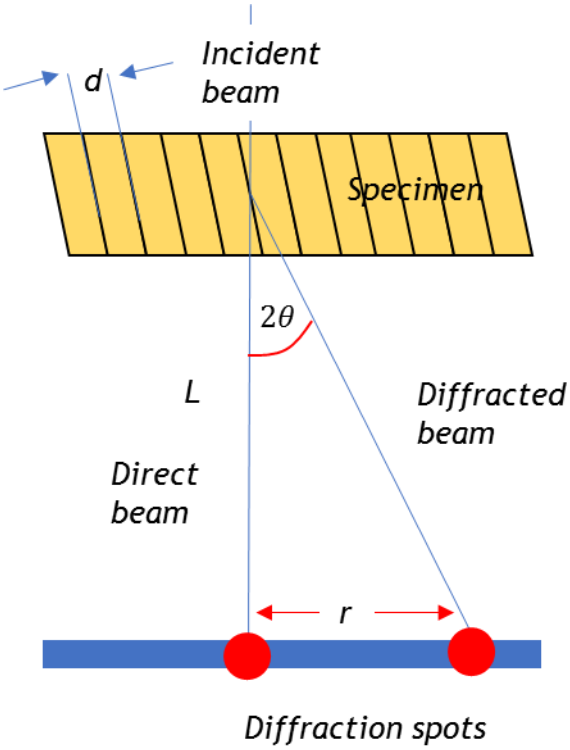

Figure 2-20 Definition of the camera length L, in TEM, a used to describe magnification in diffraction.

where λL is referred to as the camera constant. Collecting diffraction at a low camera length encompasses a wide angular range of reciprocal space, and represents a high-resolution sampling of real space.

Camera length calibrations at different L are recorded in the (S)TEM using measurements from crystalline reference specimens, and provide a working reference of the q resolution of any diffraction collected at those settings.

It is however much more prudent to perform independent calibrations of the operating conditions at the beginning of each experiments using the calibration method described in section 2-33.

2.4.5 Detection instrumentation

The simplest detector, common to all TEMs, is the viewing screen. It is commonly coated with doped zinc sulphide (ZnS) for fluorescence at ~550nm; green light is emitted in response to incident electrons, which, lying in the middle of the visible spectrum is the most relaxing for the eye.

However, the staple of image and diffraction pattern collection in the TEM, is currently done with a charge-coupled device (CCD), which can be situated above or below the viewing screen.

CCDs are metal-insulator devices that store charge generated by light or electrons in proportion to the incident intensity of the radiation; for electron detection, the CCD is covered with a scintillator plate which converts the incident electron intensity to photon intensity, whereby it is subsequently digitised by the CCD.

Conventional CCDs however do not have readout speeds high enough for STEM imaging, and instead, three semiconductor or scintillator-photomultiplier detectors are utilised as shown in Figure 2-21.

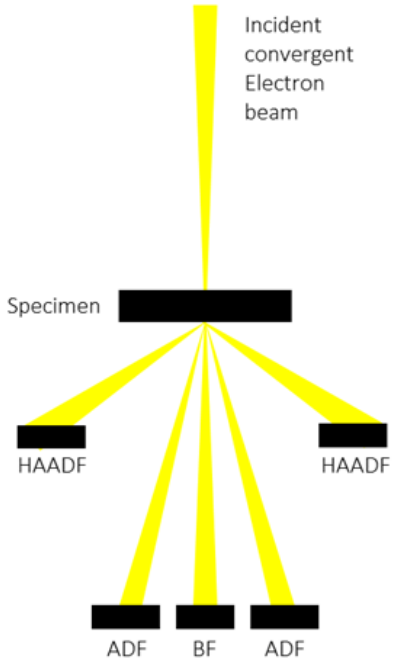

Figure 2-21 The standard imaging modalities in STEM: Bright field (BF), annular dark-field (ADF) & high-angle annular dark-field (HAADF).

They consist of a bright-field (BF) detector, which forms images using the intensity of the direct beam, an annular dark-field detector (ADF), which uses the intensity of the scattered electrons to form the image, and a high-angle annular dark-field detector (HAADF), which forms images from electrons scattered to even higher angles; all of which can be precisely controlled by altering the camera length in the post-specimen optics.

However, a new generation of direct electron counting detectors with readout speeds far in excess of CCDs are now available, allowing collection of the entire back focal plane, enabling scanning diffraction studies to be performed(122–125).

It is also possible to optically couple a TV rate video camera to the TEM viewing screen, enabling scanning diffraction studies of a somewhat less advanced degree(126,127). Both modalities are used in the scanning diffraction studies of this investigation.

The most important aspects of detector performance with respect to the diffraction work in this thesis are pixel density, dynamic range, readout speed, linearity and detector quantum efficiency (DQE).

The greater the number of pixels in the detector for a given area, the greater is the sampling resolution of reciprocal space and the angular range of diffraction recorded.

As demonstrated by Abbe, the detail available on an imaged object depends upon the recombination and interference of the spatial frequencies collected in the back focal plane of the imaging system, and as the detector records the back focal plane, more pixels means more spatial frequencies and therefore inversion of the data yields finer details of real space structures.

A high dynamic range (HDR) detector infers a highly discriminative detection of different diffracted intensity values. The higher this range the better, as electron diffraction intensities reflect the density and order of the regions from which they diffract, HDR detection provides deeper interpretation of those signals.

Furthermore, when collecting diffraction from the largest scattering angles where intensities are low, it is desirable that the detector is sensitive to these signals as well as the highest intensities of the unscattered electrons without saturating.

High readout speeds, or high frame rate detectors are of most importance in STEM, as it is a scanning method, it is desirable to record as much data as is feasible without considerable constraints on the scan durations; STEM time is expensive.

The spatial linearity of the detector response is particularly important, as different readout values in different areas of the detector, for equally incident intensities, may easily lead to erroneous conclusion drawn from the data.

DQE in a linearly responsive detector is a measure of its sensitivity to individual signals and is more important in STEM than TEM. A DQE of 1 signifies that it counts every incident electron.

2.4.5.1 JEOL ARM200cF

Diffraction investigations at the University of Glasgow were performed in the Kelvin Nano-Characterisation Centre on a JEOL ARM200F (ARM), operating at 200 keV. The ARM is a state-of-the-art atomic resolution analytical TEM/STEM with a cold FEG electron source, and is STEM probe aberration corrected for the cancellation of spherical aberration effects.

The ARM operates at accelerating voltages between 60 kV and 200 kV, and can generate electrons that are near monochromatic to within energy spread of 0.27 eV. A suite of detectors is available for chemical mapping, magnetic and electric field imaging, as well as a full range of dedicated STEM detectors. The pixelated detectors available for imaging and diffraction are the Gatan Orius SC1000A, and a custom Medipix III direct electron counter(124,125,128–130).

The Gatan Orius SC1000A is a 11 Megapixel, retractable and fiber-optic coupled CCD camera. The CCD sensor has 4008 x 2672, 9 µm pixels, covering an active area of 36mm x 24mm. The sensor has a dynamic range of 14 bits, and can record at up to 4x binning, when speed of acquisition is favoured over resolution, or if limitations on data storage are an issue.

The Orius is especially suited to diffraction studies due to its built in anti-blooming capabilities; charge overflow to neighbouring CCD pixels (blooming), due to pixel saturation from high intensity diffraction spots, has long been a challenging issue, and conventionally requires the insertion of a beam stop, to block the direct beam. The Gatan Orius SC1000A is the detector utilised in this work for the recording of diffraction patterns.

The Medipix III direct electron counting detector has been recently installed on the ARM and promises to revolutionise STEM experiments.

The 256 x 256-pixel detector is a silicon based, hybrid pixel detector, with a CMOS readout architecture; each of the 55µm pixels contains amplifiers and digitisation circuitry that determines whether the energy deposited by the electrons is within a user defined range, digitally counting those that do.

The detector records the entire back focal plane at rates of up to 1 kHz, with near perfect quantum efficiency, with a dynamic range of up to 24bits(124,125).

This detector was used to record huge scanning diffraction data sets (up to 8 GB), which were the basis for some of the fluctuation electron microscopy (FEM), and virtual dark-field imaging (VDFi) investigations, discussed later in this chapter.

2.4.5.2 JEOL JEM2100F

Initial scanning diffraction studies were performed on a JEOL JEM2100F, operating at 200 keV in nanobeam mode, at the University of Grenoble.

The JEM2100F is an analytical TEM similar in ability to the ARM, albeit without aberration correction.

It is equipped with a Schottky FEG electron source, and had been upgraded to enable scanning capability through a dedicated hardware solution by NanoMEGAS SPRL(131), which by controlling the TEM deflection coils, allows it to be operated in low convergence angle STEM mode(127,132).

The scanned diffraction datasets were recorded using an external video camera, imaging the TEM fluorescent screen with a dynamic range of 8 bits, at a rate of 100 patterns per second over the areas of interest.

2.5 Sample preparation

All but one of the amorphous mirror coatings studied in this investigation were manufactured by the Commonwealth Scientific and Industrial Research Organisation (CSIRO, Materials Science and Engineering Division, West Lindfield, NSW, Australia) using an ion-beam sputtering deposition (IBS) method.

One amorphous silica sample was studied, which was manufactured by Laboratoire des Matériaux Avancés (LMA), the ETM mirror coating vendor for aLIGO.

The deposition parameters used are a closely guarded secret by both manufacturers, and no information is available on them.

However, all CSIRO coatings studied were deposited under identical conditions, onto fused silica disc substrates, except for one which was deposited onto a silicon cantilever, with a silica thermal oxide keying layer.

Post deposition, the thermally annealed coatings were heat-treated at various temperatures in air for 24 hours.

The LMA silica specimen was taken from a tantala/silica multi-layer sample, which was also deposited onto silicon cantilever, and is believed to have been annealed for 10 hours at 500°C.

The CSIRO IBS coatings investigated were 500 nm thick single layers of pure tantalum pentoxide, and titanium cation doped tantalum pentoxide, deposited onto high quality amorphous fused silica substrate discs, measuring 25.4 mm diameter by 10 mm thick.

The tantala preparation deposited onto the silicon cantilever silicon was also 500 nm thick. The silica specimen, however, was taken from a ~200 nm multi-layer section.

Prior to investigation, specimens were prepared from the bulk samples, and thinned down to electron transparency; for crystalline materials, generally, the specimen must be ≤100 nm thick, whereas amorphous specimens require thicknesses generally ≤40 nm.

This is a general approximation and depends upon the accelerating voltage, atomic composition and structure of the specimen, as well as variations in the beam characteristics.

The thickness tolerances for crystalline specimens are however higher in general because of their periodic structure, which facilitates channelling effects of the incident electrons through the lattice.

Electron transparency can be quantified in terms of the mean free path of the inelastic scattered electrons in the specimen, as described in section 2.3.4.

The conventional cross-section method was used to prepare all coatings for TEM in this work, bar two, which were prepared by focussed ion beam milling (FIB)(133,134). These differences are not believed to hinder a meaningful comparison of the structures.

The conventional cross-section preparation begins by temporarily attaching a sample, coating face down, to a standard glass microscope slide, with hot wax (≤120 °C) to protect the coating during the cutting process. The cut is made on the uncoated side of the disc using a diamond circular saw, leaving two semi-circular pieces.

A 2 mm wide section is then cut along the diameter of one of the disc pieces, which is then cut again to remove the bulk of the substrate, and then further reduced by mechanical grinding down to a thickness of 0.5 μm.

The sample is subsequently cut in half and glued together, coating to coating, using a thin layer of epoxy resin and 'sandwiched' between sections of molybdenum rod, before insertion into a brass tube, again with a little epoxy resin.

The encapsulated material is then baked in an oven for ~1 hour at 130 °C until the epoxy resin cures. Once cured, the capsule is then cut using the diamond circular saw into 500 μm thick discs. Mechanical grinding is used once again to thin the discs down to ~ 80 μm.

The next step involves a Gatan Dimpler which grinds out a small hemispherical region of the disc using a rotating copper wheel with various grades of diamond paste, and a final polish using the finest grade of diamond paste with a felt wheel.

This is done to both sides of the disc and results in a ~ 20 μm thick area at its centre. Finally, the disc is transferred to a Gatan Precision Ion Polishing System (PIPS), and the centre is milled down to an electron transparent region of ~ 10 nm thick.

Both sides of the disc are milled simultaneously using dual argon ion beams, incident at 4 degrees normal to the disc surface, at ~4 keV, until a tiny hole is observed at the centre.

A ‘gentle’ final polish is done at ~0.5 keV, maximising the area of the electron transparent region, and minimising any roughness.

At all stages of the sample preparation process, acetone, chloroform and ethanol are used to keep the sample clean and mitigate contamination. The various stages of the sample preparation are shown in Figure 2-22.

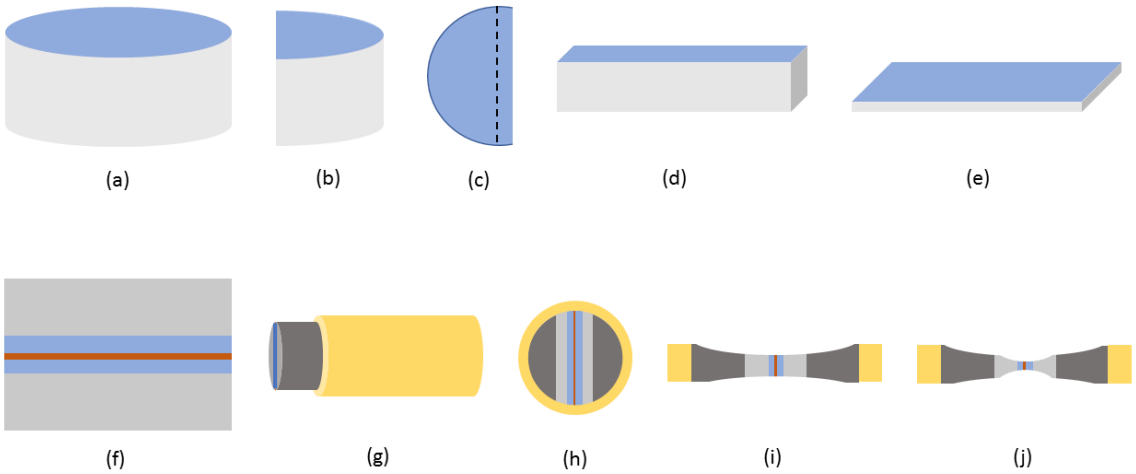

Figure 2-22: Stages of the conventional cross-section sample prep. (a) Initial 2.5” disc, (b-e) diamond saw reduction, (f) epoxy gluing of surfaces, (g-h) brass-tube, molybdenum encapsulation and sectioning, (i) hemispherical dimpling, and (j) Argon ion polished to electron transparency.

The FIB sample preparation was carried out by, and with thanks to, William smith, a technician in the Materials & Condensed Matter group at the University of Glasgow.

Strengths of FIB sample preparation are the rapid production of micron scale, site-specific and uniformly thick specimens; however, the drawbacks of the technique are FIB-induced damage, mitigated by low ~2 keV polishing, as is done in the final stage of the conventional sample preparation previously discussed.

Damage mechanisms in the FIB include formation of a damage layer that can extend tens of nano meters into the material at normal incidence, and include possible gallium contamination, which is course a significant concern as the final thickness of the specimen is in this range; however, Thomson *et. al.* performed analyses on silicon that had shown no ion mixing occurred and no detectable Gallium ions were present after a final polishing at 2 keV(135,136).

The process, roughly, involves an initial platinum or gold deposition onto the raw sample, followed by bulk removal material around the area of interest, cut-out of a U-section beneath the bulked-out area of interest, lift-out and mounting the area of interest to an Omniprobe lift-out grid, then thinning and cleaning.

An in-depth analysis of the technique, with illustrations of its strengths and weaknesses are given by Mayer *et al.*(135).

A concern remains with both techniques. It has been shown that in the argon ion-beam sputtering of polycrystalline tantalum pentoxide, oxygen is preferentially sputtered, producing a spectrum of sub-oxides, which remain even after the low kV polishing(137).

This would presumably also apply to the gallium ion sputtering in the FIB, and there is therefore additional uncertainty in the results obtained from these samples, with respect to the complimentary macroscopic studies of the same materials carried out on their bulk unprocessed samples.

The milling induced structural modification to the amorphous structure, from its original state, is much more difficult to ascertain as the atomic structure is not understood.

The result of Thomson(136) however imbues confidence that the effects of ion mixing and implantation are not significant, and especially so for the conventional cross section method, in which the final ion milling is done at considerably lower energies.

2.6 Pair distribution function analysis (PDF)

The standard method to describe an amorphous structure is by means of statistical pair distribution functions, which can be obtained from experiment, models or theory.

Whilst the PDF technique using electrons is not as common as the use of X-ray or neutron probes, it offers many advantages due to their much smaller wavelength and interaction potential.

The reduced radial distribution function, also known as the reduced density function, (rRDF), denoted by $G(r)$, is such a distribution, and is used in this work.

In an isotropic and homogeneous system, the rRDF is a statistical representation of an atomic position with respect to a central atom, giving a direct measure of the structural coherence of the sample, by the amplitude of its oscillations, and is obtained by a Fourier transform of the processed diffraction data.

The rRDF function was developed from the more commonly used radial distribution function, *J*(*r*) (RDF*)*, but is more convenient as it is obtained directly from the diffraction data, and can be computed without knowledge of a samples mean density, ρ_0.

Using this method, *J*(*r*), and the pair distribution function *g*(*r*), can be reconstructed from *G*(*r*). A comparison of the various commonly used correlation functions for describing total scattering is given by Keen(138).

The mathematical description of the work, described below follows Cockayne(139), and is based on the work of Warren(140), Cusack(141) and Debye(142).

Assuming a classical statistical mechanics description of the system, if follows that when one particle centre occupies a point at $\boldsymbol{r} = \boldsymbol{R_i}$, the one-particle density function for a system of *N* particles can be defined as,

$$v^1(\boldsymbol{r}) \equiv \sum_{i=1}^{N} \delta(\boldsymbol{r} - \boldsymbol{R_i}) \tag{2-66}$$

If N identical particles are in a fixed volume V at temperature T, thermal equilibrium requires that the thermal average $\langle \dots \rangle_{NVT}$ of this system results in a constant value for the average local density that is equal to the average density of the system, $\langle v^1(r) \rangle_{NVT} = n^1(r) = N/V$.

Then the integral, $\int n^1(r) dr$ gives the average number of particles in the system, and $n^1(r)$ is called the one-particle distribution function.

The two-particle density function is defined as,

$$v^{(2)}(\boldsymbol{r}_1, \boldsymbol{r}_2) \equiv \sum_{i}^{N} \sum_{j \neq 1}^{N} \delta(\boldsymbol{r}_1 - \boldsymbol{R_i}) \delta(\boldsymbol{r}_2 - \boldsymbol{R_j}) \tag{2-67}$$

Associated with the two-particle density function is the two-particle distribution function, $n^{(2)}(\boldsymbol{r}_1, \boldsymbol{r}_2)$. Whilst $n^{(2)}(\boldsymbol{r}_1, \boldsymbol{r}_2) \neq n^{(1)}(\boldsymbol{r}_1)n^{(2)}(\boldsymbol{r}_2)$, it can be written as $n^{(2)}(\boldsymbol{r}_1, \boldsymbol{r}_2) = n^{(1)}(\boldsymbol{r}_1)n^{(2)}(\boldsymbol{r}_2)g^{(2)}(\boldsymbol{r}_1, \boldsymbol{r}_2)$, where $g^{(2)}(\boldsymbol{r}_1, \boldsymbol{r}_2)$ is the pair distribution function.

In a homogeneous and isotropic system, it can be written that $\boldsymbol{r}_1 - \boldsymbol{r}_2 = \boldsymbol{r}$, and $g^{(2)}(\boldsymbol{r}_1, \boldsymbol{r}_2)$ is then replaced by $g^{(2)}(r)$, but more conventionally just $g(r)$, and is directly related to the local density at a distance *r*, from a central atom.

Assigning to the origin an arbitrary atom, the average number of atoms in a spherical shell of thickness dr at a distance *r*, is $\int_{shell} n_0 g(r)dr = 4\pi r^2 n_0 g(r)dr = n_0 J(r)dr$, where $J(r) \equiv 4\pi r^2 g(r)$, is the RDF as discussed above; and $n_0 = N/V$ is the average number density of atoms in volume V.

Higher order correlation functions are similarly defined; $g^n(\boldsymbol{r}_1, \boldsymbol{r}_2, \ldots, \boldsymbol{r}_n)$ represents the density probability distribution of finding *n* atoms at the positions $\boldsymbol{r}_1, \boldsymbol{r}_2, \ldots, \boldsymbol{r}_n$ simultaneously.

The pair distribution function, however, is the most accessible experimentally.

In a monatomic amorphous material, the scattering amplitude from an atom *i* at $\boldsymbol{r}_i$, in the direction $\boldsymbol{q}$, is given by,

$$\mathrm{A}(\boldsymbol{q}) = f_i(q)\exp(i\boldsymbol{q} \cdot \boldsymbol{r}_i) \tag{2-68}$$

Where $f_i(q)$, is the atomic scattering factor, and q is the modulus of the scattering vector. The scattered intensity is then given by the Debye formula(143),

$$I(q) = Nf^2(q) + f^2(q) \sum_{i \neq j} \sum_j f^2(q) \frac{\sin qr_{ij}}{qr_{ij}} \tag{2-69}$$

Where $r_{ij} = |\boldsymbol{r}_i = \boldsymbol{r}_j|$, and because an isotropic distribution is assumed, averaging is over all directions. As $g(r)$ is directly related to the local average density, integration is then performed over the sample volume,

$$I(q) = Nf^2(q) + f^2(q) \sum_j \int g(r_{ij}) \frac{\sin qr_{ij}}{qr_{ij}} dV \tag{2-70}$$

leading to,

$$I(q) = Nf^2(q) + f^2(q)\sum_j \int 4\pi r^2 \left[g\left(r_{ij}\right) - \rho_0\right] \frac{\sin qr_{ij}}{qr_{ij}} dr_{ij} + f^2(q)\sum_j \int 4\pi r^2 r_{ij}\rho_0 \frac{\sin qr_{ij}}{qr_{ij}} dr_{ij} \quad (2\text{-}71)$$

The final term in this equation has only significant contribution at small scattering angles (<~0.1 - 5 mrad)(144) , usually masked by the direct electron beam, and the common approximation, $r_{ij} = r$, is made, such that,

$$\mathrm{I}(q) = Nf^2(q) + 4\pi Nf^2(q)\int_0^\infty [g(r) - \rho_0]\frac{r}{q}\sin(qr)\, dr\,, \quad (2\text{-}72)$$

$Nf^2(q)$, is a mean intensity term that arises from the atoms scattering independently, and the second term causes a deviation from this mean intensity, if the local density at *r* deviates from the average macroscopic density, ρ_0.

A reduced intensity function is then defined as,

$$\varphi(q) = \left[\frac{I(q) - Nf^2(q)}{Nf^2(q)}\right] q \quad (2\text{-}73)$$

from which $G(r)$ is extracted, and the rRDF is defined as,

$$G(r) = 4\int_0^\infty \varphi(q)\sin(qr)\, dq = 4\pi r\,[g(r) - \rho_0] = \frac{J(r)}{r} - 4\pi r\rho_0 \quad (2\text{-}74)$$

Following this, it is possible to obtain *G*(*r*), *J*(*r*) *and g*(*r*), from a diffraction pattern by forming $\varphi(q)$ from $I(q)$, and then performing a sin Fourier transform on $\varphi(q)$.

Furthermore, it is also possible to obtain coordination numbers $CN(r_1, r_2)$ of the atoms through,

$$CN(r_1, r_2) = \int_{r_1}^{r_2} 4\pi r^2\, \mathrm{g}(r) dr = \frac{4}{3}\pi\rho_0(r_2^3 - r_1^3) + \int_{r_1}^{r_2} r\, G(r) dr = \int_{r_1}^{r_2} J\,(r) dr \quad (2\text{-}75)$$

Figure 2-23 displays a typical diffraction pattern from this work, and its radial intensity profile *I*(*q*).

The diffraction patterns, recorded from the thinnest areas of the specimen, are azimuthally averaged as indicated in Figure 2-24 to obtain $I(q)$.

A typical rRDF described by this process is shown below Figure 2-25.

The experimental procedure leading to $G(r)$ begins with alignment and calibration of the TEM(121). As $G(r)$ is a Fourier transform of a function of $I(q)$, inaccuracy in the calibration of q leads directly to errors in the scale of r, the bond lengths.

Consequently, at the beginning of each experiment a crystalline reference specimen with well-known lattice parameters is used to determine δq, the incremental value of the scattering vector modulus that is attributed to each pixel in the diffraction pattern images, and follows the procedure described in section 2.3.3.

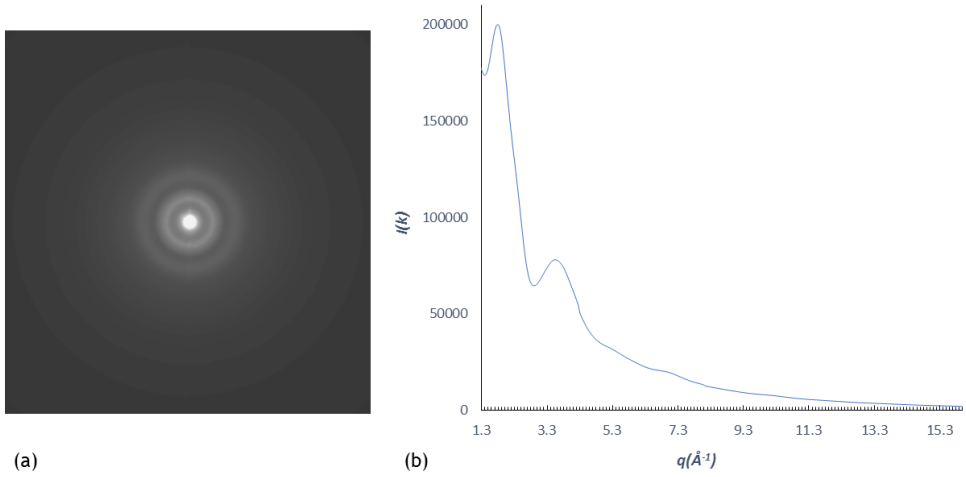

Figure 2-23: Diffraction pattern from an amorphous Ta_2O_5 specimen (left), and (right) an azimuthally averaged intensity profile of the diffraction pattern.

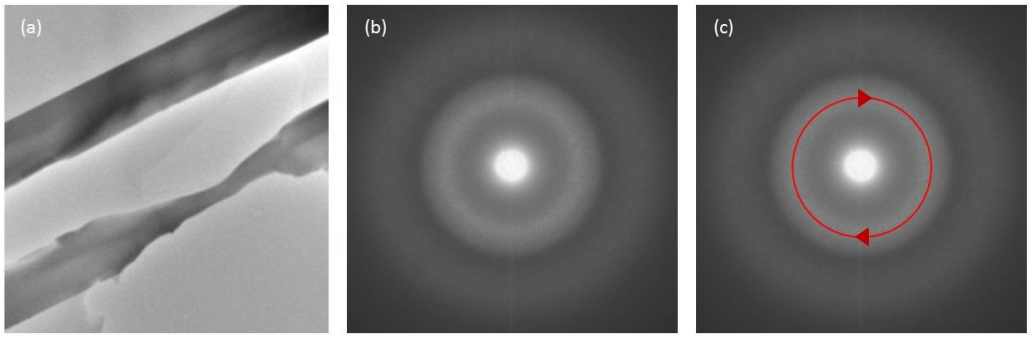

Figure 2-24: (a) A conventional cross-section prepared specimen, (b) a diffraction pattern taken from the thinnest (lightest parts of the dark bands) areas in (a), and (c) indicating the azimuthal averaging to obtain I(q).

Once the desired illumination conditions for the experiment are set, the reference specimen is replaced with the specimen to be studied, with all subsequent diffraction patterns recorded under those same conditions ensuring a stable calibration of q.

It is important to collect diffraction from as high a q-range as is practically feasible to obtain precision in $G(r)$; the resolution of the PDF, δr, directly depends on this as $\delta r = \frac{2\pi}{q_{max}}$, meaning that a q-range of 30 Å^{-1} can enable discrimination of structural features separated by 0.21 Å.

Considering this, high-dynamic-range diffraction imaging was utilised in the diffraction pattern collection.

Three different exposures were taken for each diffraction pattern and merged, with the lowest exposure giving the highest detail at low-q, whilst the highest exposure provided maximal SNR at high-q, without the saturation of the detector affecting the patterns.

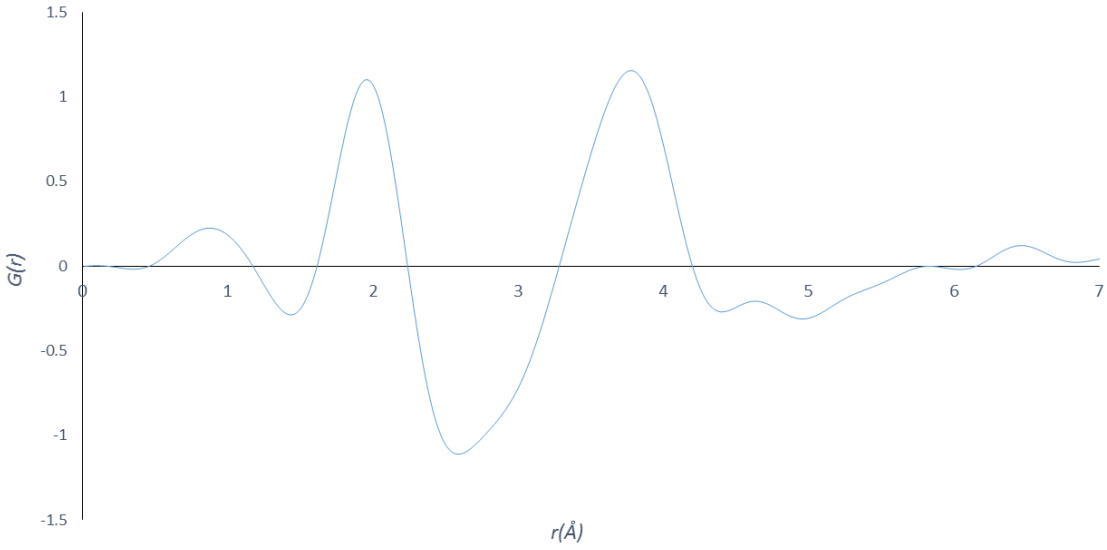

Figure 2-25 Example of a reduced radial distribution function from amorphous tantala (a-Ta_2O_5).

A Digital Micrograph (TEM control software) script was kindly provided by Bernard Schaffer of Gatan (Manufacturer of TEM hardware), which allowed this to be performed online at the microscope.

An alternative method of collecting high-q diffraction with better SNR can be effectively performed by a tilt-series, encapsulating diffraction patterns from different angular ranges, and then merging the azimuthally averaged intensity profiles(76).

The samples studied in this work are multi-component alloys, and as such, Equation 2-73 is replaced by,

$$\varphi(q) = \left[\frac{I(q) - N\langle f(q)^2\rangle}{N\langle f(q)\rangle^2}\right] q \tag{2-76}$$

where,

$$\langle f^2\rangle = \sum_i \frac{N_i f_i^2}{N} \tag{2-77}$$

$$\langle f\rangle^2 = \frac{\sum_i (N_i f_i)^2}{N^2} \tag{2-78}$$

$$N = \sum_i N_i \tag{2-79}$$

and the subscripts, i, indicate a specific atomic species; being either, oxygen, tantalum, or titanium.

The reduced intensity distribution, $\varphi(q)$, is obtained by fitting the scaled atomic scattering curve, $N\langle f(q)^2\rangle$, expressed as,

$$N\langle f_i(q)^2\rangle + I(q_{max}) - N\langle f_i(q_{max})^2\rangle \tag{2-80}$$

to the experimental $I(q)$. $\varphi(q)$ can be damped by an expression such as $exp(-bq^2)$, where b is the damping factor, to reduce the effects of a limited experimental data range and noise at high q(145), however this is only done when needs must, as it can significantly attenuate the resolution in $G(r)$.

The atomic scattering factors used for this investigation are a parameterised asymptotic representation developed by Kirkland (listed in Appendix A), using a sum of Lorenztians and Gaussians, which significantly reduces the data involved, and allows for easier analytical calculations(109); $f_{Kirkland}$ is defined as,

$$f_{Kirkland} = \sum_{i=1}^{N_L} \frac{a_i}{q^2 + b_i} + \sum_{i=1}^{N_G} c_i exp(-d_i q^2) \quad (2\text{-}81)$$

where $NL = 3$ is the number of Lorentzian (first summation), $NG = 3$ is the number of Gaussians (second summation) and a_i, b_i, c_i and d_i are the fitting parameters.

The Lorentzian have the correct behaviour at high angles and the Gaussians empirically fit the behaviour at low angles(109).

The terms $\langle f \rangle^2$ and $\langle f^2 \rangle$ used in the definitions of $I(q)$ and $\varphi(q)$ then become,

$$\langle f \rangle^2_{Kirkland} = p_O f_O^2 + p_{Ta} f_{Ta}^2 + p_{Ti} f_{Ti}^2 \quad (2\text{-}82)$$

$$\langle f^2 \rangle_{Kirkland} = (p_O f_O + p_{Ta} f_{Ta} + p_{Ti} f_{Ti})^2 \quad (2\text{-}83)$$

where $p_i = N_i/N_{total}$, and $i = O$, *Ta or Ti*, represent the composition factors of the elemental components in the mirror coatings studied in this work.

Once the parameters, N and q_{max}, have been optimised to obtain the best fit between the theoretical and experimental curves, and the uncorrelated scattering is subtracted, $G(r)$ is obtained through the sin Fourier transform of $\varphi(q)$.

In many cases, a satisfactory fit of the theoretical curve to the experimental data cannot be made, and background subtraction then is made empirically(57,146–149).

However, there is an effort here to make the results as useful as possible to the collaboration, with colleagues in mind who are endeavouring to computationally generate atomistic models of these structures to the highest accuracy possible.

The most common reason for poor agreement between the theoretical and experimental background curves is multiple scattering in thicker specimens (76,150,151). Other tests available to determine if the specimen is thin enough, include multi-slice modelling of an amorphous structure to give $I(q)$ as a function of specimen thickness(145), and measurement of the ratio of elastic to inelastic mean free paths(144,145).

There are also methods for recovering single scattering from multiple scattering data(152,153).

Additionally, energy filtering is often carried out to mitigate inelastic scattering(57,147,152,154), however, when working within the single scattering regime, little advantage is gained in using energy filtered data(145,150).

It is also noted that when using a convergent beam, as in this work, a sufficiently parallel beam is required so that $I(q)$ is not convoluted with the angular probe function(145).

However, utilising a cold FEG source and operating near the diffraction limit, the probe is described as coherent and convergent, where it is unclear whether or not $G(r)$ analysis is effected, and if correction by deconvolution could be applied(155,156).

A convenient development occurred in the field of electron PDFs in 2016. Dung Trung Tran *et al*. from the Arrhenius Laboratory, at the Stockholm University in Sweden, released "SUePDF: a program to obtain quantitative pair distribution function from electron diffraction data"(157), and is distributed as free software for academic users.

SUePDF aims to account for the effects of multiple scattering in electron-matter interactions. The software incorporates a renormalisation procedure based on number densities and the non-negative probability of finding an atom at a certain distance.

Optimised parameterisation in conjunction with mathematical modelling of the background, leads to subtraction of the uncorrelated scattering from scaled data in a loop-based routine, and the Fourier transform is performed on the normalised data.

The process is as described above, and uses the same Kirkland parameterisations of the electron scattering factors, but with the significant differences being that Equation 2-2 is replaced by,

$$q = \sqrt{\left(\frac{4\pi \sin\theta}{\lambda}\right)^2 + \left(\frac{2\pi\bar{\theta}}{\lambda}\right)^2} \tag{2-84}$$

to account for small-angle inelastic scattering, where $\bar{\theta}$, is an angle corresponding to an energy loss ΔE(144). The data scaling is performed according to,

$$I(q) = \frac{\int_{q_{min}}^{q_{max}} \langle f(q')^2 \rangle dq'}{\int_{q_{min}}^{q_{max}} [I_{raw}(q') - B_N(q')] dq'} [I_{raw}(q) - B_N(q)] \quad (2\text{-}85)$$

where,

$$B_N(q) = \sum_{k=1}^{N} \frac{c_k}{q^k} \quad (2\text{-}86)$$

is the model fitted to the background, c_k are the fitting parameters, and *N* is the fitting order which varies with sample composition.

Equation 2-21 is then replaced by,

$$\varphi(q) = \left[\frac{I(q) - \langle f(q)^2 \rangle}{\langle f(q) \rangle^2} \right] q \quad (2\text{-}87)$$

as the raw intensity data $I_{raw}(q)$, has been scaled to the weighted sum of the parameterised atomic scattering factors, in contrast to the scaling of $f(q)$ to $I(q)$ as described previously.

The rRDF is then obtained, as before, by the sin Fourier transform of $\varphi(q)$, after which normalisation and noise filtering is carried out.

Normalisation is based upon the non-negativity of the probability density in *g*(*r*), and noise filtering is based upon prior knowledge of the shortest inter-atomic distances and setting cut-off limits in *G*(*r*)(157).

2.7 Fluctuation electron microscopy (FEM)

Fluctuation Electron Microscopy (FEM) is a diffraction and/or imaging technique that quantifies medium-range order (MRO) in the ~ 1 nm to 3 nm range.

The original formulation of FEM by Gibson and Treacy(158) examines MRO by measuring spatially resolved diffracted intensity fluctuations from nano-volumes in the sample material through the normalised variance,

$$V(k, Q) = \frac{\langle I^2(\mathbf{r}, k, Q) \rangle}{\langle I(\mathbf{r}, k, Q) \rangle^2} - 1 \quad (2\text{-}88)$$

where $I(\boldsymbol{r},k,Q)$ is the diffracted intensity as a function of position $\boldsymbol{r}$ on the sample; the scattering vector magnitude $k = q/2\pi$ convention is adopted, where k is the reciprocal of an interatomic spacing, d; Q is the probe size, and $\langle \ldots \rangle$ indicates averaging over $\boldsymbol{r}$.

The technique is sensitive to three- and four-body correlations(158), described by probability distribution functions as discussed previously; the fluctuations are maximally sensitive when the electron probe size is of comparable length scale to the MRO structural ordering being probed.

In this case, the extent of MRO is quantified through the magnitude of the variance of the diffracted intensity, as a function of scattering vector over a length scale determined by the size of probe used.

Originally proposed by Gibson and Treacy(158), the technique was initially carried out using dark-field imaging in the TEM, although an equivalent experiment can be carried out using scanning diffraction(74).

This latter experimental approach has distinct advantages, especially on modern scanning transmission electron microscopes, where probes well below 1 nm in diameter can be routinely produced, provided the diffraction patterns can be acquired reasonably quickly (which is now possible due to advances in imaging detectors).

Atomistic models have shown that the variance displays clear trends as a function of the size and volume fraction of the ordered regions(86,95), and to date, the technique has been employed to show variation in the nanoscale order of amorphous silicon(159–164) and amorphous germanium(74,165,166) thin films, phase change chalcogenide materials(167–169), and a selection of amorphous metals(169,170).

In these experiments, qualitative differences in FEM variance were observed and attributed to fundamental physical phenomena such as differences in film deposition conditions(164), the existence and thermal ripening of subcritical nuclei that precede crystallisation(168,169), and the effect of alloying on crystallisation kinetics(171).

Quantitative FEM analysis has thus far proven challenging, but with recent developments such as variable resolution FEM, information about the extent of the nanometre-scale ordering can be extracted(71,163).

Nevertheless, several recent studies have been successful in relating the scattering covariance and angular correlations in FEM data to structural information(172–174).

In recent work, scanning nano-diffraction FEM was used to collect data, in a similar way to that described by Voyles and Muller(165), and demonstrated the existence of MRO in *a*-Ta_2O_5(175).

In the version of FEM applied in the present work, we depart from the standard formalism in Equation 2-88, and by assuming noise-free kinematic coherent diffraction to be Gaussian distributed, compute the variance of standardised correlation coefficients obtained from a normalised cross-correlation of a Gaussian filter with the raw diffraction data(127),

$$V(\gamma,k,Q)=\{\langle\gamma^2(I(\mathbf{r},x,y,Q),t)\rangle-\langle\gamma(I(\mathbf{r},x,y,Q),t)\rangle^2\}_k \qquad (2\text{-}89)$$

where γ, the correlation coefficient is obtained from:

$$\gamma(x,y)=\frac{\sum_{x,y}\left(I(x,y)-\overline{I}_{u,v}\right)\left(t(x-u,y-v)-\overline{t}\right)}{\sqrt{\sum_{x,y}\left(I(x,y)-\overline{I}_{u,v}\right)^2\left(t(x-u,y-v)-\overline{t}\right)^2}} \qquad (2\text{-}90)$$

In Equations 2-89 & 2-90, *t* is the Gaussian filter, $\langle\ldots\rangle$ indicates averaging over ***r***, and *I* is as in Equation 2-88 with the exception that here the variance is computed on a pixel by pixel basis (*x*,*y*) through the diffraction pattern stack resulting in a variance map which is thereafter azimuthally averaged (represented by $\{\ldots\}_k$) to obtain the variance as a function of scattering vector *k*.

Equation 2-89 is a standard expression for variance which can be found in any statistical reference manual and is easily recognised by the mnemonic “mean of the square minus square of the mean”.

It differs in form from Equation 2-88 by the change of variable and the normalisation factor in the denominator; the data is normalised through Equation 2-90 prior to computing the variance.

Whilst the Gaussian filtering was initially intended to mitigate noise in data with extremely low SNR, it became apparent that a change of variable in the variance calculations from intensity to a normalised score of the intensities structural significance, simultaneously removed noise, background and standardised the datasets.

Furthermore, this approach may be a robust method, as the shape and size of distributions of the diffracted intensity correspond to the shape and size of the structural features from which the electrons diffract, whereas the magnitude of the diffracted intensity is dependent upon the orientation of the structural motif with respect to the illumination conditions.

In Equation 2-90, $I(x,y)$ denotes the intensity value of the diffraction pattern at the point (x,y), $\overline{I}_{u,v}$ is the mean value of $I(x,y)$ within the area of the Gaussian filter t at the point (x,y), and $\overline{t}$ is the mean value of the Gaussian filter.

The denominator in Equation 2-90 contains the variance of the zero-mean diffraction pattern function $I(x,y)-\overline{I}_{x,y}$, and the zero mean Gaussian filter function, $t-\overline{t}$, at the point (x,y).

The 2-D normalised cross correlation is used here as a standardised means to evaluate the significance of the raw diffracted intensity at each point in the diffraction pattern, and is scored upon the similarity of the local distribution of intensity around each point, to the simplified diffraction maxima model centred on that point.

The diffraction maximum model is a 7x7 pixel rotationally symmetric normalised Gaussian filter, with a two-pixel standard deviation, obtained by fitting a 2-D Gaussian function to a sharp Bragg spot in a diffraction pattern from the same sample series, which had crystallised after an 800 °C heat treatment.

Using this approach, the absolute magnitude of the scattered intensity is irrelevant and instead, it is the shape of the intensity distribution around each pixel that becomes relevant, allowing coherent diffraction with poor SNR to emerge from the background.

The resulting normalised correlation map is then a standardised transform of the diffraction pattern into a map of the diffracted intensity's structural significance, where scores range in value between -1 (maximally anti-correlated), zero (uncorrelated) and 1 (maximally correlated).

Only positive scores are deemed structurally significant as the coherent diffraction has been assumed to be approximately Gaussian, whereas the diffuse background and single pixel events are not Gaussian distributed.

The negatively scored intensity contributions are removed from calculations, which anti-correlate with the model Gaussian filter, and it is assumed that much of the noise and diffuse background in the system is included in this negative range of scored intensities.

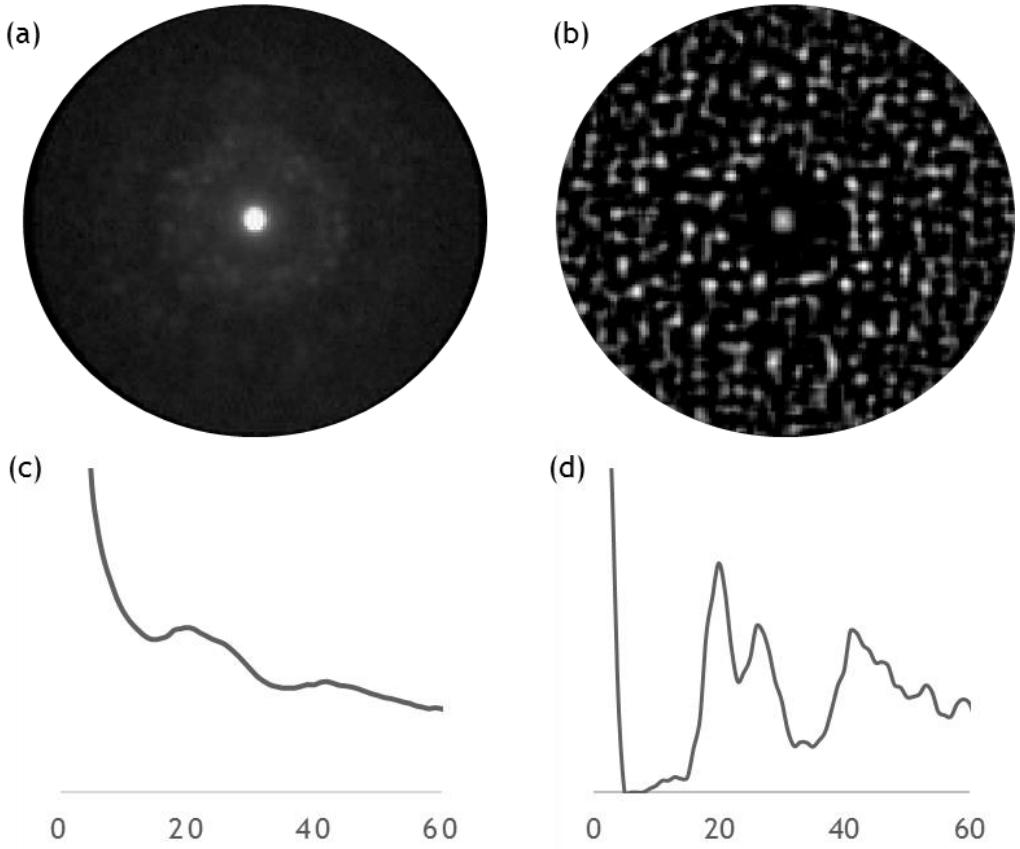

Figure 2-26. (a) Raw diffraction pattern & its radial profile (c); (b) diffraction pattern cross correlated with normalised Gaussian filter & its radial profile (d). The x-axis values of (c) & (d) represent the number of pixels from the central beam.

Because of this normalisation, $\gamma(x, y)$ is invariant to brightness or contrast variations in the diffraction patterns (including from diffuse inelastic scattering), which are related to the values of the mean and the standard deviation.

This has the effect of standardisation of the data-sets and preservation of diffraction events deemed structurally significant through positive correlation, whilst rejecting single pixel noise or X-ray events.

An example of the conversion from a raw diffraction pattern to a map of its normalised structurally significant diffraction is shown in Figure 2-26; their accompanying azimuthally averaged radial profiles illustrate the enormous gain in structural detail achieved in utilising this methodology.

Intuitively, this approach seems well suited to the study of structural change due to thermal annealing; each diffraction pattern across the sample series is rendered statistically equivalent by the transformation of raw intensity pixel values to a normalised correlation coefficient, which itself is determined by the similarity of that pixel and its surrounding area (size of the filter) to the Gaussian filter centred on that pixel.

As the Gaussian filter is a representation of diffraction maxima from the specimen that has attained long range order by thermal annealing at 800°C, it serves as a reference in which the distribution of diffracted intensity in the remaining thermal annealing series, which have not attained that level of order, can be meaningfully compared using the relative values of the assigned correlation coefficients, which describe the degree of structural significance that the raw intensity values contribute to the diffraction pattern.

However, more important than the shape or size of the filter, is consistency in the application of a constant filter across all of the datasets.

Inspired by methods used in image analysis for feature tracking, this approach renders the data invariant to inconsistencies in the illumination conditions during data acquisition(176), and removes the need to normalise after the variance is computed.

It has also been shown that reliable extraction of information using the formal FEM technique is highly dependent upon the quality and reproducibility of the experimental data, and as such, steps have been laid out to accurately identify and correct artefacts in affected datasets(177) which is considered in relation to the data. The variance is also computed in this work using the classic intensity based approach to highlight the validity of the cross-correlation method.

In addition to the classic variance-based analysis of the scanned diffraction data(74), it is also possible to image features of the scanned diffraction dataset in real space, due to the spatially indexed nature of the diffraction pattern.

Using the Virtual Dark-Field (VDF) approach of Rauch and Véron(126), real space images are formed from the indexed scanned diffraction dataset by using the intensity (the term 'intensity' is retained for convenience in lieu of the intensity significance score) from selected parts of each diffraction pattern.

The value of this approach should not be underestimated; The idiom "a picture is worth a thousand words" has been repeated across generations and cultures and describes the notion that complex ideas and information can be conveyed more efficiently pictorially than by a textual description.

Feynman diagrams are a notable example(178). This is maybe not too surprising considering that over millions of years of animal evolution, an effectively parallel processing method of visual information developed as a matter of survival, in contrast to the serial processing of the written word which is in its infancy in evolutionary terms.

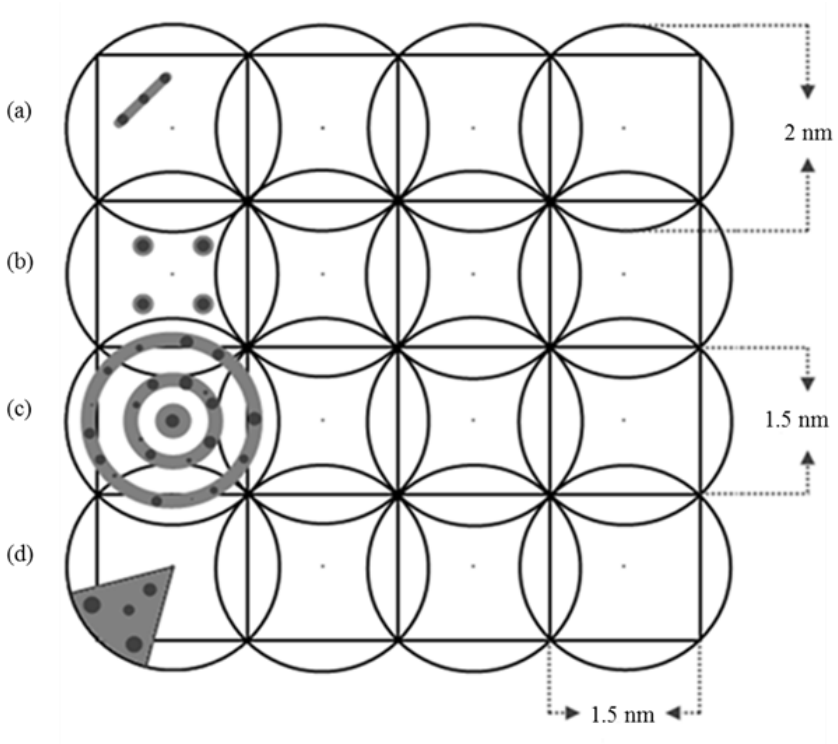

Figure 2-27: VDF technique enabled by the indexed scanning diffraction data, and showing elements of the diffraction patterns that can be used to generate the pixel values in the virtual real-space images.

This concept is being actively exploited in many areas of science(179–181); a recent example is the chess puzzle drawn up by Sir Roger Penrose which supercomputers fail to solve, yet humans can, by visual inspection in a matter of minutes.

Of course, the computer can only do what it is programmed to do, and thus the point of his exercise is to harness the power of the human consciousness' abstract and parallel processing power to develop better computers by understanding the rationale of the human derived solutions.

The visual interpretation of complex information encoded in an image, in contrast to its textual descriptor, may be thought of as analogous to the vectorisation of a for-loop in computer programming; instead of fetch-process-repeat, operations are carried out simultaneously.

VDF imaging is a counterpart to classic dark field imaging, in which images are formed using only selected scattered electrons instead of the un-diffracted central spot; this is realised by the insertion of a physical aperture in the back focal plane of the objective lens, and has the effect of masking almost all the diffraction pattern as illustrated in Figure 2-17, except the one reflection which is visible through the aperture.

For the VDF image construction(126,182), the whole back focal plane is collected with a spatially resolved detector and later numerically reconstructed to rebuild real space representations of the materials, using any desired combination of integrated intensity (unlimited combinations of numerical apertures can be employed) out of the diffraction patterns, to create the pixel values of the reconstructed real-space images.

The concept behind the Virtual Dark-Field (VDF) technique is shown in Figure 2-27. Each of the circles represents a diffraction pattern whose resolution *Q,* is dictated by the size of the incident electron probe, which is rastered across the sample surface.

Each of the 1.5 nm x 1.5 nm squares represent a pixel of the reconstructed virtual image, and are the step size in which the electron beam is rastered, of course any step size can be chosen. The intensity of each pixel is the integrated intensity of any part of the diffraction pattern selected.

Figure 2-27 (a) shows the selection of a line segment containing three Bragg reflections; integrating the resultant intensity from the same location in each diffraction pattern, an image is obtained highlighting the persistence of that structural motif in such a volume over a user defined area.

Likewise, shown in Figure 2-27 (b), (c) and (d), any numerical aperture, or combination thereof, can be created to enable investigation of the persistence of such nanoscale order over any desired area. This has one clear advantage over conventional dark field imaging: the whole back focal plane is collected, allowing any number of different dark field images to be reconstructed afterwards, whereas conventional dark field imaging has just one reflection selected per image.

Naturally, this comes with a downside, that a vast quantity of data needs to be collected to map any reasonable scan area at a sensible spatial resolution, when only a tiny fraction of data is used in the production of each virtual image.

To date, the technique has been used to spatially map phases and orientations of polycrystalline materials(126,183); here, the concept of FEM is extended to map the evolution of medium range order and nano-crystallite nucleation in glassy materials as a function of doping and thermal annealing, and effectually, spatially resolving the FEM results.

Instead of a 1-D plot of variance as a function of scattered intensity $I(k)$, the entire dataset can be visualised simultaneously, as a spatially resolved variance map at a chosen scattering vector. This is like FEM using dark-field imaging, in which the intensity is collected in the form of real space images, which have one scattering vector k, one probe size Q, and many spatial samples; r, k and Q get changed, and the next image is acquired.

On the contrary, in this method of STEM nano-diffraction, $I(r,k,Q)$ is obtained in the form of an electron diffraction pattern acquired with a nanometre-sized probe, which has one Q, one r, and many k values. That probe is then rastered across the sample to acquire many r(184). VDF image construction therefore enables FEM data acquired via scanned diffraction to be quantified in innovative ways, by combining the real space and reciprocal space representations in one analysis.

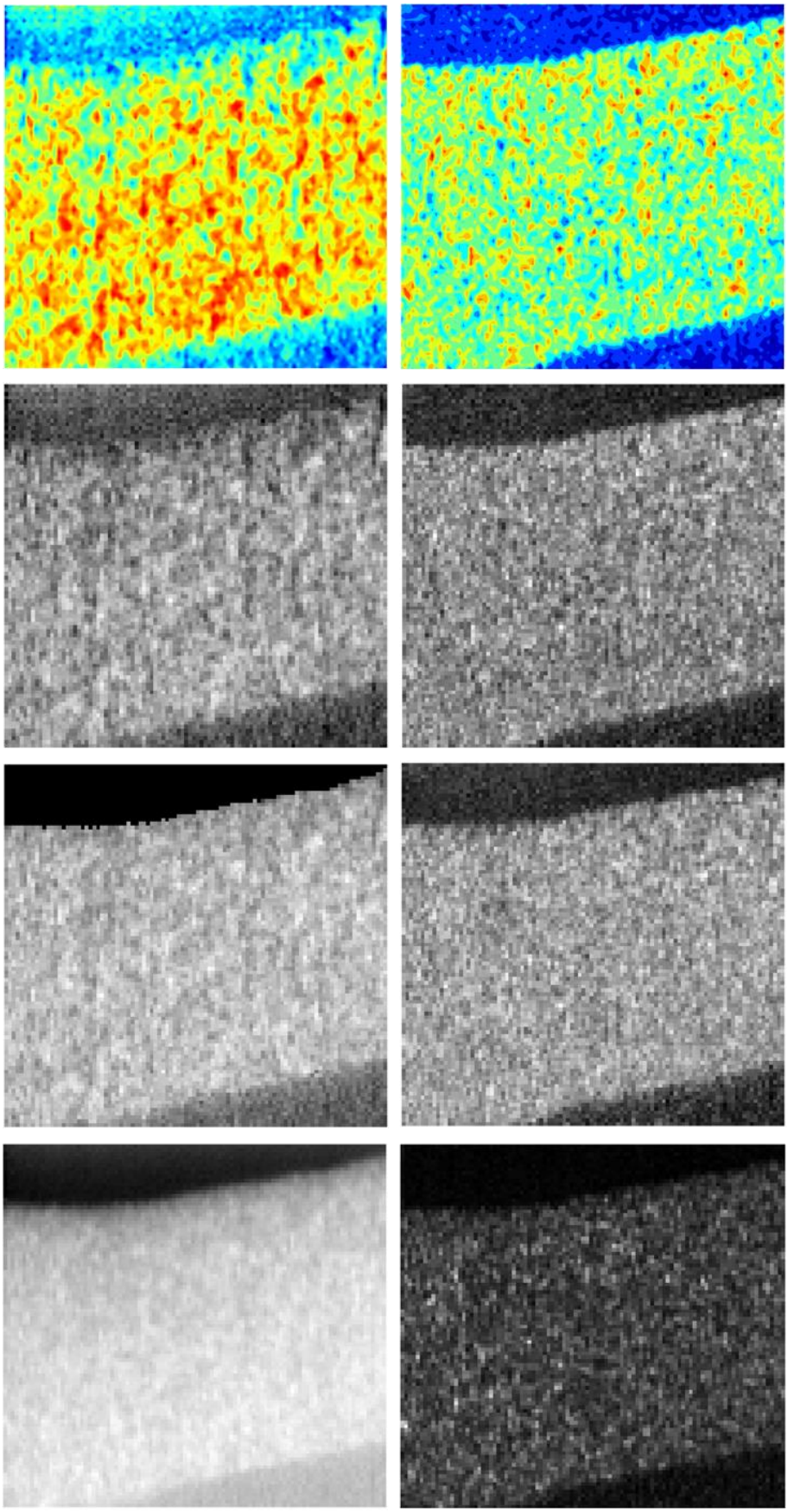

Figure 2-28 VDF images with pixel values representing the azimuthally averaged I(k) (left), and V(I(k,θ)) (right), of individual diffraction patterns. Blue (black) indicates the lowest level of relative structural order and bond disorder for I(k) and V(I(k,θ)) respectively, with red (white) the highest level.

The VDF images generated in this work take two forms based on Figure 2-27 (c); in the first, the image pixels represent the azimuthally integrated intensity $I(k)$ of annuli at a specific k, with higher intensity indicative of increased ordering in that region.

In the second image, pixel values represent the variance in intensity around those annuli, $V(I(k,\theta))$, with increasing variance indicative of increased bond disorder in that region.

The images are thereafter plotted in contour format, where for a pixel value, z, lines are drawn connecting the (x,y) coordinates where that z value occurs.

Examples of the images are shown in Figure 2-28 for an un-doped tantala specimen that has been annealed at 600°C for 24 hrs in air; they are each an image of the same area of the specimen, 142.5 nm in the y-direction and 150nm in the x-direction.

The boundary at the top of the images is specimen-vacuum interface; the lower boundary is the coating-substrate interface (tantala-silica). There are four images shown for each form of the described images, with the left column representative of the azimuthally integrated intensity $I(k)$ images at $k = 0.31$ Å^{-1}, and the right column the $V(I(k,\theta))$ images at the same *k-vector*.

The top row images are the contour plots, generated with both the positive and negative cross correlation coefficients previously discussed, as they result in images with superior contrast, and are used to represent the data in Chapter 4; the false colour representation was chosen because it enables clearer comparison between the different specimens.

The second-row images are generated in the same way as the first-row images, the only difference is that they have been plotted as standard greyscale images instead of contour plots.

The third-row are the same data again plotted in greyscale, however they were generated using only the positive cross correlation coefficients that were used for the variance calculations.

The final row images were generated using the raw intensities of the unprocessed diffraction patterns; the annular variance image is far superior in detail.

The azimuthally integrated intensity $I(k)$ images of the left column are clearly equivalent, and the same features are observed.

However, the images generated with the positive and negative cross correlation coefficients are of much higher contrast, and have much greater detail visible in the structure, especially in comparison to the intensity based image which appears saturated.

Although the false colour contour plot may not appear as clear as its greyscale counterpart, the value of the representation is apparent in the comparison with other structures in Chapter 4.

The different representations of the $V(I(k,\theta))$ images are less clear in similarity, and require a longer inspection. This is expected in consideration of the measured angular variance of data that has undergone distinct levels of reduction.

The methods for variance calculation and VDF image reconstruction were developed and carried out in MATLAB, the commented code is listed in Appendix B.

2.8 Discussion & Summary

The research in this thesis utilises the experimental techniques discussed herein to investigate the atomic structure of tantala, and titania doped tantala mirror coatings.

The primary goal is to find any differences in their atomic structures by doping and thermal annealing, which may contribute to their thermal noise spectrum, and gain insight into the internal friction mechanisms responsible.

The PDFs produced in this work are expected to be used as the experimental input for atomistic modelling, using Reverse Monte Carlo (RMC) and molecular dynamics methods by the collaboration, with the end goal of engineering mirror coatings with the desired properties by design.

The results of the FEM and VDF studies offer further constraints upon the possible structures obtained by atomistic modelling, and it is expected that these will be utilised soon.

3. Pair distribution function analysis of amorphous mirror coating atomic structures

3.1 Introduction

The focus of this chapter is upon the effect of post-deposition thermal annealing and Ti-cation doping on the atomic structure of ion-beam sputtered *a*-Ta_2O_5, using the pair distribution function methods described in Chapter 2.

This work follows directly from prior PDF analyses carried out by the collaboration(185,186), in which correlations were made between a homogenised *a*-Ta_2O_5 nearest-neighbour distribution through Ti-cation doping, and mechanical loss; however, they were unable to discern significant changes in the atomic structures that could elucidate the mechanisms behind the large observed changes in macroscopic mechanical loss(187,188).

Furthermore, most of the samples investigated in this thesis have also been studied using extended X-ray fine structure measurements (EXAFS), from which PDFs were obtained with specificity in the atomic-scatterer, giving detailed average nearest neighbour distances, coordination number and shell structure(189,190).

Unfortunately, further insight into the mechanism(s) responsible for mechanical loss were not found. The past electron PDF experiments (ePDF) were hardware limited, in such that the maximum effective region of reciprocal space available for sampling was $q \approx 11$ Å^{-1}, however with the hardware available in this investigation, it should be possible to routinely sample reciprocal space out to $q = 30$ Å^{-1}.

The main effect of going to high-q is that better real space resolution in the PDF can be obtained, as $2\pi/q_{max}$ determines the smallest oscillation of the Fourier transform in $G(r)$; the main drawback, however, is that in sampling to higher-q, the SNR decreases significantly, which is mitigated in this work by high dynamic range diffraction imaging, as discussed in the previous chapter. It is then envisaged that the increased real space resolution may elucidate atomic scale structural changes of greater significance in relation to the observed changes in their macroscopic losses.

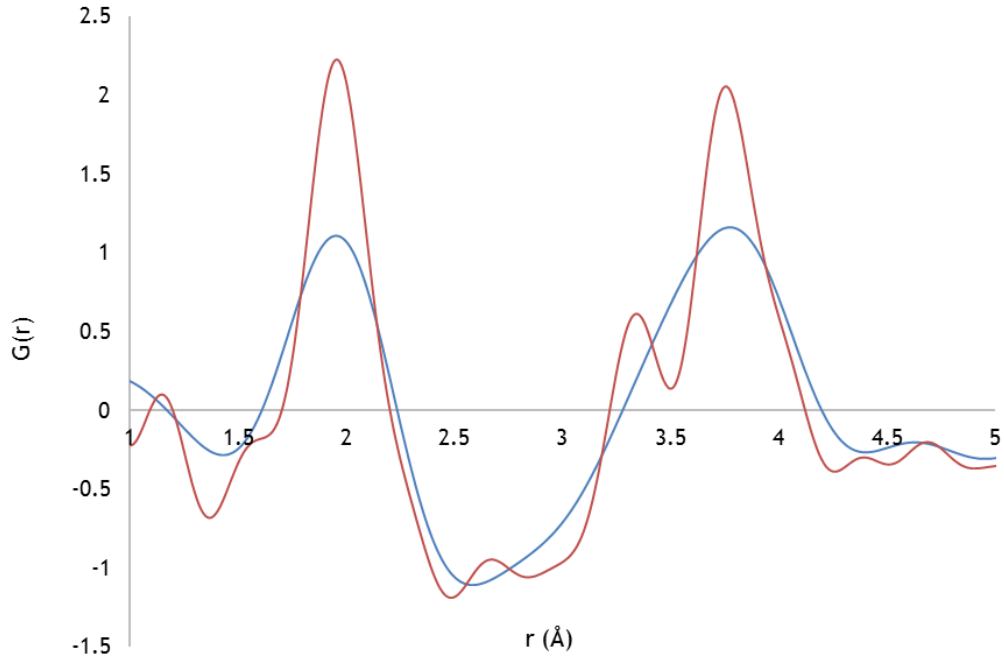

Figure 3-1 Improvement in rRDF real-space resolution by increased reciprocal-space sampling from q_{max} = 10 Å^{-1} (blue) to q_{max} = 16 Å^{-1} (red).

In Figure 3-1, the improvement in real space resolution gained over previous ePDF experiments is highlighted, specifically the splitting of the ~3.8 Å peak in the q_{max} = 10 Å^{-1} data.

All diffraction patterns for PDF analysis were collected on the JEOL ARM200F scanning electron microscope with Dr Ian MacLaren, who performed the TEM alignment, and set the experimental conditions; the author is not an authorised solo user of the ARM200F.

Experiments were performed in TEM mode at 200 keV under nominally identical collection conditions, with a 10 µm condenser lens aperture (CL2), used to obtain a minimally convergent beam of ~ 0.92 mrad, small enough not to require deconvolution(191).

Unless otherwise stated, all diffraction patterns were recorded at the lowest reported camera length available of 80 mm (121 mm in practice, effecting a q_{max} ≈ 24 Å^{-1}), allowing collection of diffraction out to the highest momentum transfer physically possible, and limited by a hard cut-off in these experiments, believed to be the differential pumping aperture.

3.2 Initial challenges

Initial attempts at producing a PDF with greater *q*-range than 12 $Å^{-1}$ proved impossible; no good fit between the theoretical and experimental curves could be made for effective background subtraction, giving results that were no improvement upon the previous work carried out on inferior TEMs.

The first suspect in relation to the problem was the high dynamic range imaging script used to increase the usable *q*-range; this however, was not the culprit as there was no difference in the fit when producing a rRDF from a single exposure diffraction pattern. The next consideration was specimen thickness; this was assumed not to be an issue, and whilst there was no strict control over the parameter, EELS relative thickness measurements(144) indicated that diffraction were collected from areas less than half the inelastic mean free path (thickest area of coating), as shown in Figure 3-2.

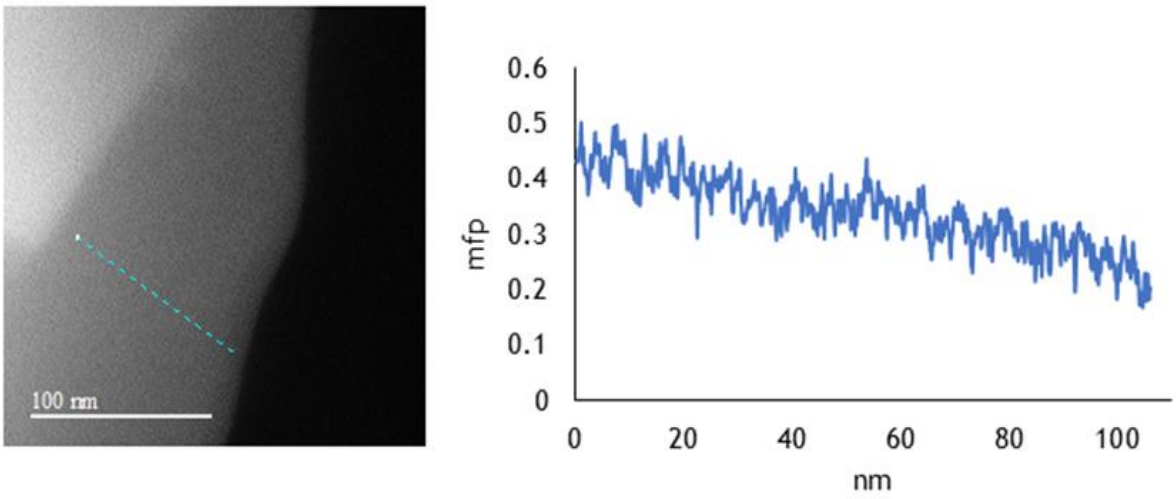

Figure 3-2 Dark-field image of a-Ta_2O_5 (left), and (right) the relative thickness measurement by EELS along the line perpendicular to the substrate, in units of inelastic mean free path (mfp).

Whether the diffraction pattern was taken from the thinnest area or the thickest area of the specimen, the problem persisted, and at first approximation, thickness was deemed not to be the dominant source of disparity; better agreement between backgrounds would be expected in going from thicker to thinner areas.

It was thought possible that the atomic electron scattering potentials used to generate the background may be inappropriate at these momentum transfers.

There are several parameterizations(109,112,113), and the Kirkland parameterizations are regarded to be the most accurate(109,157); however, they were tabulated out to only q = 12 Å^{-1}, and extrapolated to higher values, incidentally, where the fitting issues arose.

The problem was also thought to possibly arise from the complex electronic structure of the tantalum atoms, in that the underlying assumption of a spherically symmetric potential maybe too much of an approximation for its scattering behaviour(109). Another assumption implicit in the analysis is that the amorphous structures are homogeneous and isotropic. However, a test with a silica sample, and an amorphous chromium sample, highlighted the same problem with fitting past q = 12 Å^{-1}, and indicated that the problem likely lay elsewhere.

At this point, there was a strong temptation to empirically fit the background, but also a strong aversion to doing so as the cause of the bad fit between theory and experiment remained unresolved. Few studies were found in the literature of high-q ePDF work with amorphous materials, and the majority of those that utilised scattering between q = 14 Å^{-1} and q = 30 Å^{-1} of 200 keV electrons, used selected area diffraction (parallel beam), empirical background subtraction and energy filtering(57,146,148,149,154,192).

Other investigations, working at 120 kV, employed tilt-series and energy filtering, achieving a usable q-range of q = 20 Å^{-1}, and used theoretical background subtractions (76,152). Some other investigations worked with 300 kV electrons and achieved successful theoretical background subtraction up to q = 25 Å^{-1}, using selected area diffraction(150,193).

Whilst it is assumed that the electron probe in this work was sufficiently parallel as not to effect analysis of $G(r)$, no specific reference to the use of a convergent beam in amorphous ePDF work was found in the literature, where theoretical background subtraction was employed.

However, success has been achieved with theoretical background subtraction at q-ranges up to q = 25 Å^{-1} using 200 kV electrons without energy filtering(139,145,157). In any case, the consensus appears to be that multiple scattering due to sample thickness is the prime cause of poor theoretical background fits.

Reassessing prior assumptions made, and considering the prerequisites of circularly symmetric, distortion free diffraction patterns for precise electron scattering intensity analysis, a potential problem with the experimental conditions was identified. The prerequisite symmetry of the diffraction is usually taken for granted after a careful alignment procedure of the microscope has been performed, which is by default performed with rigour.

However, the diffraction calibration data taken from a silicon crystal reference sample at the beginning of a data collection session indicated that the prerequisite of circularly symmetric, distortion free linear diffraction patterns had not been met.

At the lowest order diffraction spots, at the lowest camera length (121mm), there was a three-pixel deviation from circular symmetry which deviated non-linearly in the radial direction away from the central spot. The best fits to the Si [220] and [400] diffraction maxima indicate a Δq = 0.13 Å^{-1} azimuthal and radial deviation from linearity at q = 10 Å^{-1}, which at q = 18 Å^{-1} increases to a Δq = 1 Å^{-1} deviation from linearity in the radial direction, resulting in a ~6% uncertainty in the determination of bond distances, r.

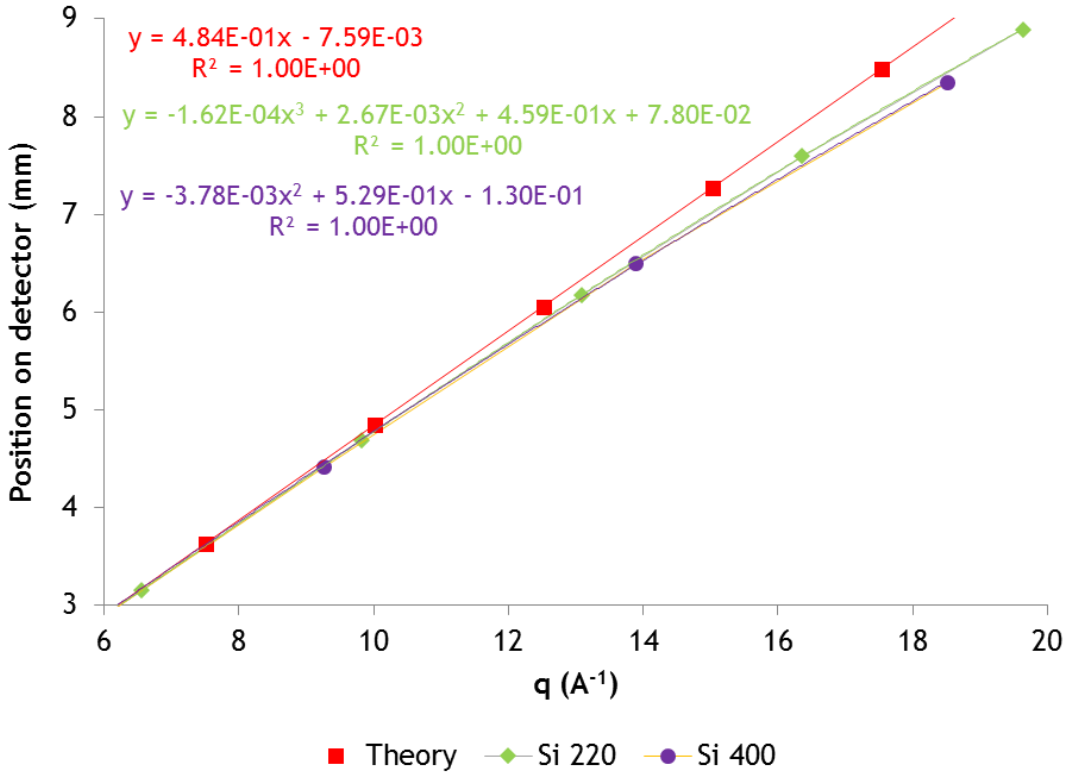

Figure 3-3: Deviation from I(q) in silicon crystalline reference diffraction pattern.

Figure 3-3 illustrates the non-linearity in a plot of the position of diffraction spots from the [001] zone of silicon on the detector CCD, versus the modulus of the scattering vector *q*. The non-linearity of the deviation was unequal in azimuth as can be seen from the different curves corresponding to the diffraction spots of the [220] and [400] directions, indicating the geometrical distortion of the diffraction in addition to simple non-linearity, which may have been more apparent in other plane directions.

Using an average of the best fit curves to the diffraction data in Figure 3-3, the uncertainties in the measurements of *q* are given in Figure 3-4, as fractional errors of the theoretical values.

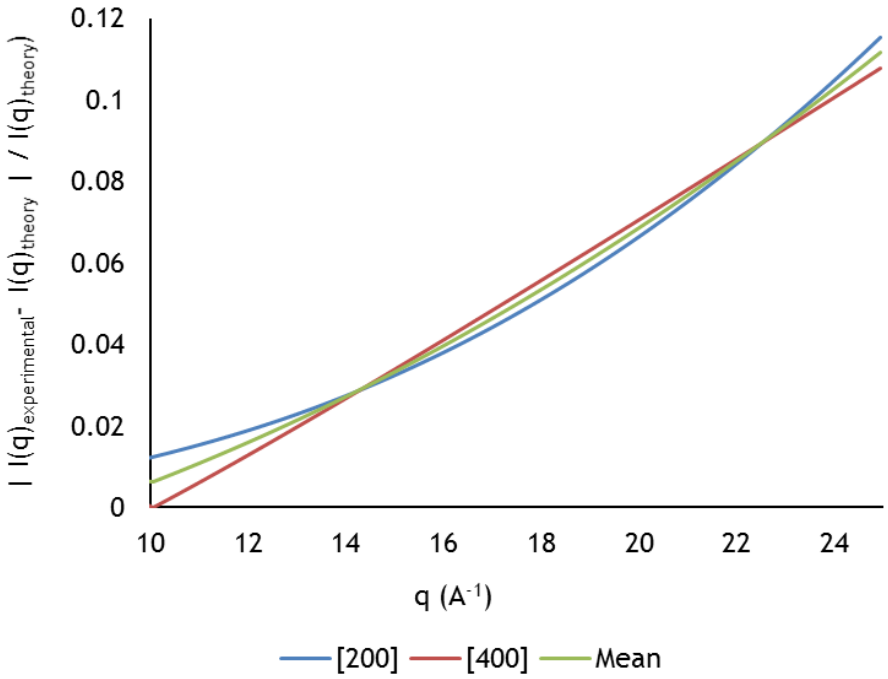

Figure 3-4 Fractional errors of the measured diffraction, due to non-linearities.

If the bad background fit was due only to thickness issues, the less quantitative empirical background fit may have been appropriate, as the background independent structural motifs would be read at the correct spatial frequencies, and only peak magnitudes would be uncertain.

On the other hand, performing an empirical background subtraction on data suffering the non-linear distortions as highlighted, the location and amplitude of the diffracted intensity on the CCD would be incorrect and would translate directly into errors in the RDF peak positions and amplitudes.

Without correction of the non-linearities, the horse falls at the first hurdle; precise and stable calibration of q cannot be made with the mixing of spatial frequencies during azimuthal averaging of the diffraction patterns, determination of other factors affecting agreement between theoretical and experimental backgrounds is made unclear, and precise quantitative analysis of the structures becomes unfeasible.

To ascertain the extent of the non-linearities effect upon the analysis of $G(r)$, a thirty-degree sector was cropped from a diffraction pattern which was most linear in azimuth as shown below in Figure 3-5. The sector was azimuthally averaged and then cleaned up slightly using a smoothing spline before the $I(q)$ data was interpolated onto a new scale, using inbuilt functions in MATLAB, to re-establish linearity.

The new scale was derived from an average of the non-linear $I(q)$ behaviours of the Si [220] and Si [400] directions shown in Figure 3-3 which were fitted with a 3rd order polynomial. The rRDF obtained from this heavily processed data was usable to q = 16 Å^{-1}; beyond this momentum transfer fits failed, most likely due to averaging the non-linear behaviour shown in Figure 3-4, and the increasing error with q.

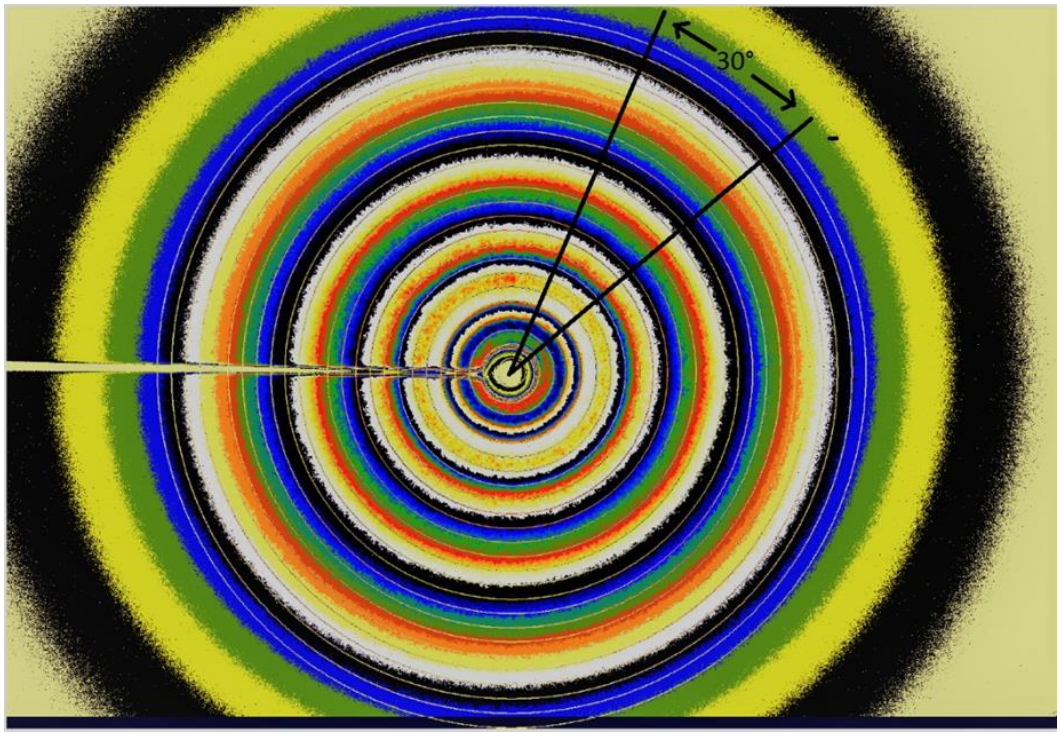

Figure 3-5: Thirty-degree sector, linear in I(θ), non-linear in I(q).

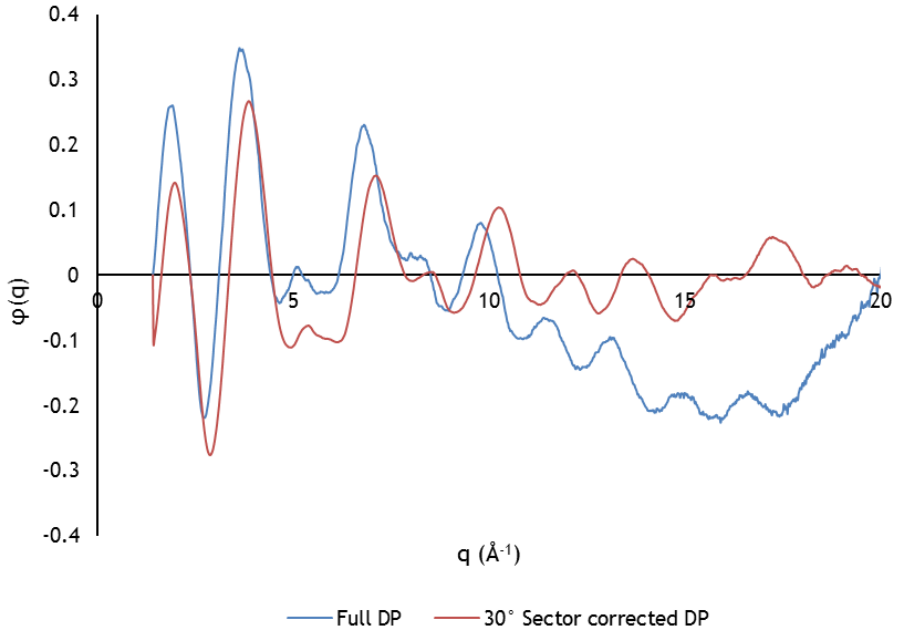

Figure 3-6: Comparison of reduced intensity functions from linear and non-linear data.

The difference in the RDFs produced from the entire raw diffraction pattern and the corrected 30° sector is illustrated in Figure 3-7, with Figure 3-6 illustrating the reduced intensity functions of the same data.

The function $\varphi(q)$ should oscillate around zero, tending to zero at high-q, failure do so is usually attributed to ineffective background subtraction due to multiple scattering effects, and the result is a noisy and unreliable rRDF.

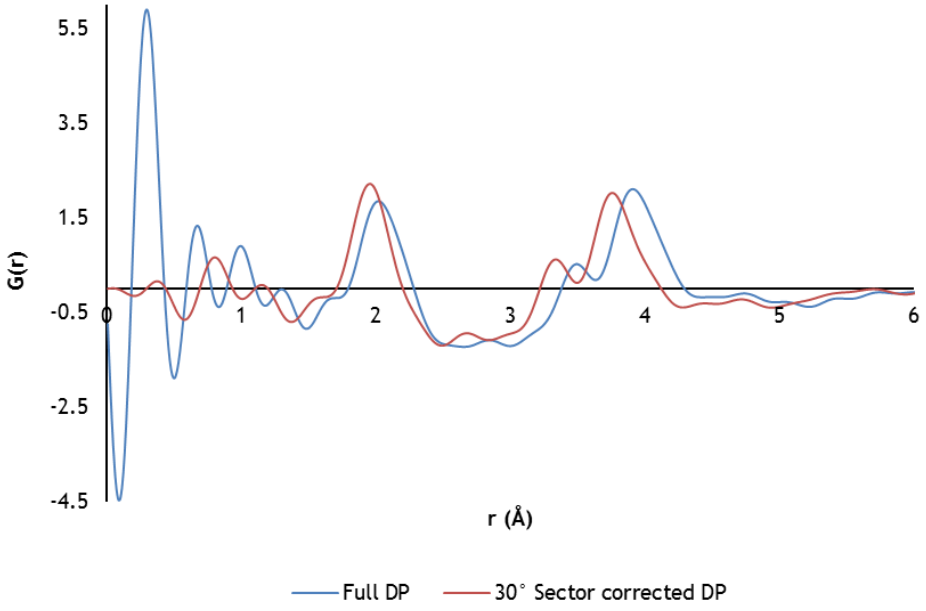

Figure 3-7: Comparison of reduced density functions from linear and non-linear data.

The improvement, however substantial, was not perfect. Whilst it is evidently possible to correct some sections of the data for analysis, it is wholly impractical in terms of the time required for the quality of the result. In discussion with experts, regarding the observed distortion and non-linearity in the diffraction, it was advised that the proper analysis and correction of these effects could fill a PhD thesis alone.

Brief mention was found in the literature concerning the issue of non-linearity in $I(q)$, and the possibility for its correction in post processing with calibration data(139); the discussions however, appeared to exclusively focus upon the linearity between the input signal and the output response of the detectors. It is therefore unclear whether these issues are common place, or if they are just not considered.

Figures 3-6 & 3-7 demonstrate that the poor fit between theoretical and experimental backgrounds is primarily due to these non-linearities, and not specimen thickness, with the 0.15 Å (4%) difference in r, at $r \approx 3.8$ Å correlating perfectly with the 4 % error predicted by the averaged non-linear behaviour in Figure 3-4 for a measurement at $q = 16$ Å^{-1}.

Details of the non-linearities were presented to the department, conjecturing that the CCD may be misaligned (as it had recently been in and out of the column), and highlighted the difficulty it posed in making advances over past PDF work. There were suggestions that some physical misalignments in the microscope may be significant to the problem. However, it was not possible for users to compensate for these effects within the limitations of machine control allowed to users.

Later in this PhD, a work-around was developed on-site by Dr Hidetaka Sawada of JEOL to adjust objective astigmatism whilst in diffraction mode, to correct diffraction pattern symmetry; unfortunately, two years had passed before the issue was addressed. It has since been confirmed that there is indeed a slight misalignment of the TEM column; discussions are presently ongoing with JEOL regarding the remedy of this fault. In this time, the author focussed upon collaborative work with international colleagues, locally in the Institute for Gravitational Research and the Materials & Condensed Matter Physics groups, and explored other avenues of investigation for this thesis.

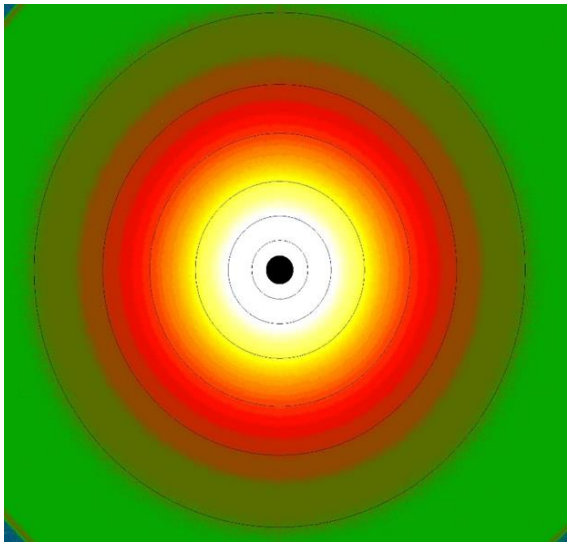

Figure 3-8: Circularly symmetric diffraction obtained using the custom script from Dr Hidetaka Sawada.

The work-around consisted of a custom script which enabled control over additional diffraction lenses, normally only accessible in engineering mode, and not available to the user; its function enabled tweaking of the lens currents to force circular symmetry in the diffraction pattern.

Although the process was time consuming and unintuitive, it appeared to work well and made it possible to collect circularly symmetric diffraction, apparently linear in q and azimuth to at least q = 16 Å^{-1}.

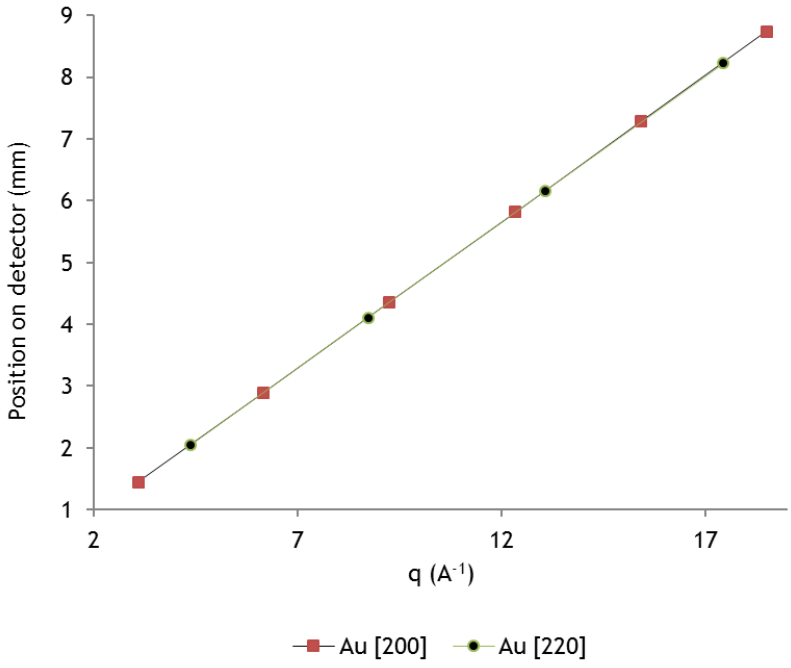

Figure 3-9: Demonstration of linearity in I(q) after using the 'work-around' script.

Figure 3-8 shows an example of a diffraction pattern, with superimposed circles displaying the correct projected geometry, in contrast to Figure 3-5, whilst Figure 3-9 illustrates perfect linearity in $I(q)$ measured from a crystalline gold reference sample.

However, it was found that after the data was collected that a stable camera length, discussed in section 2.4.4, was not maintained and precise calibration of q using the crystalline standard, described in section 2.3.3, was ineffective.

This was evident from significant differences in, and unphysical peak positions obtained for the metal-oxygen and metal-metal nearest neighbour distributions in $G(r)$ for near similar tantala specimens.

The example highlighted below in Figure 3-10 is the worst case for specimens measured during the same session, whilst some specimens were not affected significantly at all.

However, more significant deviations were apparent in calibrated measurements taken on different days. More importantly, the corrections made for circular symmetry did not improve the background fitting.

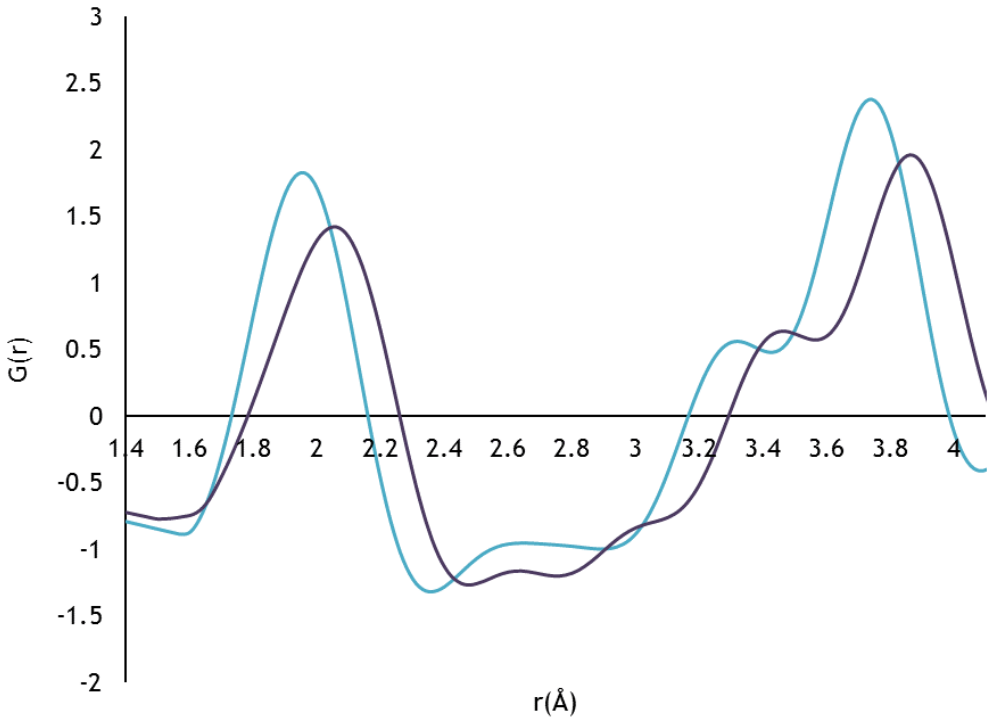

Figure 3-10 Unphysical atom pair separations obtained for similar samples, despite correcting for non-linearities using the previously described work-around, and calibrating the system with an external crystalline reference specimen.

Shown below in Figure 3-11 are two azimuthally averaged intensity profiles of the Au crystalline reference sample; one used for the calibration of δq, and the other, the exact same sample after being removed from the ARM and re-inserted, highlighting the hysteresis effect.

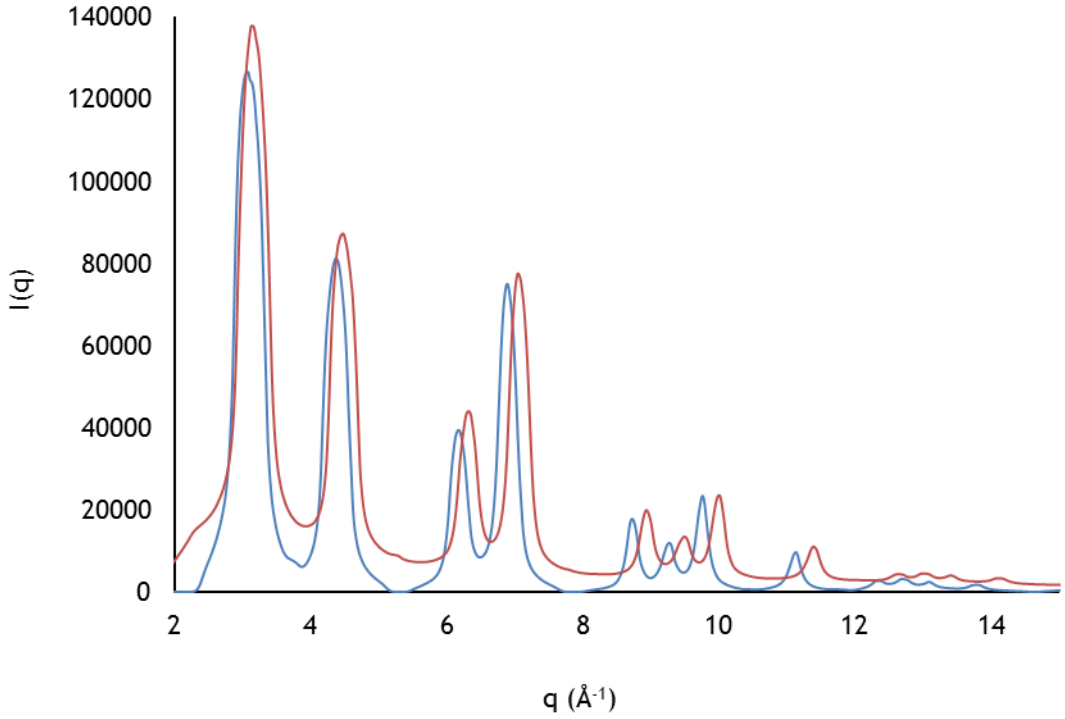

Figure 3-11: Camera length calibration of δq was not maintained, as shown by the I(q) profiles of the Au crystalline standard, after removal and reinsertion into the ARM.

This was assumed to occur due to hysteresis in the projector lenses of the microscope when switching between image and diffraction mode, meaning that, in future experiments, diffraction pattern symmetry correction and calibration needs to be performed for every specimen, preferably using an internal standard. However, the custom diffraction lens control most likely contributed to the effect.

Further checks were made on the linearity of the diffraction in $I(q)$ by plotting twelve 30-degree sectors of the re-inserted Au crystalline reference sample. It can be seen below, in Figure 3-12, that azimuthal non-linearities remain in $I(q)$ after the correction for circular symmetry.

The maximum non-linearity in azimuth is 1.5% and reduces resolution by blurring the diffraction maxima. The maintained radial linearity of *I(q)* is demonstrated below in Figure 3-13, and the hysteresis leading to uncertainty in the calibration of q is shown.

It is unclear however, how the manual forcing of circular symmetry in the diffraction patterns using the custom script, affects the hysteresis in the projection optics between specimen changes, and this therefore does not constitute conclusive evidence that significant non-linearites do not appear through subsequent specimen changes.

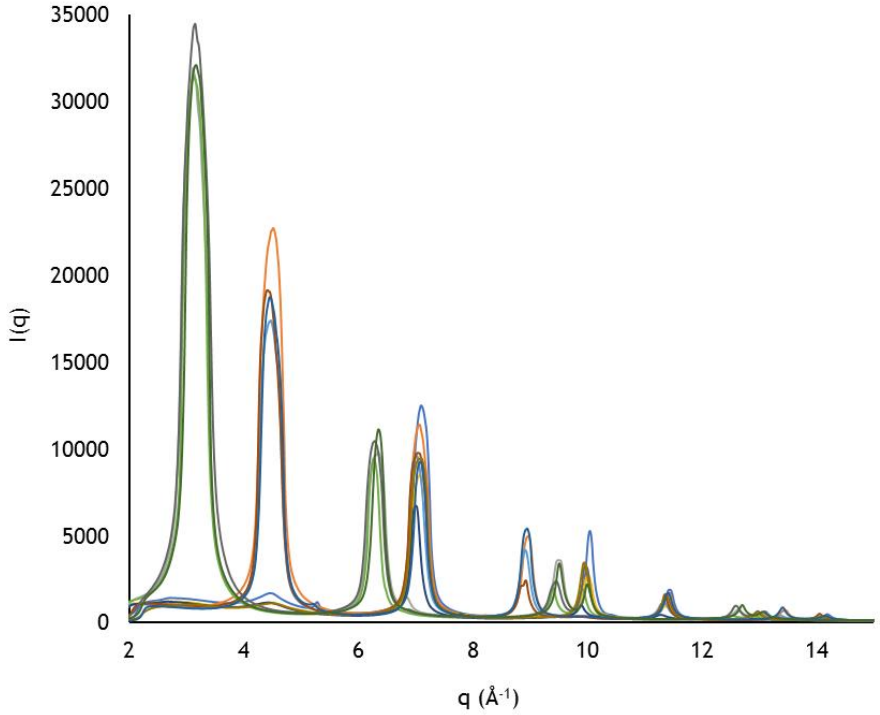

Figure 3-12: Twelve 30-degree sectors of the Au crystalline reference sample azimuthally averaged, highlighting remnant non-linearity in azimuth after correction.

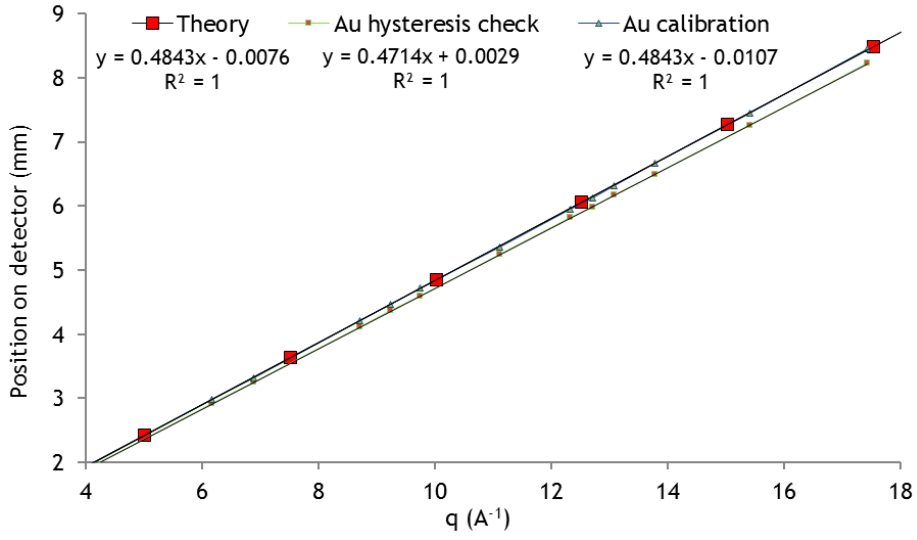

Figure 3-13 Hysteresis check of the Au calibration specimen, demonstrating a change in camera length from the correction procedure; the radial non-linearities have been corrected, and remnant non-linearity in azimuth is averaged out.

A reason postulated for the camera length changes between specimen changes, by the ARM200F chief technician, is that the stigmator coils of the lower objective element is potentially significant to the diffraction plane.

In using the 'workaround' script, the pattern gets squeezed in one axis which could cause a slight change in the cross over position into the top of the projector lens stack, in turn getting magnified as it goes down the column.

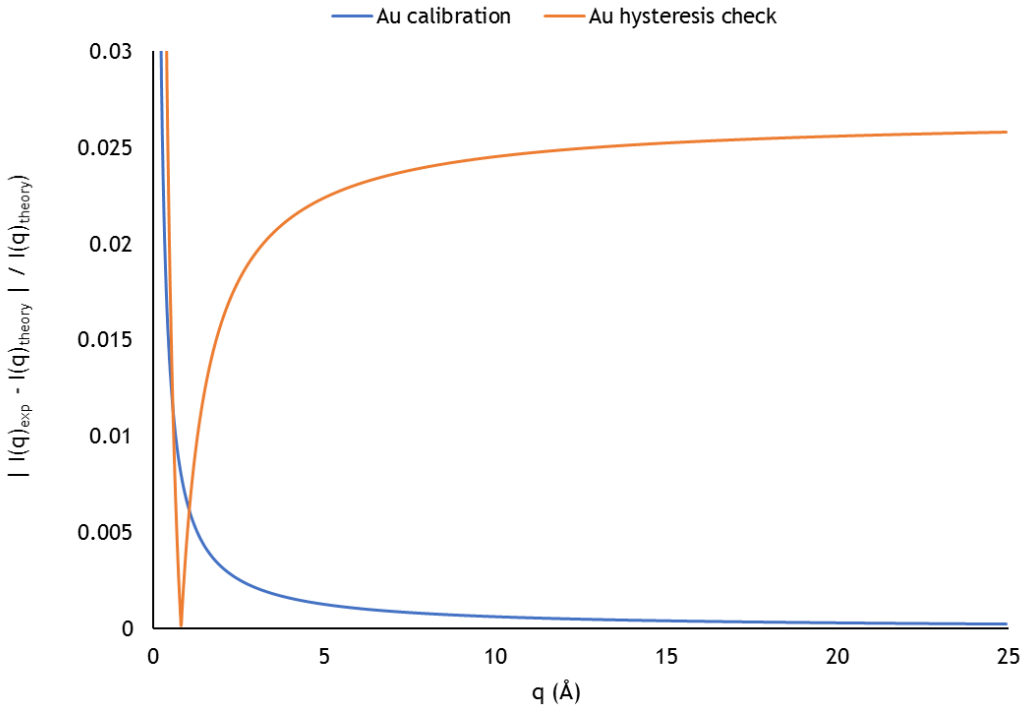

Figure 3-14 Fractional errors in the measured diffraction after correction for non-linearity.

In Figure 3-14, the fractional errors are shown for the Au calibration sample in relation to the theoretical predicted behaviour. After initial corrections made for geometry and non-linearity, the diffraction behaviour is as predicted; after re-insertion, a 2.5% error is introduced due to hysteresis, reflecting the changing camera length.

However, the error is almost constant up to the highest scattering angles, highlighting a 75% improvement over the uncorrected calibration data shown in Figure 3-4.

The error estimate in the accuracy of the calibrated diffraction is not indicative of all the data recorded; on retrospection, the camera length, and thus δq, was found to have varied significantly.

The PDFs shown in Figure 3-10 exemplify the extreme example of the calibration problem; the relative error in those measurements was ~3%.

An alternative method was devised to re-calibrate the data post-analysis, that worked particularly well, such that it was justified to consider the 2.5% error estimate from Figure 3-4 as an upper limit for the camera length uncertainty, which, added to the 1.5% error from azimuthal non-linearities highlighted in figure 3-12, results in the unfortunately large uncertainty of 4% in atomic spacings across all the PDFs.

The author collaborated on EXAFS PDF experiments(189,190) at the SLAC National Accelerator Laboratory, in Palo Alto, California, which provided average nearest neighbour distances, on an element specific basis for most of the samples studied here, and provided an indirect method for the calibration of the ePDFs.

This was done by fitting a Gaussian to the first peak of the ePDFs (metal-oxygen distribution), and then scaling the x-axis of the radial distribution function, $J(r)$, until the peak of the Gaussian matched the weighted average of the metal-oxygen distances and their amplitudes, as determined from the EXAFS corresponding to this first peak.

EXAFS based corrections were used for all data except for the 400 °C annealed samples which were not included in the EXAFS study. The un-doped 400 °C annealed data scaling was approximated by matching the maximum of the Gaussian fit of the first peak, to the average value of that determined for the 300 °C and 600 °C annealed data; this approximation was also applied for the 14 % Ti cation doped Ta_2O_5 sample annealed at 400 °C, as no 14 % Ti doping 300 °C data was available.

Error bars are omitted from all but the first ePDF which is given as illustration of the indicative uncertainties; their inclusion would mask all structural features, and all changes in peak position fall within these experimental uncertainties. However, on average, four diffraction patterns were used for each of the presented curves, and the applied scaling at enables meaningful comparison of the structures. The main relative features of the data appear secure, despite the uncertainty in position and magnitude, and interpretation of the results will proceed as presented.

The SUePDF(157) software described in Chapter 2 was used to produce all of the PDFs in this chapter, primarily in response to the problems of poor background subtraction that still did not improve after the correction for circular symmetry.

Whilst the primary cause for poor agreement between the theoretical and experimental background curves was attributed to calibration error and non-linearity in $I(q)$, the SUePDF software attempts corrects the raw $I(q)$ data affected by multiple and inelastic scattering, which by the same methods ensure a smooth oscillation of the reduced intensity function around zero, asymptoting to zero at high-q, irrespective of the relative contribution from multiple scattering in these data.

Whatever the cause of the bad fit, it aims to remove them to ensure these conditions. Examples of background subtraction on data, pre-correction, post correction, and finally using SUePDF are shown below.

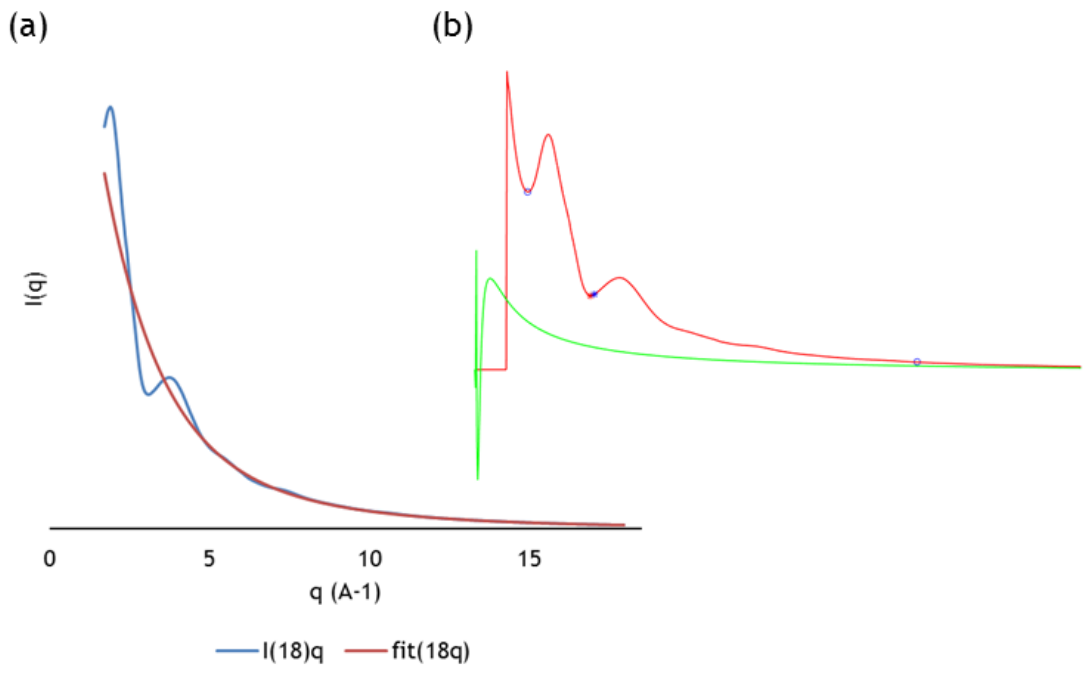

Figure 3-15 (a) Manual background fitting. (b) SUePDF automatic background fitting.

Figure 3-15(a) shows the original method of background fitting, where $f^2(q)$ is adjusted until a best fit to $I(q)$ is obtained, determined by its well-behaved oscillation around zero in $\varphi(q)$ after subtraction. The automatic background subtraction in SUePDF, (b), requires a mouse click on the first minima and on the beginning of the tail, after which it performs an optimised fit.

The reduced intensity functions shown below in Figure 3-16 represent the best background subtracted intensity functions obtained before corrections were carried out to achieve circularly symmetric diffraction patterns; the fits deteriorated rapidly with increasing *q*.

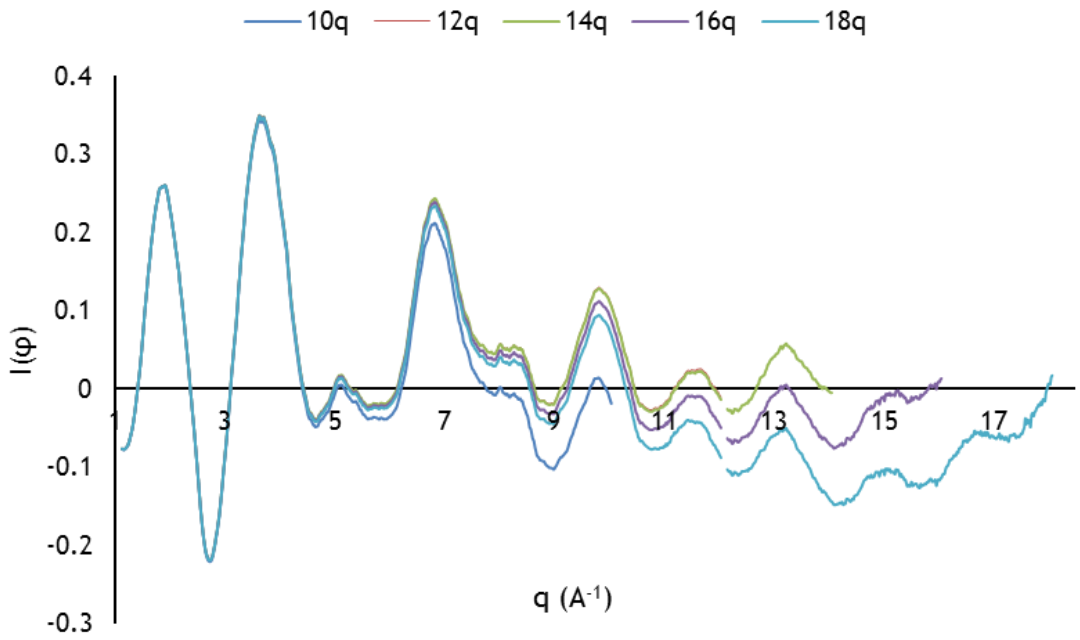

Figure 3-16 Best fits obtained prior to circular symmetry correction.

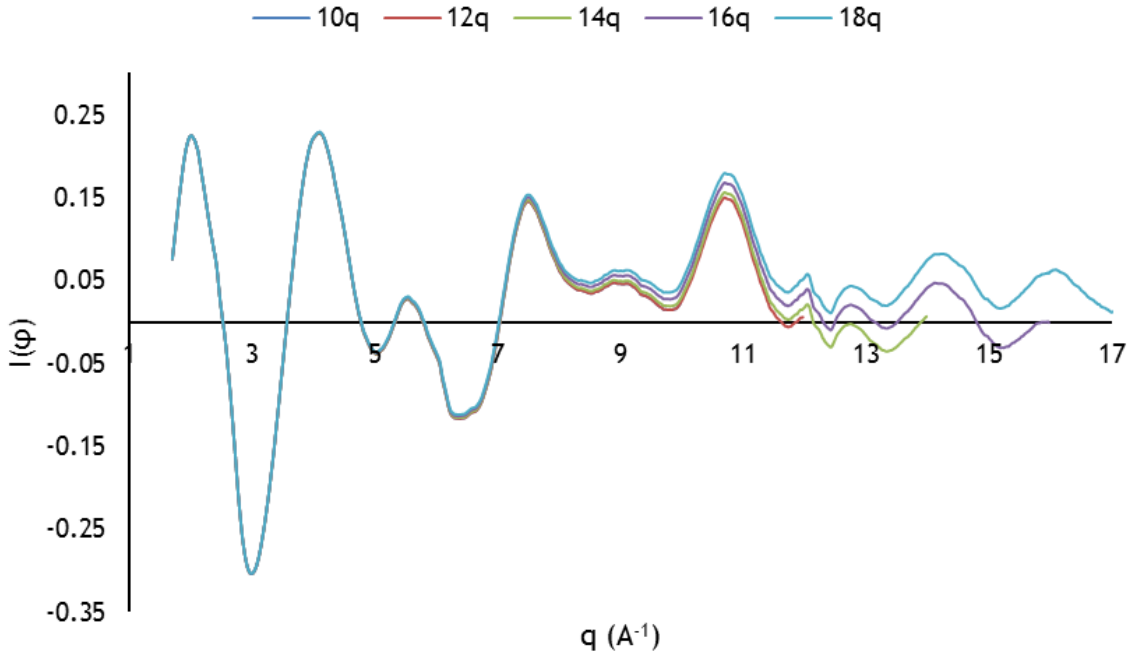

Figure 3-17 Best fits after circular symmetry correction, with introduced distortions at q = 12 Å^{-1}.

After the corrections were performed, the fitting did not improve, and the best fits achieved are shown in Figure 3-17. Furthermore, distortions were introduced as can be seen around $q = 12$ Å^{-1}, which were also visible in other data.

It appears that the use of the custom diffraction lens script for correcting the non-circular patterns has distorted the intensity distribution in areas that were not visible in the crystalline reference specimen of Figure 3-9.

It also appears likely that these unintended consequences of forcing circularly symmetry are the reason adequate background subtraction was not achieved.

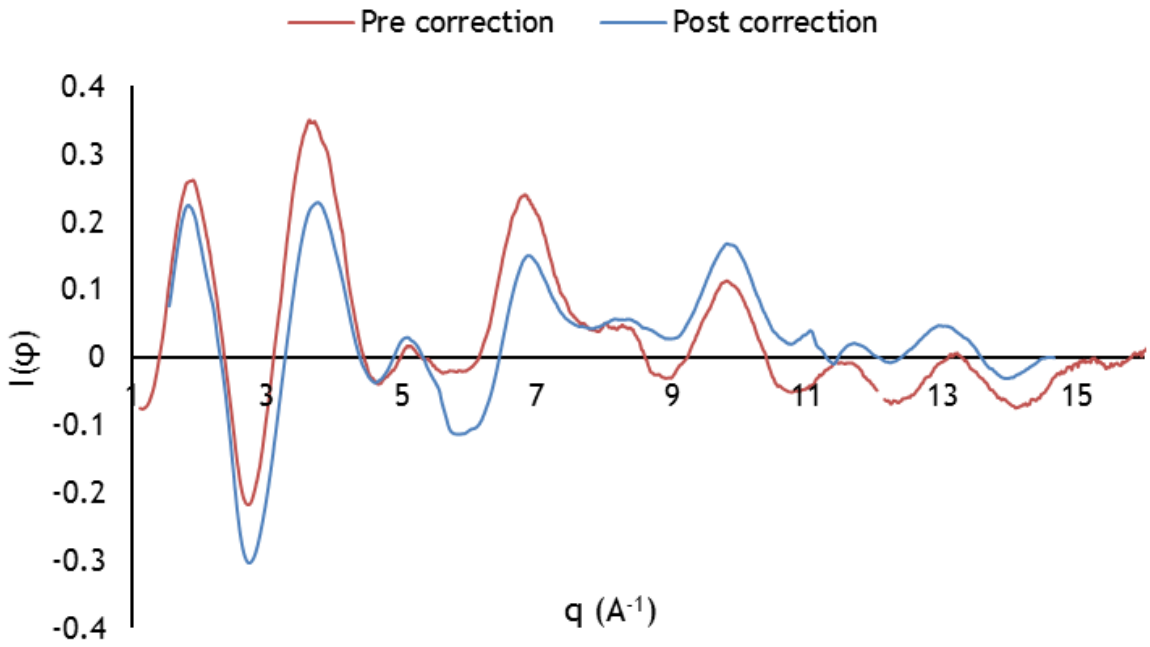

Figure 3-18 Manually background subtracted intensity functions before and after corrections were made for circular symmetry.

The best-fit reduced intensity functions, incorporating scattering up to $q = 16$ Å^{-1}, before and after correction are compared in Figure 3-18; The data obtained after the correction procedure has been rescaled to account for camera length instability; the non-linearities are also apparent in this comparison.

The method for correcting circular symmetry needs further testing, as not only has it made no improvement, but reduced the quality of the data, even though it does have circular symmetry.

In Figure 3-19 shown below, the same data, after correction, and manual background subtraction is compared with the reduced intensity function obtained with the SUePDF software.

The first approximation of the reduced data is similar to that in Figure 3-18, however, after performing optimisation routines on the subtracted data, the improvements are impressive.

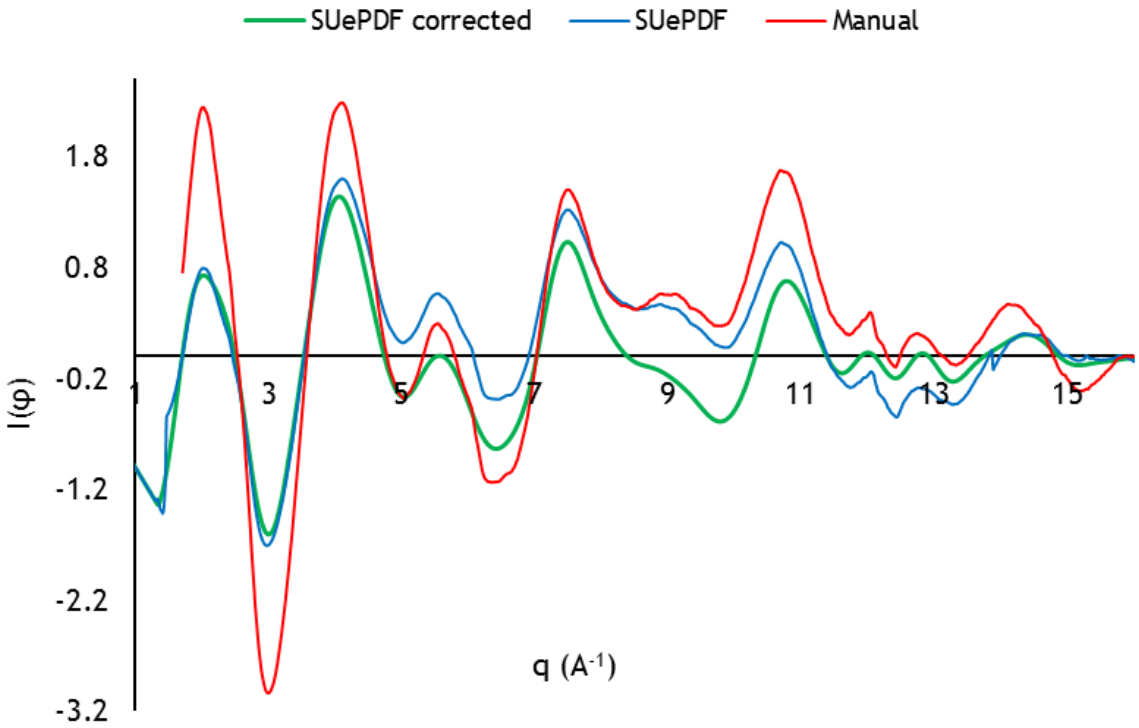

Figure 3-19 The improvements to the data obtained with SUePDF in comparison to performing the manual background subtraction.

The reduced intensity function oscillates around zero in the correct manner, and the distorted data at $q = 12$ Å^{-1} has also been corrected, highlighting its high utility and convenience for correcting poor data, regardless of the cause.

3.3 Pure Ta_2O_5 thermal annealing

The rRDFs from the thermal annealing series of pure tantala are shown below in Figure 3-20, and whilst there are minimal visible differences in structure, there is appreciable structure visible out to ~9 Å, common in all three samples.

This alone can be viewed as a positive result of the experiments; no discernible structure past 4 Å was evident in previous investigations of these samples by the collaboration(186,194).

In Figure 3-20 are the only PDFs that demonstrate confidence intervals in lateral peak positions, resulting from the non-linearities, distortions, and failure of the ARM to maintain set operating conditions between the specimen changes, configured during the calibration procedure described in Chapter 2, section 2.3.3.

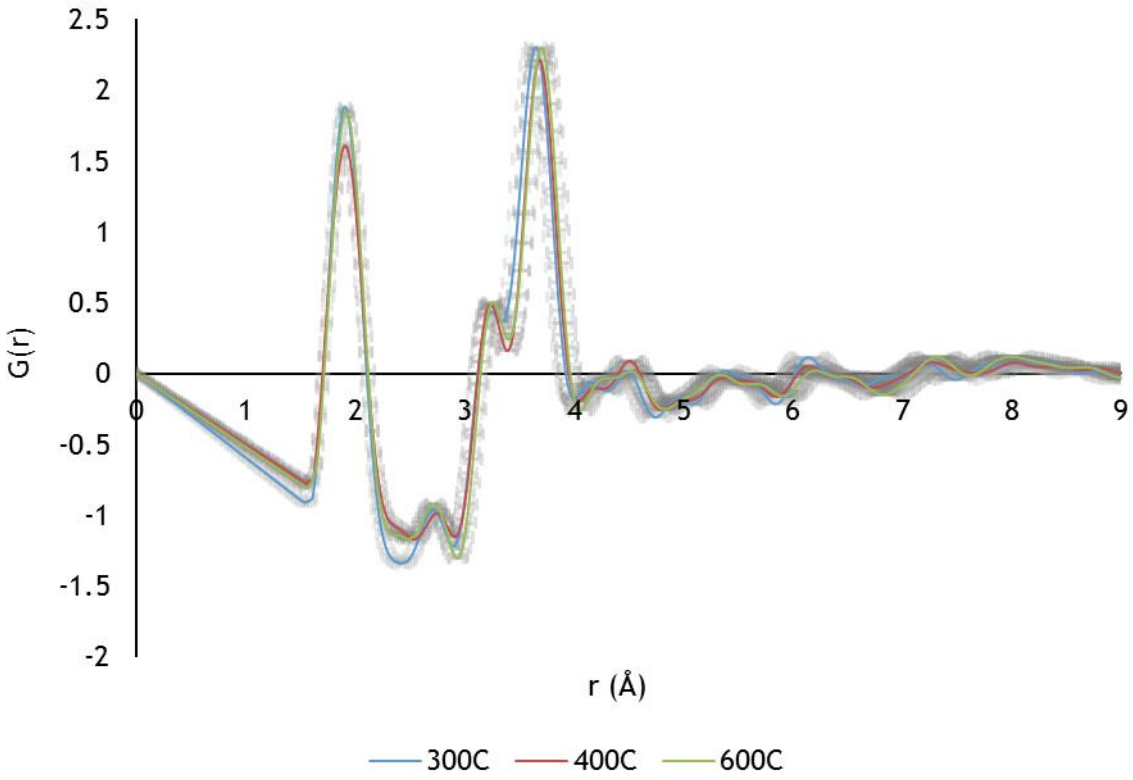

Figure 3-20 Reduced density functions (q = 16 A^{-1}) of pure Ta_2O_5 annealed for 24 hours in air at 300°C, 400°C and 600°C.

G(*r*), the pair distribution function directly obtained from the diffraction data, and thus most closely related to the experimental data, directly measures the structural coherence of the sample by the amplitude of its oscillations.

It can be seen in Figure 3-20 that there are large amplitude oscillations up to 4 Å, representative of the short-range order (SRO), that extend to the third nearest neighbour, after which the amplitude of oscillations plummet, whilst still exhibiting structure until ~9 Å.

It is therefore assumed that the medium-range order (MRO) in these samples can be defined from r > 4 Å, and that the peaks in this range define the separation and connectivity of structural units, made up of the possible configurations constrained by the SRO, as is similarly observed in PDF work on Fullerene(195).

This characterisation is shared in a recent complementary grazing incidence x-ray PDF (GIPDF) study of IBS tantala(82), plotted in Figure 3-21, against the 600°C annealed tantala sample shown in Figure 3-20, as well a crystalline tantala specimen.

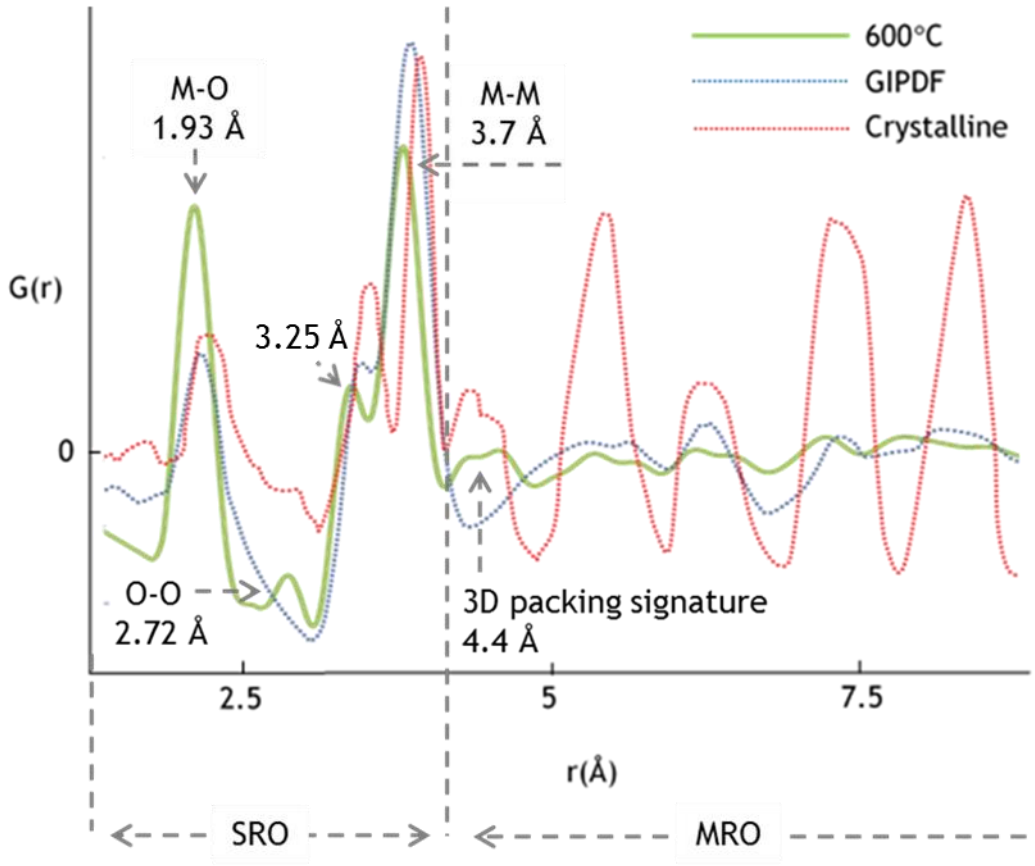

Figure 3-21 Similarities between tantala structures in the GIPDF study & this one. A crystalline tantala structure is also shown for reference which displays the signature for 3D packing, absent in the X-ray study, and observed throughout this work. The position of the metal-oxygen, oxygen-oxygen, and metal-metal distributions are highlighted for the 600°C tantala structure studies here. The transition from the SRO to MRO regions are illustrated.

The structural models described by the GIPDF data are illustrated in Figure 3-22, with bond lengths indicative of those in this study.

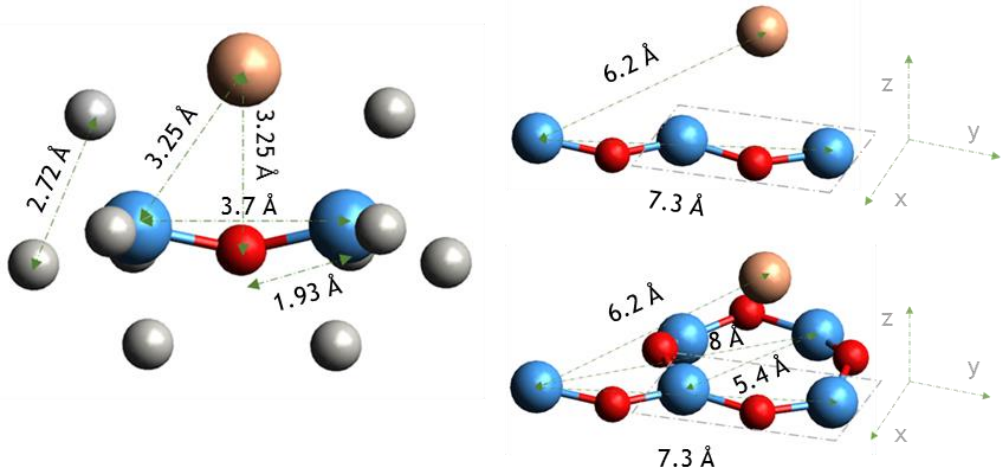

Figure 3-22 GIPDF structural models, with bond distances reflecting those of this study. The primary structural unit (PSU) (a) is indicated by oxygen (red) bonded to two tantalum atoms (blue), the grey spheres are the oxygens required for charge balance, and the gold sphere is an interstitial tantalum atom. (b) The zig-zag chain linking two PSUs. (c) Cross linking of PSUs to form 2D order.

The authors of the GIPDF study derive a PSU of Ta-O-Ta that join to form a sinusoidal chain, the backbone of the amorphous tantala structure(82). In their model, the backbone is 'decorated' with interstitial Ta, often only partially occupied, and when it is occupied, the PSU oxygen coordination goes up to 3 from 2; surrounding oxygens are disordered, and occupation is based upon fulfilment of charge balance and stoichiometry. Their model describes the PDF data here well, and is followed to in relation to the structures explored here.

The 600°C annealed structural features in Figure 3-21 all appear comparatively lower in r with respect to the other structures, except at the onset of the M-M peak at 3.7 Å, and is possibly an indication of high compressive stress; there is also likely to be an effect from the uncertainty in *δq*. The SRO of the structures are shown more clearly in Figure 3-23.

The straight lines joining the origin to the start of the first peaks in Figure 3-20 have slope $-4\pi\rho_0$ and represent the average number density of the sample as derived from the diffraction data in the SUePDF software(157). The data indicates that the sample annealed at 300°C has the highest density, which is reduced after annealing at 400°C. After a 600°C anneal, the number density has decreased with respect to the 300°C data, but not to the same extent as the 400°C data.

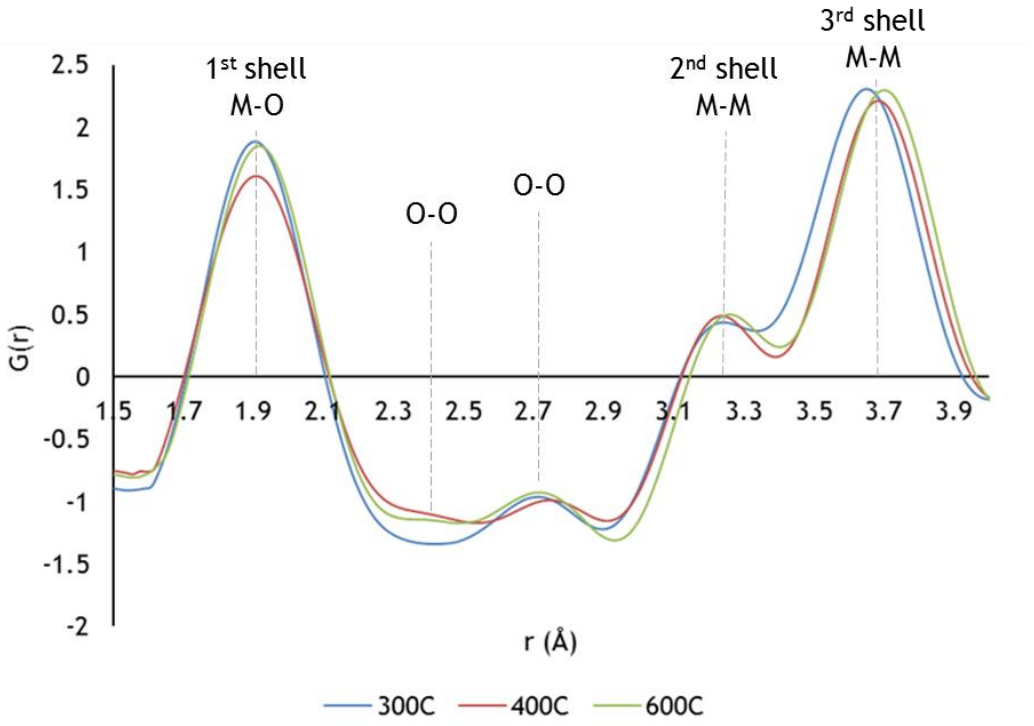

Figure 3-23 A closer inspection of the short-range order in the thermally annealed tantala samples, highlighting the relation of the peak positions to shells of atoms located in spheres at specific radii, and illustrated in Figure 3-24 in 2D.

It is not surprising that there is a decrease in density for the 400°C sample with respect to that at 300°C; as-deposited ion beam sputtered *a*-Ta_2O_5, and other metal-oxide thin films are commonly found to be in a state of compressive stress(196–200) and oxygen deficiency(196,201), and thermal annealing is commonly utilised to relax the structure, and improve stoichiometry(196,202–205).

The lower density for the 400°C sample may then be attributed to the relief of compressive stress, not fully realised by a 300°C anneal, inducing expansion of the structure; this was demonstrated by the manufactures of these coatings in which a thin film IBS sample of tantala, annealed at 400°C for 14 hours in air underwent a stress reversal from compressive to tensile stress(196).

Furthermore, a decrease in film density has been observed following thermal annealing, experimentally and in simulation(206,207). The 600°C sample on the other hand being slightly higher in number density than the 400°C sample could indicate that the structure passed through a maximum in relaxation of the compressive stress, then flipped back from tensile to compressive stress, with uptake of oxygen from the annealing ambient.

The peaks below 2 Å in Figure 3-23 are representative of the Ta-O nearest neighbour distributions, centred around 1.9 Å, showing a subtle expansion of the first coordination shell with increasing heat-treatment, consistent with relaxation of a compressively stressed structure subjected to increasing temperature thermal anneals.

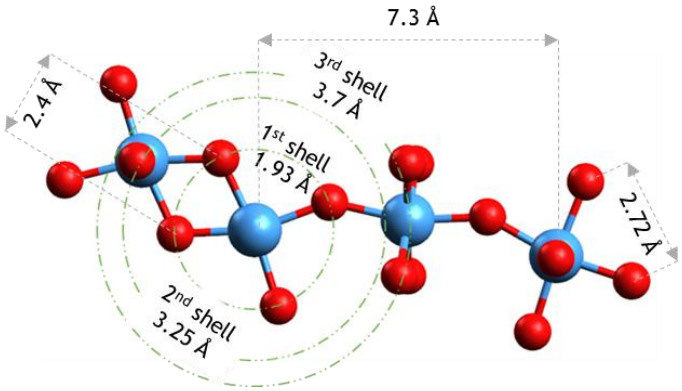

Figure 3-24 Atomic configurations describing the coordination shells; the 1st shell are Ta-O pair correlations, the 2nd shell contains the shorter Ta-Ta pairs, and the 3rd shell contains the longer Ta-O pair separations.

The second peak in Figure 3-23, at ~2.7 represents the O-O separations of the first coordination shell, as has been reported in the grazing X-ray PDF study of *a*-Ta_2O_5, mentioned before(82). Furthermore, the samples annealed at temperatures greater 300°C show an interesting signature just below 2.5 Å; where the 300°C data shows a distinct minimum, the 400°C and 600°C data suggest the emergence of another pair correlation which reflects the shorter O-O separation in edge-shared polyhedra.

This may indicate phase separation, or merely be the result of increased order in the lower density structures. Around 3.2 Å lies the third peak of the rRDF, corresponding to the second coordination shell of the central atom, and contains Ta-Ta pair correlations. Ball-and-stick atom models are shown in Figure 3-24 to visualise the coordination shells.

The peaks around 3.7 Å in Figure 3-23 contain contributions from a second Ta-O and Ta-Ta shell(189), and likely some O-O contribution(208). The increase in peak position appears to correlate with the increase in heat-treatment temperature. The EXAFS data for these samples, averaged over volumes orders of magnitude larger, had shown an increase of 0.01 Å in the bond length distribution of these Ta-Ta pairs in the 600°C annealed sample over the 300°C sample.

However, it indicated that the 600°C anneal resulted in an increased tantalum density, and reduced oxygen density in this case with respect to the 300°C sample(189). It would appear there is an overall trend of peaks moving higher in *r* with increasing temperature heat-treatment, commensurate with the relaxation of a compressively stressed structure.

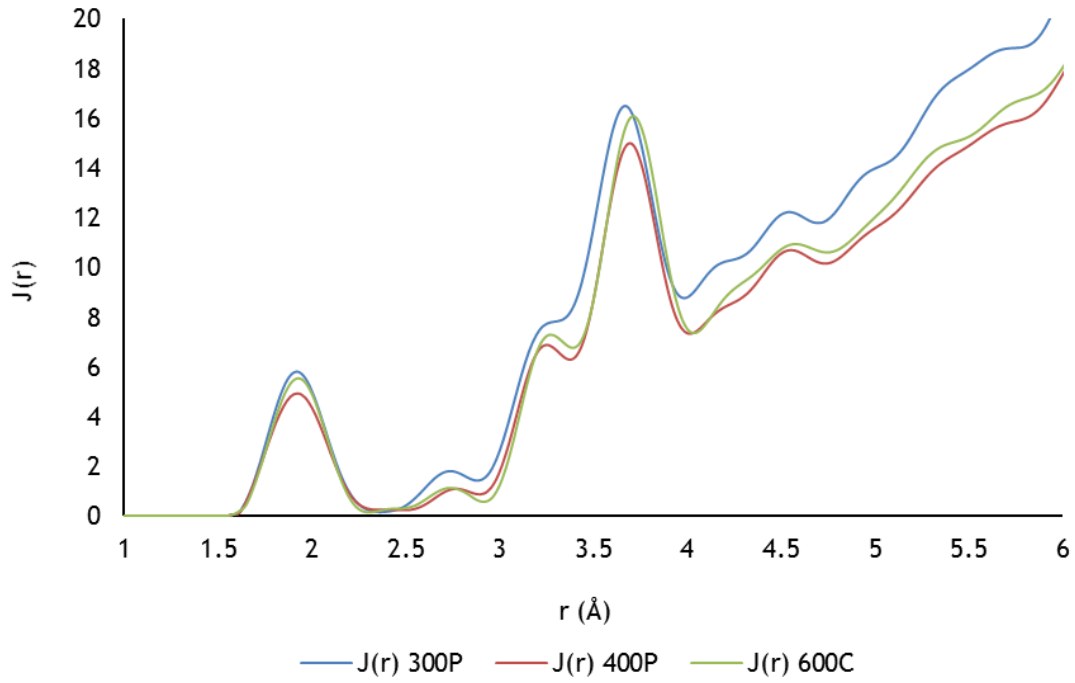

Figure 3-25: Radial distribution functions (q = 16 A^{-1}) of pure Ta_2O_5 annealed for 24 hours in air at 300°C, 400°C and 600°C.

Before examining the MRO (r > 4 Å) visible in $G(r)$ of Figure 3-20, the data are transformed to the radial distribution function $J(r)$, and are plotted in Figure 3-25. $J(r)$ is the pair distribution function that is most related to the actual physical atomic structure of the material as the direct integration of the peak intensity area gives the coordination number of the atom at the origin; the functions are related by, $J(r) = r[G(r) + 4\pi r\rho_0]$.

The data plotted in this form can allow subtle differences in the short-range structure to be visualised, as peaks of the function reflect the precise shape of the pair-probability distribution for unambiguous atom pairs(209). After the first peak, the function peak widths increase consistently and reflect the static (distribution of bond lengths) and dynamic (thermally induced) disorder of the structure.

Coordination numbers, $CN(r_{1,}r_2)$ are calculated by evaluation of the integral $CN(r_{1,}r_2) = \int_{r_1}^{r_2} J(r)dr$, where r_1 and r_2 here define the position of the peak being integrated. The first shell CN obtained for the 300°C sample was 2.07, well below the expected value of ~5; the reason for this is thought to be an underestimate of the sample number density ρ_0.

A reason for this underestimate, aside from the previously discussed problems with the collected diffraction, may be inappropriate background subtraction; as there is a sharp distinction in *G*(*r*) between the SRO (*r* < 4 Å) and the medium range order, it is possible that the addition of a separate particle form factor(157) may have been appropriate to better model the background.

The number density, ρ_0, is also determined by user input of the position of the first physical peak in *G*(*r*); Any oscillations below the initial metal-oxygen distribution were deemed unphysical and culled from the data. Alternatively, it is possible that the value may not be far off, and that the low oxygen content may result from the preferential sputtering of oxygen during sample preparation, and loss of weakly bound oxygen to vacuum in the TEM after specimen heating.

However, EELS stoichiometry measurements (by others, in unpublished work) indicate that this underestimate is an artefact of the data analysis. In any case, the underestimate appeared to be systematic throughout the data series, and as all data were subject to the same normalisation procedures, a scaling constant has been applied to the computed CNs, which was determined by dividing the CN determined by EXAFS for the same 300°C annealed sample with the number obtained here.

After correction, the CNs for the first Ta-O distributions are 5.01 at 300°C (almost perfect stoichiometry), 4.41 at 400°C (oxygen poor) and 4.68 at 600°C (oxygen poor). The CN of 4.68 for the 600°C sample after scaling is slightly less than the value of 4.75 determined by EXAFS(189), indicating that the scaling has worked well. The calculated coordination numbers follow the same trend as the reported number densities, and indicate the possibility of oxygen loss during thermal annealing at 400°C, sample preparation, possibly indicating that the structural relaxation of compressive stress may not be the only cause of bond lengthening; the increasing tensile stress characteristics could result from the purging of weakly bound oxygen and any other contaminants liberated by thermal annealing.

Crystalline Ta_2O_5 is understood to have an orthorhombic phase up to ~1360°C, beyond which a hexagonal phase transition occurs(210,211). In the orthorhombic phase tantalum is predominantly coordinated by 6 oxygen in octahedral arrangements(208), whereas 7-8 coordinated oxygen is most prevalent in the hexagonal phase(212), In the amorphous phase oxygen coordination is predominantly between 5 and 6(189,213); these configurations are depicted in Figure 3-26. The reduced coordination of the 400°C sample with respect to that of the 300°C may then indicate a population of < 5 coordinated tantalums.

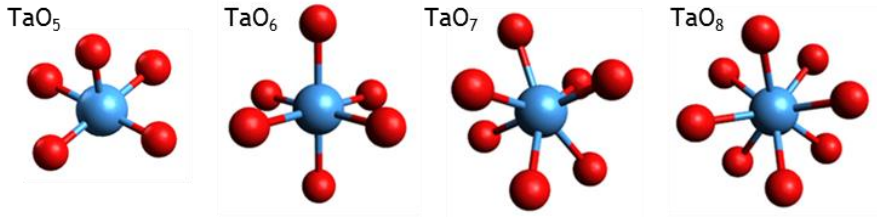

Figure 3-26 Five, six, seven and eight oxygen (red) coordinated tantalum (blue).

Ion beam sputtered *a*-Ta_2O_5 has indeed been shown to contain sub-oxide species(214). This could affect the lower occupancy and larger separation of the O-O distribution, leading to ordering and reduction of the first Ta-Ta pair density correlations, as well as ordering and extension in *r* for the second Ta-Ta / Ta-O shell, as indicated after 3.5 Å in Figure 3-25. The 600°C sample whilst having better stoichiometry than the 400°C sample, looks almost identical in the O-O distribution, but has increased pair density correlations sitting at slightly higher *r* for the first Ta-Ta shell, the same trend applies for the second Ta-Ta / Ta-O shell.

Annealing at $T > 300$°C apparently causes marked reduction in the number density of the structure, indicated by the slopes from the origin in Figure 3-20, as well as the area of the first peak in Figure 3-25; and whilst annealing at 600°C appears to be on the right track to re-establishing stoichiometry, it does so imperfectly, without commensurate densification of the subsequent coordination shells. This may imply a degree of porosity, or void formation occurring where these samples have been annealed at $T > 300$°C, which can be attributed to an agglomeration of oxygen vacancies(215).

Furthermore, the increased scattering at 2.4 Å in figure 3-23, indicative of the shorter pair correlations of the O-O separations in edge-shared polyhedra, can also result from the charge density fluctuations inherent to oxygen vacancies(216–218).

The 300°C data exhibits distinctly less scattering in this region with respect to the 400°C and 600°C data. The greater fraction of under-coordinated oxygen suggests a larger ratio of corner-shared to edge-shared octahedra(208,219), which are visualised in Figure 3-27.

Density deficits may result, with imperfect coordination also implying a tightening up of localised structures in line with the reduction of ionic radii(220), which form at the expense of density in adjacent regions. It seems obvious that there are thermally activated mechanisms modulating the structure at annealing temperature T > 300°C.

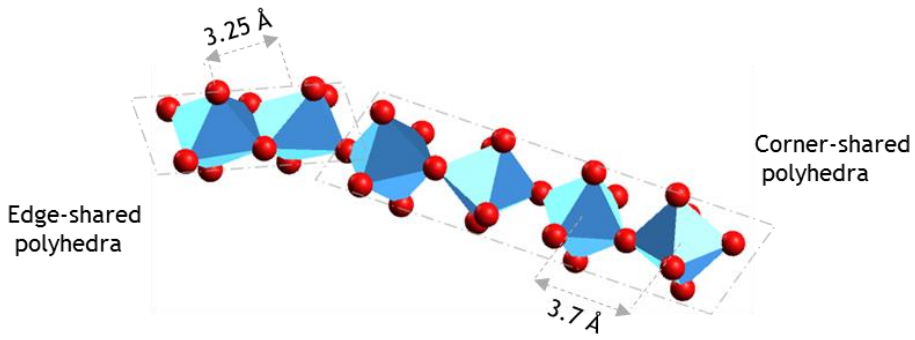

Figure 3-27 Schematic of tantalum in the centre of edge-shared and corner-shared polyhedra.

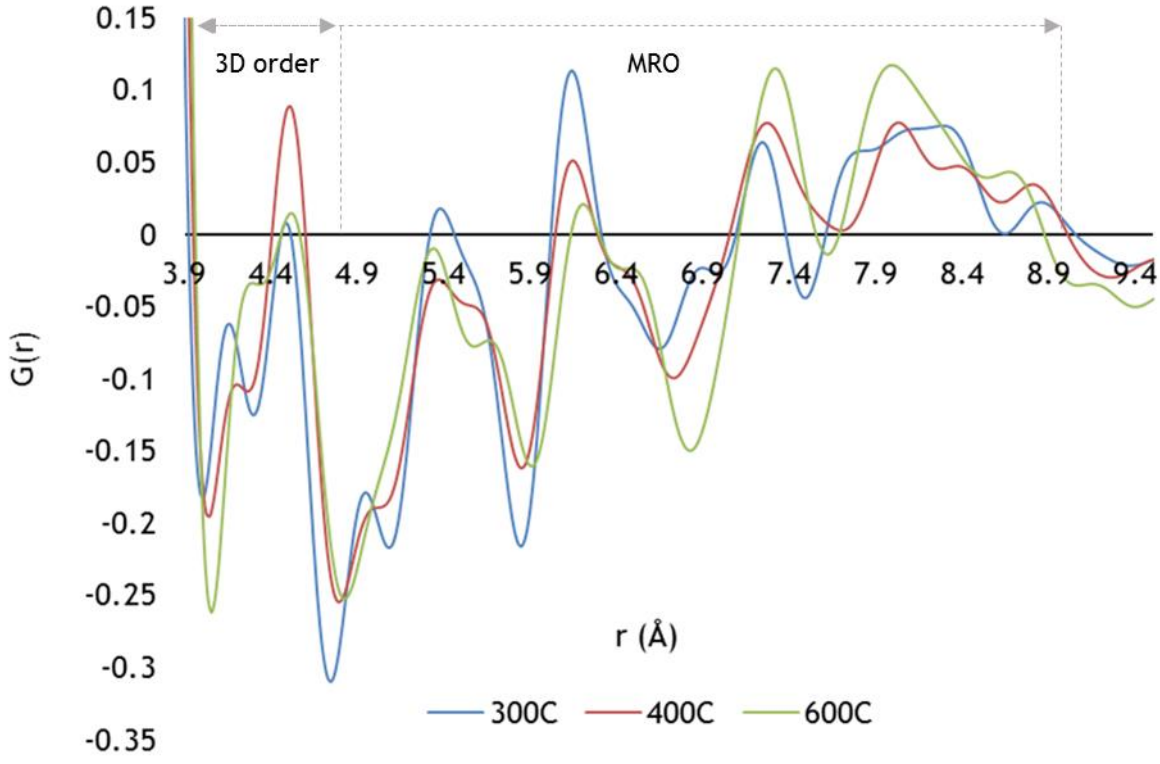

Figure 3-28 MRO of the un-doped heat-treated specimens shownin greater detail.

Turning attention back to the MRO (r > 4 Å) visible in $G(r)$ in Figure 3-28, the three samples have a similar degree of order with subtle differences. Between 4 Å & 5 Å lie two well defined peaks for the 300°C (~4.1 Å, ~4.5 Å) and 400°C (~4.2 Å, ~4.5 Å) samples, which are also found in crystalline tantala(82), with the 300°C data showing a greater prominence in both peaks, and the 400°C data exhibiting a much greater prominence at 4.5 Å, with a highly suppressed peak extended in r to ~4.2 Å.

This extended order can be thought of as linkages between the structural units constrained by the SRO which have been shown in molecular dynamics simulations(221) to be Ta-O correlations, and are visualised in Figures 3-22 and 3-29.

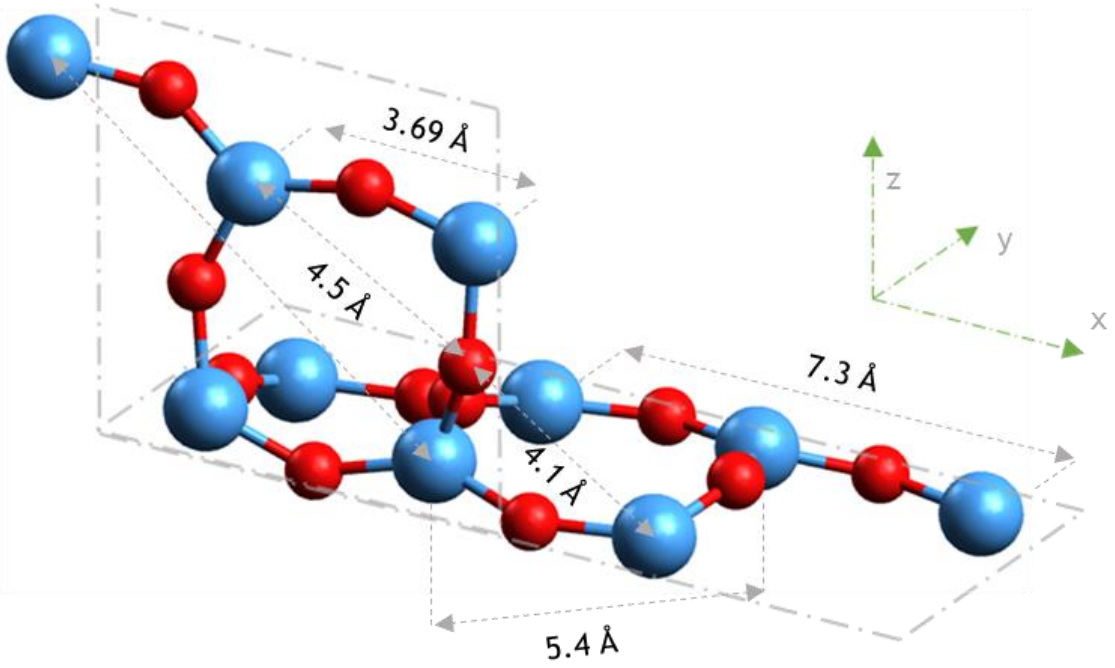

Figure 3-29 Schematic of 3D ordering, with cross-linked PSUs in perpendicular packing.

In the 600°C data of Figure 3-28, the 3D order correlations become incoherent, and the two peaks merge, plateauing between the peaks of the 300 and 400°C data, indicating severe attenuation of the ordered connectivity between the oxygen polyhedra.

The recent grazing incidence X-ray PDF (GIPDF) study carried out on IBS tantala(82) remarkably mirrors all the features seen in the PDFs shown here, with the exception of the O-O correlations at ~2.7 Å and the Ta-O correlations between 4 and 4.5 Å.

The absence of these peaks is not too surprising given the insensitivity of X-rays to low-Z atoms, however, the absence was noted and the authors suggested the presence is an indicator of 3D order, in which the lower dimensional structures are linked in their model, and is illustrated in Figure 3-29.

After the peak at 4.5 Å in Figure 3-28, there is a correlation at ~4.9 Å for the 300°C data, which is absent in the 600°C data, and appears as a shoulder in the 400°C data; this is absent in the GIPDF work and is likely an oxygen correlation given the relative sensitivities to the element between the techniques.

At ~5.3 Å, all three samples share a correlation, with the 300°C data most prominent and broad, trailing off with a shoulder at ~5.7 Å.

The 400°C data mimics the 300°C data but with smaller magnitude; the 600°C data however, peaks slightly lower in *r* and has a clear peak instead of a shoulder. The only sample in the GIPDF study to share this correlation was the 600°C annealed tantala, it was however broad and lacking the detail here.

The next correlation at ~6.2 Å in Figure 3-28 is again seen in all the data here, although the peak position increases and peak amplitude decreases with increasing annealing temperature; these correlations are also observed for all the tantala samples in the GIPDF study.

The ~6.2 and ~7.3 Å correlations in the GIPDF model correspond to Ta-Ta separation (or O-O) when two PSUs are linked together in a zig-zag fashion, and appear in this work to be secure structural motifs.

At ~5.3 and ~8 Å are correlations corresponding the cross-linking of two PSUs, leading to 2D order(82), and are prevalent in all samples, with the 300°C the most prominent. These correlations are visualised in Figures 3-22 and 3-29.

The main difference between these samples is that the 300°C annealed sample has the highest packing density of the coatings, with practically perfect stoichiometry, whilst the higher temperature anneals are sub-stoichiometric.

The 300°C sample in fact has been reported to have the lowest value of mechanical loss out of these samples at the temperatures ranges measured(188), it would then seem intuitive to assume the 300°C samples mechanical performance is correlated with the highest density of packing.

However, the difference in mechanical performance between the 300 and 400°C samples are minimal, and do not appear to correlate with the difference in number density.

The 600°C sample on the other hand has much higher reported mechanical loss than both the other coatings in the same temperature ranges(188), but is similar in number density with the 400°C sample.

In any case, information came to light with respect to the inaccuracy of the loss measurements that make attempted correlation of measurements unfeasible.

The first major disparity is found in the pair correlations between 4 and 4.5 Å in Figure 3-28; the 300 and 400°C samples have well defined peaks, whereas the correlations for the 600°C sample at this distance are frustrated and ill-defined.

These structural differences may prove important in understanding the link between atomic structure and internal friction, as this motif has been shown to be responsible for establishing 3D order in the structures by packing perpendicular to the zig-zag PSUs and their cross-linked 2D structures(82), as illustrated in Figure 3-29.

3.4 14% Ti:Ta_2O_5 thermal annealing

In this section, the differences in atomic structure as a function of heat treatment temperature are explored for 14% titania doped tantala. It should be noted that in the current understanding of titania doped tantala, titanium directly substitutes for tantalum, perturbing somewhat, but not heavily modifying the structure(190,208,221), with approximately equal ionic radii of 0.68 Å.

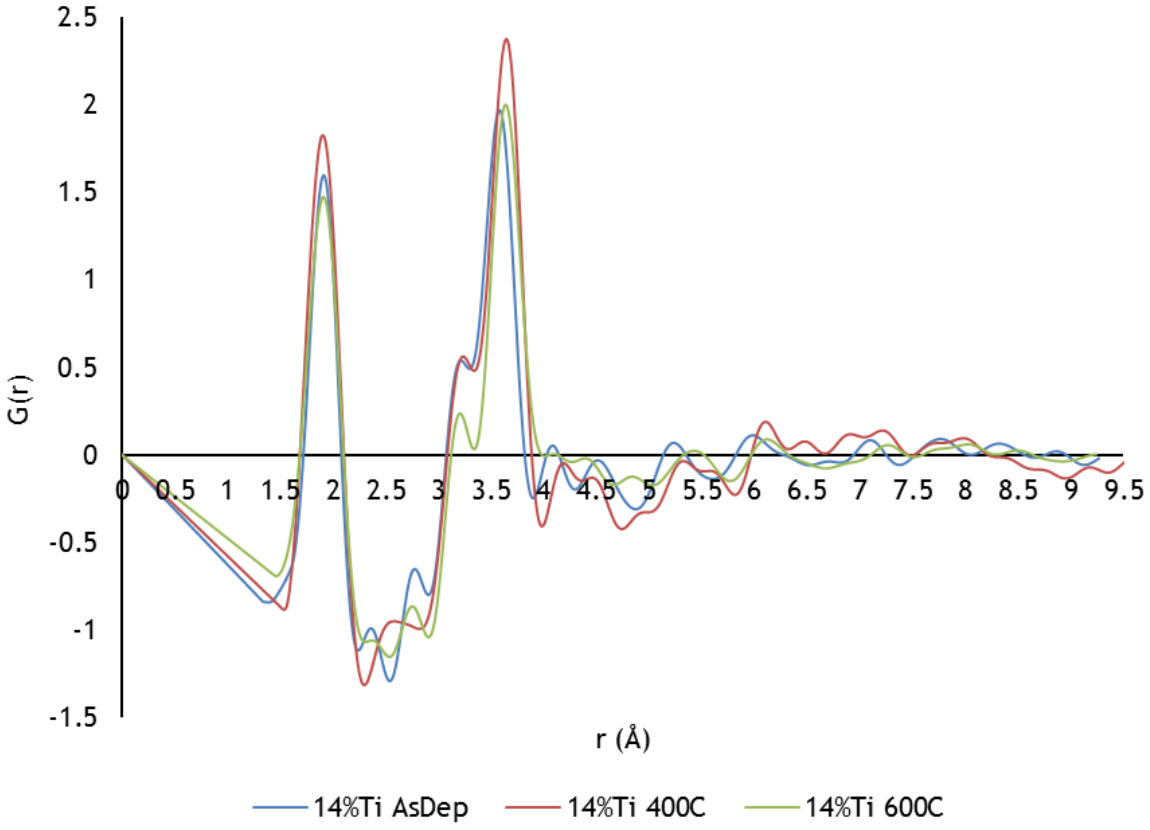

Figure 3-30: Reduced density functions of 14% Ti:Ta_2O_5, as deposited and annealed for 24 hours in air at 400°C and 600°C.

As with the pure Ta_2O_5 thermal anneal series, the 14% titania doped tantala thermal anneal series also exhibits structure visible out to ~9 Å. And likewise, the limit of SRO is defined at ~4 Å, with pair correlations at higher r > 4 Å representative of the MRO. The reduced pair density functions, $G(r)$, of the 14% Ti:Ta_2O_5 thermal annealing series are shown in Figure 3-30.

The data in Figure 3-30 indicates that the as deposited sample has the highest density, which reduces very slightly after annealing at 400°C. After a 600°C anneal, the reduction in number density is much larger with respect to both the as-deposited and the 400°C data.

The reduction in number density may be attributed at first approximation to relaxation from an initially compressive structure. The significant reduction of the 600°C density with respect to the as-deposited and 400°C data however may involve other mechanisms.

As in the previous section, peaks below 2 Å are representative of the metal-oxygen nearest neighbour distributions, with 14% of the distribution now having a probability of Ti-O NN constitution, and are centred around 1.9 Å. The SRO is plotted for clearer inspection in Figure 3-31.

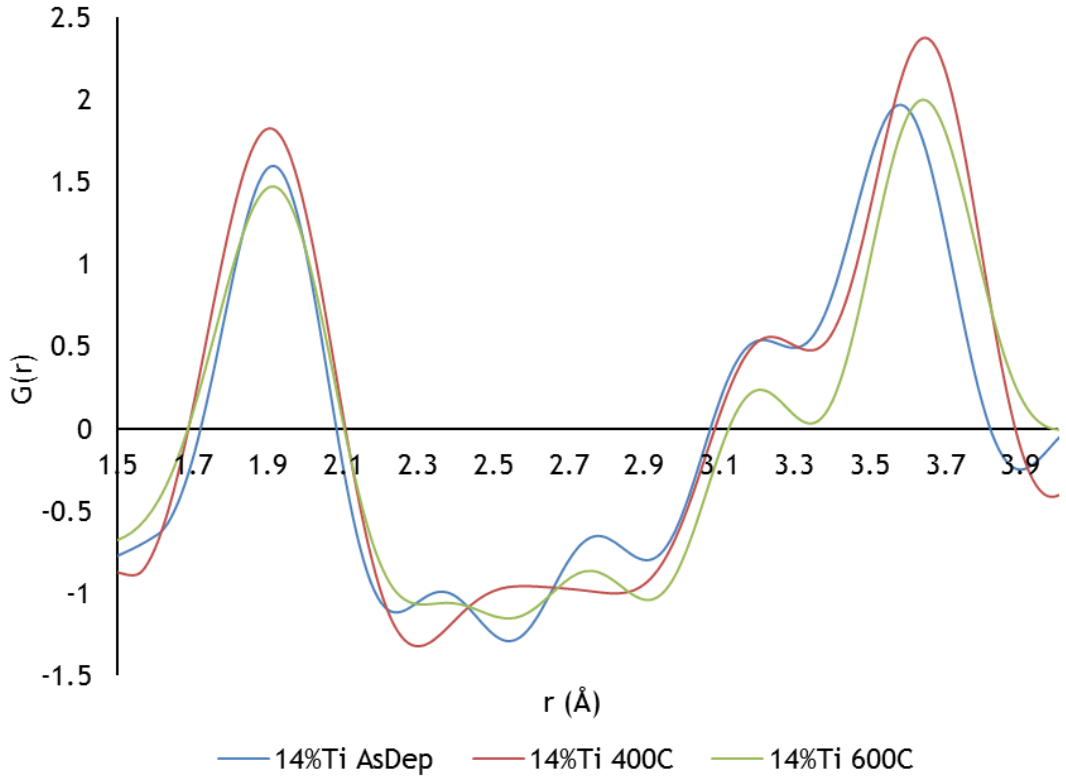

Figure 3-31 A closer inspection of the short-range order in the thermally annealed Ti-doped tantala samples.

There is insignificant movement of the first peak after a 400°C anneal, however, in contrast to the expansion of the first coordination shell in the un-doped samples with increasing heat treatment, the 600°C anneal data undergoes a minute contraction.

With the apparent reduction in number density with increasing heat-treatment, a continuing trend of NN shell expansion could be expected, however the contraction in the 600°C data indicates a possible reversal of stress sign again, as for the un-doped Ta_2O_5 discussed above.

The deviation from the average density of the samples for first NN pair correlations are visible from the relative peak heights. The 400°C NNs are more prevalent with respect to the as deposited sample, indicating a more orderly coordination with respect to the average number density of the samples; from the trends in the previous section, the sample with highest number density would be expected to have the highest order in the first shell, but is not observed here, however no as-deposited pure tantala sample was available for direct comparison.

The 600°C data in Figure 3-31 does however appear to follow the number density trend, and the reduction in the first peak height with respect to the 400°C data is similar to the reduction of the 600°C average number density. However, the as-deposited data has the smallest peak width, indicative of a lower spread in bond angles, and thus the most orderly, and increases after a 400°C anneal to a larger width than the 600°C data.

The peaks between 2.3 and 3 Å in Figure 3-31 again are separations of oxygen in the M-O NN distributions. In contrast to the pure tantala data, here the pair correlations clearly illustrate the two discrete O-O separations of the edge and corner-shared polyhedra in the as-deposited and 600°C data, illustrated below in Figure 3-32; the 400°C data however plateaus between the peaks of the other samples and exhibits an elevated level of disorder.

The O-O distributions for the as-deposited data are the most prominent, with the 400°C distribution appearing more random, and the 600°C distribution which is more similar in form to that of the as-deposited data but of lesser magnitude and spread. Thermal annealing clearly modifies the orientation and occupancy of the oxygen distributions; the peaks are suggestive of an initially phase separated character in the as-deposited sample that is homogenised by a 400°C anneal, but less so at 600°C, and presumably affects the distributions of higher-order pair correlations. Furthermore, the spread of O-O separations in the as-deposited specimen can suggest a higher concentration of sub-oxide species(88).

Between 3 and 3.5 Å in Figure 3-31 is the third peak, corresponding to the second coordination shell of the central atom (shown below in Figure 3-32), which contains Ta-Ta, Ta-Ti and possibly Ti-Ti pair correlations. The 600°C data is the most dissimilar here, it is greatly reduced in amplitude with respect to the other two samples which overlap with the next peak, and appears much more ordered.

Annealing at this temperature seems to result in higher ordering of this shell, as can be seen from its reduction in width and splitting from the M-M peak. It may be the case that Ti prefers this shell position within the structure(190), as indicated in Figure 3-32, and will fill it preferentially when enough thermal energy is driven into the system, leading to sharper distinctions in the positions of the M-M distributions as observed in Figure 3-31. The preference for Ti to occupy this position in titania doped tantala has been shown elsewhere to be the most energetically favourable position(222).

Simulations of stoichiometric films have also shown that titanium forms almost equal proportions of 5 & 6 coordinated oxygen, whereas in pure tantalum pentoxide the fraction of 6 coordinated oxygen is ~70%(208).

This suggests an increased tendency for edge-shared polyhedra in titanium-doped tantala, which itself may explain the improvements gained in mechanical loss by its substitution; a higher ratio of edge-shared polyhedra implies a more mechanically stable structure through increased structural connectivity, which is more likely to be maintained during thermal annealing in comparison to pure-tantala, due to the apparent preference of titanium for this shell position.

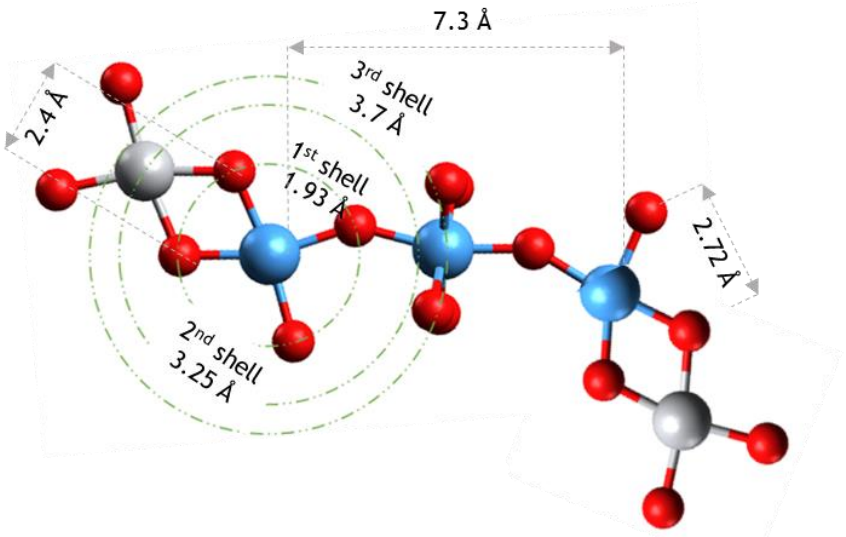

Figure 3-32 Schematic of the coordination shells around an average tantalum atom (blue). The 1st shell consists of the intra-polyhedral oxygen nearest neighbours (red), the 2nd shell next nearest-neighbour inter-polyhedral metal is thought to be preferentially occupied by titanium (grey), and the the 3rd shell inter-polyhedral NN is pedominantly occupied by tantalum.

The peaks between 3.5 and 4 Å in Figure 3-31 contain contributions from a second Ta-O and Ta-Ta shell, peaking around 3.6 Å.

There are assumed to be insignificant Ti-Ti correlations at this distance due to the low dopant concentration and preference for the shorter M-M distance.

The heat-treated samples in this region both show an increase in peak position, but whilst the 400°C peak width expands slightly, the 600°C peak width contracts, giving some credence to the separation of metals into preferential shells at this higher annealing temperature.

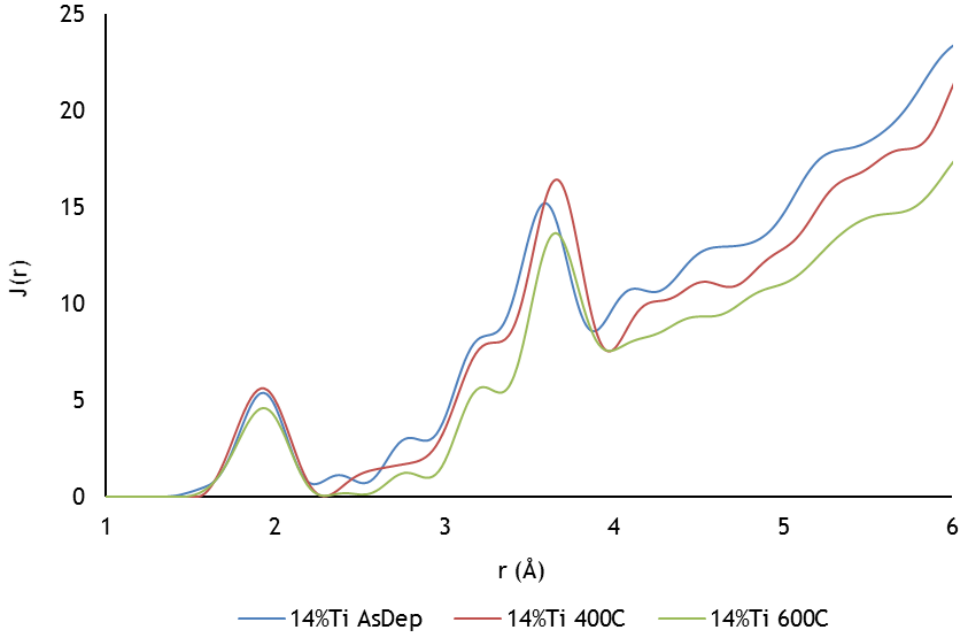

Figure 3-33: Radial distribution functions (q = 16 A^{-1}) of 14% Ti:Ta_2O_5, as deposited and annealed for 24 hours in air at 400°C and 600°C.

Figure 3-33 shows the conversions of the data from $G(r)$ to $J(r)$, the radial distribution function. Although the peak corresponds to Ta-O and Ti-O pairs, an average metal-oxygen coordination number is presented for all titania doped samples.

The as-deposited data shows an average of 4.58 oxygens surrounding a central cation and is oxygen deficient, whereas the 400°C data has 4.96 oxygens per central cation, and is over-stoichiometric.

After a 600°C anneal, the sample is further from stoichiometry, with the data indicating only 4.43 oxygens per central cation. The 400°C data appears closest to stoichiometry, which is expected to be 4.86 oxygens per central cation at 14% Ti; however, this assumes that the structure is composed solely of TiO_2 and Ta_2O_5, and is probably unrealistic.

This is interesting in comparison to the pure tantala in the previous section, which when annealed to 300°C was stoichiometric; and although there was no data available for the pure as-deposited coating, it was assumed that it was sub-stoichiometric, and that the number density of the coatings increased through oxygen absorption, improving coordination during thermal annealing. This may be indication of a greater range of sub-oxides within the samples.

It may be posited that stoichiometry improvement may also occur by the redistribution of oxygen already within the structure, optimised by a 300°C anneal in pure tantala, homogenising the phase.

And a pure 400°C tensile structure in which weakly-bound oxygen possibly outgasses under the higher temperature driving force and greater free volume, whilst the slightly higher 600°C sample density could be explained by having less of a tensile stress characteristic, with lesser free volume and mean free path for oxygen diffusion.

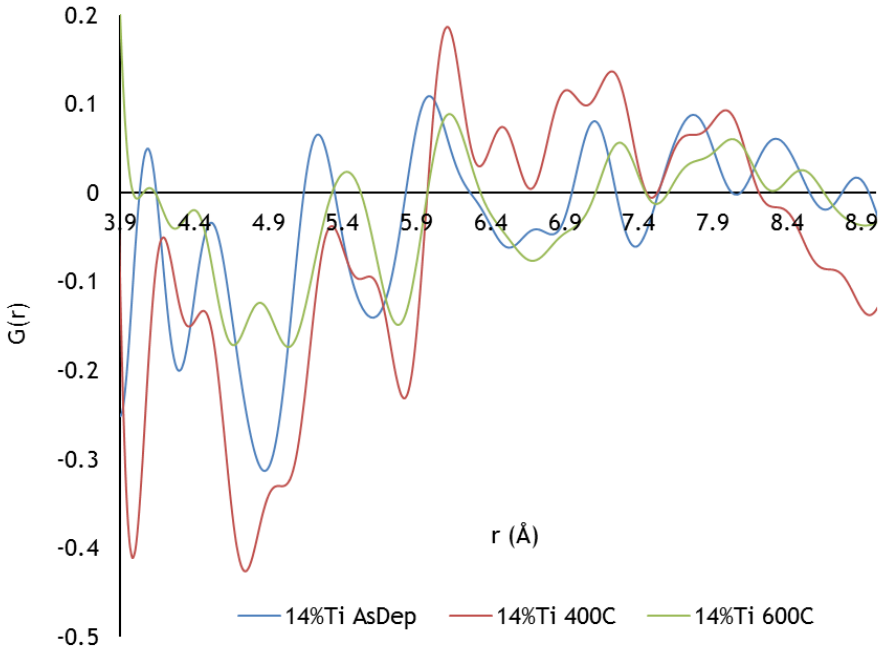

Figure 3-34 Closer inpection of the MRO in the 14% Ti-doped tantala thermal anneal series.

Now with the 14% doping, stoichiometry is almost met at the higher annealing temperature of 400°C, indicating that titania doping may inhibit oxygen diffusion during thermal annealing, and a that higher driving force is required to redistribute the oxygen in comparison to a pure tantala system.

This may be plausible, given the greater oxygen affinity of Ti over Ta, and that titanium effectively reduces tantala(223,224).

The lower coordination and density of the 600°C, doped sample, may be explained similarly; the higher thermal driving force in combination with a more tensile structure could affect increased diffusion of oxygen out of the structure, leading to the formation of sub-oxides, and may be supported by the observed increase in optical absorption due to Ti-cation doping(33).

It appears that titania doping may have a pronounced effect upon stress and oxygen diffusion in thermally annealed Ti:Ta_2O_5.

The MRO (r > 4Å) in these samples, plotted in Figure 3-34, displays the same structural motifs as the pure tantala discussed in the previous section, with varying offsets of the peak positions; the 400°C data however may suffer from ringing artefacts of the truncated Fourier transform between 6.5 and 7 Å, as these are not observed in the other data, but then again, they may represent a higher degree of structural coherence and connectivity.

In any case, as with the pure tantala, there are the same signatures found in Figure 3-34 for the Ta-O-Ta backbone, and the cross-linking into 2D structures as described in the previous section(82). The peaks between 4 and 4.5 Å however are proposed to be the salient feature relating to mechanical stability of the structure, as they are hypothesised to be the signature for cross-linking perpendicularly to both the Ta-O-Ta backbone and cross-linked 2D structures, creating 3D order within the structure as illustrated in Figure 3-29.

The as-deposited data in Figure 3-34 displays the highest degree of order after 4 Å, with two well defined peaks at 4.1 and 4.5 Å; annealing at 400°C causes a shift of the 4.1 Å peak to higher in r, merging with the withdrawing 4.5 Å peak into disorder; after annealing at 600°C the peaks level out and pair correlations all but disappear, indicating the highest degree of disorder in this region between the samples. Entertaining the premise that this structural motif is an indicator of 3D structural cross-linking, and that this may be a major factor affecting the mechanical stability of the tantala and titania doped tantala coatings, it could be used as a predictor of low thermal noise preparations of the coatings.

3.5 52% Ti:Ta_2O_5 thermal annealing

In this section, the effect of a 600°C anneal upon 52% titania doped tantala is investigated. *G*(*r*) plots are shown below in Figure 3-35. The data indicates that after annealing at 600°C, the structure becomes denser, in contrast to previous trends of decreasing number density with increasing heat treatment.

The apparent density increase could possibly be explained by absorption of oxygen into the structure, reorganisation into higher packing configurations, and possibly even by the repair of sub-nm porosity; this could be an effect of stress modulation by Ti at higher doping concentration.

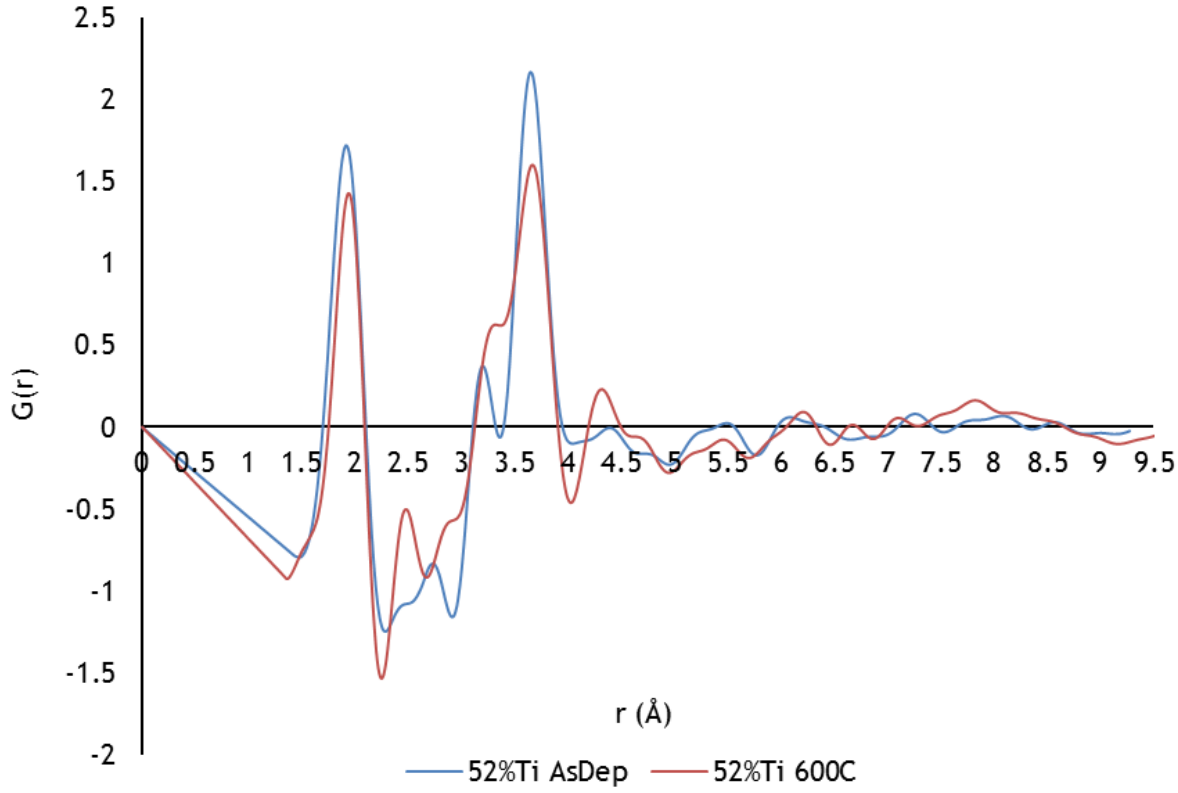

Figure 3-35: Reduced density functions of 52% Ti:Ta_2O_5, as-deposited and annealed for 24 hours in air at 600°C.

The first metal-oxygen distribution peaks at ~1.91 Å for the as-deposited sample and after annealing at 600°C, shifts to ~1.94 Å. The as deposited sample displays a wider distribution of NN distances than the annealed sample, and shows more ordering of these pairs with respect to its average number density. The SRO is plotted again in Figure 3-36, below, for better clarity.

Between 2.3 and 3 Å, the O-O distributions, display two distinct sites as in the 14% titania doped samples for the edge and corner-shared polyhedra. This appears to be a strong feature of titanium influence upon the structure, and suggests increased phase separation.

The as deposited data shows a weak correlation at ~2.4 Å and a more prominent peak at ~2.7 Å, whereas after a 600°C anneal, the ~2.4 Å peak is amplified and extends in *r*, whilst the 2nd peak becomes less defined and shifts out to ~2.8 Å, overlapping with the next peak.

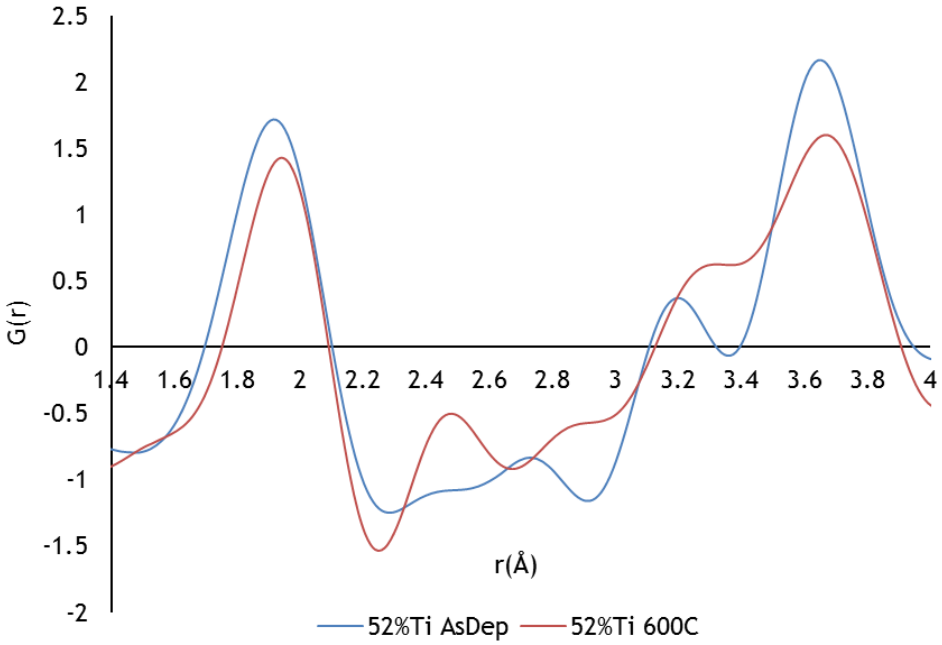

Figure 3-36 A closer inspection of the short-range order in the thermally annealed 52% Ti-doped tantala samples.

In fact, for the 600°C anneal, all pair correlations in Figure 3-36 between the first O-O shell and final coordination shell of the short-range order become difficult to disentangle, and may represent greater disorder of the structure with randomised substitutions of Ti and Ta into the in Ta and Ti centred polyhedra.

However, the pair correlations between the 1st and final peak in the 600°C data show a much higher packed system and could account for the increased number density.

In Figure 3-36, between 3 and 3.5 Å lies the third peak of the rRDF, corresponding to Ta-Ta, Ta-Ti and Ti-Ti pair correlations.

The as-deposited data has the centre of this well-defined distribution placed at 3.2 Å, and after a 600°C anneal it expands to 3.3 Å, losing definition, increasing in magnitude and merging with the next peak, indicative of a high degree of randomisation between polyhedra.

The peaks between 3.5 and 4 Å of Figure 3-36 contain contributions from a second Ta-O and Ta-Ta/Ta-Ti shell, peaking around 3.7 Å. The slight difference in peak position may be an indication of compressive stress relaxation or expansion due to the filling up of the lower order coordination shells.

Furthermore, the skewing of the as-deposited data to lower in *r* may further indicate heterogeneous phase separation, homogenised somewhat after annealing at 600°C, and possibly account for the decrease in peak magnitude.

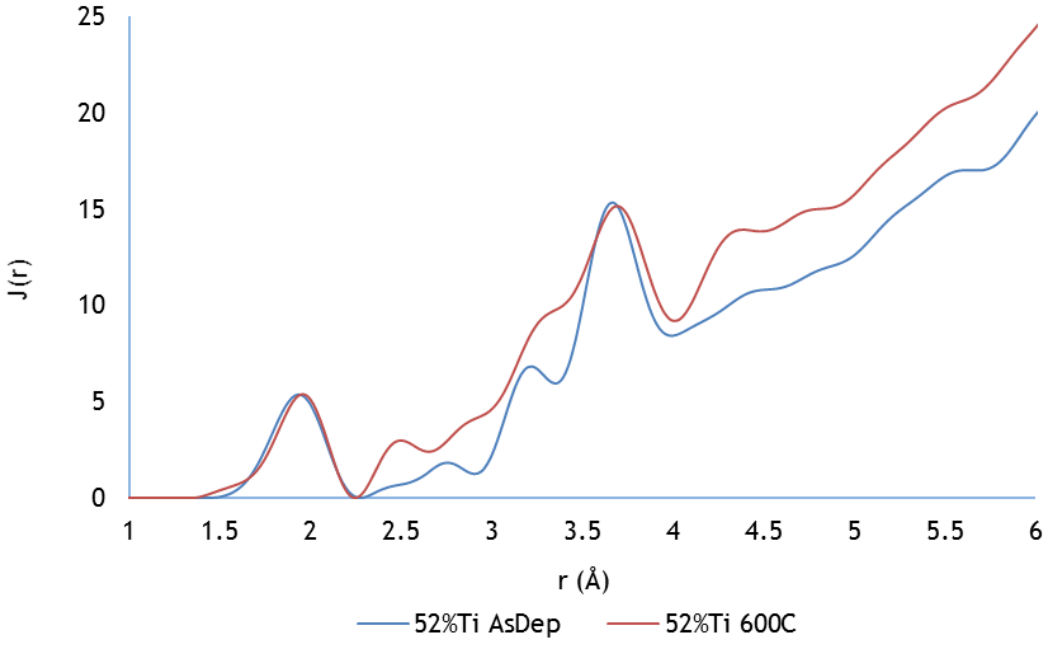

Figure 3-37: Radial distribution functions (q = 16 A^{-1}) of 52% Ti:Ta_2O_5, as-deposited and 52% Ti:Ta_2O_5 annealed for 24 hours in air at 600°C.

J(*r*), the radial distribution function is shown for the data in Figure 3-37, highlighting the possible source of the derived high number density.

There is a significant increase in the pair correlations associated with the two peaks lying between the first and final coordination shell of the SRO, confirming a higher density random packing of polyhedra, greater in number and composition than in the as deposited sample.

At 52% Ti-doping, and in the absence of sub-oxides, stoichiometry should be achieved with an average of 4.48 oxygens per central cation.

The as-deposited 52% data indicates an average of 4.80 oxygens surrounding a central cation and is over-stoichiometric, whereas the 600°C data is closer to the ideal value, with 4.54 oxygens per central cation.

However, unpublished optical absorption measurements of this annealed structure revealed its performance was far from the strict < 0.5 ppm requirement(33), and indicate the structure to be more complicated than previously assumed.

Looking at the MRO in *Figure 3-38,* again the correlations match the signatures of the proposed structural units previously described as the building blocks of tantala and titania doped tantala, illustrated for pure-tantala in Figure 3-29, and allowing for variation in the peak positions owing to the spread of M-O-M bond angles and distances.

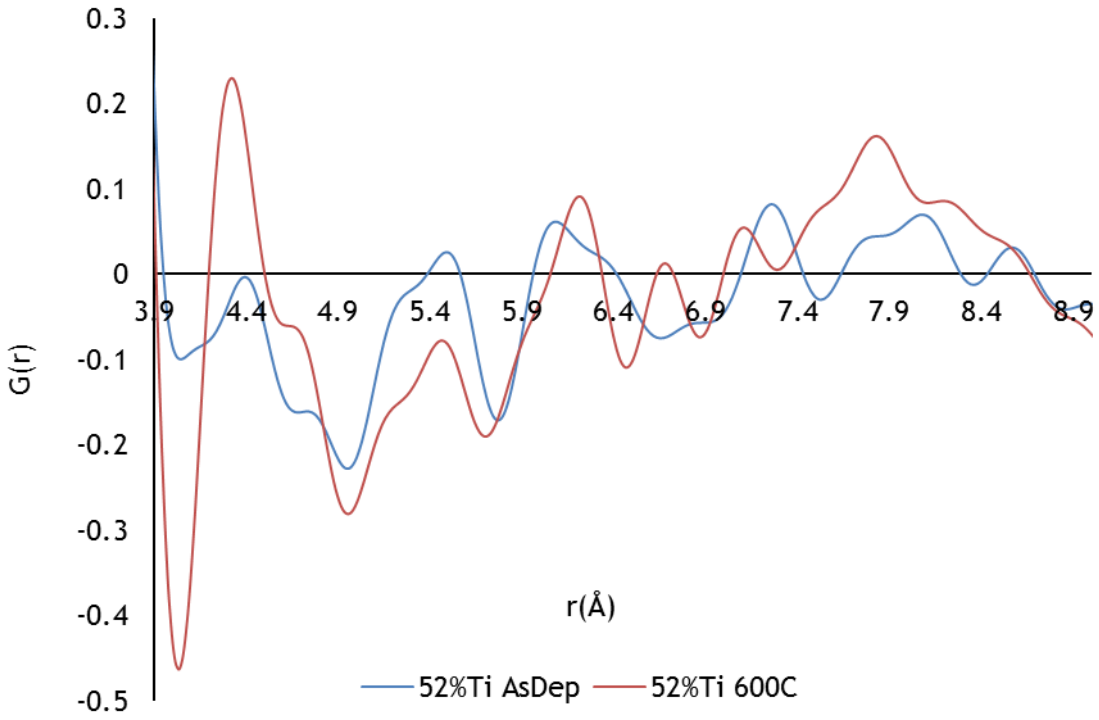

Figure 3-38 Closer inpection of the MRO in the 52% Ti-doped tantala thermal anneal series.

Once more, attention is focused upon the pair correlations between 4 and 4.5 Å in Figure 3-38, the proposed signature for 3D ordering(82), and visualised below in Figure 3-39. Interestingly, at this level of titania doping only one significant peak appears, and indicates homogenisation of the links making the 3D packed structure, possibly due mainly to Ti atoms bridging the structures.

The 600°C annealed sample is by far the most prominent in this region, and is predicted to be the most mechanically stable; predominantly by way of its very strong 3D packing signature, its highly-ordered oxygen distribution and apparent randomised mixing of the metals throughout the structure.

Furthermore, it has been shown that equal cation concentration in transition metal metal-oxides stabilise the octahedral frameworks, improving mechanical stability(225,226).

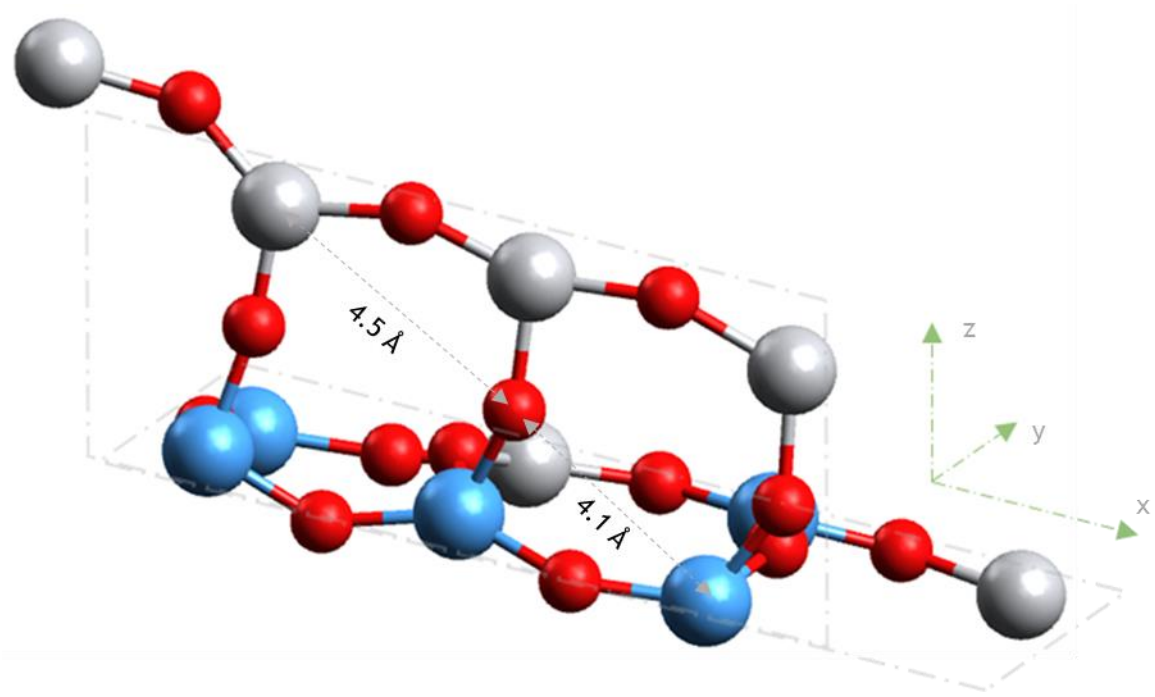

Figure 3-39 Schematic of the atomic configurations in 52% Ti-doped tantala, described by the pair correlations of Figures 3-35 to 3-38.

3.6 As deposited Ti:Ta_2O_5 coatings

The differences in atomic structure as a function of titania doping are here explored for the range of as-deposited samples. The reduced pair density functions, $G(r)$, of the doping series are shown in Figure 3-40.

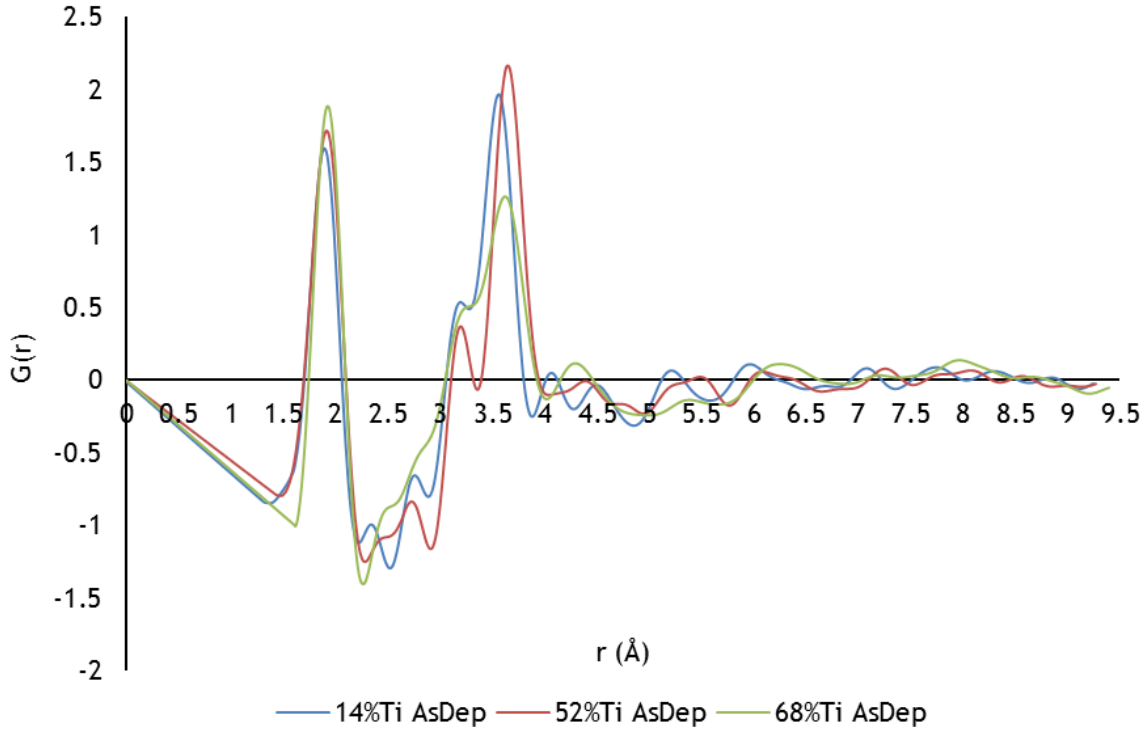

Figure 3-40: Reduced density function of as-deposited 14%, 52% and 68% Ti:Ta_2O_5.

The 14% and 68% doping samples show the highest density, whereas the 52% doping results in a slightly lower number density film. This may be an indication that the highest packing density can be achieved when Ta or Ti constitute a predominant fraction of the metal content.

With low Ti concentration, Ti appears to have preference for the lower r shell position; Ta may fulfil an equivalent role in the low Ta concentration case. In both these cases, no major modification of the structure is expected and dense packing of similar structural units are expected.

On the other hand, a sputtered binary cation oxide film with roughly equal cation concentration, as in the 52% doped sample here, will likely have more of a phase separated heterogeneous character upon deposition rather than well-mixed and homogenous, which would imply sub-optimal packing of the different metal-centred polyhedra.

This gives rise to the possibility of sub-nm voids, common in titania films, which may explain the low density, and extension of bond lengths in the higher titanium content films.

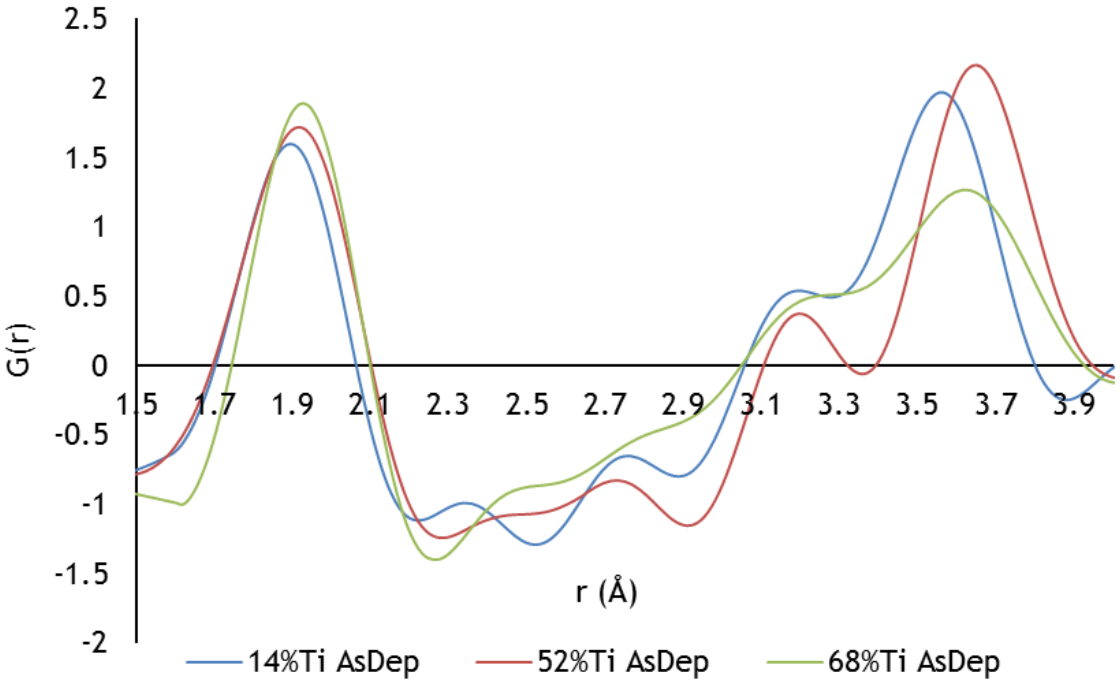

Figure 3-41 A closer inspection of the short-range order in the as-deposited Ti-doped tantala samples.

The first metal-oxygen distributions peak at ~1.92 Å and are plotted again in Figure 3-41. The increasing concentrations of titanium appears to shift the M-O peaks higher in *r*, however, the shapes of these distributions are maybe more informative.

The 52% doped sample peak width displays the limits of the roughly equal bond length distributions for Ta-O and Ti-O. In the 14% Ti doping data, the distribution is skewed to the left and lines up nicely with the lower *r* side of the 52% distribution, consistent with a lower Ta-O bond length in comparison to Ti-O(190).

The 68% data mirrors this this structural characteristic, skewing to the right, reflecting the longer Ti-O bond lengths in the distribution. Again, deviation from the average density of the samples for first NN pair correlations are visible from the relative peak heights.

After the first pair correlations in Figure 3-41, the 14% sample has its first well defined peak at ~2.3 Å and second at ~2.8 Å; the first peak of 52% doped sample is found at slightly higher *r* and is less prominent than at 14%; it is also less defined, as it merges with the less prominent shorter second peak at ~2.7 Å.

The 68% sample displays these peaks at higher *r* than both the previous samples with the overlapping peaks indicating a much higher degree of disorder in this sample, with less apparent localisation of the edge and corner-shared polyhedra.

Between 3 and 3.5 Å in Figure 3-41 are the Ta-Ta, Ta-Ti and Ti-Ti pair correlations, appearing around 3.2 Å. The 14% data here is not well defined, but is of larger magnitude than the much better defined 52% peak.

This could indicate better homogeneity of a structure holding a majority in one cation species through better mixing in un-annealed samples. he peak of the 68% data here is the least defined and sits at slightly higher *r*, and again displays a more randomised structure with one cation species domination the concentration.

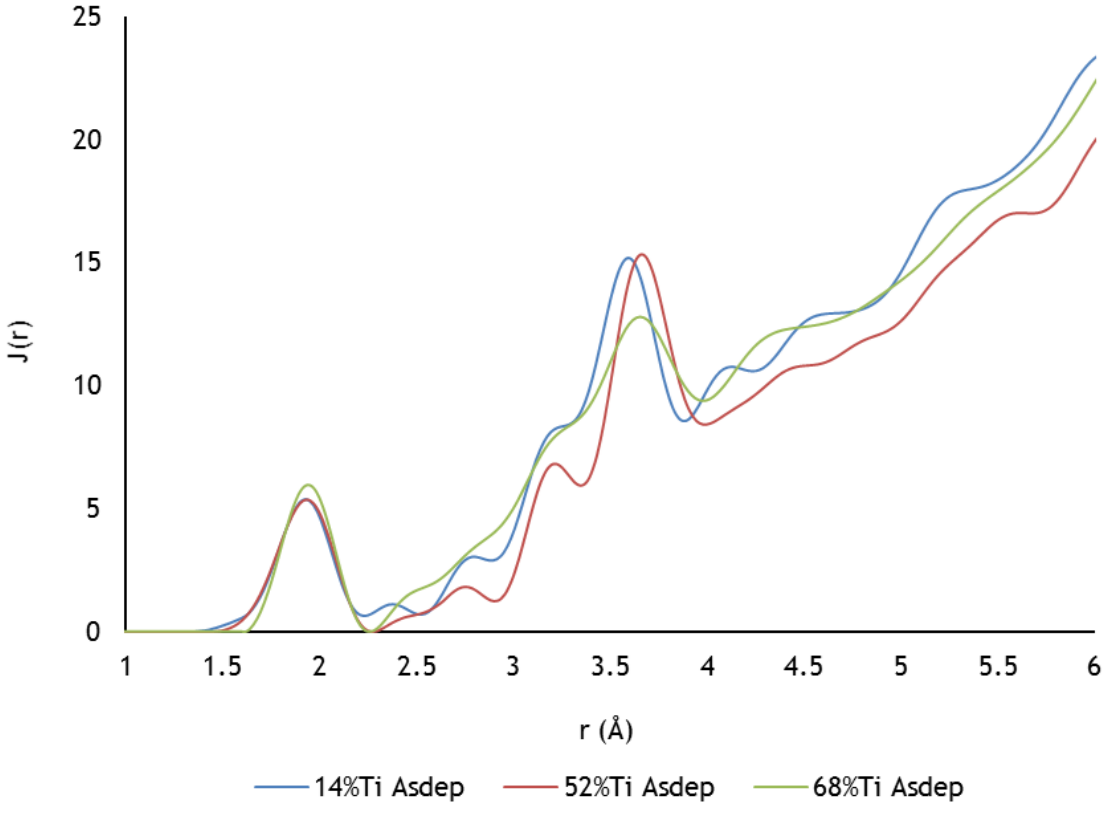

Figure 3-42: Radial distribution function of as-deposited 14%, 52% and 68% Ti:Ta_2O_5.

The peaks between 3.5 and 4 Å in Figure 3-41, representing the next Ta-O, Ta-Ta and Ta-Ti shells, peak at ~3.6 Å. The shorter pair correlation of the 14% sample in contrast to the other samples could imply that higher Ti concentration inhibits the compressibility of the structure during deposition.

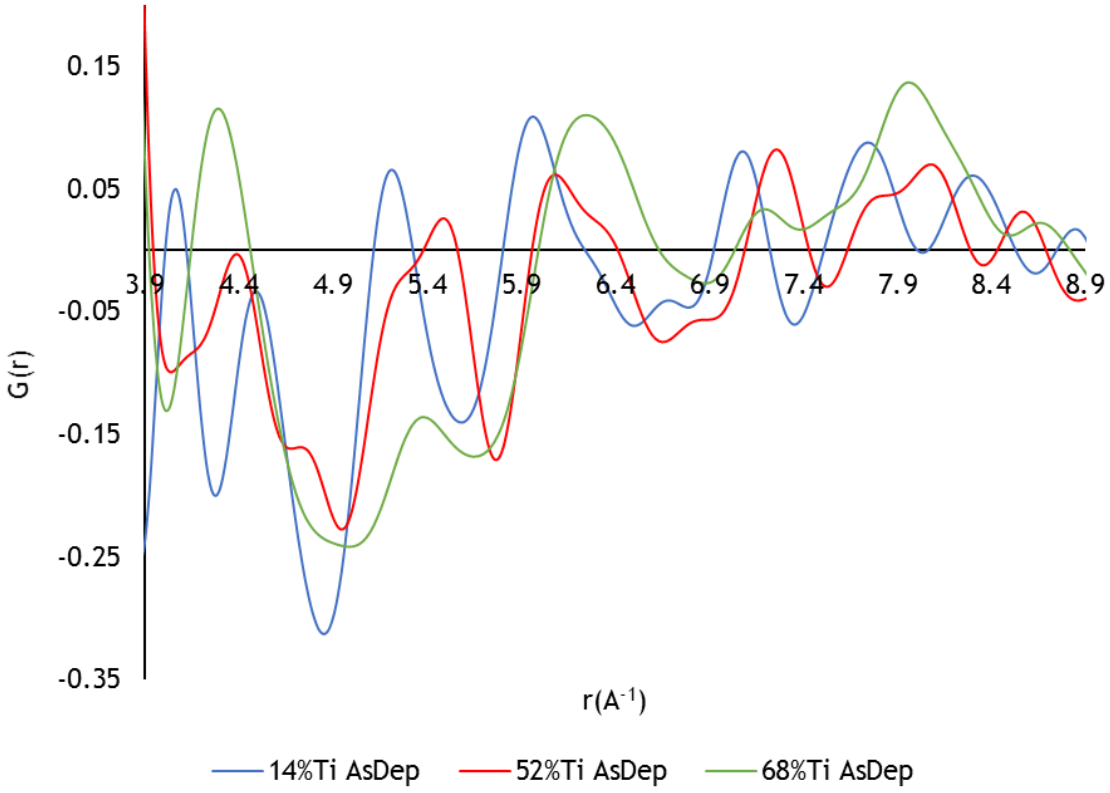

Figure 3-43 Closer inpection of the MRO in the as-deposited Ti-doped tantala samples.

However, a higher Ti-cation concentration implies an increased population of edge-shared polyhedra, which have a much tighter M-O-M bond-angle distribution than in corner-shared polyhedra.

The longer M-M separations support the posited nano-porosity of these higher titanium content structures, or of heterogeneous phase separated structure interspersed by low-density regions.

Figure 3-42 shows the conversions of the data from $G(r)$ to $J(r)$. Integration of the first peak indicates a low coordination of 4.58 oxygens surrounding a central cation for the 14% data, the 52% data indicates a high mean coordination of 4.80 oxygens per central cation; the 68% data infers a high mean coordination of 4.52 oxygens, which should ideally be 4.32 if composed of only TiO_2 and Ta_2O_5.

The reason for imperfect coordination is not yet certain; the overall lower oxygen coordination of Ti doped samples should primarily result from the lower oxidation state of titanium(208), however, inconsistencies are apparent and contributions may include porosity, oxygen vacancies, heterogeneous phase separation and a range of sub-oxides.

The section will once again close with comment on the MRO, plotted in Figure 3-43. The pair correlations extending to ~9 Å are consistent with the linking of PSUs of varying bond length and bond angle as shown in Figure 3-39.

As the correlations between 4 and 4.5 Å are believed to be the salient features that dominate the mechanical stability of the structure, discussion shall be limited to them.

The 14% sample in Figure 3-43 has two peaks in this region, and are presumed to signify Ta and Ti 3D-crosslinking for the ~4.1 and ~4.5 Å correlations respectively, as shown in Figure 3-39. In the 52% data, the ~4.1 Å peak is practically unrecognisable, and the ~4.5 Å peak increases in amplitude at slightly lower *r*, giving strong indication for the preference of titanium for this location.

This is corroborated by the 68% doped sample which also has one well defined peak, the highest in magnitude of the three, and sits slightly lower in *r* with respect to the 52% sample.

3.7 400°C annealed Ti:Ta_2O_5 coatings

The difference in structure between pure tantala and 14% titania doped tantala annealed at 400°C is investigated next; their *G*(*r*) plots are shown in Figure 3-44.

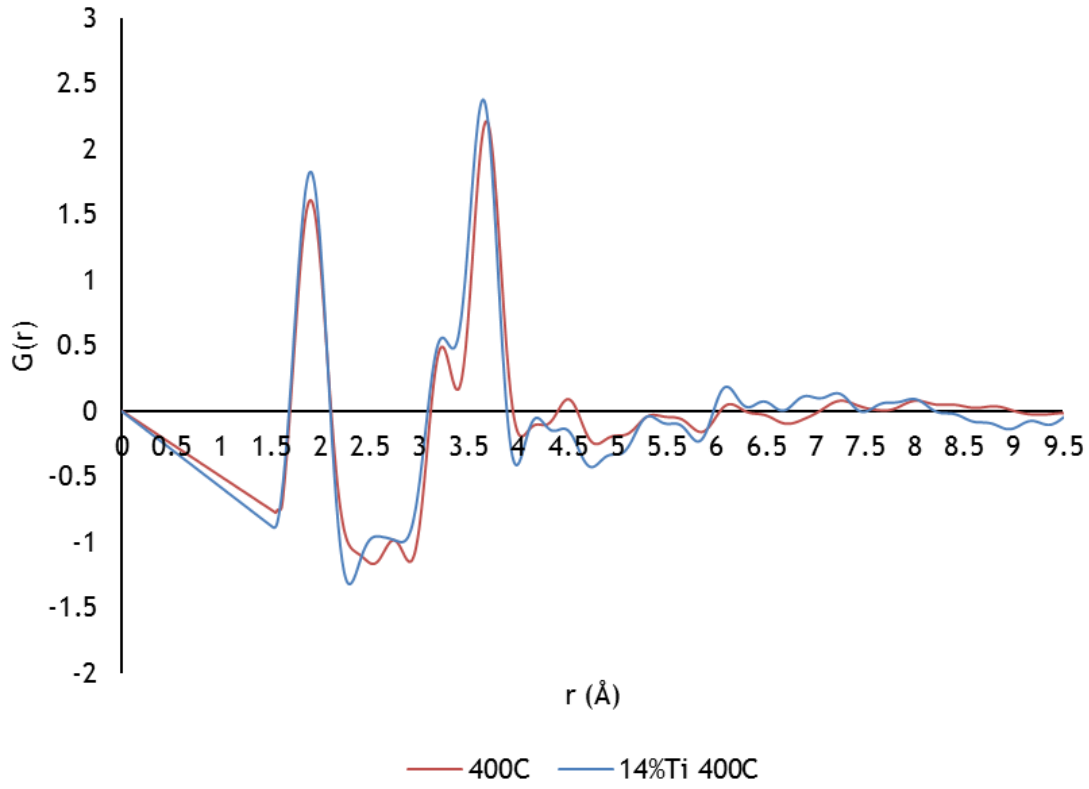

Figure 3-44: Reduced density functions of 400C annealed Ti:Ta_2O_5.

The 14% Ti-doped structure has the higher packing density; a sign mentioned before, possibly indicating that Ti doping inhibits the diffusion of oxygen out of the structure during thermal annealing if that indeed occurs.

On the other hand, if Ti is undercoordinated, its greater oxygen affinity than tantalum may increase the efficiency of oxygen uptake from the annealing ambient. A factor that certainly contributes to the higher density of the doped sample is the greater propensity for edge-shared polyhedra in Ti-doped tantala.

The first metal-oxygen distribution peaks around 1.9 Å, and is shown more clearly in Figure 3-45. The doped sample indicates, by greater deviation from the average sample density, more order in this shell with respect to the pure sample, corroborating others assertion that Ti doping homogenises the first M-O distribution(190,208).

The O-O distribution peaking between 2.3 and 3 Å in Figure 3-45, for the 14% doping is not well defined compared to the pure sample; it plateaus and implies a broad, highly occupied and randomised distribution, possibly filled by thermally activated oxygen diffusion, enhanced by the titanium doping.

However, if titanium is mainly occupying the lower M-M shell position, the stronger scattering of tantalum over titanium may mask the O-O signal of the Ti-centred edge-shared polyhedra.

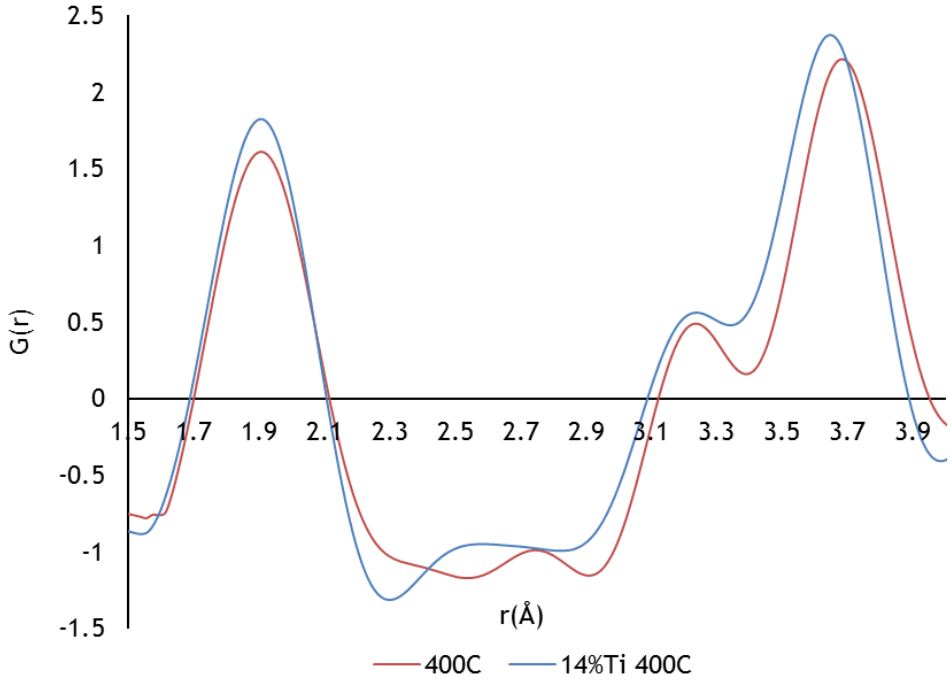

Figure 3-45 A closer inspection of the short-range order in the 400°C annealed samples.

The Ta-Ta and Ta-Ti pair correlations between 3 and 3.5 Å in Figure 3-45 are similar for both samples, peaking around 3.2 Å.

The 14% peak is not well defined compared to the pure sample, it is however of slightly higher density with respect to the average structure than the much better defined pure tantala peak, and can be explained by the loss in certainty of this peaks cation distribution.

The peaks between 3.5 and 4 Å, representing the next M-O and M-M shell, appear around 3.7 Å. The shorter distance for the 14% sample peak, which also displays a relatively higher pair density correlation, may be further indication of a constraining influence by titanium substitution, inhibiting the tendency towards tensile stress during thermal annealing.

A certain factor contributing to the shorter M-M separation of the doped sample, as mentioned before, is its greater ratio of edge to corner-shared polyhedra than in the un-doped sample, with a tighter distribution of M-O-M bond-angles.

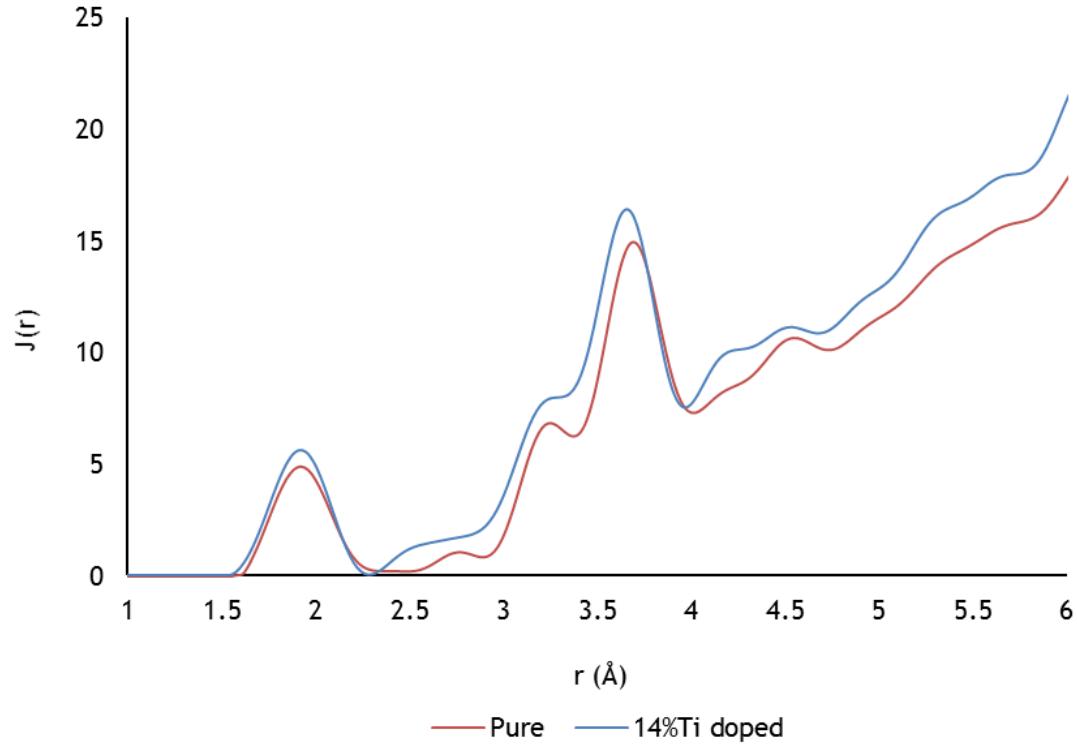

Figure 3-46: Radial distribution functions of 400°C annealed Ti:Ta_2O_5.

The radial distribution functions are shown in Figure 3-46.

Integration of the first peak indicates a coordination of 4.41 oxygens for the pure sample; the 14% data has a coordination number of 4.96, and suggests that doping indeed improves stoichiometry and the homogeneity of the first shell. The curves highlight the density inequality.

From the MRO, plotted with greater detail below in Figure 3-47, the signatures for 1D and 2D linking of PSUs are present, there are however some spurious looking correlations for the 14% sample between 6.5 and 7Å.

In any case, the correlations between 4 and 4.5 Å are thought to be significant in respect to mechanical stability, mediating the 3D-crosslinking of the structure illustrated in Figure 3-29.

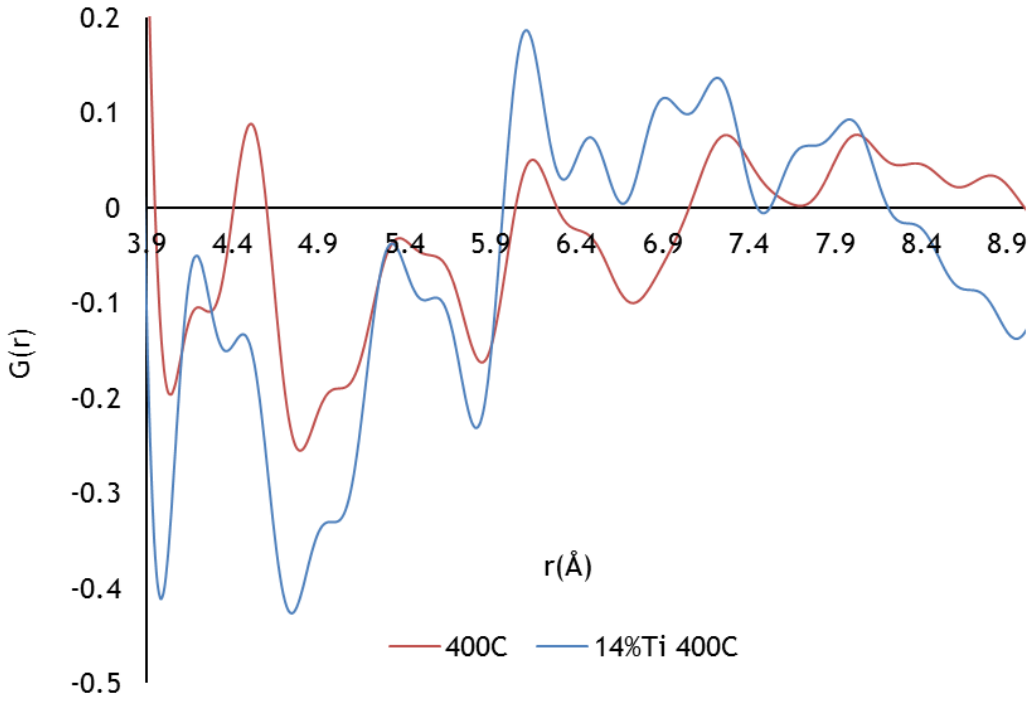

Figure 3-47 Closer inpection of the MRO in the 400°C annealed samples.

In this region both samples have a peak lower and higher in *r*, with greater prominence at low *r* for the doped sample, and at high *r* for the pure sample.

The 14% doped sample may then be more mechanically stability, based upon its higher prominence 3D-crosslinking signature at lower *r*.

This is indicative of a tighter bound, denser structure, with *J*(*r*) in Figure 3-46 suggesting the higher occupancy of the 3D cross-linking region, between 4 and 4.5 Å.

3.8 600°C annealed Ti:Ta_2O_5 coatings

In this last section, the differences in structure between 0%, 14% and 52% Ti:Ta_2O_5, thermally annealed at 600°C, are investigated.

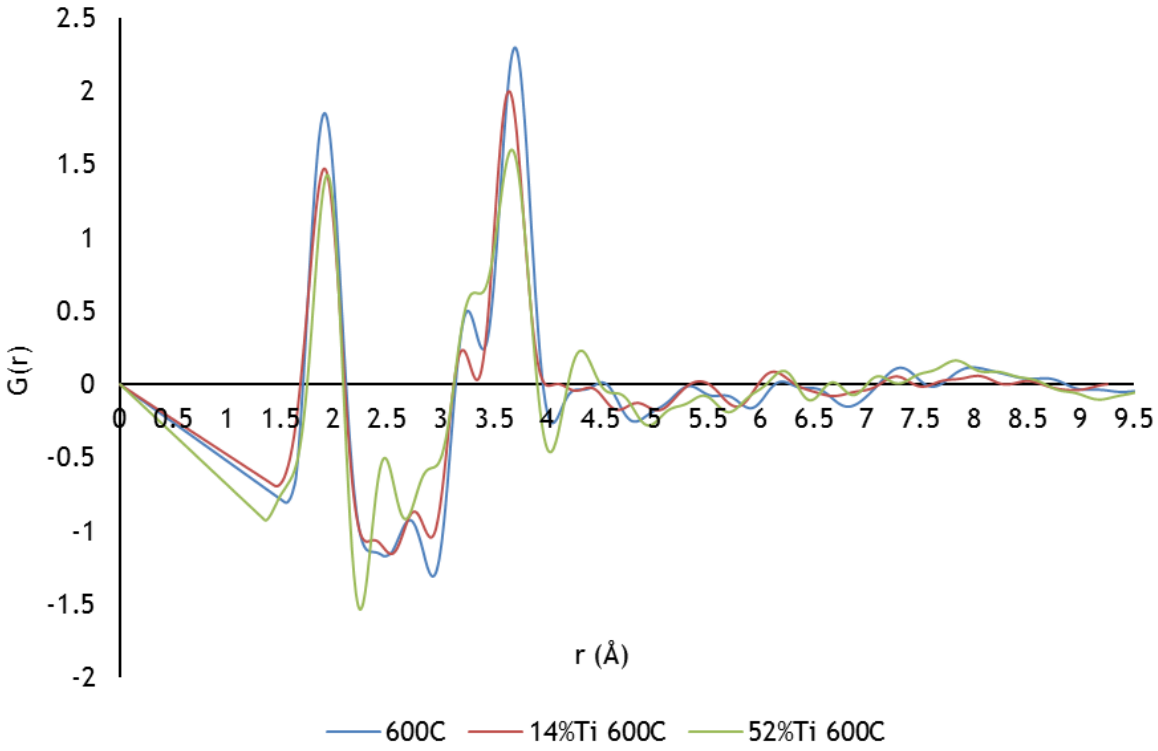

Figure 3-48: Reduced density functions of 600°C annealed Ti:Ta_2O_5.

From the *G*(*r*) plots in Figure 3-48, the 52% sample displays the highest number density, the 14% sample has the lowest, and the pure sample is slightly greater than the 14% density.

The highest density of the 52% sample is presumed to result from the highest concentration of cation occupation in edge-shared polyhedra; there may also be contribution from thermally driven diffusion of oxygen during annealing, into the large free volumes postulated to exist in its as-deposited counterpart.

The slightly lower number density of the 14% doped sample than the un-doped sample is thought to result from its relatively poorer stoichiometry.

In figure 3-49 below, the first metal-oxygen shell shows some variability, centred around 1.9 Å.

The pure sample is most prominent here; the peaks extend slightly higher in *r* with increasing Ti content, with a slight decrease in the peak prominence of the 52% sample with respect to the 14% sample, and a noticeable narrowing of the distribution occurs.

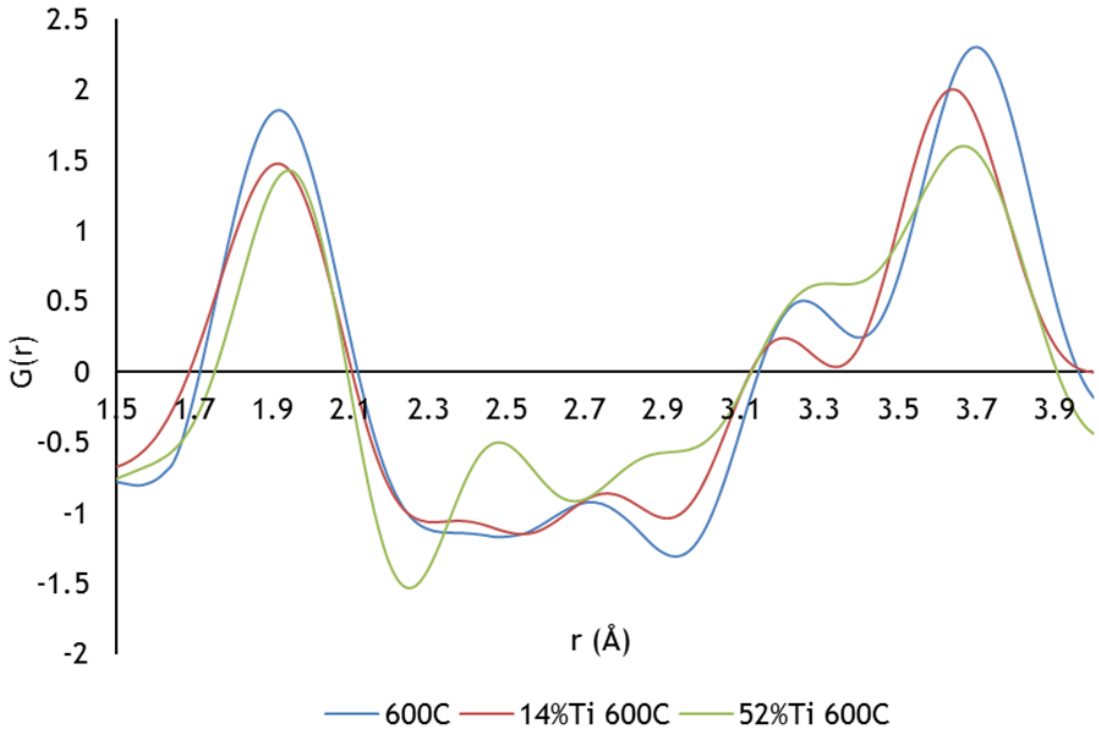

Figure 3-49 A closer inspection of the short-range order in the 600°C annealed samples.

A slight skewing of the distributions of the doped samples can be seen here again, with the 14% Ti M-O distribution weighted to the left due to the shorter Ta-O bond length, and the 52% Ti structures M-O distribution weighted in the opposite direction due to the longer Ti-O bond lengths.

The O-O distributions peaking between 2.3 and 3 Å of Figure 3-49 show considerable variation with increasing Ti content.

The effect of Ti doping in this region is clear observation of the O-O pair correlations resulting from the higher concentration of edge-shared polyhedra.

They are most prominent in the 52% data and spread higher in *r*, with the larger separated oxygen pairs suggestive of phase separated structure by low density regions, indicated by the well-defined lone peak at ~ 2.5 Å.

In Figure 3-49, between 3 and 3.5 Å are 1st shell M-M pair correlations.

This distribution is centred around 3.3 Å, and is greater in magnitude for pure sample than the 14% sample, at a slightly lower separation, and is likely due to the preference of titanium to occupy this position.

The peak of the 52% data here is the least defined and sits at slightly higher *r*, presumably due to a randomised occupancy of metal-centred polyhedra with less certainty of the cation distribution at that position.

The peaks around 3.7 Å represents the next M-O and M-M pair distributions, and progressively decrease in magnitude with Ti concentration, highlighting the stronger scattering by tantalum.

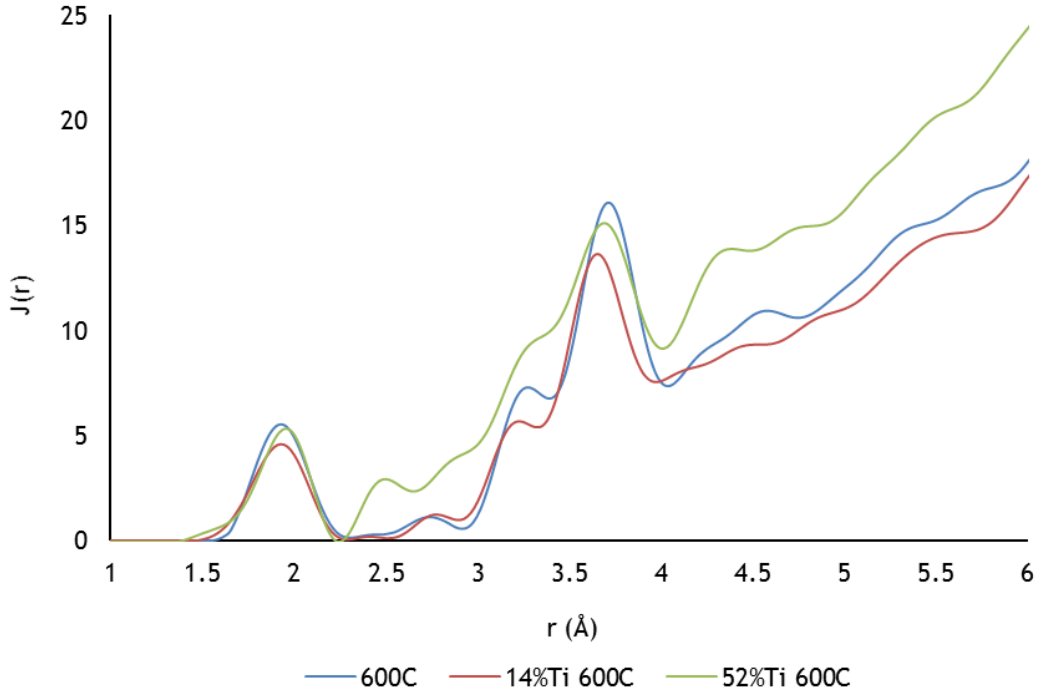

Figure 3-50 Radial distribution functions of 600°C annealed Ti:Ta_2O_5.

The radial distribution function, *J*(*r*), is shown in Figure 3-50 for these samples.

The first shell average coordination number for the pure sample is 4.68 (ideally 5.0), 4.43 for the 14% sample (ideally 4.86 assuming TiO_2 substitution) and 4.54 for the 52% sample (ideally 4.48 assuming TiO_2 substitution), indicating that a denser packed structure is likely to have closer to the correct stoichiometry.

From the first feature of the medium range order, shown more closely below in Figure 3-51, and based upon previous assertions, the 52% sample should be the most mechanically stable structure.

In addition to the stable octahedral framework(225), its signature for 3D-crosslinking(82) is large and unambiguous in comparison to the other two samples.

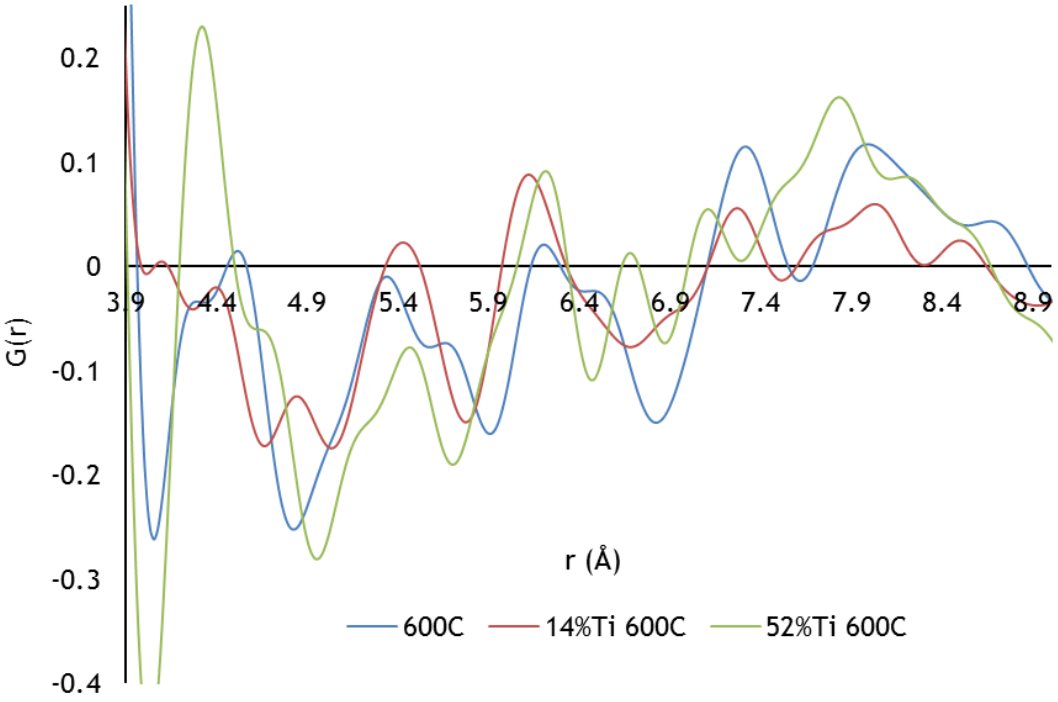

Figure 3-51 Closer inpection of the MRO in the 600°C annealed samples.

For the pure and 14% samples, the signals are a less clear in the cross-linking region, as they both have two peaks of similar magnitude.

However, despite the poorer stoichiometry and lower number density of the 14% doping sample, it may have better mechanical stability than the pure sample, due to its 3D packing signature appearing much lower in *r*.

This may bestow some rigidity and attenuation of thermally driven atomic displacements, constituting a stabilising effect of the aliovalent substitution.

Incidentally, in Figure 3-51 the 600°C annealed 14% Ti doped tantala preparation is thought to be the closest in composition to that chosen for the aLIGO multi-layer coating, out of the selection of samples investigated here.

And whilst the 600°C annealed, 52% Ti doped tantala preparation would appear to be a better choice for the aLIGO high-*k* dielectric multilayer mirror in terms of mechanical stability, its optical performance was found to be significantly inferior by the collaboration.

This could be, as previously discussed, due to porosity in higher Ti content films, but equally plausibly could result from sub-oxide concentrations within the structure.

There will exist an optimum doping percentage for the aliovalent substitution, which will compensate the charge imbalance arising from sub-oxide populations, and narrow the bandgap; however, depositing an optimal coating formulation in practice will be an even bigger challenge.

3.9 Discussion & Summary

High-*q* electron diffraction measurements for the pair distribution function analysis of amorphous structures, whilst still a niche field in comparison to the complementary neutron and X-ray total scattering methods, has many benefits.

The sensitivity of electrons to low-*Z* atoms, their high interaction cross-sections, sub-Ångstrom wavelengths, and nano-metric sampling of volumes are clear advantages of ePDF experiments.

A major advantage is the ability to conduct these experiments in the lab, in contrast to the proposals for and securing of beam time at national facility synchrotrons or spallation sources; additionally beneficial are the in-situ analytical tools of the (S)TEM that can utilised concurrently for chemical analyses.

Furthermore, as well as precise quantification of the average short-range ordering possible through ePDF work, sharp distinction can be found in the limit of such correlations, providing some insight into the onset, extent and nature of longer-

range ordering in amorphous structures.

The additional benefits of the ePDF method are however accompanied with additional sources of uncertainty which require stringent control, for the reproducible quantitative analyses in the comparison of structures.

This was lacking in the presented work, but does however motivate similar future investigations to precisely quantify the dimensions of the specimens studied, the radiation with which they are dosed, the geometry of the incident and collected radiation, and the detectors response to such.

The distortions within the projection system appeared to have the largest determinable effect on the analyses carried out in this work; whilst the microscope was initially properly aligned, non-linearities in diffraction manifested concurrently radially and in azimuth, resulting in disagreement between theoretical and experimental background subtraction, and uncertainty in the PDFs obtained.

It was shown that some of these effects could be corrected for, by selecting the least distorted sectors of diffraction patterns, and by performing non-linear calibrations.

However, this approach was unfeasible with the uncertainty in the precise nature and extent of the nonlinearities, and the quantities of data involved.

Although a work-around was implemented near the end the PhD, it wasn't satisfactory, as it appeared to introduce camera length instability and needed to be done for every new sample inserted, which was only apparent after all the data was collected.

These issues would likely not have been noticed if an initial empirical background subtraction method was employed, and with the commonality of these issues unknown, the findings may be of relevance to other workers using high-q data where empirical background subtraction is employed by routine.

Whilst the changes observed in the ePDFs may not have the statistical significance required to make conclusive statements on the effects of titanium doping and thermal annealing, many of the structural features appear secure, and many changes appear to correlate well with those in complementary structural studies.

The results as presented, indicate that thermal annealing of pure Ta_2O_5 in air for 24hrs at $T > 300^{\circ}C$ results in sub-stoichiometric, lower density films with characteristics of tensile stress, in agreement with studies conducted by the coatings manufacturer(196).

Low concentration Ti-cation doping (14%) achieves improved stoichiometry at a higher annealing temperature of 400°C, whereas annealing at 600°C results in poorer stoichiometry and lower density films, possibly due to a combination of higher thermal forcing and tensile stress characteristic.

52% Ti-cation doped tantala, results in an as-deposited film which is over-stoichiometric, yet much lower in number density than its 600°C annealed counterpart; it is postulated that the as-deposited structure has some degree of sub-nm porosity (likewise for the 68% Ti structure), which is improved somewhat by thermal annealing.

For doping in general, the highest number density films in the as-deposited state appear to be obtained when there is a large inequality in the ratio of the aliovalent dopant.

Comment upon the stoichiometric quality of the structures however, rest upon the assumption of them being solely composed of Ta_2O_5 or Ta_2O_5/TiO_2 mixtures, which may not be the case.

Increased temperature thermal annealing for both pure and Ti-cation doped tantala appears to have a huge influence on stoichiometry, packing density and connectivity, possibly mediated through attenuation of oxygen diffusion, and a variation of structural stress characteristic.

The greatest benefit of titanium substitution into tantala is however its tendency to form greater ratios of edge to corner-shared polyhedra, which can explain many of the observed trends, and likely is the main factor in lower reports of mechanical loss in those structures.

The first pair correlations in the MRO, just before 4.5 Å, appear to be the signatures of 3D-crosslinking order within the amorphous structures discussed in the complementary X-ray PDF study of amorphous tantala(82), and may be correlated with mechanical stability.

However, some insight gained through this work, yet to be explored by the collaboration, is the likely significant effect of different stress distributions in the coating structures upon their macroscopic properties, and how they are mediated through different thermal annealing temperatures, of which, the duration effect should also be examined.

In any case, the heavily averaged structures obtained by the PDF technique is one of its main limitations, and local structural features that may disproportionately contribute to internal friction may be masked by the inherent averaging.

Outstanding questions therefore remain at present as to the existence of significant structural heterogeneities at scales inaccessible by this method.

Attempted correlation between these results and macroscopic internal friction measurements are however still unfeasible at present. Not only because of the uncertainties in this work stemming from unknown structural modifications caused by sample preparation, sample heating in vacuum, and diffraction irregularities, but also the unaccounted-for contributions in the frequency dependent mechanical losses which show significant variation(188).

The reported mechanical loss results are believed to be overestimated.

It has been demonstrated in an unpublished Raman spectroscopy study of these same coatings, that significant chemistry occurs between the silicon substrate and the coating preparations.

An initial 1.2 nm pre-oxidised silica keying layer was shown to grow non-linearly with increasing annealing temperature, and increased by ~8 orders of magnitude during the 600°C anneal, fuelled by oxygen from the tantala layer.

The reason for using silicon cantilevers in low temperature mechanical spectroscopy measurements, in lieu of silica, is due to the known loss peak of silica at those temperature intervals. This issue has been widely reported and overcome in the semiconductor industry(210,227–233).

In the following chapter, true nano-volumes of the samples are explored with fluctuation electron microscopy, providing local insight into short and medium-range correlations within the structures.

This is the next logical step forward using (S)TEM in the investigation of mechanisms responsible for macroscopic mechanical loss, which is a globally averaged measure of internal friction, and for which no mechanisms have been ascertained at the length scales probed to date.

The absence of statistically significant structural motifs in the PDFs, and the recourse to largely qualitative arguments for levels of internal friction, may possibly be overcome through study of higher-resolution, longer-range correlations.

4. Fluctuation electron microscopy (FEM) analysis of amorphous mirror coating atomic structures

4.1 Introduction

The focus of this chapter, is upon the effect of post-deposition thermal annealing and Ti-cation doping on the short & medium-range order in thin film *a*-Ta_2O_5, using the fluctuation electron microscopy (FEM) method discussed in chapter 2.

The technique overcomes limitations of the heavily averaged PDF method used in Chapter 3, by way of a much denser sampling of reciprocal space, in terms of quantity and resolution.

The chapter is divided into two main sections consisting of FEM studies of various tantala preparations, first with an optically coupled scanning diffraction setup, and a shorter section, utilising the Medipix III direct electron counting detector in a scanning diffraction setup.

These sections are further subdivided into two, encompassing Virtual dark field (VDF) imaging of the FEM data sets, enabling a real-space representation of the data for observation of the structural disorder at the nano-scale.

Whilst the magnitude of diffracted intensity has been explicitly substituted in the main calculations, the term 'intensity' has been retained for convenience, but more accurately describes the amplitude of structural correlations.

All images are cross sections of the samples, and are oriented such that they are parallel to the substrate with the coating surfaces in the direction of the top of the images, this is clarified in Figure 4-1.

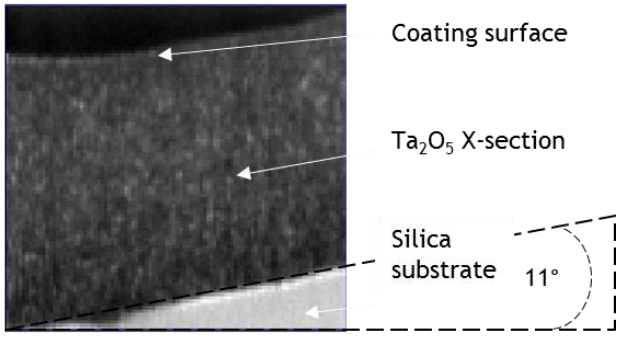

Figure 4-1 The VDF images shown later in this chapter, of the specimens cut perpendicular to their surfaces, are reoriented such that the substrate is parallel with the bottom of the page, allowing comparison of the structures in equivalent orientation.

The virtual images utilise both the positive and negative coefficients of the cross-correlation method from the reduced diffraction data, in contrast to only the positive coefficients for calculating the variance, as was illustrated in Chapter 2.

The rationale, is that for the variance plots the desire is to compare what structure is there, uninfluenced by what is not, as the relative contributions are less clear in a 1-D functional representation; on the other hand, with the 2-D functional representation of the data, the convolution of these relative contributions improves the contrast and resolution of the images and their interpretability.

As discussed in Chapter 2, the reason for the change of variable to normalised correlation coefficient from recorded intensity, was in response to poor SNR in the data from the optically coupled diffraction setup, which could not be simply corrected for; the FEM results using the formal method are also given.

With later access to the direct electron counting detector for collection of scanning diffraction data, and whilst not subject to the inherent noise of the previous setup, the same method of calculation using normalised correlation coefficients was maintained for consistency; the results obtained utilising the formal method are again included for comparison.

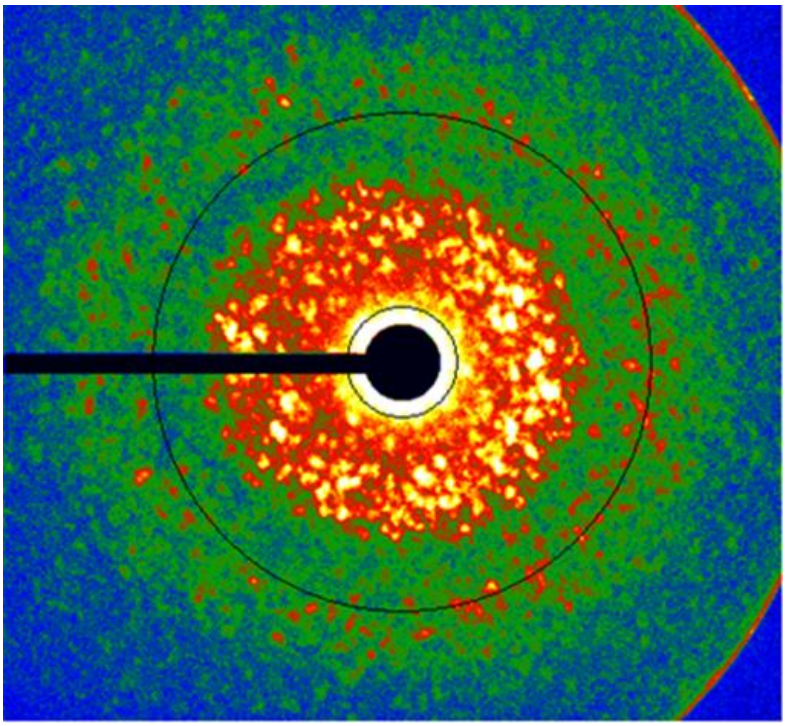

Figure 4-2: Speckled diffraction pattern, typical of FEM experiments utilising a ~2 nm probe.

Initial FEM experiments were performed on the JEOL ARM200cF, with diffraction collected on the Gatan Orius CCD detector, used in the ePDF work of Chapter 2.

And whilst it was shown that MRO exists in IBS *a*-Ta_2O_5 thin films(175), it was found later that the experiment was also affected by the non-linearities discussed in Chapter 2, as can be seen from Figure 4-2 by the deviation from circular symmetry, and the higher intensity of the pattern's right hand side.

The diffraction was non-linear in $I(q)$, geometrically, and apparently in detector response also, and are further highlighted in Figure 4-3. Six 60° sectors were azimuthally averaged from the diffraction pattern in Figure 4-2, and fitted with a smoothing spline to highlight the non-linearities, as the plots appeared noisy due to the high pixel density of the Orius CCD.

The bottom curve deviates from the intensity of the direct beam due to masking of the beam-stop.

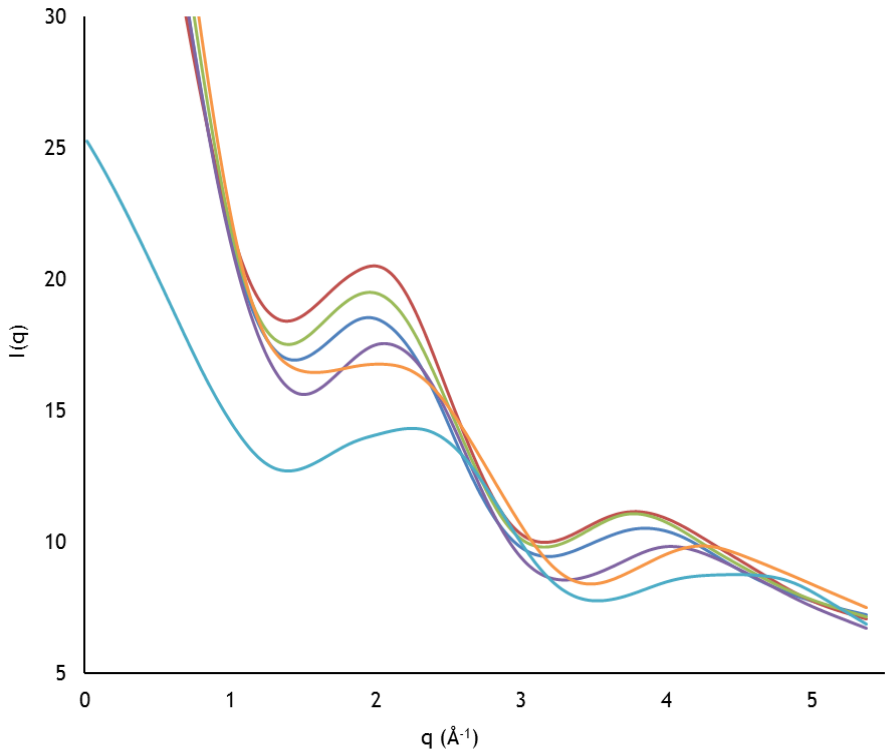

Figure 4-3: Non-linearity of six 60° sectors in I(q), obtained from azimuthal averaging of the diffraction pattern in Figure 4-2.

As the non-linearites were significant at such low scattering angles, further experiments were put on hold until the issue was addressed.

In the meanwhile, however, there was opportunity to collect scanning diffraction data during a hardware demonstration of the NanoMEGAS ASTAR(131) system at the University of Grenoble.

The optically coupled scanning diffraction was performed at SIMAP, in the University of Grenoble, with Muriel Véron and Edgar F. Rauch, during a demonstration of the NanoMegas ASTAR system(131) arranged by Stavros Nicolopoulos of NanoMegas SPRL. The breadth of data analysed herein constitutes what was possible to collect in the timeframe of the demonstration.

A slight error in the scaling of the scattering vector-*k* was discovered since publication of the FEM results of the pure tantala samples in the Journal of Non-Crystalline Solids(127), and has been corrected here; however it did not affect any of the findings or conclusions drawn.

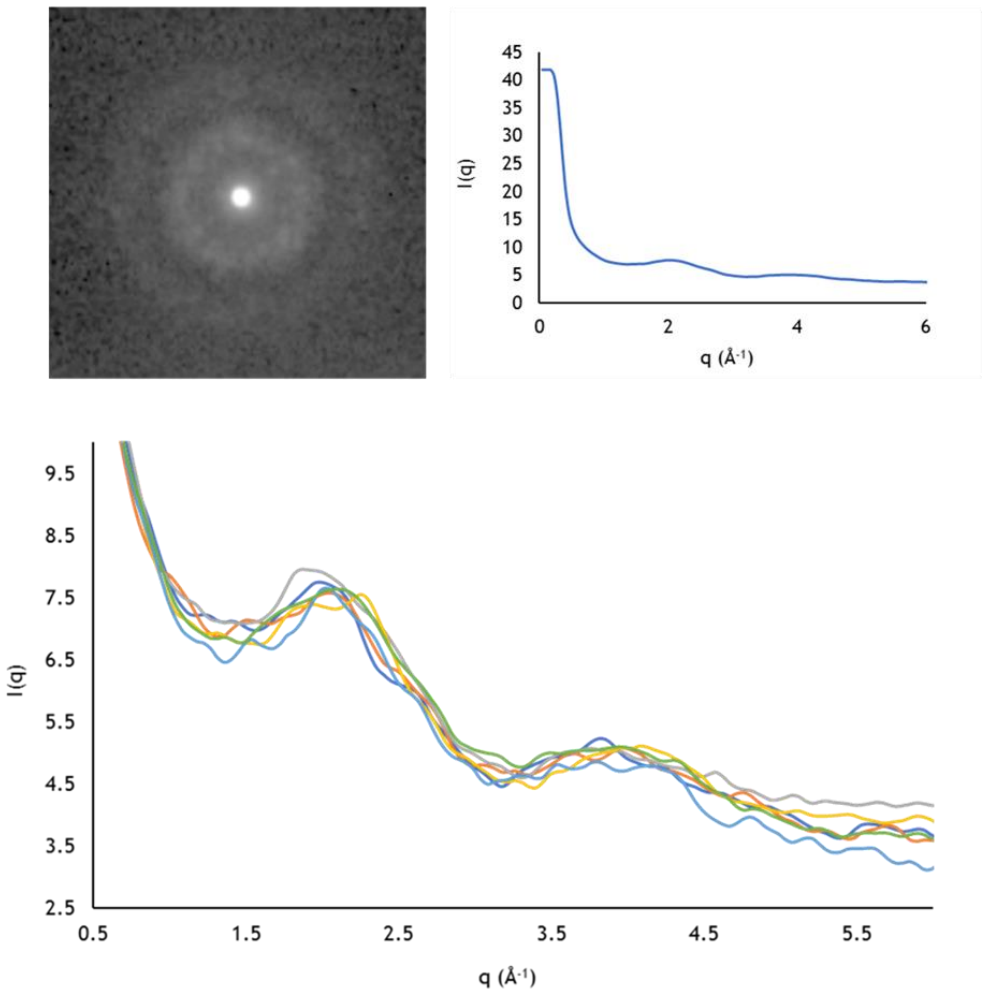

Figure 4-4: (Top) Typical diffraction pattern used in the experiments, with its azimuthally averaged intensity profile. (Bottom) Six 60° sectors in I(q), from the same pattern, highlighting linearity, and the noise higher in q.

Furthermore, in this work, the averages of ten variance curves are plotted from 500 diffraction pattern samples, in contrast to the published work, in which averages of five variance curves were plotted from 1000 samples.

This was to demonstrate that the low uncertainties in the published results were not due to excessive averaging. The differences are very slight and do not negate the results of the published work.

The scanning electron diffraction datasets were collected on a JEOL JEM2100F operating at 200 keV. The microscope was set to nano-beam mode in TEM, encapsulating diffraction from a volume set by the 2 nm beam diameter, with a dedicated ASTAR hardware solution by NanoMEGAS SPRL which controlled the deflection coils of the TEM allowing it to be operated in a ~2 mrad low convergence angle STEM mode(131,234,235).

Spatial resolution, covered in Chapter 2, was determined to be sufficient using the Ronchigram method(236).

The Ronchigram is the blown-up undiffracted disc at the centre of a CBED pattern, shown in Figure 2-19; optimal focus is indicated, and hence resolution, when the largest possible circular region of uniform intensity is observed in the CBED central beam, which is when it is symmetrical, and collinear with the optic axis.

It is an essential step in calibration of the scanning diffraction conditions, to ensure that aberrations are minimised, and the beam is aligned and the probe is optimally focussed on the specimen.

Although the probe current was not measured absolutely, it was low enough that there was no speckle movement under the stationary beam, indicating that no significant modifications of the atomic structures were induced by the beam.

The diffraction patterns were recorded using an external CCD Stingray video camera, imaging the TEM fluorescent screen with a dynamic range of 8 bits, at a rate of 100 patterns per second over the area of interest.

Diffraction patterns were linear unsaturated measurements of the diffracted intensity, each triggered by the ASTAR system so that recording was synchronous with the 100 Hz scan frequency.

The Stingray camera was placed in front of the TEM viewing screen via a specialised mechanical adapter, and the viewpoint then necessarily required that the camera was inclined at an angle with respect to the viewing screen.

The recorded diffraction patterns were therefore ellipsoidal, they were all however geometrically corrected online with the 'Transmission Electron Microscope (TEM) Diffraction Pattern Acquisition' ASTAR software prior to data transfer.

As in Figure 4-3, the diffraction obtain in this experiment was checked for non-linearity; six 60° sectors were azimuthally averaged from the diffraction pattern shown in Figure 4-4, without smoothing, as well as the $I(q)$ profile from the entire angular range to highlight the low SNR over the available dynamic range, which is apparent enough from the diffraction pattern.

Figure 4-4 is indicative of the diffraction across all datasets used, and were unaffected by the non-linearities shown for diffraction in the JEOL ARM200F.

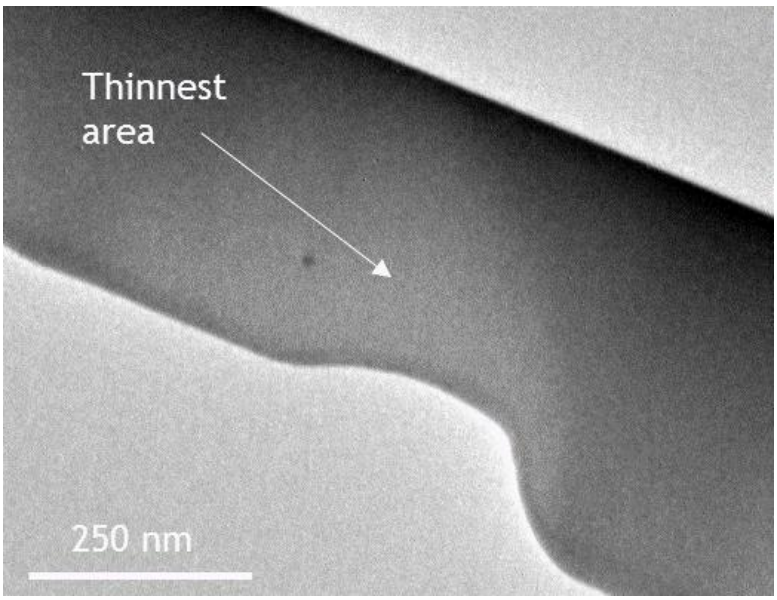

Figure 4-5 BF image indicating the optimal area of the specimen from which to collect data.

Li *et al.*(177) provided a basis upon which FEM can be performed with confidence in the quantitative magnitude of the data, which entails the identification of common artefacts in the datasets.

These noise sources have been examined in relation to the reduced data, as they were present in all the raw intensity data; however, they were undetectable after data reduction.

As the datasets used in this work were predominantly from conventionally prepared, and two FIB, cross sectional samples, they contained some thickness variations; although, care was taken to choose areas for analysis which were extremely thin and with very small thickness variations, indicated by the brightest area in shown in the bright-field image of Figure 4-5.

Thickness issues can pose a problem to the FEM analysis(237,238), however, the relative thickness of the samples studied here were generally less than half the inelastic mean free path, at the thickest areas of the specimen, as shown in Figure 3-2 of Chapter 3, falling well within the single scattering approximation. Thickness issues between samples were therefore thought not to be significant to the analysis.

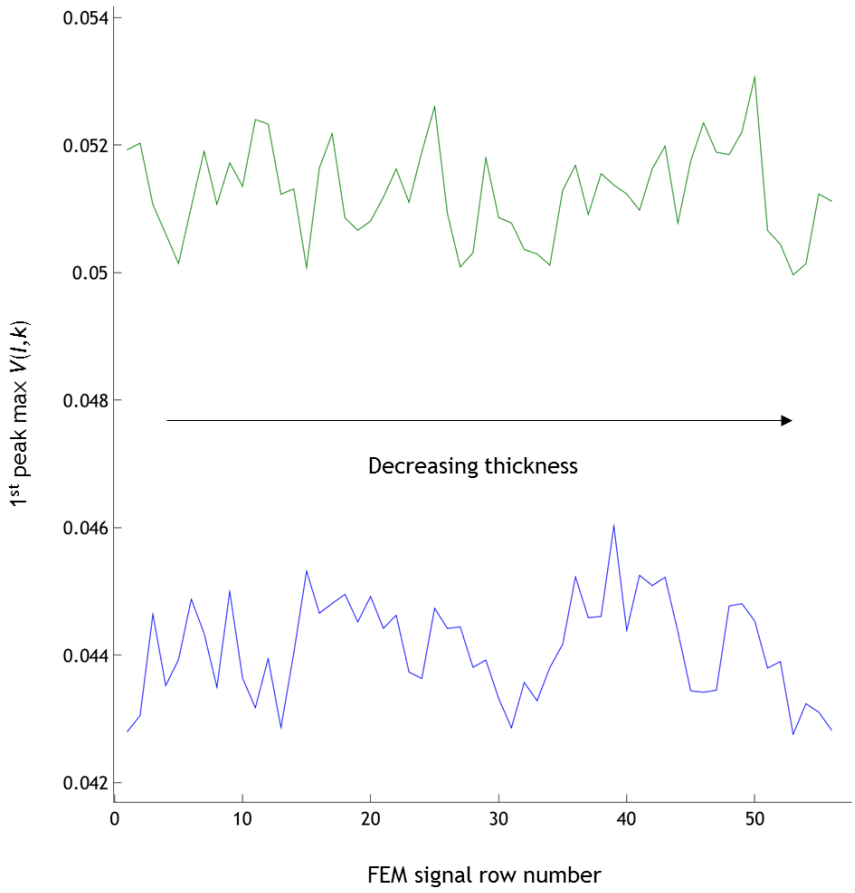

Figure 4-6: Maximum variance of the 1st peak in V(y,k,Q), as a function of thickness for the 300°C (lower curve) and 600°C (upper curve) data. Results are indicative of all the specimens studied.

Consequently, no saw-tooth pattern was visible in a plot of *I(k)* versus pattern number at high-*k*, which would indicate a thickness change significant to the analysis.

To be certain, a robust check for dependence of the variance upon specimen thickness was made; the 1st variance peak of 56 FEM signals, each based on 100 diffraction patterns, from parallel lines normal to the small thickness gradient in the 300°C and 600°C datasets, were calculated and are plotted in order of decreasing thickness, shown in Figure 4-6.

The artefacts in the raw intensity data are therefore best explained by variations in illumination conditions, which are very significant in this optically coupled setup; this further highlights the utility of the newly developed approach to the FEM analysis, by performing calculations on cross correlation coefficients of structurally significant diffraction, derived from the raw intensity data.

The result confirms that any differences in the volumes of the samples studied were inconsequential to the present analysis(177). The remainder of the data were sampled from similar regions of the 300°C and 600°C datasets, underwent identical sample preparation, and indicated minimal thickness variation within each sample, and from sample to sample.

No large voids were identified, which would manifest as artificial peaks and increased variance magnitude; neither were any roughness effects which would show up as large intensity variations, and be reflected in the uncertainties.

During data collection, some carbon contamination was visible, and was treated with a ‘beam shower’; this involved spreading the beam over the extent of the viewing screen and leaving it for half an hour(239), with no effects visible in the final data.

Furthermore, no multiple scattering effects or large nanocrystals were observed, which also would be reflected in the uncertainties. The usual FEM signal is also somewhat sensitive to probe coherence; however, using a small semi-convergence angle, and by performing calculations only where scattered intensities have been determined to be structurally significant by cross correlation coefficients, as opposed to the total scattered intensity, the sensitivity is reduced.

No theoretical formalism is provided for the approach used here; the method is however qualitatively sound when one considers the relation of the spatial distribution of the diffracted intensity to the structural order within the material(240,241).

Furthermore, it is proved a viable approach statistically by the very low uncertainties in the obtained results, and the broad agreement with the formal method. Each curve represents the mean variance of ten individual variance curves, each computed from 500 diffraction patterns, selected from random patches of the samples, with the error bars representing the standard error on the mean.

4.2 Pure Ta_2O_5 thermal annealing

In Figure 4-7, the normalised structural variance is plotted for the pure Ta_2O_5 data annealed at 300°C, 400°C and 600°C, using the standard formulation of FEM.

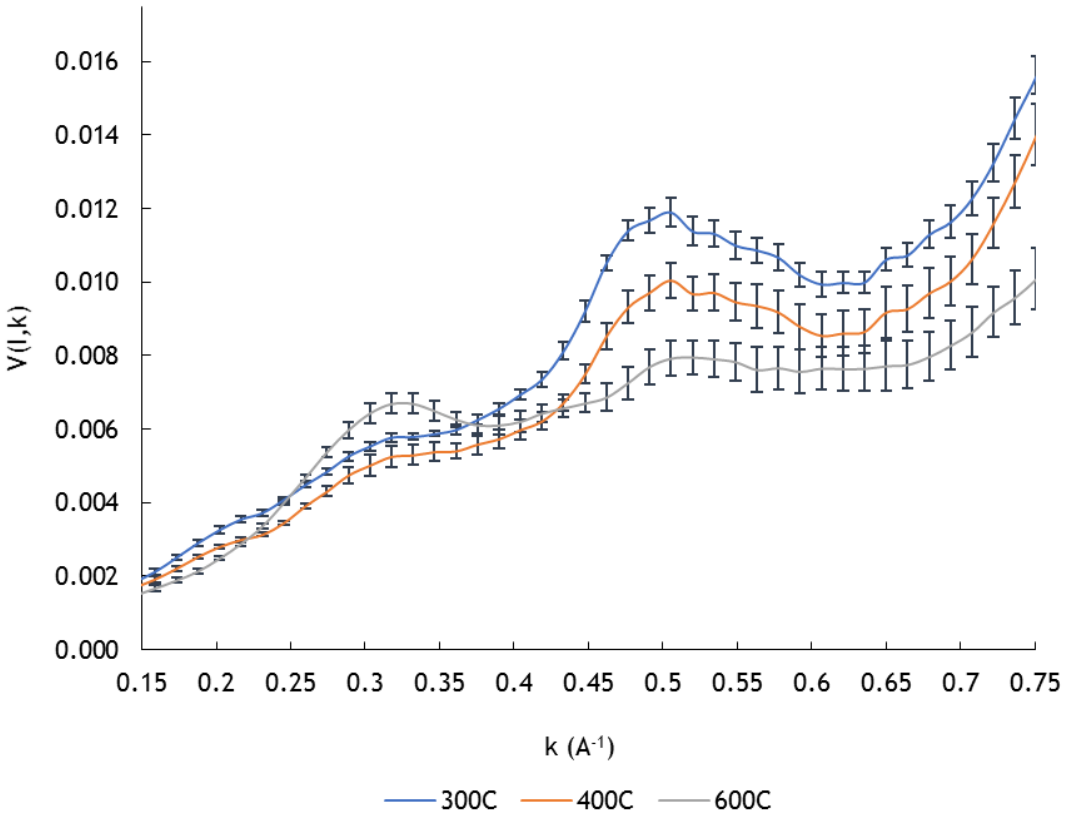

Figure 4-7: Normalised variance, V(l,k), of a-Ta_2O_5, thermally annealed for 24 hours in air, at 300, 400 and 600°C.

The effect of noise is apparent; after the first variance peak at $k \approx 0.31$ Å^{-1}, the variance climbs higher in k, and whilst this behaviour is typically attributed to thickness issues, and indeed contributes here, it is amplified by the experimental conditions.

The optically coupled setup, with such a low dynamic range is not best suited to this type of analysis, in which small variances of the diffracted intensity are measured.

Much more control over the experimental parameters are required, especially in quantification of specimen thickness, and ideal illumination conditions, which was not possible during the brief hardware demonstration in which these data were recorded.

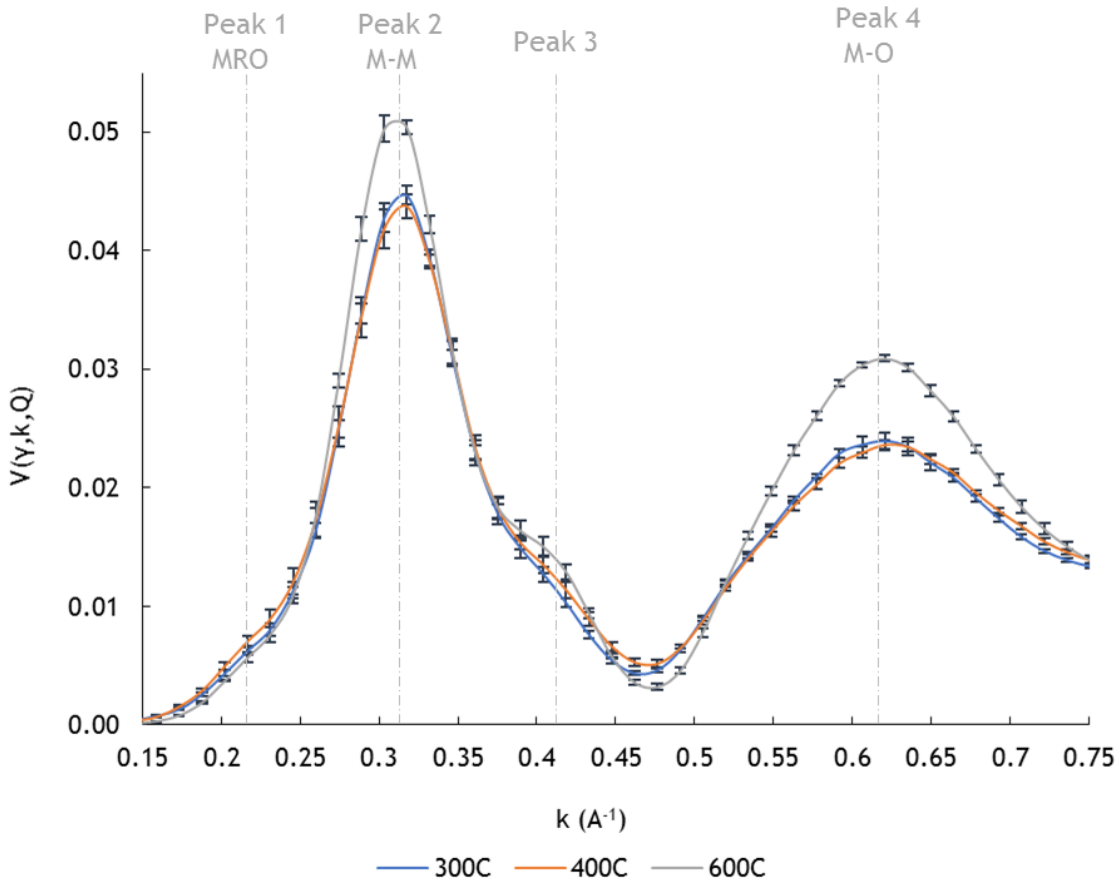

Figure 4-8: Normalised variance, V(y,k,Q), of a-Ta_2O_5 thermally annealed for 24 hours in air, at 300, 400 and 600°C.

At first glance, the uncertainties imply secure structural features; however, greater uncertainty is implied by the variance rising higher in and with increasing k, where the FEM signal should be fading.

Furthermore, the peak at $k \approx 0.5$ Å^{-1} is unphysical, and there is expected to be a signal from the M-O distribution around $k \approx 0.63$ Å^{-1}. The signals from the M-M distributions at $k \approx 0.31$ Å^{-1}, do on the other hand appear secure.

The rise in peak magnitude follows the trend in increasing heat-treatment temperature observed using the new method, and arises from the first and most intense ring of the diffraction patterns, where the counting statistics are highest.

In Figure 4-8, the same data is plotted, using the new technique of variance computation with normalised cross-correlation coefficients.

This method effectively cuts through the noise to uncover structurally significant deviations from homogeneity, and appears to be rather insensitive to thickness fluctuations and artefacts in the data.

Although it is a rather unconventional and unintuitive approach, in that the absolute magnitude of the raw diffracted intensity is rendered irrelevant, it can be a powerful compromise in similar situations when the experimental facilities are sub-optimal, or the need is for quick comparative analysis of structures without detailed quantification of noise sources.

The first main peak in the variance, occurring at $k \approx 0.31$ Å^{-1} can be attributed to the heterogeneity of the metal-metal (M-M) distribution, and follows the same trend in the intensity based approach of Figure 4-7.

The data simultaneously confirms the presence of MRO, and of a change in short range atomic structure, due to increased temperature thermal annealing.

The next main peak, at $k \approx 0.62$ Å^{-1} is attributed to the heterogeneity of the metal-oxygen (M-O) NN distribution.

At this 2 nm scale, the change in atomic structure due to thermal annealing is apparent.

The magnitude of the 600°C variance is significantly larger than that of the 300°C and 400°C data, indicating further deviation from homogeneity that may be explained in terms of the structure beginning to organise itself into regions of greater order, consistent with other investigations into the effects of increased temperature thermal anneals on amorphous atomic structures(72,242–245).

Furthermore, the extension to lower in *k* for the 600°C M-M variance distribution, adds weight to the observed extension to higher in *r* for this same M-M distribution, observed in the PDF work of Chapter 3, and corroborates the inferred tensile stress characteristic of this structure.

However, although the FEM results are informative in a broad sense, they do not convey what is going on locally, as is the common problem with averaged data.

Between 0.2 and 0.25 $Å^{-1}$ is a weak peak, just before the M-M variance distribution, and is indicative of the longest-range order observable in Figure 4-8, and is related to the medium-range order in the region after 4Å, shown and discussed in the PDFs of Chapter 3.

In this region, the 300°C data is most prominent, followed by the 400°C data, with the 600°C data lowest in variance.

After the M-M variance distribution, is another less subtle significant peak between 0.35 and 0.45 $Å^{-1}$, which represents the region encompassing the first M-M pair correlations shown in the PDFs of Chapter 3.

In this region. The prominence of the 300 and 400°C data follows the same trend as the smaller peak at ~0.22 $Å^{-1}$; however, for the 600°C data, there is reversal of trends in comparison to the ~0.22 $Å^{-1}$ peaks and the variance is significantly higher.

The variance curves represent departures from the average structural homogeneity, and therefore do not differentiate between homogeneously ordered and disordered systems.

To this end, the Virtual Dark-Field Imaging (VDFi) approach of Rauch and Véron(126) has been adapted for amorphous materials, to image features of the scanned diffraction dataset in real space, made possible by the spatially indexed nature of the diffraction pattern collection.

To date, it has not been possible to invert or refine the FEM data to provide a model of the disordered structure(246). With this representation of the data however, further strides in this direction may be achieved through visualisation of the spatial distribution of ordering responsible for the FEM signal.

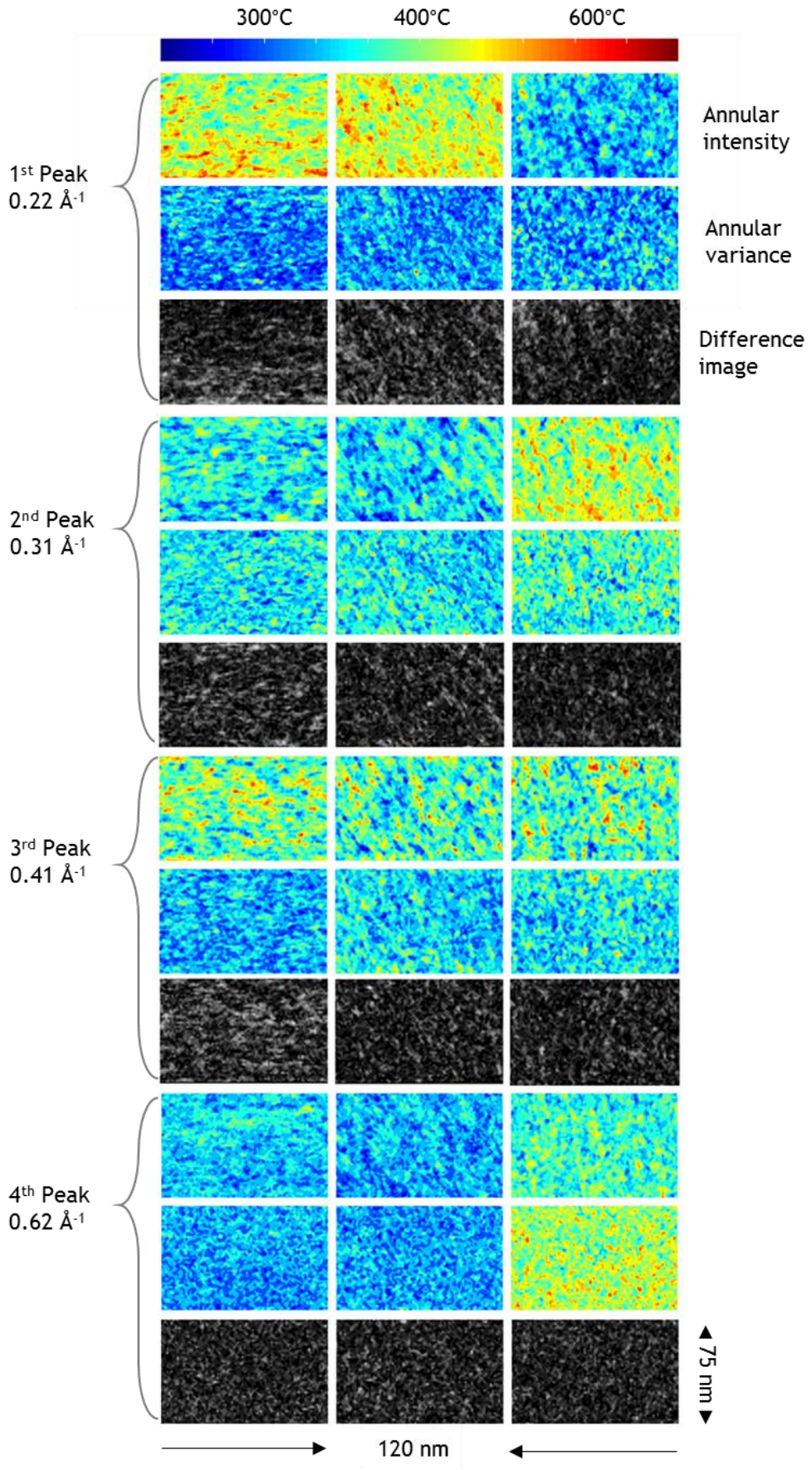

Figure 4-9 VDF images of the Pure Ta_2O_5 heat-treated samples. Annular intensity, annular variance and their difference images. The contrast in the difference images point to regions of possible correlation between the images. The images of the first peak appear positively correlated, whilst those of the second peak appear anti-correlated.

Figure 4-9 displays a series of 75 nm x 120 nm VDF images generated for the 300°C, 400°C and 600°C annealed tantala samples. There are images for each of the heat-treated sample; the rows represent the different specimens, and the columns correspond to the variance peaks of Figure 4-8.

Each peak of Figure 4-8, is represented with three images in Figure 4-9; first is the annular integrated intensity images, followed by the corresponding annular variance images, then a difference image is shown for the normalised images, which points to regions of correlation, before moving onto the next peak.

The image pixel values of Figure 4-9 correspond to a mean value of three pixels (0.0144 $Å^{-1}$ per pixel), one either side of, and centred on the peaks of Figure 4-8. The data was collected from the brightest regions of Figure 4-10.

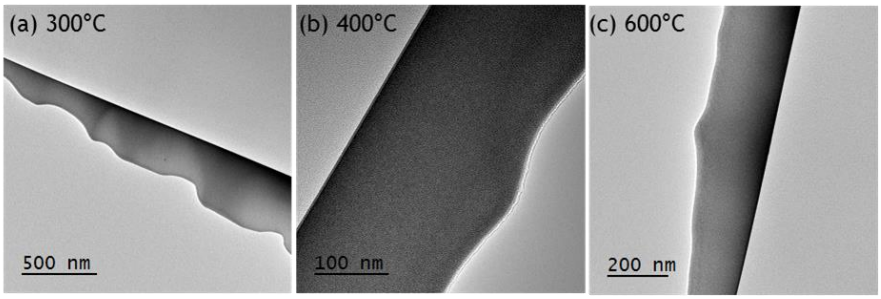

Figure 4-10 Bright-field images of the 300 (a), 400 (b) and 600°C (c) specimens.

The VDFi data is presented here in a false colour contour plot, commonly used to represent a 3-dimension surface, where for a given pixel value, *z*, lines are drawn that connect the (*x*,*y*) coordinates where that *z* value occurs. The contours can thus be qualitatively interpreted as the connectivity of regions with structural similarity.

The images of Figure 4-9 have been normalised such that all intensity values for each peak image have a one-to-one correspondence, with the colour bar representing the linear scale of all image *z* values from the minimum (blue) to maximum (red).

However, the intensity values are only comparable across the rows for the different heat-treated samples, on a peak-by-peak basis, as to allow simultaneous visualisation of the different structure distributions.

The 2nd peak images would realistically display the highest intensity levels from all the images; the shape and distribution of structure between the peak images are however perfectly valid for comparison.

Visual inspection of Figure 4-9, immediately highlights the reproduction of the key features in the variance plot of figure 4-8; for the annular intensity images, there is slight difference in ordering for the 300°C and 400°C samples in comparison to the 600°C annealed sample which has many high intensity regions.

There also appears to be some preferential orientation; the 300°C images display horizontally distributed structure, whilst the 400°C images appear inclined to ~45°, and the 600°C images have less discernible orientation.

However, this is thought to be an artefact of the scanning diffraction collection, as the apparent orientation of the 400°C images are close to the angle through which they were reoriented.

The additional structural information encoded within the images of Figure 4-9 is remarkable; not only is the subtle indication of organisation into regions of greater order, intimated by the 1-D variance functional representation clearly relayed, but a spatial representation and relative density of the ordering.

The contrast of the pixel intensities of the images further inform the extent of ordering; the 300°C and 400°C images exhibit a comparatively low degree of structural order after the first peak with a low level of variation, ascertained by the connectivity of low intensity regions separated by islands of somewhat higher intensity regions. This is especially true for the second peak, corresponding to the shorter M-M distances, and the M-O distributions.

On the other hand, the 600°C annealed sample in Figure 4-9 shows generally less connectivity of similarly structured regions, broken up by many more smaller islands, much more disparate in their degree of order. It is plausible that internal friction may be correlated with the greater degree of high & low density structural boundaries shown in the images(127).

The connectivity of similarly ordered regions may promote greater structural stability by reducing the degrees of freedom into which energy can be lost, perhaps by delocalisation of their phonon density of states.

Some of the latest research in amorphous atomic structures suggests that long range phonon damping scales exist in amorphous solids, and are mediated by long-range correlations of local stress and elasticity(247).

The higher ordered M-M distribution of the 600°C annealed sample likely engenders an overall tensile characteristic, as posited in Chapter 3, and would result from localised densification as indicated by the sharp contrast regions of the intensity images in Figure 4-9.

An increased tensile characteristic likely involves an increase in the M-O-M bond angles, as no appreciable differences in the M-O bond lengths were apparent in the PDFs of Chapter 3. This provides a highly plausible reason for increased levels of thermal noise; as the bond angle increases, the bond vibrations take more of a stretching character in contrast to bending, as illustrated in Figure 4-11.

Stretching bond vibrations are of considerably higher frequency than bending vibrations in tantala, roughly two orders of magnitude(208); even though these vibrations are in the THz range, and thermal noise limits sensitivity in aLIGO in the region around 100 Hz, the effect of the higher frequency vibrations would be to deposit heat into the system at a higher rate.

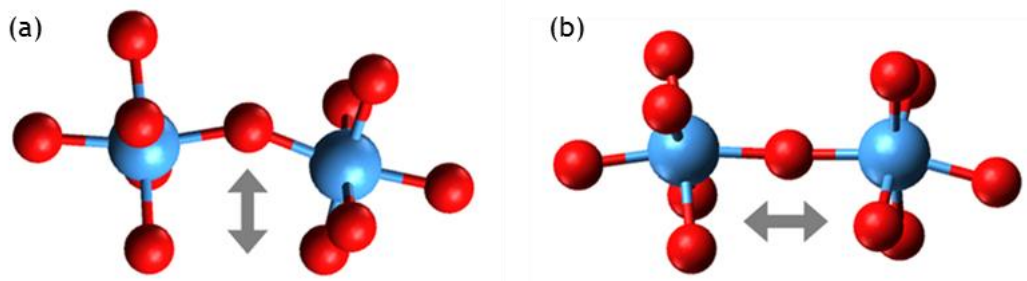

Figure 4-11 Illustration of inter-polyhedral oxygen vibrations, (a) bending mode, and (b) stretching mode.

Larger ordered regions, as observed in Figure 4-9 for the 600°C annealed specimen M-M distribution (2nd peak), may result in increased low frequency vibrations due to the increased oxygen stretching vibrations impulse contribution to the heat bath.

Furthermore, low frequency vibrations may be attenuated by the longer-range structural order discussed in Chapter 3, with signals of which found after 4 Å, are represented by the 1st peak in Figure 4-8, and visualised in Figure 4-9.

Indeed, the most striking differences in the annular intensity images are those corresponding to the 1st peak of Figure 4-8, indicative of MRO in the structures.

The 300°C and 400°C samples display a much greater degree of order in this region with respect to the 600°C data, and may explain the absence of the signature for 3D packing shown in Figure 3-21, from the GIPDF study(82) of 600°C annealed tantala discussed in Chapter 3.

The annular variance images in Figure 4-9 represent a more discrete and complementary visualisation of the homogeneity of structural connectivity, and more so in terms of bond disorder, or heterogeneity of the ordering.

Whilst the features of Figure 4-8 are appreciable in this representation, they are not as immediately apparent as in the annular integrated intensity images.

However, likewise with the increased ordering due to increased temperature thermal annealing, there appears to be a commensurate change in the annular variance, indicating local changes in the bonding environment.

This is most apparent in the variance images of the 600°C annealed sample, in which distinct red spots appear in sharp contrast to their surroundings.

The complementarity of the annular variance images to the annular intensity images is apparent from their corresponding difference images; black regions indicate areas that are equivalent in relative levels of ordering, whilst significant structure correlation between the variance and intensity images is inferred by the bright regions when similar structure in either image is apparent; indeed, there seems to be a high degree.

This is not surprising as the contrast in the annular intensity images is expected to arise from the structural ordering, whereas the corresponding contrast in the annular variance images is expected to arise from variations in the ordering.

The 1st peak annular intensity and variance images appear positively correlated, with the 300°C sample the least apparent.

The regions where the intensity rises and falls are significantly mirrored, with the variance rising and falling in those same regions, indicating the heterogeneity of the ordering.

Conversely, the second peak images appear to be mostly anticorrelated; a region of an intensity image going from low-to-high-to-low intensity has many corresponding regions in the variance image that go from high-to-low-to-high, and indicate homogeneous ordering in those localised areas. The 4th peak, M-O distribution images appear uncorrelated in comparison.

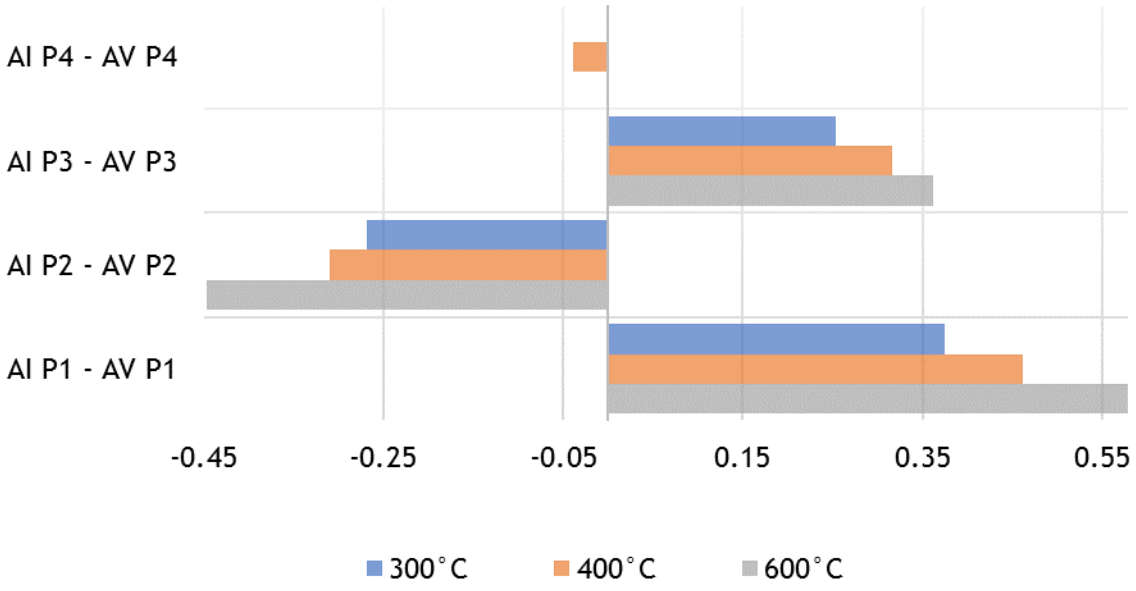

Figure 4-12 Correlations between the complementary annular intensity (AI) and annular variance (AV) VDF images at the different peak positions (P), with 95% confidence levels.

There are twenty-eight possible image combinations in total, for each of the heat-treated samples, that can be compared in relation to the variance peaks of Figure 4-8.

Correlation coefficients were computed for each combination to quantify the differences in structure inferred by the images, and ascertain which, if any peaks were correlated significantly with another.

The results are shown in Figure 4-12 for the complementary structure/variance images of each peak; the VDF image peak correlations are abbreviated such that 'AI P1 – AV P1' represents the correlation between the 1st peak annular intensity image and the 1st peak annular variance image of Figure 4-9.

Only correlation coefficients with p-values < 0.05 are used for comparison, indicating a confidence level of 95% in the correlations.

The correlations shown in Figure 4-12 for the complementary intensity/variance peak images, show that the 600°C specimen displays the highest positive correlation for the first peak, indicative of the MRO shown in the PDFs and discussed in Chapter 3.

The correlations suggest that heterogeneous ordering in this region is increasing with increasing annealing temperature; the 600°C specimen has the lowest levels of relative ordering between the samples, and the highest relative level of structural variance, as illustrated in Figure 4-9.

This suggests that annealing the sample to 600°C for 24 hours in air discretises the structure, breaking down the connectivity at the MRO range; it is possible however that longer range ordering does occur at this annealing temperature, but is out with the sampling range of these images.

The large anti-correlation for the 2nd peak in Figure 4-12, the main M-M distribution, is highest also for the 600°C specimen; it also increases with increasing annealing temperature, suggesting that the M-M distribution highly-ordered regions become more homogeneous with higher annealing temperatures.

The correlations for the 3rd peak images of Figure 4-12, largely representative of the shorter M-M pair separations, follow the same trend as the 1st peak correlations and highlight the greater coincidence of high-order/high-variance and low-order/low-variance structure above the background levels with increasing annealing temperatures.

Figure 4-9 however shows similar high-order regions for all the specimens at the 3rd peak, in contrast to only the 300 and 400°C specimens at the 1st peak; their distribution and connectivity is more heterogeneous after a 400°C anneal with a commensurate increase of the variance in that ordering; after annealing at 600°C, the ordered regions become larger and increasingly heterogeneous.

The 4th peak M-O distribution shows only a slight anti-correlation for the 400°C specimen in Figure 4-12, and suggests that some regions are ordered more homogeneously in an otherwise uniform distribution.

The lack of correlation for the 300 and 600°C specimens suggest a uniform and randomly distributed variation of structural order.

However, in Figure 4-9 the 300 and 400°C specimens appear most similar in their annular intensity and variance images, with the 600°C structure displaying the highest levels of heterogeneity of its ordering.

The images of Figure 4-9, in which distinct spatial distributions of high-order structure emerge from the amorphous matrix, and changing dramatically at the increased annealing temperature of 600°C, strongly support a model of heterogeneous phase separation for these structures.

The fluctuating correlations of Figure 4-12 describe the nature of the structural ordering and its variance shown in Figure 4-9, constituting a step forward in the interpretation of the structural heterogeneity inferred from the 1D FEM variance plots of Figure 4-8.

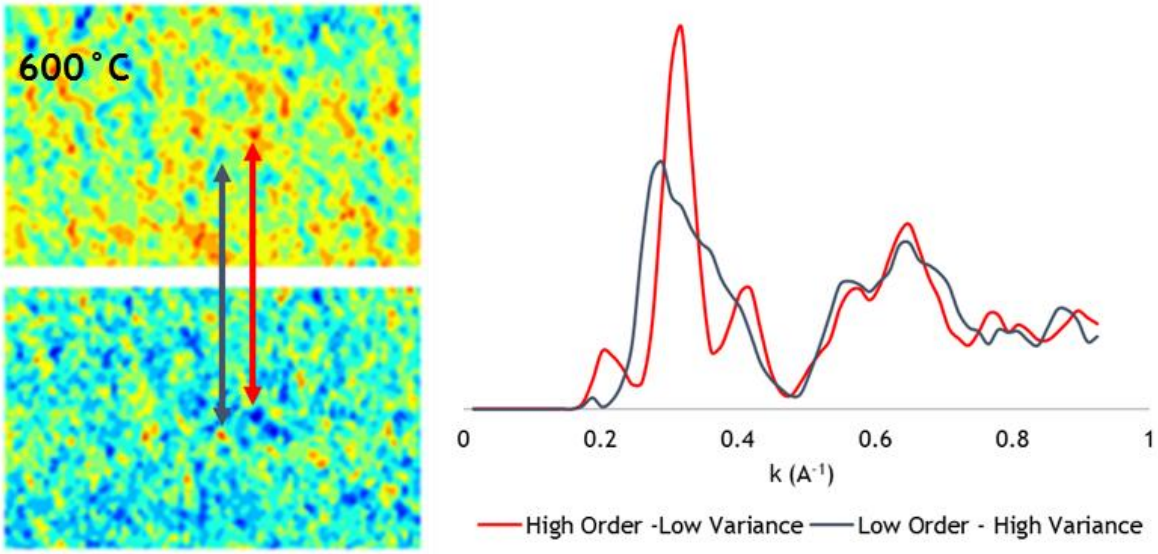

Figure 4-13 Intensity profiles of the 600°C data, illustrating the highly ordered regions immersed in the low-ordered amorphous matrix. Also highlighted is the splitting of the M-O distribution around 0.6 Å-1.

The phase separation is illustrated in Figures 4-13 & 4-14, with the intensity profiles of the diffraction patterns responsible for the high-order/low-variance regions of the 600°C 2nd peak images of Figure 4-9.

The intensity profile from a highly ordered region of the 600°C specimen, shown in Figure 4-13, shows a remarkable separation of the peaks compared to that from a region of low-order.

The comparative order between high and low-order regions can be appreciated by the different texture of the diffraction patterns shown in Figure 4-14.

The left-hand side diffraction pattern displays a distinct separation of the 1st and 2nd diffraction rings in comparison to the pattern on the right, and predominantly represents the two Ta-Ta separations. The high-order region may be considered para-crystalline.

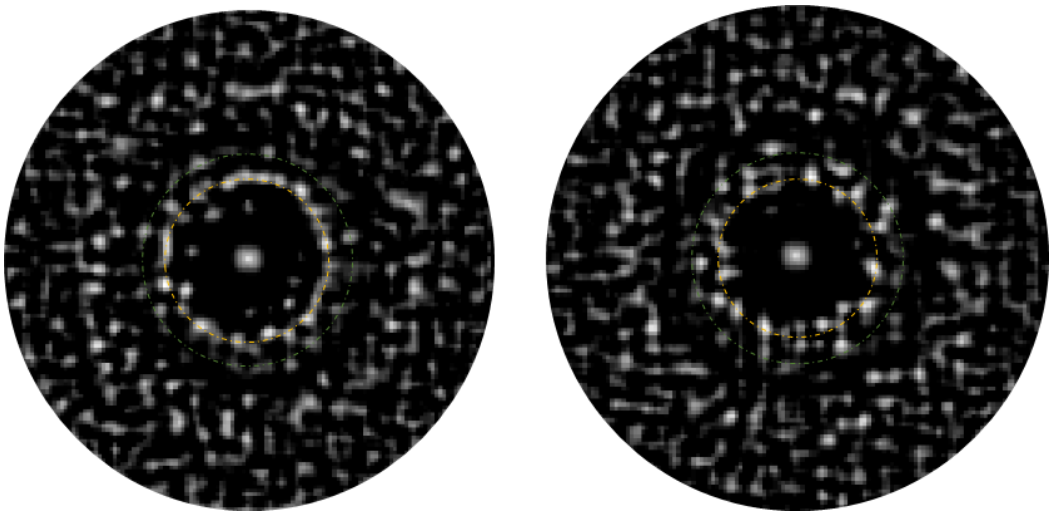

Figure 4-14 Diffraction patterns responsible for the regions of high-order/low-variance (left), and low-order/high-variance (right). The faint superimposed circles highlight the higher (inner circle) and lower (outer circle) shell positions of tantalum in the M-M distribution. The spots closest to the centre of the left-hand side diffraction pattern give clear indication of MRO.

The large variation in structure shown in the intensity profiles of Figure 4-13 makes apparent that the 4th peak M-O VDF images do not explicitly address the two distinct peaks shown within the M-O distribution, and may explain the absence of correlations in Figure 4-12.

Intensity profiles are shown again in Figure 4-15 for the 300°C specimen; additional annular intensity images have been generated corresponding to the positions shown for the split M-O distribution, positioned to the left and right of the central M-O distribution of Figure 4-8. These new peaks are abbreviated 'Al P4(O1)' and 'Al P4(O2)' in the following figures.

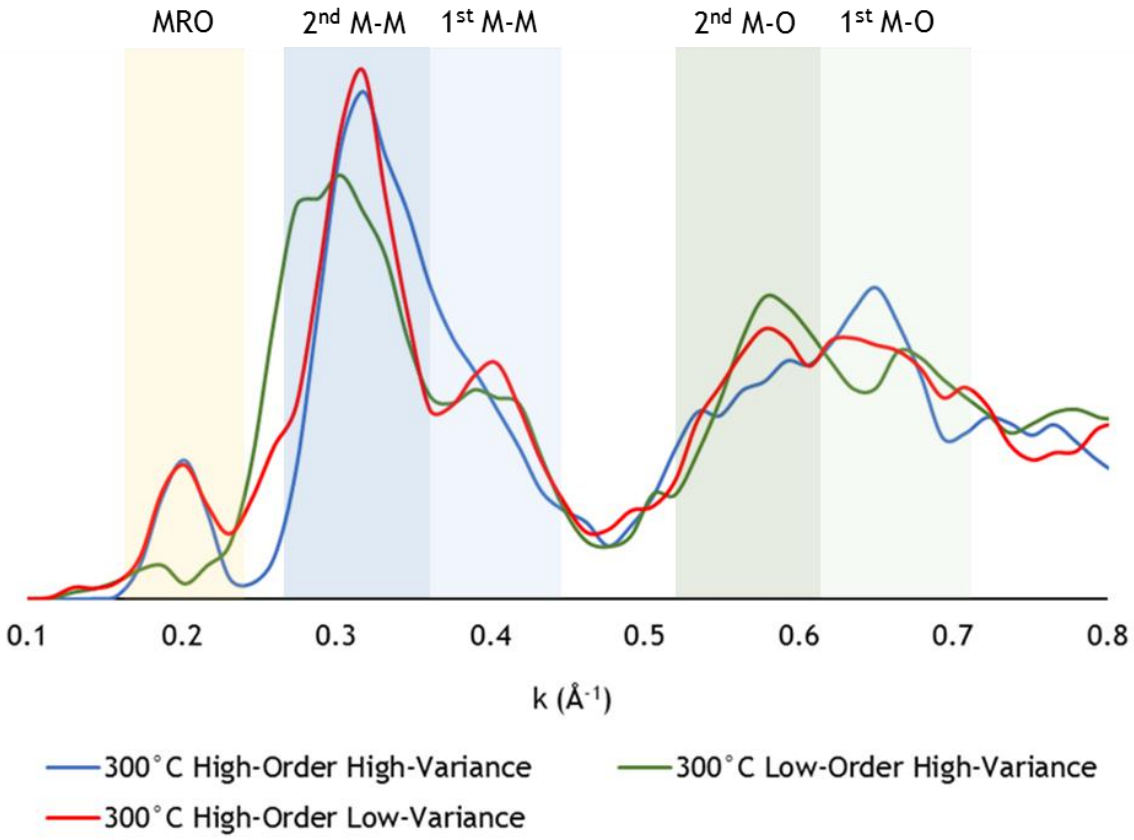

Figure 4-15 Intensity profiles from the 300°C specimen displaying a large variety in structure, with well-defined MRO correlations in the high-order regions. The highlighted regions represent the extended sampling of reciprocal space used for the correlations shown in Figure 4-16, to account for the large variation in structure.

In the following comparison of annular intensity images for the different peaks, the data has been resampled so that the images are averaged over a greater range of reciprocal space, as highlighted in Figure 4-15.

This is done to account for the variation in structure observed in the intensity profiles, and whilst important for the complimentary structure/variance images of Figure 4-9, it increases the validity of the correlations between different peak positions.

Figure 4-16 shows the correlations between the annular intensity peak images. Zero correlation suggests a uniform distribution, with no propensity for the high/low ordering of a peak to coincide with the high/low ordering of a different peak over the sampled structure.

Likewise, zero correlation suggests no propensity for the high/low ordering of one peak coinciding with low/high ordering of another peak.

A positive correlation indicates an above average coincidence of high (or low) ordered structure in the volumes probed related to those pair separations.

A negative correlation suggests above average levels of order (disorder) in one peak position coinciding with the disorder (order) of a different peak position over the sampled structure.

The interpretation of their structural relevance however requires reference to the following composite VDF images.

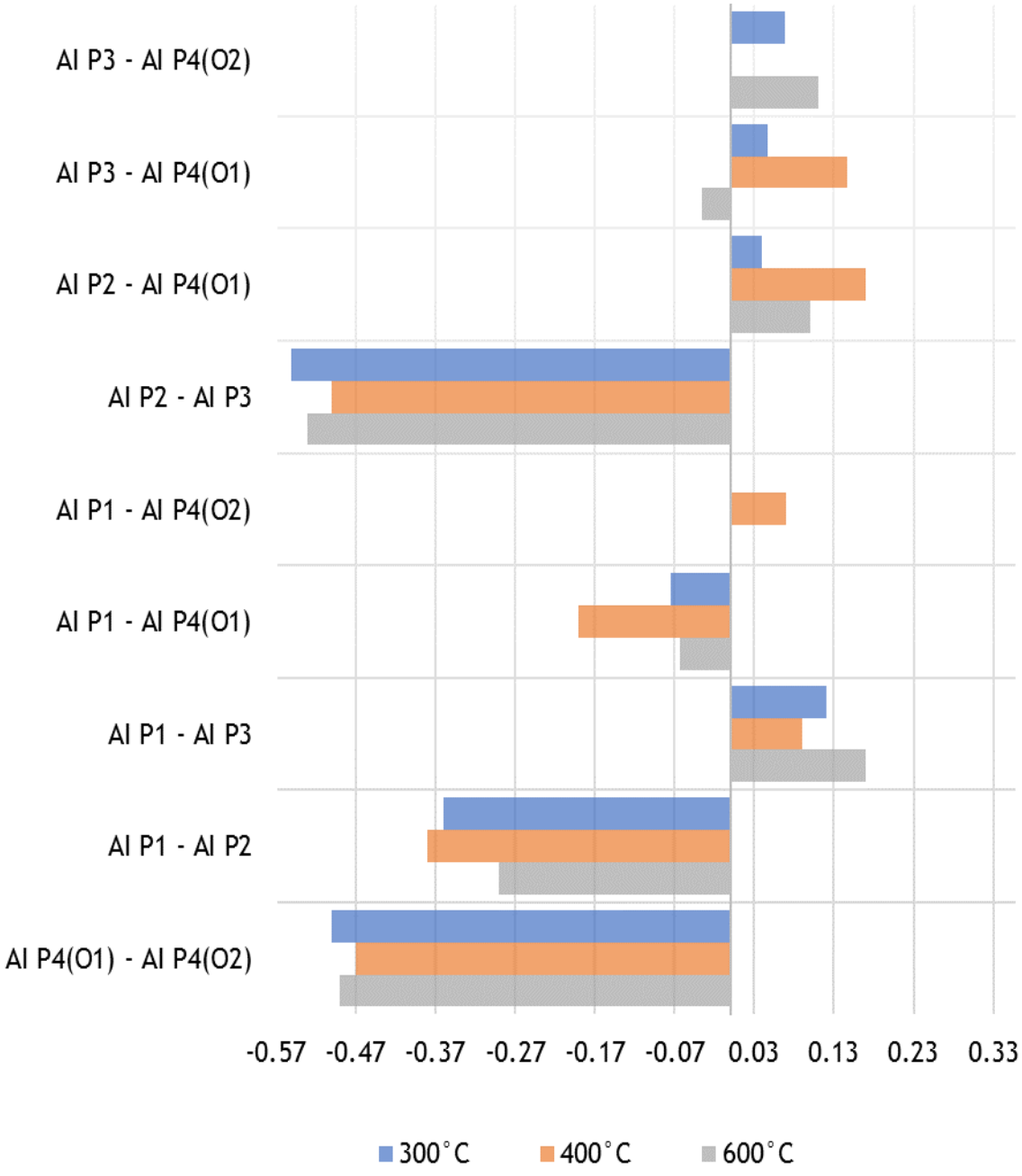

Figure 4-16 Correlations indicating significant variation in the ordering of the samples, inferred from the annular intensity peak images of Figure 4-9.

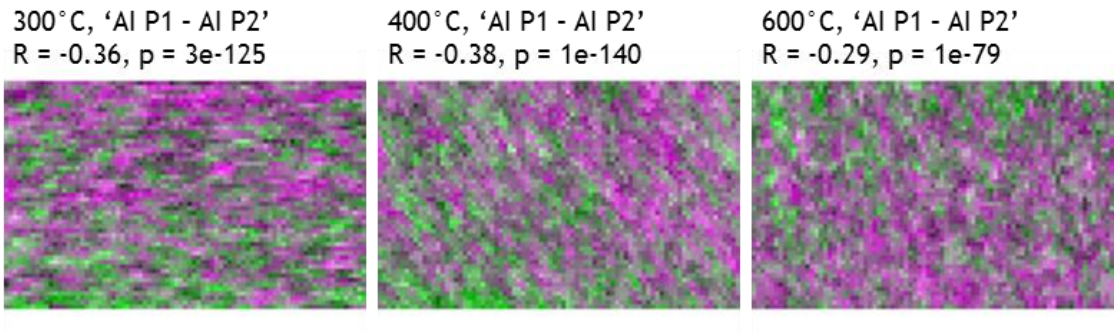

Figure 4-17 Composite VDF images of the 1st Peak MRO and the 2nd peak main Ta-Ta distribution. Intensities are scaled as in Figure 4-9 to highlight the relative distribution of ordering, such that the normalised images of each peak position span the true values of the different specimens corresponding to that peak. Grey areas are where levels of structural order are equivalent, green areas indicate higher relative structural ordering of the 1st peak, and magenta areas indicate the higher relative order of the 2nd peak structure.

The correlations between the 1st and 2nd peak images are shown in Figure 4-17, in which the composite VDF images are scaled to illustrate the spatial distribution of the ordering corresponding to the different pair separations.

The different specimen images are normalised at each peak position, such that they span the true values of the individual specimens, allowing valid comparisons to be made between peaks.

Grey areas of the images indicate equivalent levels of ordering between the peak structures, with the darkest areas representative of the lowest ordering and the bright grey areas indicating the highest equivalent ordering; green areas represent the spatial distribution of the relatively higher-ordered 1st peak structure, and the magenta areas highlight the 2nd peak structure distribution where relative levels of ordering are higher.

The 300°C specimen indicates elevated levels of heterogeneous structural ordering for both the 1st and 2nd peaks in Figure 4-17, with the ordering of the 1st peak structure more pronounced closer to the substrate (bottom of image).

The relative ordering associated with each peak appears clustered, and dominates specific regions. There is however significantly higher correlation between the highest ordered regions of the 2nd peak and the lowest ordered regions of the 1st peak.

The correlation between high and low ordered regions is slightly higher for the 400°C specimen, however, the contribution appears to be equivalent between both peak structures; the spatial distribution of the structural order also appears to be less homogeneously mixed after annealing at 400°C.

Greater concentrations of high structural order agglomerate in specific regions for the different peaks, and an appearance of increased phase separation with increased annealing temperature is apparent.

The 600°C anneal indicates a significant modification to the tantala structure shown in Figure 4-17; the lower magnitude of the correlation coefficient suggests a less heterogeneous structure, but it is more so an apparently greater homogeneity, resulting from the lack of 1st peak ordering with respect to the dominating 2nd peak structural order.

Furthermore, almost diametrically opposite to the 300°C specimen, the structural order corresponding to the 2nd peak position now appears closer to the substrate, with the higher-ordering of the 1st peak structure closer to the surface.

The dominance of the 2nd peak structural ordering in Figure 4-17 suggests that annealing at 600°C favours the growth of this peak structure over longer-range ordering, with the densification of the ordered regions becoming more noticeably segregated by contiguous low-density regions.

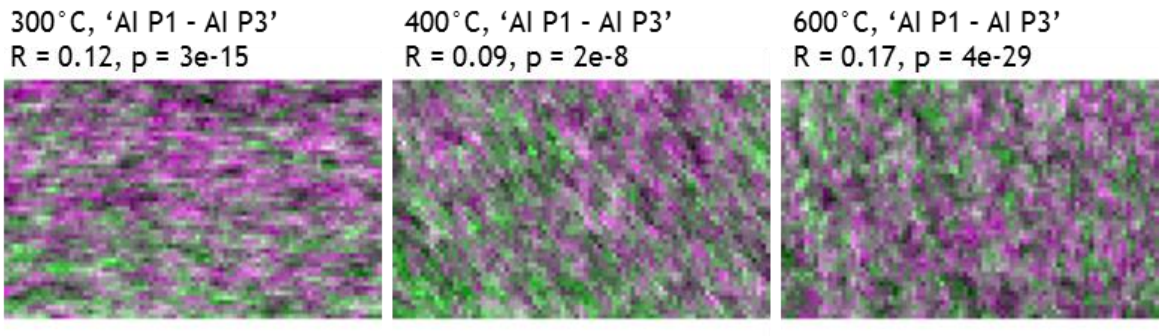

Figure 4-18 Composite VDF images of the 1st Peak MRO and the 3rd peak shorter separation Ta-Ta distributions, with accompanying correlation coefficients.

The comparison of the 1st and 3rd peak annular intensity images with their correlation coefficients are shown in Figure 4-18.

In contrast to the anti-correlation of the 1st and 2nd peaks, the positive correlations indicate an above average coincidence of low/low or high/high order regions over the volumes probed.

The darkest grey areas indicating the coincidence of low-order regions appear most prevalent in the 300°C specimen, which also appears the most contiguous in terms similarly-ordered structure, and is followed by the 400°C specimen.

The 600°C specimen has the highest coincidence similarly ordered regions, however, the comparative ordering of the peak structure is more discrete than in Figure 4-17, with higher contrast between high and low-ordered structure, and less continuity of structure with similar levels of ordering.

The longer-range structure of the 1st peak distribution, and therefore the 3D crosslinking of the structural fragments shown in Figure 3-22 of Chapter 3, is inferred to link more through the 3rd than 2nd peak structures due to the greater coincidence of ordering.

The 3rd peak structure represents the shorter M-M pair separations of tantalum in edge-shared polyhedra, in which three coordinated oxygen is most prevalent, so the greater coincidence of these ordered structures are not surprising.

This is corroborated by the numerical study of amorphous Ta_2O_5 structures by Damart *et. al.* who concluded that 80% of the Ta atoms reside in the centre of corner-shared polyhedra, and 13% are located within edge shared polyhedra(208).

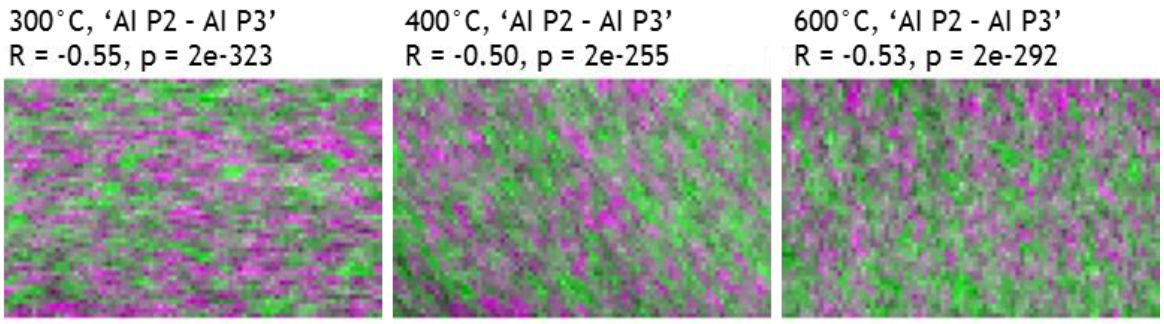

Figure 4-19 Composite VDF images of the 2nd (green) and 3rd peak (magenta) Ta-Ta distributions, with accompanying correlation coefficients.

Figure 4-19 displays the composite images of the 2nd and 3rd peak structure spatial distributions, which relate to the longer and shorter Ta-Ta separations respectively.

These appear as the 3rd and 2nd nearest neighbour distributions (3rd and 2nd shells) in the PDFs of Chapter 3, and are illustrated in the schematic of Figure 3-24.

These high-order peak structures are most homogeneously distributed and mixed in the 300°C specimen, with a large coincidence of high to low-ordered regions between the peak structures.

After annealing at 400°C the 3rd peak structural order intensifies into distinct distributions whilst maintaining similar levels of relative ordering between the distributions, suggesting an elevated level of heterogeneous phase separation.

After a 600°C anneal, the highly-ordered 2nd peak structure is dominant; however, the connectivity of similarly ordered regions is diminished and interspersed with many more low-density regions.

The large anti-correlations in Figure 4-19 further support the visually apparent heterogeneous phase separation, where high-order regions of one peak structure appear dominant in most of the volumes probed.

This may explain the higher number density of the 300°C specimen which decreases with increasing annealing temperature, indicated by their PDFs in Figure 3-20 of Chapter 3.

Annealing at 400°C appears to segregate the highly-ordered 2nd and 3rd peak structures, increasing the population of low-density regions, whilst at 600°C the low-density regions become more randomly distributed, with the 2nd peak structural ordering appears more contiguous with respect to the diminished ordering of the 3rd peak structure.

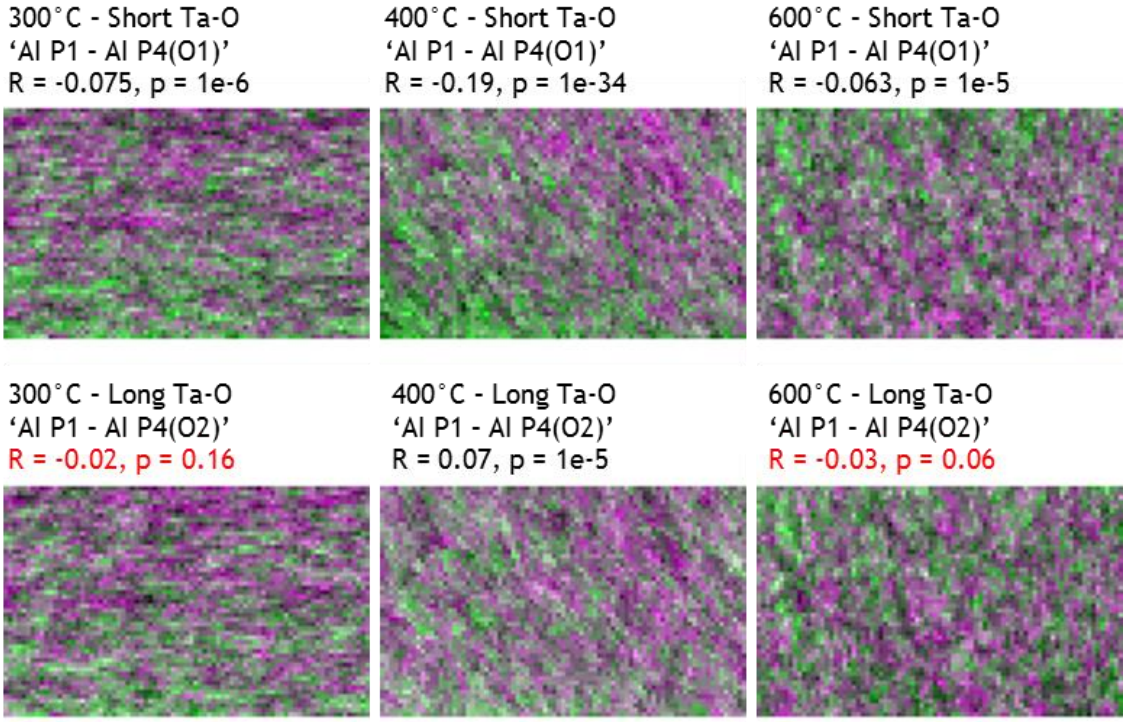

Figure 4-20 Composite VDF images of the 1st Peak MRO and the split oxygen distributions; the 1st peak structure is tinted green, and the split 4th peak structure is tinted magenta. The grey areas indicate regions of equally high or low-order.

In Figure 4-20, the 1st peak annular intensity images are compared with the annular intensity peak images for the split oxygen distribution (P4(O1) & P4(O2)) shown in Figure 4-15.

The most significant correlation between the ordering of the peaks is for the 400°C specimen, which is anti-correlated with the shorter separation M-O distribution and less correlated with the longer separated M-O distribution.

Oxygen dominates the tantala structure, making interpretation of the relative ordering difficult; simply splitting the M-O distribution as shown in Figure 4-15 is therefore unrealistic for the identification of any clear trends in its ordering.

However, the 600°C specimen does have much poorer connectivity between the 1st peak structure and the oxygen distribution in comparison to the 300 and 400°C annealed specimens.

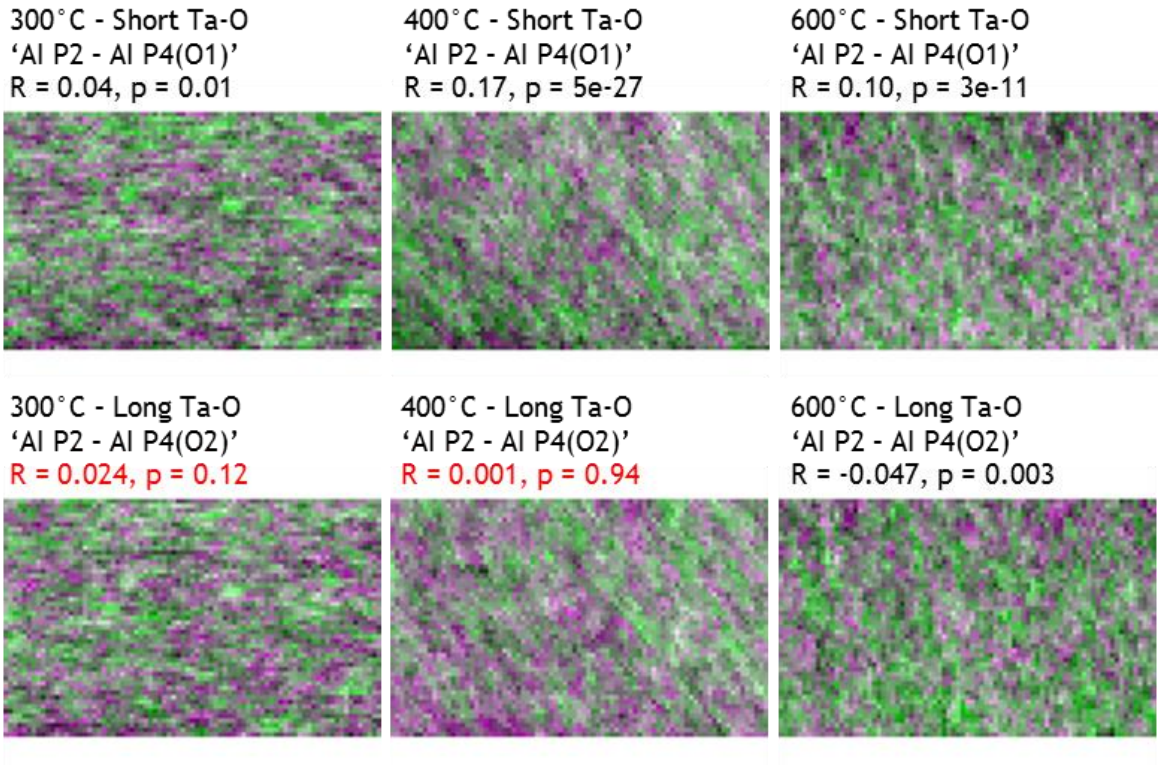

Figure 4-21 Composite VDF images of the 2nd peak Ta-Ta (green) and P4(O1)/(O2) (magenta) oxygen distributions.

The distribution of the 2nd peak ordering is overlaid with the ordering of the oxygen distributions in Figure 4-21, with an apparent high degree of correlation between the top and bottom row composite images.

The images for the 400°C specimen infer it to be the most homogeneous of the structures, due to the lowest levels of contrast and the highest levels of contiguous similarly ordered regions.

However, as in case of Figure 4-20, interpretation of the oxygen distribution ordering is difficult due to the relative quantity of oxygen in the structures, and the multiple overlapping peaks visible in Figure 4-15.

The 600°C specimen images in Figure 4-21 once again illustrates heterogeneous pockets of highly-ordered regions, surrounded by regions of lower density; these regions are however believed to be responsible for elevated levels of internal friction associated with their boundaries.

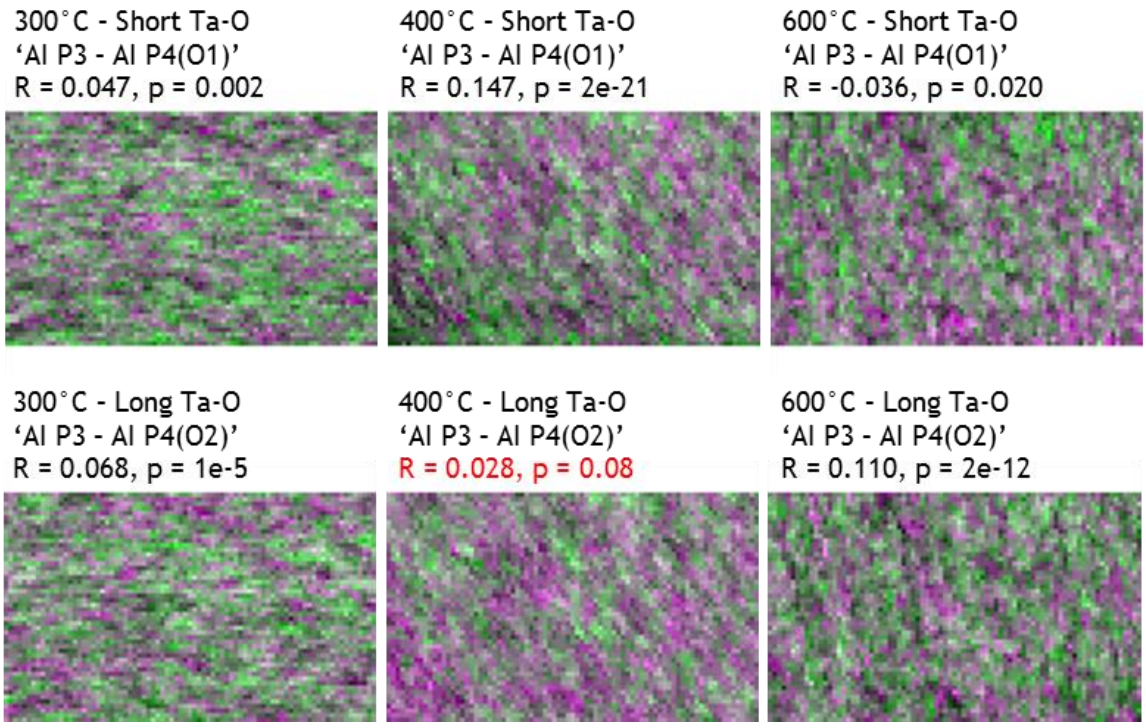

Figure 4-22 Composite VDF images of the 3rd peak Ta-Ta (green) and P4(O1)/(O2) (magenta) oxygen distributions.

In Figure 4-22, the relative order of the oxygen distributions appears much more pronounced in comparison to the 2nd peak distributions shown in Figure 4-21, indicative of the lower concentration of 3rd peak structure in comparison to 2nd peak structure, and the higher density of oxygen in edge-shared polyhedra.

The correlation coefficients in the top row of Figure 4-22 are informative; the significant increase in the correlated order after the 400°C thermal anneal, in conjunction with the spatial distribution of the ordering, suggests that homogeneous reordering and distribution of the structure resulted.

The process is more indicative of structural relaxation, observed in all the 400°C composite images. In contrast, the heterogeneous structural changes after a 600°C anneal, most apparent in the 'Al P3 – Al P4(O2)' correlation image, show a large defect region running from top to bottom, dividing the highly ordered regions, correlating with the high-order M-M distribution in the same position as its equivalent image in Figure 4-21.

The final VDF annular intensity composite images are shown below in Figure 4-23 for the two halves of the split M-O distribution.

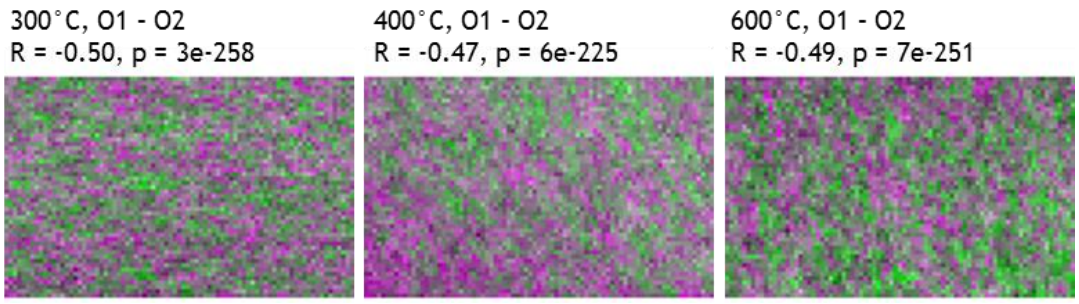

Figure 4-23 Composite annular intensity images corresponding to the shorter Ta-O distances (O1 green, indicative of edge-shared polyhedra), and the longer Ta-O distances (O2 magenta, indicative corner-shared polyhedra).

A homogeneous random mixing of the ordering illustrated in Figure 4-23 would suggest a continuous random network model for these structures; however, these results, and the previous VDF images show that the structure of amorphous tantala may be better described by a phase separated heterogeneous model than the continuously uniform random network model of Zachariasen.

The results are reminiscent of the recent work by Treacy and Borisenko on the local structure of amorphous silicon, in which they found para-crystalline structures containing local cubic ordering at the 10 to 20 Å length scale, which appears to be the case for tantala also.

Other studies have shown favour to this same nano-crystalline theory of glass(248–250). Furthermore, it is suggested that the increased heterogeneous ordering affects the number and energetics of defects forming double well potentials at boundaries between paracrystallites, with a relatively low energy barrier between two metastable state, similarly to the mechanical loss mechanism proposed for amorphous silica(251).

Furthermore, the long contiguous bands of high-structural order, observed in the VDF and the composite images are reminiscent of the long octahedral chains found in crystalline Ta_2O_5(208), and of the Ta-O-Ta backbone structure of amorphous tantala posited in the GIPDF study discussed in Chapter 3(82).

With increasing temperature thermal annealing, a commensurate increase in heterogeneous structural ordering ensues, including an apparent collapse of longer-range order at 600°C. It is not yet certain what role a certain pattern of structural ordering may play in contribution to internal friction, however, tantalising clues are apparent and point to new avenues of investigation.

4.3 14% Ti:Ta_2O_5 thermal annealing

In this subsection, the remainder of the optically coupled scanning diffraction data obtained during the hardware demonstration at the University of Grenoble is presented.

The analysis, presentation and processing of the data is identical to that in the previous subsection; these datasets however consist of 14% Ti cation doped Ta_2O_5, thermally annealed for 24 hours in air at 300, 400 and 600°C.

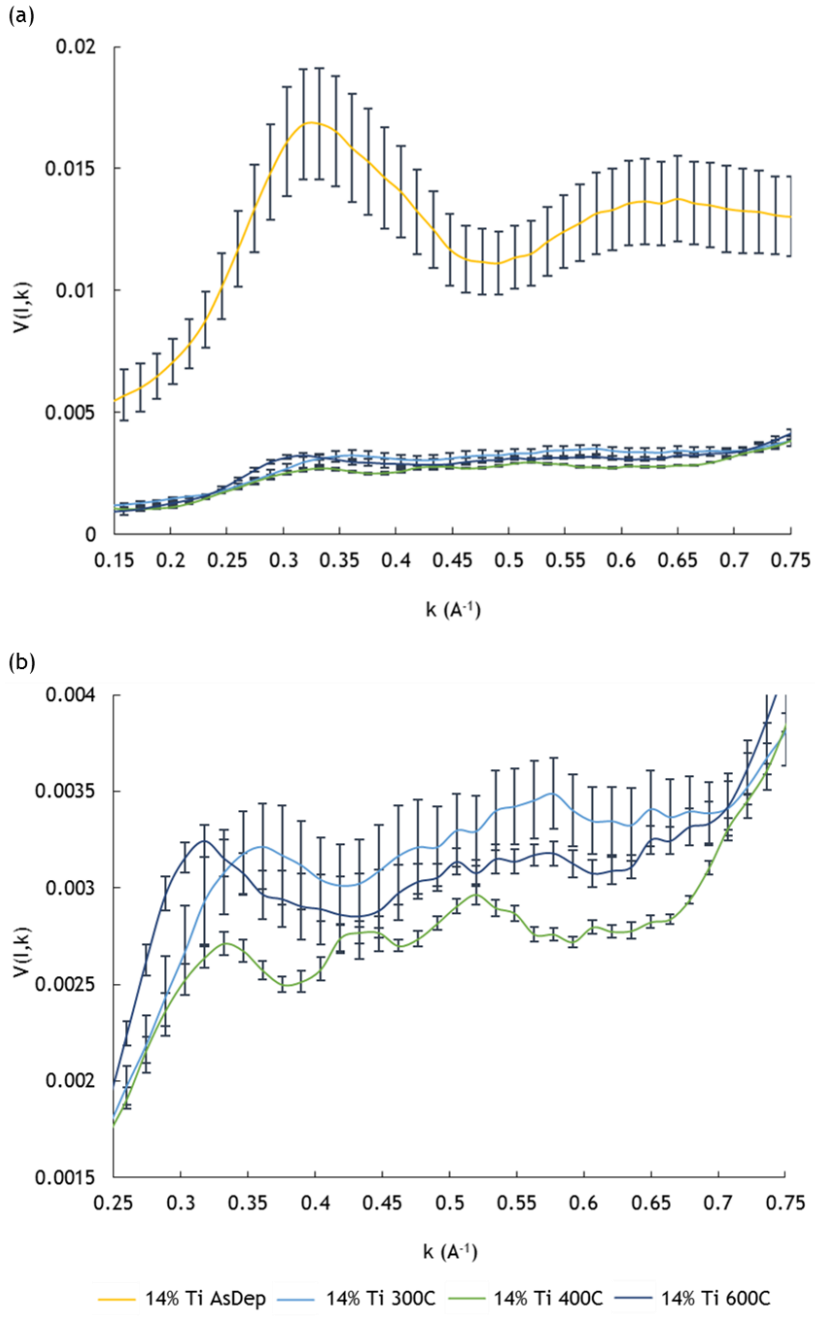

Figure 4-24: (a) Normalised variance, V(I,k), of 14% Ti-cation doped a-Ta_2O_5, thermally annealed for 24 hours in air, at 300, 400 and 600°C. (b) Enlarged region of the closely spaced curves in (a).

In Figure 4-24, the structural variance computed for these samples is first shown using the standard FEM approach; however, the as-deposited sample displays variance an order of magnitude higher than the rest of the data, likely sampled from a region significantly thinner than the other data, and are plotted separately below.

A larger structural variance is expected for the as-deposited sample, however, its relative magnitude with respect to the other samples is not considered to be a true representation of its comparative level of disorder.

Discussion with colleagues in the LIGO collaboration indicated as much; they observed no such significant differences in their past macroscopic investigations into these coatings for mechanical loss, scattering and absorption; however, none of the data were readily available, and did not feature in publication.

In any case, a higher level of heterogeneity in the as-deposited sample is not surprising; the sputtering of a polycrystalline target, by nature inhomogeneous, cannot be expected to deliver a homogeneous single atom sputter product.

A distribution of sputter products ranging from single atoms to disparate clusters of atoms should be expected; this can be appreciated from Figure 1-7 in Chapter 1 which illustrates the IBS process and the primary ion beam interaction with the sputter target. Sputtering is generally regarded to be an atomistic process(50), which is too much of an approximation.

Woodyard and Cooper(252) studied features of sputtered Cu atoms with 100 keV Ar+ using mass spectrometry, and discovered that 95% of the sputter product consisted of single Cu atoms, and the remaining 5% were Cu_2 molecules.

Indeed the sputtering of molecules has been reported often(253–255), and further consideration must be given to its effect, especially in the context of mirrors used in ultra-high precision interferometry such as LIGO.

It cannot be assumed that amorphous, polycrystalline, or single crystal targets will deliver a truly homogeneous sputter product, considering that surface damage and preferential channelling of the target can be effected by the ion beam(256), and probably oxidation if pure metal, contributing to a spectrum of energy transfer between the sputtering atoms and the target surface.

Furthermore, post-deposition thermal annealing in sputtered coatings is performed to promote relaxation of the structures, which are generally deposited such that atoms settle before finding their most favourable energetic minima; it is then a fair assumption, and indicated in the previous section, that annealed specimens, up to a threshold of phase transformation, will be more homogeneous.

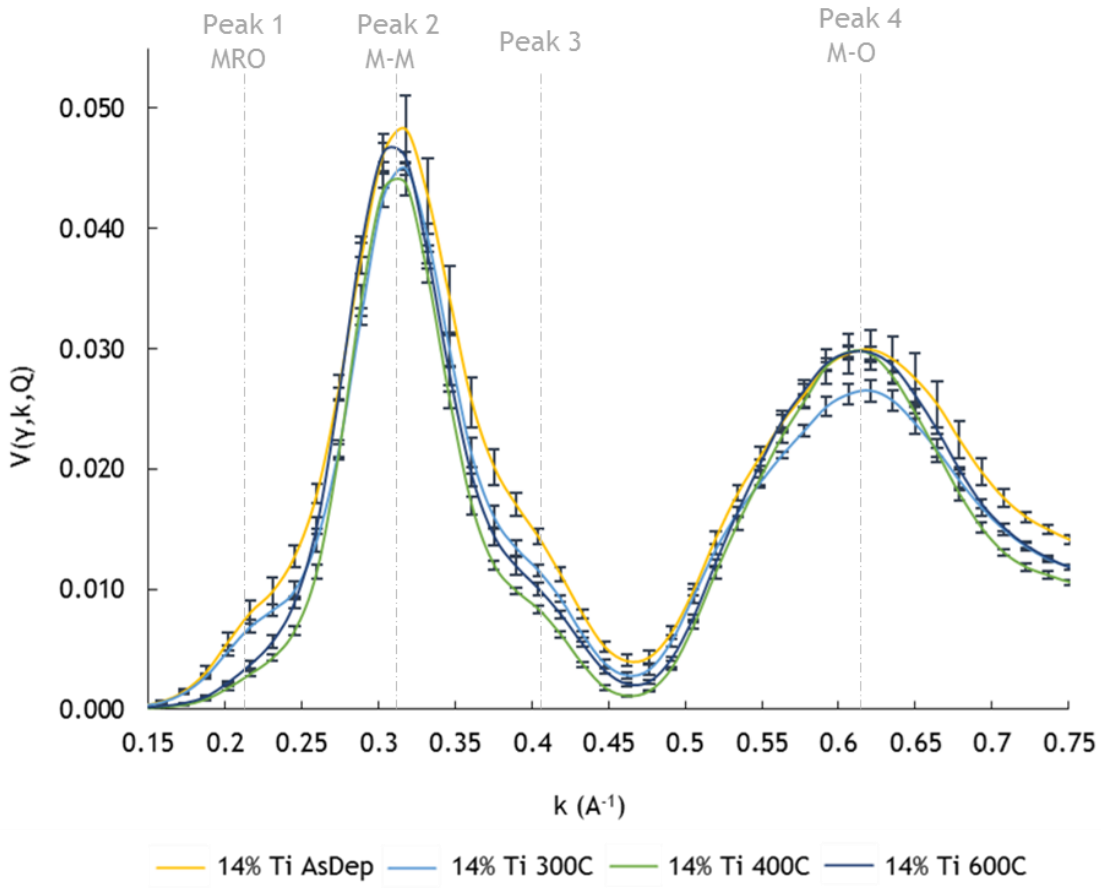

Figure 4-25: Normalised variance, V(γ,k,Q), of 14% Ti:Ta_2O_5, as deposited and annealed for 24 hours in air at 300, 400 and 600°C.

In Figure 4-25, the data is plotted again, using the method of variance computation by normalised cross correlation coefficients.

Further confidence in its applicability is obtained from the agreement with the intensity based approach at low-*k*. Across almost all spatial frequencies, the unannealed and the highest temperature annealed samples display the highest degree of structural variance.

The exception is the small peak around $k \approx 0.22$ Å^{-1}, in which the 300°C annealed sample shares the feature with the as-deposited sample, whilst it is absent for the 400°C and 600°C annealed samples.

The peak represents the MRO region illustrated in Figure 3-28 of Chapter 3, and is much more prominent than the corresponding peaks for the un-doped samples in the previous section.

Also apparent are the larger error-bars, predominantly in the as-deposited data, and especially on the higher-*k* side of the M-M distribution, which accurately picks out the location where titanium has been shown to prefer occupation(190,222), with the uncertainty reducing with annealing, and indicative of heterogeneously deposited sputter products not yet undergone a homogenising relaxation process.

The 400°C sample appears to have the most homogeneous M-M distribution, whilst the 300°C sample is more so in the M-O distribution. The 300 and 600°C data also have appreciably larger error-bars than their un-doped counterparts, and is a likely reflection of the incorporated titanium.

It is likely that the addition of titanium attenuates the reordering during relaxation, and a higher temperature anneal is required for appreciable change in the structure, as evidenced by the 1st peak at $k \approx 0.22$ Å^{-1}, and indicates that a 600°C anneal effects these materials in a more transformative manner than relaxative, as was observed for the un-doped tantala.

The larger spread in variance around $k \approx 0.4$ Å^{-1}, not observed in the pure tantala data, correlates with the lower-*r* M-M pair correlations observed in the PDF work of chapter 3.

It has been reported that titanium doping of tantala reduces internal friction by up to 40%(33), the greatest reduction from the dopants investigated, and thus was selected for the high index layers of the aLIGO ETM coatings(15).

Molecular dynamics simulations by the LIGO collaboration, of tantala and tantala with titanium doping have closely reproduced the internal friction results(96), however, their validity must be questioned in this regard and as to their relevance to the real-world IBS samples.

These ~1000 atom models, comparable to a ~10x10 nm^2 region of the VDF images shown here, take no account of their known sub-stoichiometry, or of the previously discussed nature of sputter products, and are not representative of the heterogeneity apparent at the length scales shown here.

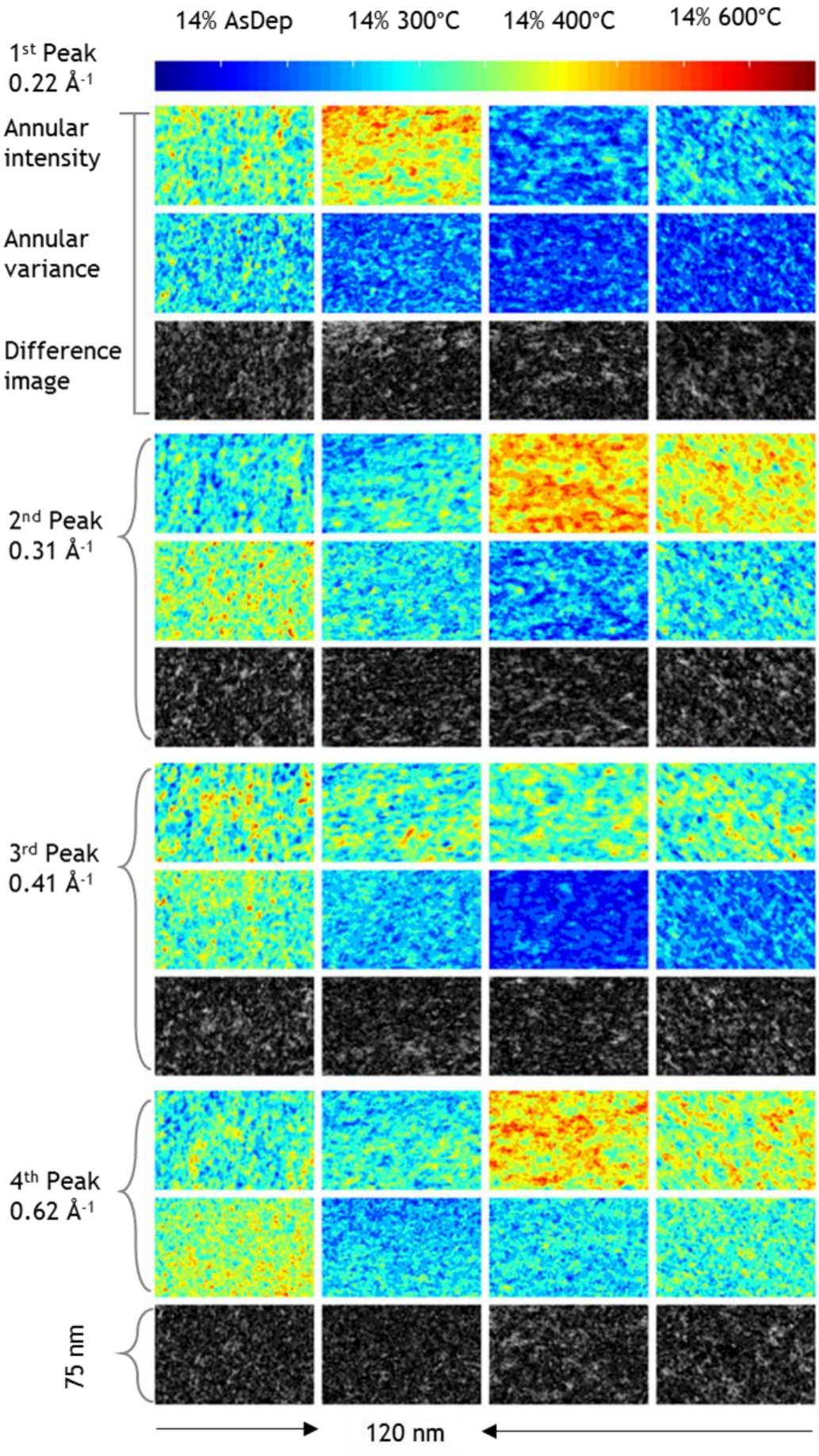

Figure 4-26: Virtual dark field annular intensity, annular variance and their difference images for the 14% Ti-cation doped a-Ta_2O_5.

The VDF images for these structures are shown in Figure 4-26. The 400°C structure visualisation here, in contrast to its M-M variance peak in figure 4-25, appears the most highly ordered, and further illustrates the value of this representation of the data.

Being the most highly ordered, and yet lowest in variance, highlights the weakness of the FEM method in its inability to differentiate structures that are homogeneously high or low in order.

In terms of the highly-ordered regions inferred by image intensities, all samples have such ordered regions; the 300 and 400°C samples appear to have the greatest level of similarly connected regions, be they of high or low order, whereas the as-deposited and 600°C annealed sample displays much greater heterogeneity in the connectivity of their ordered regions.

The 300°C specimen images of Figure 4-26 notably appear to be the most ordered at the longest length scale, as seen in the intensity image of the first peak, albeit non-uniformly. The regions of the sample from where these data were collected are shown in Figure 4-27.

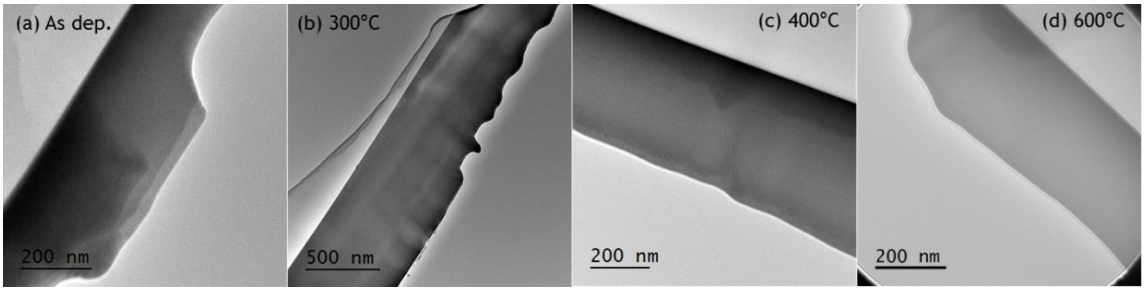

Figure 4-27 Bright-field images of the regions where data was collected.

These patterns of heterogeneity are reflected in a reduced form in their variance plots of Figure 4-25, but also point to a possible mechanism of internal friction analogous to grain boundary interaction, usually more appropriately attributed to polycrystalline structures, as has been proven in the case of nano-crystalline aluminium(257).

The rationale here is that a structure with many similarly connected, structurally ordered regions, in contrast to one with many unconnected ordered regions, can be thought of being composed of large grains and small grains respectively; the larger grained structure has in comparison smaller areas over which interaction with dissimilar structures occur and into which energy can be lost.

Furthermore, the frequency dependence of mechanical loss spectroscopy measurements have demonstrated correlation with grain size(257).

Whilst 'grains' are generally not valid in the discussion of amorphous materials, this is more of an analogy to illustrate differences between regions of high and low order, in which the interface states are more likely to be metastable with respect to the regions of high or low order alone(258–261). These metastable regions are proposed to have a relatively low energy barrier between them.

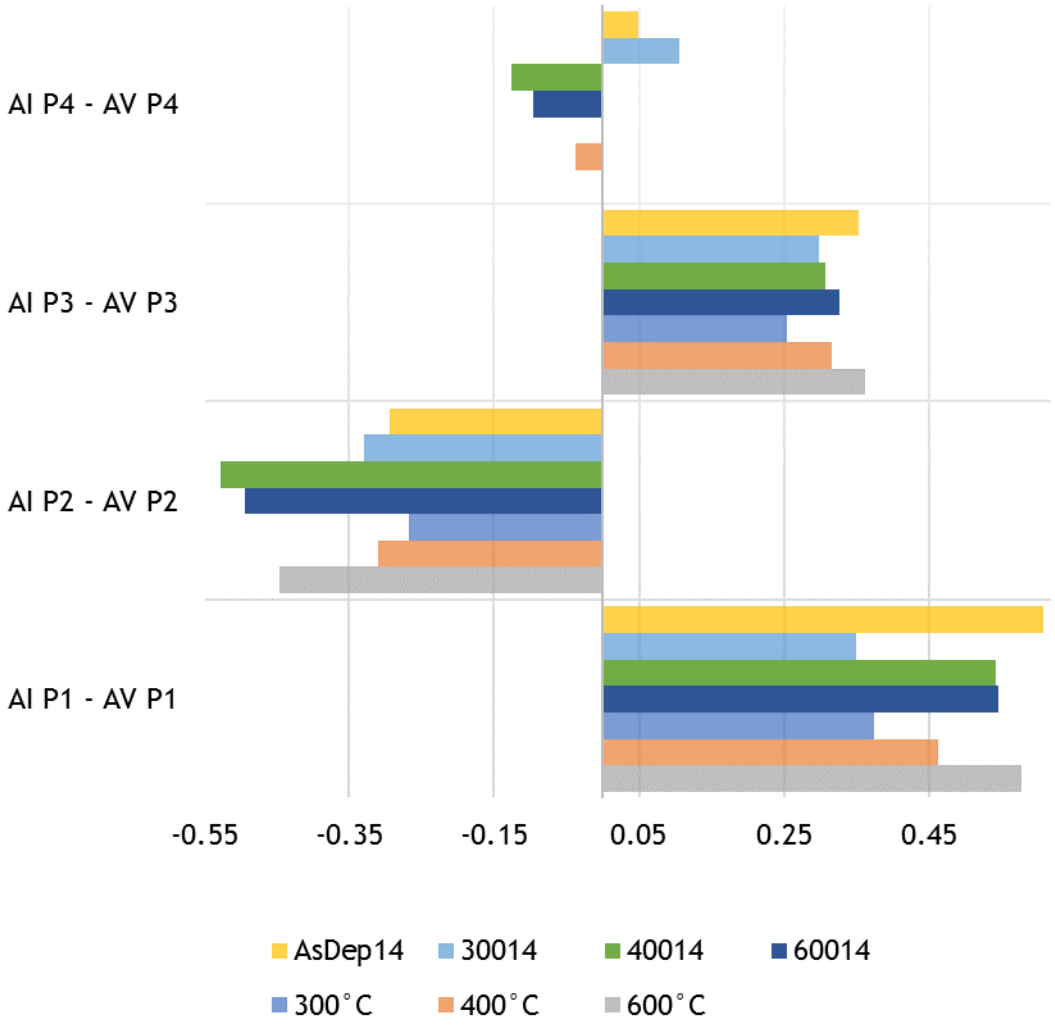

Figure 4-28 Correlations between the complementary VDF images, annular intensity (AI) and annular variance (AV) at different peak positions (P), with p-values < 0.05. The un-doped tantala data from the previous section is included for comparison.

The 14% Ti 300°C sample in Figure 4-26 appears the most homogeneous of the structures in terms of variance between similarly connected regions, with a significant reduction of incommensurately connected structures with respect to the as-deposited sample; whereas for higher heat-treatment temperatures, the homogeneity of the structures appear to decrease commensurately.

This indicates that annealing at 300°C may be the optimal heat-treatment temperature for a homogeneously relaxed structure by the current annealing procedures.

The correlations between the peak images shown in Figure 4-28 quantitatively relate the relative homogeneity of ordering with respect to the mean structures.

These correlations are for the complementary intensity/variance images only, but also include the correlations from the un-doped samples of the previous section for comparison.

In Figure 4-28, The 'AI P1 – AV P1' correlation is largest for the 14% Ti as-deposited specimen, such that regions of high-order/high-variance and low-order/low-variance are significantly coincident in the volumes probed; it is however not much larger than that for the un-doped 600°C annealed specimen.

Annealing at 300°C appears to homogenise the distribution somewhat, such that the 14% Ti 300°C specimen is the most highly ordered and homogenous comparatively of all the specimens at the medium-range, but only slightly more so than its un-doped counterpart.

Annealing the 14% Ti-doped structures at > 300°C also increases their character of heterogeneous phase separation; however, the ordering of the 400 and 600°C Ti-doping annealed specimens appear equally heterogeneous in this region of Figure 4-28.

This adds weight to the assertion made in Chapter 3 that Ti doping may attenuate structural reordering during annealing, such that higher temperature anneals are required for the similar structural changes observed in un-doped tantala.

The 'AI P2 – AV P2' anti-correlations of Figure 4-28, like the un-doped specimens, further support the heterogeneous phase separated model for the structures.

The high-order/low-variance character of the 2nd peak increases with increasing annealing temperature.

The homogeneous ordering of the 400°C Ti-doped specimen appears elevated with respect to the average structure, more so than the 600°C specimen, and highlights the increased complexity of structural reordering due to annealing when titanium is introduced into the structure.

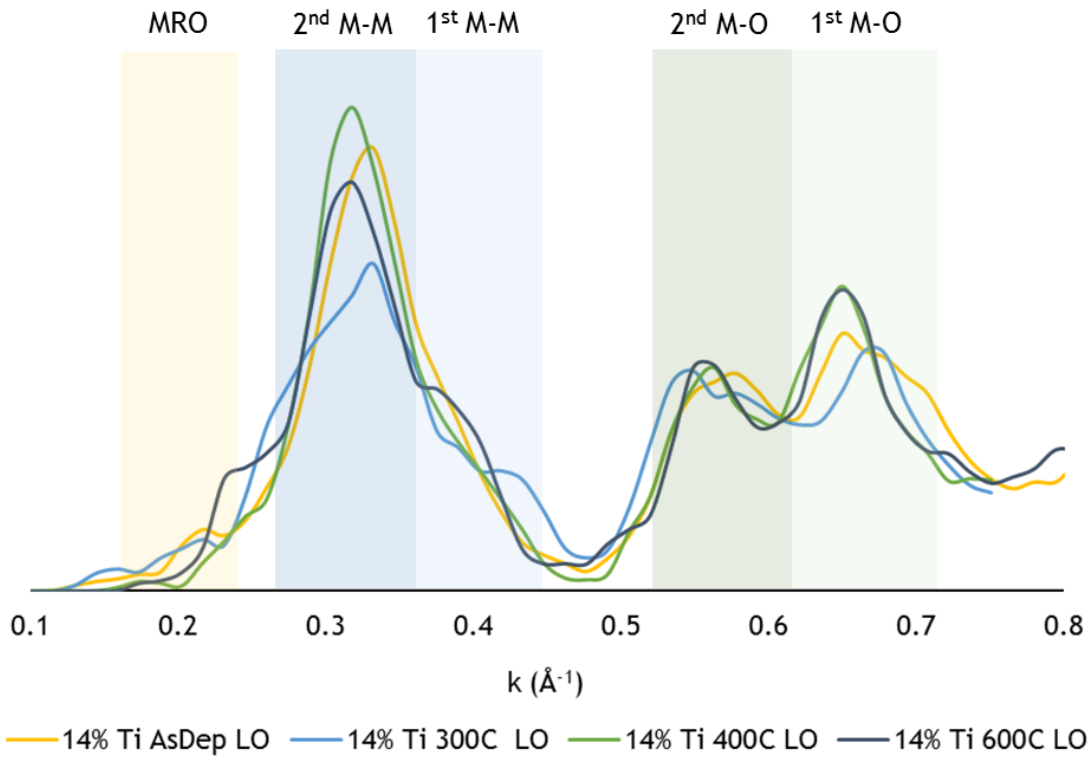

Figure 4-29 Intensity profiles taken from low-order (LO) regions of the 2nd peak annular intensity images in Figure 4-26.

The positive 'Al P3 – AV P3' correlation of Figure 4-20, indicates significantly less variation between the Ti-doped samples than in the un-doped samples.

This is suggestive of titanium's preference of this location at the centre of edge-shared polyhedra, illustrated in Figure 3-27 of Chapter 3.

The final correlations between the complementary images shown in Figure 4-28, 'Al P4 – AV P4', indicate significant homogenisation of the M-O distribution ordering for the Ti-doped samples when annealed at 400 and 600°C, in contrast to the relative heterogeneity of the ordering observed for the as-deposited and 300°C samples.

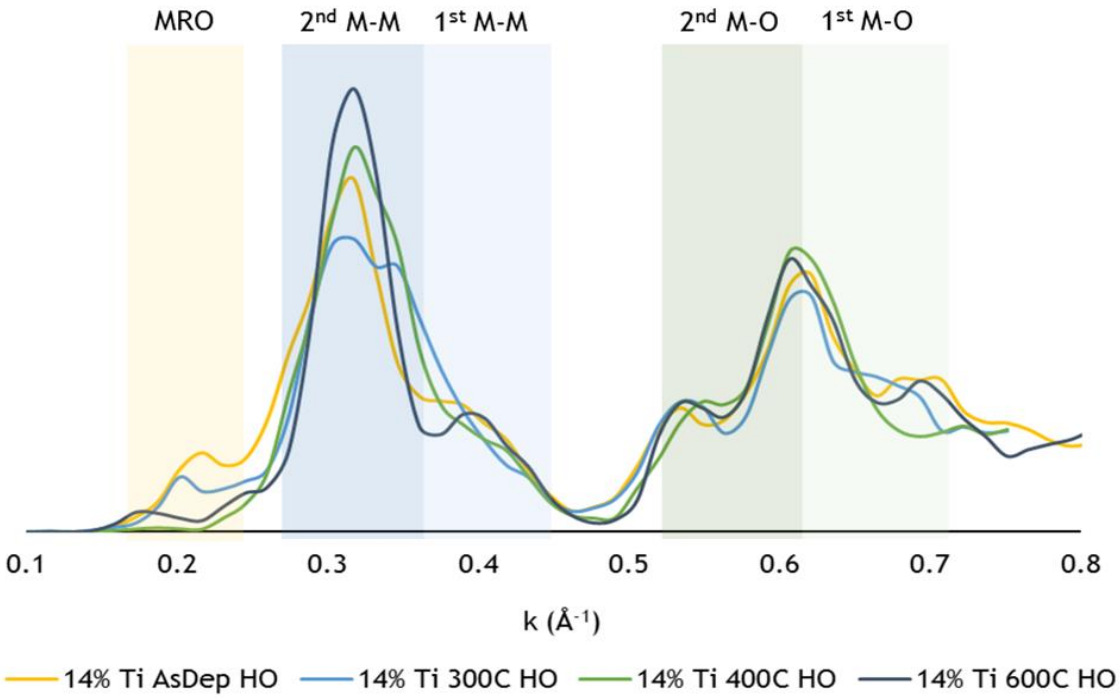

Figure 4-30 Intensity profiles taken from high-order (HO) regions of the 2nd peak annular intensity images in Figure 4-26.

In Figures 4-29 and 4-30, intensity profiles from the lowest and highest-order regions of the 2nd peak annular intensity images of Figure 4-26 are shown for the 14% Ti-doped specimens.

The shaded regions indicate the range of reciprocal space averaged, to account for variations in the positions of the peak distributions, as was observed in the un-doped specimens of the previous section.

This was again carried out in consideration of the increased sensitivity to peak positioning over that of the complimentary structure/variance images, for the following peak image correlations analysis.

However, the variations in the intensity distributions of the 14% Ti-doped samples shown are highly constrained with respect to those of the un-doped tantala specimens.

The increased homogeneity from such a modest titanium substitution is surprising, and is presumed to result from a higher concentration of edge-shared polyhedra(208), which appear to persist after the thermal annealing processes.

The most noticeable effect of titanium substitution observed in the intensity profiles of Figure 4-30, is the homogenisation of the M-O distribution which has been reported elsewhere(190).

Furthermore, the persistence of the ~ 0.62 $Å^{-1}$ in the centre of the M-O distribution was not observed in the case of the un-doped tantala.

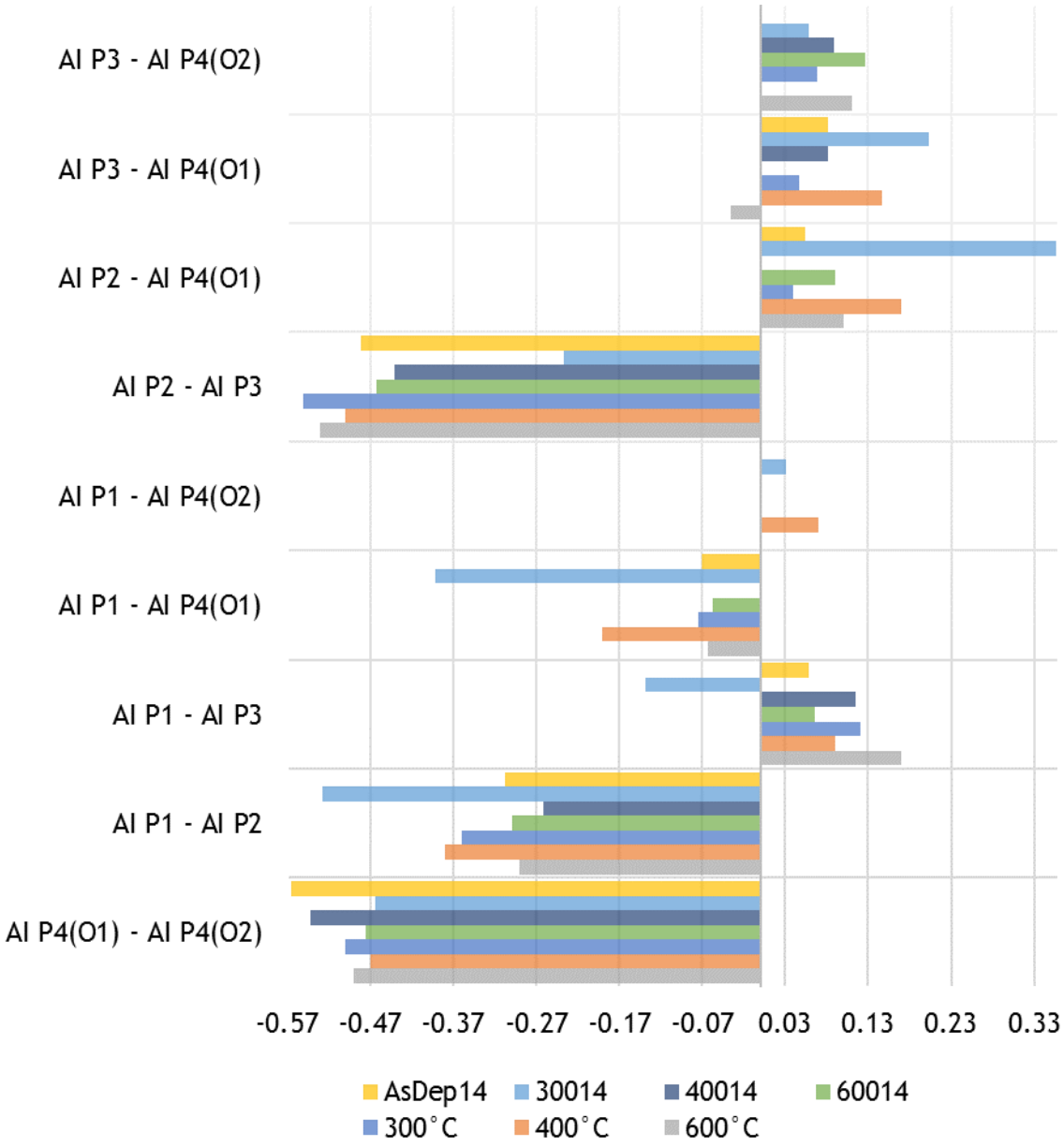

Figure 4-31 Correlations between the structural order in the VDF annular intensity images of the various peaks, including those of the un-doped samples for comparison. Interpretation of their significance over that of heterogeneous phase separation is aided by the composite VDF relative structure images in Figures 4-32 to 4-35, and Appendix C.

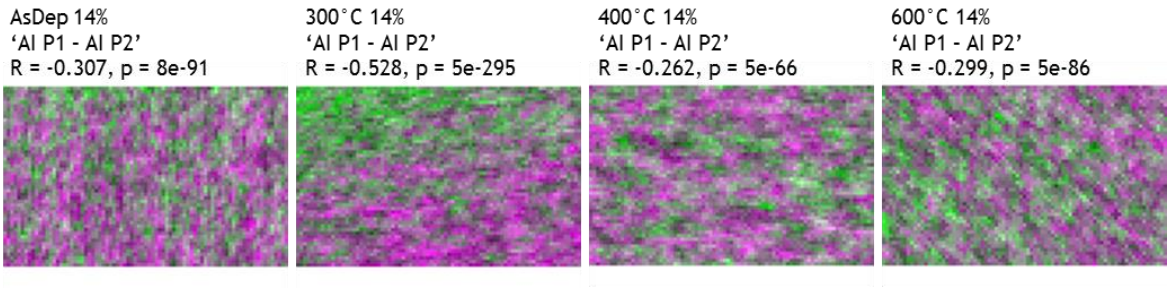

Figure 4-32 Composite VDF images of the 1st Peak MRO and the 2nd peak main M-M distributions. Intensities are scaled as in Figure 4-26 to highlight the relative distribution of ordering, such that the normalised images of each peak position span the true values of the different specimens corresponding to that peak. Grey areas are where levels of structural order are equivalent, green areas indicate higher relative structural ordering of the 1st peak, and magenta areas indicate the higher relative order of the 2nd peak structure.

In Figure 4-32, correlations between the 1st and 2nd peak images are given to aid interpretation of the correlations plotted in Figure 4-31; all are indicative of heterogeneous phase separated structure, with a predominant coincidence of high (low) order in one peak distribution with low (high) order of the other.

As-deposited, the Ti-doped specimen relative ordering of the peak structures appear dispersed throughout the volumes, but are highly clustered and heterogeneous in their connectivity.

Annealing at 300°C results in more contiguous clustering of the relative structural ordering, although almost exclusively predominant in separate volumes, with the 2nd peak highest-order regions appearing closest to the substrate.

When annealed at 400°C, the relative structural ordering appears to be the most homogeneous of the specimens, although the mixing is very poor in comparison to the as-deposited specimen.

The structural order after 600°C annealing improves the relative distribution of high-order regions, however, the heterogeneous phase separated character whilst apparently better connected, is much more pronounced.

In contrast to the un-doped samples of Figure 4-17, the relative structural ordering of the 14% Ti-doped sample only approaches similar levels of mixing in the 300°C pure specimen at the higher annealing temperature 400°C.

Furthermore, the Ti-doped specimen annealed to 600°C, develops a balance between the relative ordering of the peaks, whilst its un-doped counter-part is dominated by its 2nd peak relative order; although the discrete heterogeneity of the ordering in the doped structure is more pronounced.

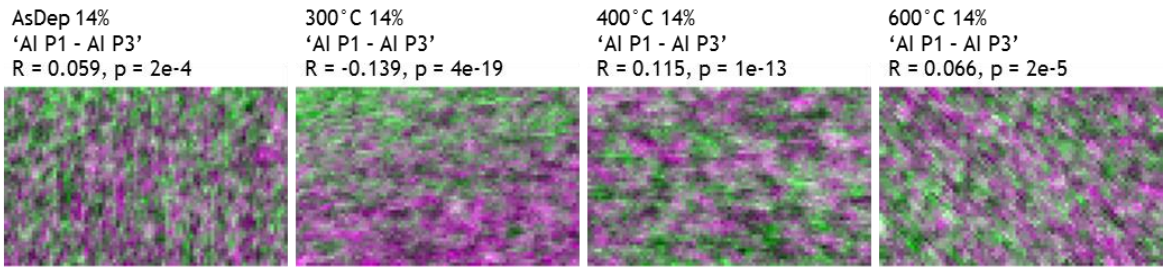

Figure 4-33 Composite VDF images of the 1st Peak MRO and the 3rd peak shorter separation M-M distributions, with accompanying correlation coefficients.

The comparative structural ordering in Figure 4-33 between the 1st and 3rd peaks, is similar to the relative changes in ordering due to thermal annealing observed in Figure 4-32.

However, with the exception of the 300°C annealed specimen, the correlations are positive and indicate more significant coincidence of regions with similar levels of relative ordering.

The 300°C anneal appears not to have facilitated the same level of structural reordering observed with its un-doped counter-part in Figure 4-18, confirming the assertion that higher temperature anneals are required in these Ti-doped samples for equivalent levels of structural change.

A greater population of corner-shared polyhedra, in conjunction with the greater oxygen affinity of titanium can explain the observed resistance to structural reordering, facilitating a more rigid interconnected structure.

An additional factor is the lower oxidation state of titanium, which constrains the possible bonding configurations it can participate in with respect to tantalum.

Whilst the composite images of Figure 4-33 are highly correlated with those of Figure 4-32 over various regions, they contain significant dark patches of very low order, congruent with the high-order regions of the 2nd peak structure and is suggestive of rigid interlocking structures, also observed in the un-doped specimens of Figure 4-18, but more pronounced.

Furthermore, in comparison to the 1st and 3rd peak composite images of the un-doped tantala in Figure 4-18, the homogeneity of the 400°C annealed structure is approached only after annealing the Ti-doped specimen of Figure 4-33 at 600°C, further illustrating the stability titanium bestows upon the structure of tantala with modest 15% cation doping.

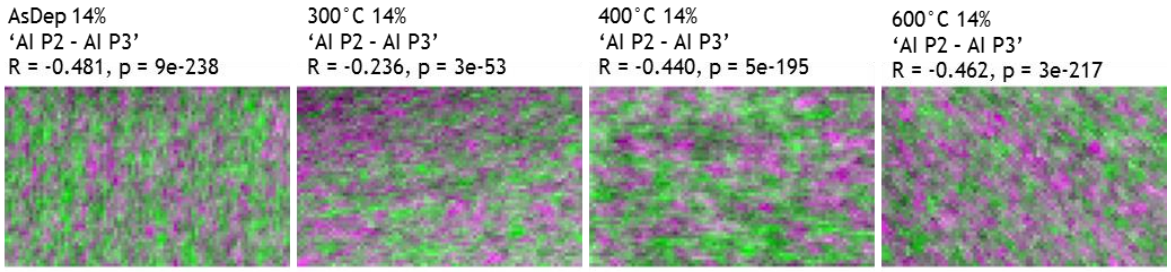

Figure 4-34 Composite VDF images of the 2nd (green) and 3rd peak (magenta) M-M distributions, with accompanying correlation coefficients.

The composite images of the 2nd and 3rd peaks of Figure 4-34, the 14% Ti-doped samples appear to follow the opposite trend of their un-doped counterparts shown in Figure 4-19.

With increasing heat-treatment temperature, the relative structural ordering of the 3rd peak increases, and appears dominant at the highest annealing temperature of 600°C, whereas the un-doped specimen 2nd peak order decreases commensurately, with the 2nd peak relative structural order becoming dominant after a 600°C anneal.

The doped specimens also have lower anti-correlation indices, indicative of comparatively less heterogenous ordering relative to the other peak structural order.

In un-doped tantala, increasing temperature thermal annealing is believed to increase the ratio of corner to edge-shared polyhedra, accounting for the lower density and poorer coordination of the 400°C annealed specimen with respect to the 300°C annealed structure; which is indicated in Figure 4-19.

In Figure 4-34, the increased ordering of the 3rd peak structure appears to maintain its ratio of edge to corner-shared polyhedra upon annealing to 400°C.

This behaviour may explain the higher density of the 14% Ti-doped structure over that of the un-doped tantala structure, also annealed at 400°C, as shown in their PDFs in Figure 3-44 of Chapter 3, as well as its better oxygen coordination.

The trend however is not followed by the 600°C annealed specimens in Figure 3-48, Chapter 3, in which the 14% Ti-doped sample has a slightly lower number density and poorer relative stoichiometry.

There is however and optimal ratio of edge-shared to corner-shared structure for a Ta-Ti mixed oxide which with to too high a ratio of edge to corner-sharing will result in a sub-stoichiometric mixture.

The dominant 3rd peak structure after annealing at 600°C in Figure 4-34 may then also explain the trend observed in the PDFs, by increasing its ratio of edge-sharing in comparison to maintaining it.

However, there is also the possibility that during the 600°C annealing, the high oxygen affinity of titanium may prevent its diffusion into oxygen poor regions deeper within the structure.

The final composite VDF images in Figure 4-35 are shown only for the two sides of the split M-O distribution. However, the composite images for the 1st, 2nd and 3rd peak structure comparisons with the oxygen distributions can be found in Appendix C for reference.

They have not been included here because their interpretation yields no more easily extractable information than has already been discussed. They all do however corroborate the heterogeneous phase separated character of the tantala structures.

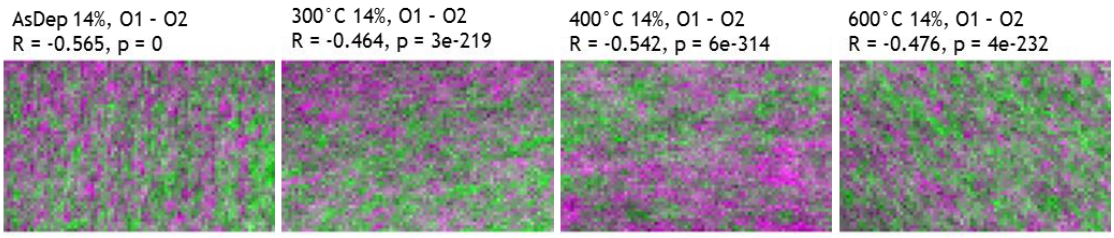

Figure 4-35 Composite annular intensity images corresponding to the split M-O distribution shown in Figures 4-29 and 4-30.

The comparison of the relative O-O distribution ordering shown in Figure 4-35 is similar to that of the equivalently heat-treated un-doped samples of Figure 4-23.

However, the highly-ordered regions of the Ti-doped samples appear much better connected throughout the structure, with large contiguous regions of high-order for both peaks, with comparatively fewer low density regions interspersing the order.

And whilst mixing of the relative ordering between the distributions is poorer than achieved with un-doped tantala at the same annealing temperatures, the structural stability gained through Ti-doping is demonstrated by the requirement of higher-temperature thermal annealing to elicit comparative heterogeneous structural reordering.

These results further support the heterogeneous phase separated model of the tantala structures, evidenced by the correlations between the complementary annular intensity and annular variance images in Figure 4-26, and the composite VDF annular intensity images of the different peak structures and their correlations.

4.4 Medipix III direct electron counting scanning diffraction

This concluding section is much more experimental in that it utilises a latest generation direct electron counting detector for the scanning diffraction(125) which was still in preliminary stages of implementation at the time of data collection.

It is the newest addition to the JEOL ARM200cF in the Kelvin Nano-Characterisation Centre at the University of Glasgow, used for the HDR diffraction collection in chapter 3, and which was operated in low-magnification aberration corrected STEM mode for these experiments.

The detector did not yet have a retractable mount and required manual installation through the 35mm camera port above the viewing screen prior to each experiment, and once installed, other imaging detectors were mostly inaccessible, making it difficult to precisely capture areas of interest.

Whilst efforts were made to keep the experimental conditions as close as possible to that of the data collected for the previous analyses, it proved unrealistic, and direct comparison of the results presented here with those of the optically coupled scanning diffraction data cannot be directly made.

The Medipix III is a 256 x 256 pixel silicon based hybrid detector with CMOS readout architecture, and is therefore ideally suited for classical FEM based diffraction experiments where noise strongly affects the quality of the data(177).

The 256 x 256-pixel resolution, double the resolution of the detector used in previous sub-sections, was maintained in the FEM analysis; however, it did not appear to be beneficial, as computational overheads increased significantly and artefacts in the data were amplified.

The detector recorded at a dynamic range of 12 bits, and whilst this was eventually made irrelevant by the substitution of variables from intensity to normalised cross-correlation coefficients, the higher dynamic range enabled finer discrimination between ordered patches of intensity.

The microscope, operating in STEM mode with a 40μm condenser, with ~1 mrad convergence angle, resulted in a probe size of ~1.2 nm. The probe current was unaccounted for and it is unknown if there was any speckle movement under the beam, which would be indicative of induced structural change.

Whilst all diffraction patterns were unsaturated measurements of the diffracted intensity, they were unfortunately non-linear.

The same problems discovered in TEM mode diffraction that hindered the PDF work which was described in Chapter 3, were also present in the scanning diffraction data collected in STEM mode.

It was hoped that the effect would be less pronounced, due to the Medipix detector placing much higher up in the column; however, the slight misalignment of the column appears to have a significant affect upon the back focal plane. A typical diffraction pattern from these datasets is shown in Figure 4-36.

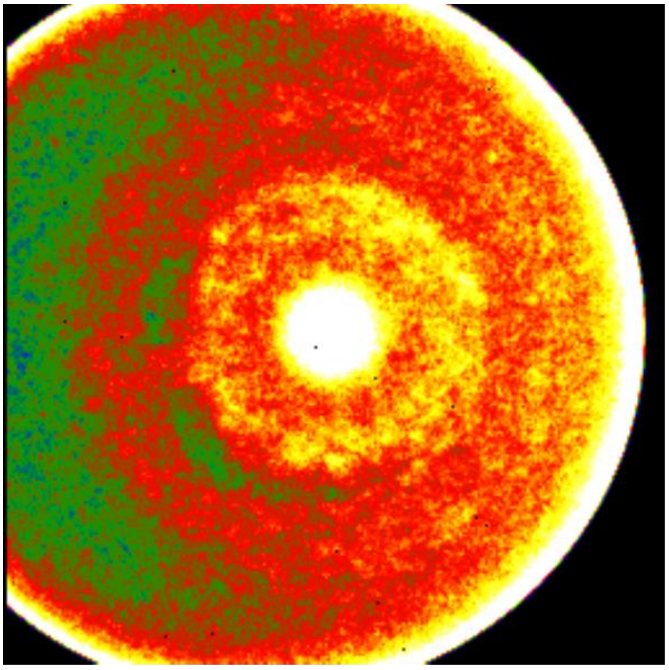

Figure 4-36: Typical diffraction pattern of the FEM datasets recorded on the Medipix 3 detector, in the JEOL ARM200F, with clear indication of the non-linearity in I(k).

The same effect of non-linearity in the diffraction patterns of Chapter 3, also demonstrated at the beginning of this chapter in the initial FEM experiment, is shown here for the scanning diffraction collected on the Medipix detector.

There is a pronounced weighting of the electron counts to the right-hand side of the pattern, however, clear indication of geometrical distortions is not so apparent, due to the smaller angular range of the collected diffracted intensity.

The effect occurs throughout the datasets, to greater or lesser degree, and was not straightforward to correct for in post-processing. The instability of camera length calibration discussed in Chapter 3 is also thought to manifest here, but has not been accounted for.

It is not a significant issue however, regarding the interpretation of the following results, especially for the VDF images, which portray the structures in relation to their maximum variance peaks, irrespective of their precise location in reciprocal-space.

As performed on diffraction pattern examples from previous datasets, six 60° sectors have been azimuthally averaged from the pattern in Figure 4-36, and are shown in Figure 4-37.

The non-linear behaviour of $I(k)$ varies significantly in azimuth, and is reflected in the formal intensity based approach of FEM, as can be seen in the variance curves of Figure 4-38, below.

The effect is like that in the optically coupled setup, where the poor SNR at high-k resulted in the variance rising with increasing k, although the causes are different.

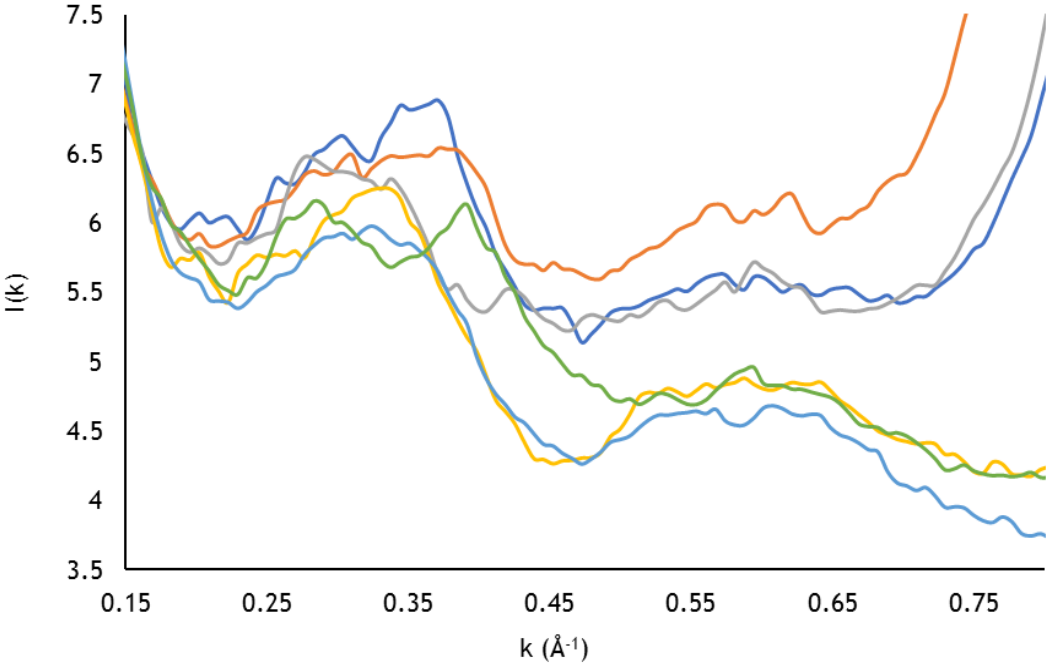

Figure 4-37: Azimuthally averaged I(k) of six 60° sectors from the pattern in Figure 4-39.

The structures studied in this section consist of 52% Ti:Ta_2O_5 annealed at 600°C, an as-deposited 68% Ti:Ta_2O_5 specimen, and an IBS silica specimen which was annealed at 500°C in air for 10 hours, in contrast to the 24 hours in air for other annealed samples.

The samples doped with greater than 50% titanium are obviously tantala doped titania, however this is the naming convention used in the LIGO coating group, and is adhered to in this work.

The inclusion of a silica sample here is for comparison of the titania/tantala structures to this archetypal mechanically stable amorphous structure; their variance curves are plotted in Figure 4-38 & Figure 4-39, for the intensity based approach and the cross-correlation coefficient method respectively.

The datasets used in this section, except for detector pixel density, are of the same dimension as the last two; each variance curve is an average of ten variance curves that were each calculated from 500 diffraction patterns, with the error-bars representing the standard error on the mean.

The low uncertainties in the results are certainly a consequence of the lower noise in the data recorded on the Medipix detector, irrespective of the non-linearities, which appear systematic throughout the data.

The sporadically appearing larger uncertainties are due to dead pixels in the Medipix detector, which were not fully removed in post processing.

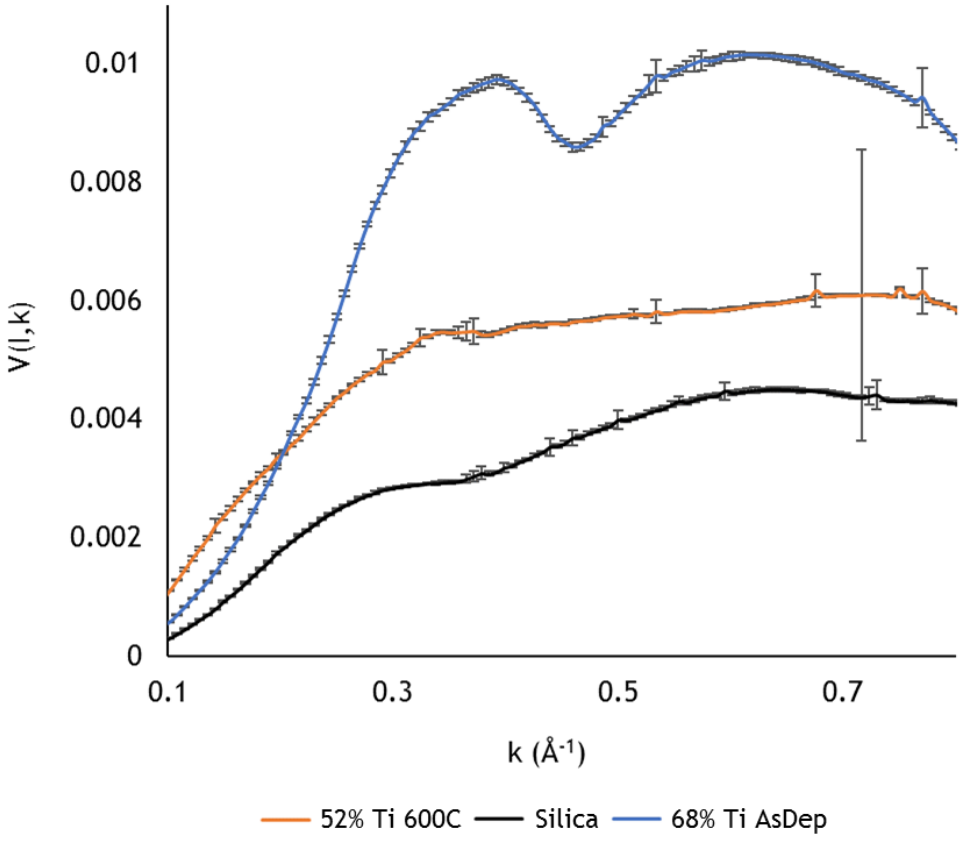

Figure 4-38: Normalised variance of 52% Ti:Ta_2O_5 annealed at 600°C, an as-deposited 68% Ti:Ta_2O_5 specimen, and IBS silica from the aLIGO multilayer coating, obtained using the formal intensity based FEM approach.

The as-deposited 68% data displays the highest variance over all spatial frequencies, the 52% Ti:Ta_2O_5 annealed at 600°C is considerably lower, and the silica specimen shows the lowest levels of heterogeneity.

The relative levels of variance in Figure 4-38 are qualitatively sound; considering that an as-deposited structure should be expected to be the most heterogeneous, not having undergone a post-deposition relaxation process.

The 52% Ti sample may be expected to be less heterogeneous in consideration of its post deposition relaxation by annealing, and that similar metal-cation concentrations in a ternary metal-oxide promote a more homogeneous and stable structure.

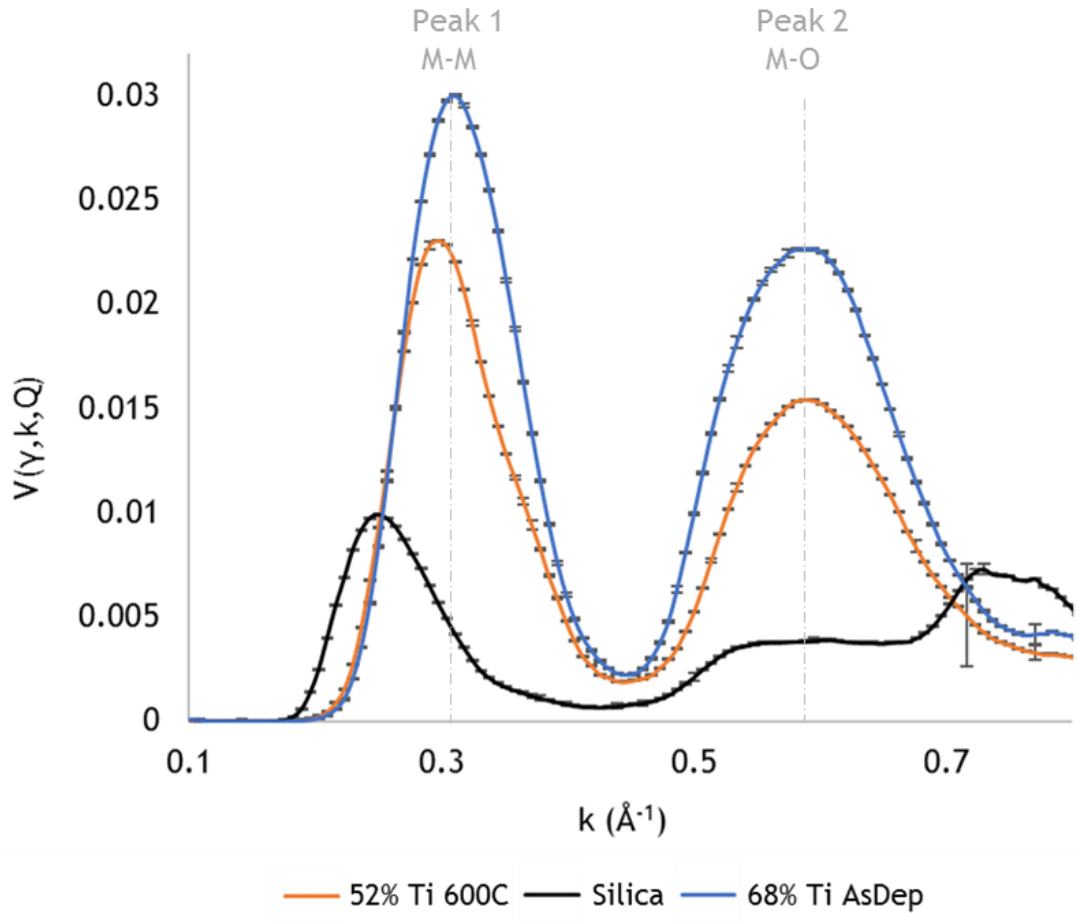

Figure 4-39: Normalised variance of 52% Ti:Ta_2O_5 annealed at 600°C, an as-deposited 68% Ti:Ta_2O_5 specimen, and IBS silica from the aLIGO multilayer coating, computed using the normalised cross-correlation coefficient method of FEM. Although only two peaks are apparent in the Ti/Ta data, the position of peak one and two from the previous sections are included for reference to their VDF images.

Finally, the lowest levels of heterogeneity are expected in silica, the archetypal mechanically stable amorphous structure. A reason for the homogeneity and stability of silica may be explained by the fulfilment of stoichiometry by its primary structural unit, the SiO_4 tetrahedra.

Tantala, on the other hand, has a more complicated electronic structure, and readily forms sub-oxides in which charge is presumably balanced over various length scales.

Titanium is less so due to its lower oxidation state, and may promote stability and homogeneity in tantala by constraining the volumes over which charge is balanced, in addition to its propensity to form greater ratios of edge-shared to corner-shared polyhedra.

The data are plotted again in Figure 4-39, using the alternative FEM method of variance computation by normalised cross-correlation coefficients; although the relative magnitudes are not the same, the order of maximum variances agree with the intensity based approach, confirming again the validity of the novel approach.

Furthermore, in addition to the insensitivity to noise, the method also appears insensitive to the non-linearities, indicated by the expected behaviour of the variance at high-*k*.

The 1st and 3rd peaks apparent in the previous datasets are not observed in Figure 4-39, and is thought to result from the greater averaging carried on the higher density of recorded reciprocal-space data.

The 68% Ti structure is rather symmetric in its M-M variance peak in comparison to the 52% Ti structure, which skews to lower in *k*, indicative of the longer Ta-Ta pair separations and the predominance of Ti-Ti correlations preferring closer separations in the shell structures(190) illustrated in Figure 3-32 of Chapter 3.

The broader peak of the M-O variance distribution in the 68% Ti could be attributed to the heterogeneity of an unrelaxed structure, however, its extension to lower in *k* be an indication of the porosity suggested in Chapter 3.

Furthermore, the skewing to lower in *k*, with respect to the more symmetric M-O variance distribution in the 52% Ti data, may also arise from phase separation in the structure that thus far appear ubiquitous in tantala based structures(190), .

Unpublished measurements of the 600°C annealed 52% sample has in fact been reported to have the second lowest recorded internal friction for a tantala-titania mix, and thus has the lowest levels of internal friction of all the samples studied in this thesis.

It may appear then, that measurements of structural variance at these length scales could be a good predictor of a coating preparation's internal friction.

The sample with the lowest structural variance is unsurprisingly that of silica, the data after $k \approx 0.7$ Å^{-1} are however artefacts unrelated to the structure.

The centre of the silica diffraction patterns was offset by 15 pixels compared to the 52% and 68% Ti diffraction data, which were much nearer the centre of the detector; the oval edge of the condenser aperture projection was included in the azimuthal averaging as an unintended consequence.

The silica data shows a flat M-O variance distribution, indicative of its homogeneous structure, whereas its M-M variance distribution, whilst very low in comparison to the others, indicates deviation from its ideal network glass structure, and is worthy of further investigation.

Some significant differences between silica and tantala alloys are obvious. In the sputtered scenario, silica would be formed using a single crystal silicon target, so based on prior discussion, any material sputtered from a single crystal should be more homogeneously deposited than one would from a polycrystalline target.

Then there is its lower oxidation state than that of tantalum, and the fact that stoichiometry is fulfilled by its primary structural unit, the SiO_4 tetrahedra; the directional constraints on this covalently bonded structure facilitate a solid 3D jigsaw-like network with rare opportunity for structural variation.

It would be interesting to ascertain the different length scales over which stoichiometry is attained in the different tantala preparations studied here, and what if any effect it has upon the mechanical stability of the structures.

It can be assumed that stoichiometry attained over different length scales will have a significant impact on the optical properties of the coatings, and therefore would be an interesting investigation to carry out for optical and internal friction correlations.

This could be done in EELS, for example, as a function of probe size, as is done in FEM to pinpoint the length scale of peak heterogeneity.

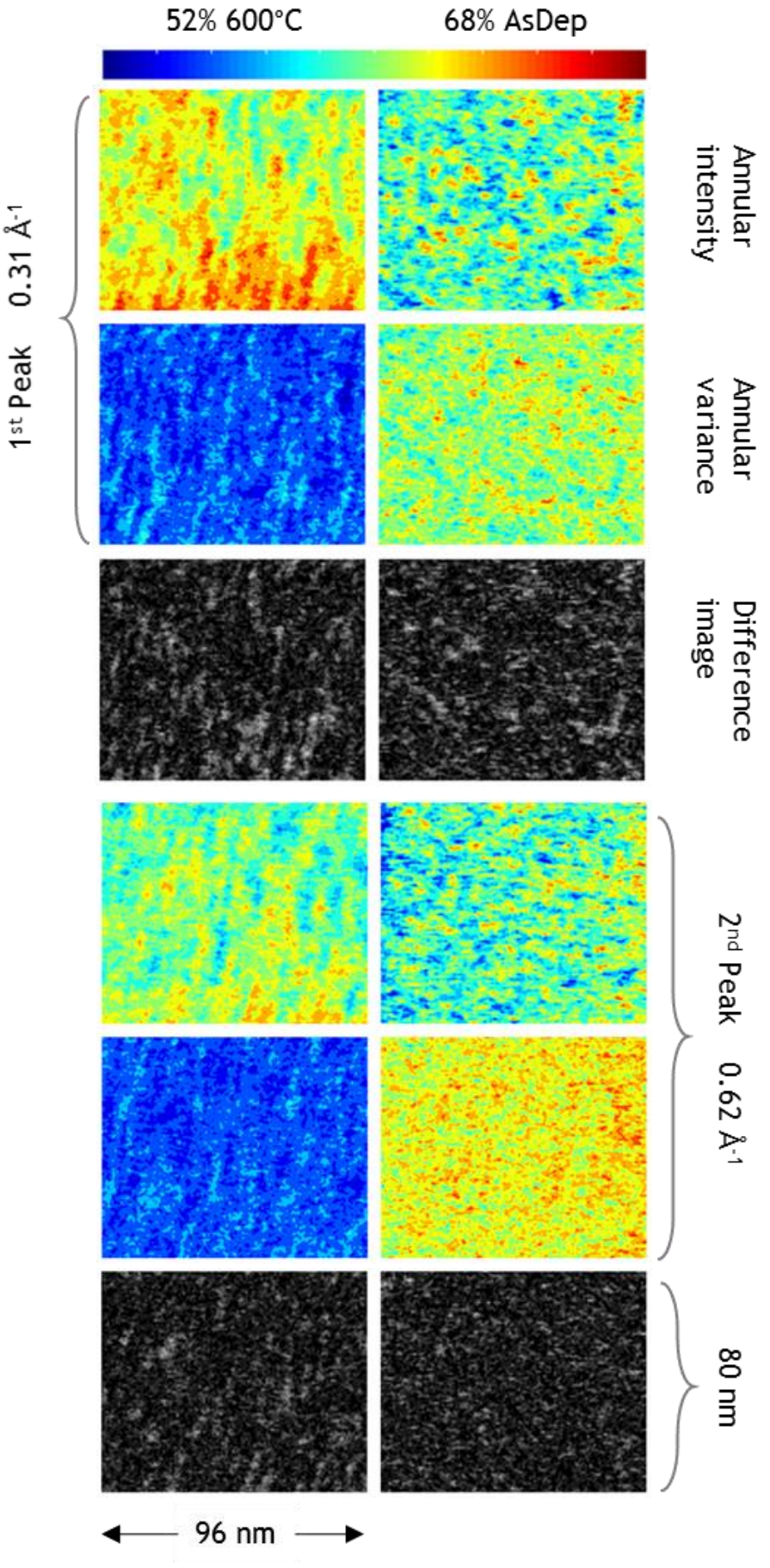

Figure 4-40 Virtual dark field annular intensity, annular variance and their difference images for the 600°C 52% Ti-cation, and as-deposited 68% Ti-cation doped a-Ta_2O_5.

The virtual real-space images for these structures are shown in Figure 4-40, without the 1st and 3rd peaks positions shown in the images of the previous sections, which is due to the lack of the signals in their variance curves and intensity profiles.

The images are a direct representation of the coating structural cross-sections, as in the previous virtual images, but are of higher definition due to the smaller 1.2 nm probe size, 1 nm scan-step size, better SNR, and greater reciprocal space resolution of the diffraction.

The normalisation of the images is equivalent as before, with the colour bar indicating the magnitude of the variable increasing from its lowest value (blue), to its highest (red). The silica data is not included in these images due to a different scan-step size used in the data collection.

The annular intensity images clearly illustrate the source of the variances plotted in Figure 4-39. The 52% Ti structure is the most homogeneous across all peak distributions. Furthermore, the 'grain boundary' picture of internal friction is useful here.

The 52% Ti data has a much smaller distribution of dissimilar regions compared to the 68% Ti data, with its similarly ordered regions forming large island like structures of low contrast with respect to their surroundings, and thus smaller dissimilar surface areas over which high frictional losses may occur.

The 68% Ti images, on the other hand, are high in contrast, indicative of many adjacent high and low-density regions. The small isolated regions of high and low order signify much larger surface areas over which energy can be lost to internal friction.

After the 1st peak image of the annular variance images in Figure 4-40, the 52% Ti structure appears strikingly more homogeneous in comparison to that of the 68% Ti structure, with very little contrast between regions; the comparable sized and number of large light and dark islands in 1st to 3rd peak images are highly indicative of phase separated structures.

The corresponding variance images of the 68% Ti specimen in Figure 4-40, appear equally as heterogeneous as its annular intensity peak images.

It seems plausible that a more stable, low internal friction structure can be achieved when tantalum acts as a 'network modifier' dopant into titania instead of the other way around.

Moreover, the complex electronic structure of tantala appears to engender an equally complex physical structure that can be somewhat constrained by titanium doping as indicated in the previous section; conversely, tantalum doping of titania may give flexibility to an otherwise rigid structure.

Whilst the variance data of Figure 4-39 were collected from slightly smaller volumes, and under a different experimental setup, they are still compared with the data from the previous sections in Figure 4-41.

The differences in the volumes probed are not considered to be of great significance, and the comparisons are valid as the correlations for each specimen are self-consistent; they are a measure of how homogeneous or heterogeneous the structural ordering is with respect to its own mean structure.

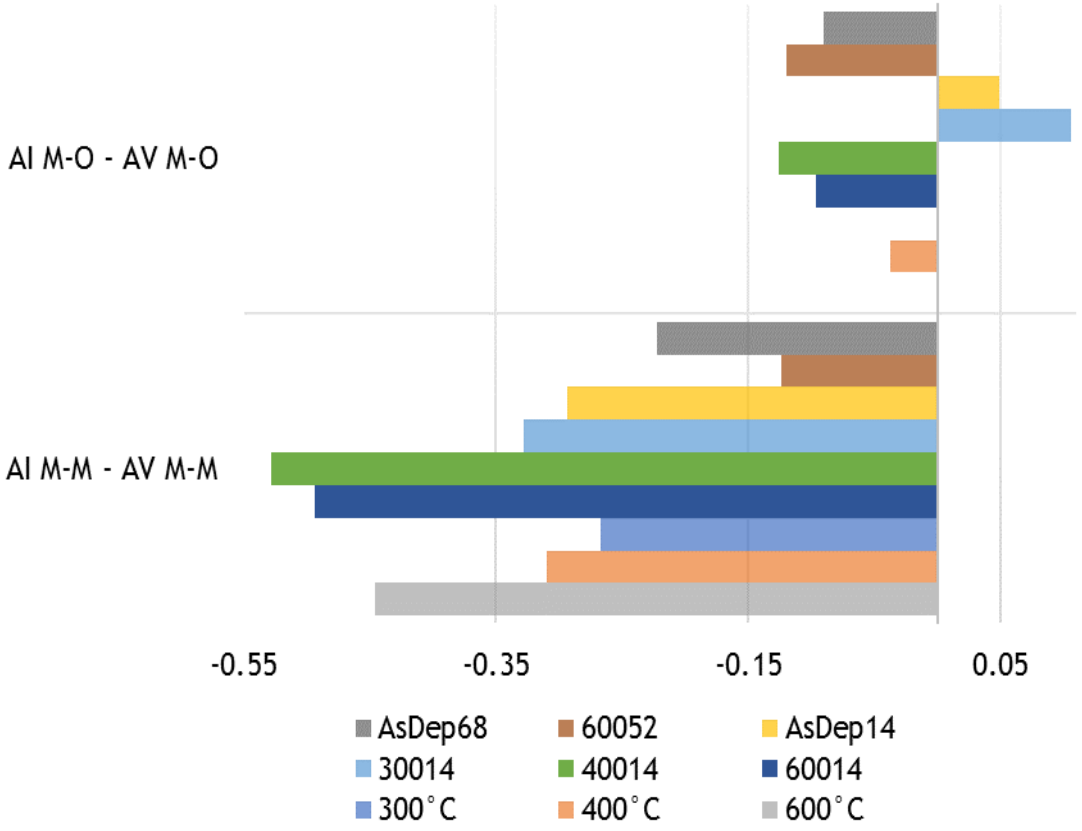

Figure 4-41 Correlations between the complementary VDF, annular intensity (AI) and annular variance (AV) images at the peak positions (P) indicated in Figure 4-40, corresponding to the main M-M and main M-O distributions. Data from the previous sections are included for comparison.

Immediately apparent from Figure 4-41 is the greater homogeneity, of both the 52% and 68% Ti-doped samples in their M-M distribution, compared to the other tantala preparations, and would appear to be the result of their predominantly titanium cation constitution.

With the assumption of titanium preferring occupation at the lower-*r* shell position in Ti-Ta mixtures (illustrated in Figure 3-32 of Chapter 3), whilst forming almost equal proportions of edge and corner-shared polyhedra, it would suggest than the significant homogeneity of the 52% Ti structure M-M distribution is due primarily to the almost exclusive occupation of titanium and tantalum occupation of the lower and higher positions of the M-M shell respectively.

The 68% Ti specimen necessarily has more structural variation due to unequal fraction of the aliovalent dopant

The 4th peak correlations are the exception, and are possibly of less relevance due to peak splitting shown in the previous sections.

Whilst the magnitudes of the 52% and 68% Ti variance peaks appear reasonable, further investigation is required to ascertain the reason for the absent peaks clearly visibly in the previous sections.

However, this section was intended to be more of a testbed for the techniques, with the main body of the encompassed in the previous two sections.

4.5 Discussion & Summary

The computation of structural variance, by the novel use of normalised cross-correlation coefficients developed during this PhD, appears to be a valid and robust alternative to the classical formulation of FEM(262). The results agree with the intensity based approach in the order of the variance maxima for the different samples studied, across all spatial frequencies in the Medipix collected data, and at low spatial frequencies in the optically coupled setup, which was dominated by noise at high-*k*.

A weakness of the FEM method, however, is that it does not differentiate between deviations from a homogeneously disordered structure, and deviations from a homogeneously ordered structure; the FEM signal solely indicates relative levels of heterogeneity.

Virtual dark-field image reconstruction of the data enables visualisation of the real-space distribution of the structural ordering responsible for the FEM signal, and may also help to overcome the longstanding problem of inverting the FEM data into structural models; extraction of pertinent diffraction in offline analyses is made easy by the indexed nature of the scanned diffraction datasets. The VDF imaging technique developed by Edgar Rauch and Muriel Veron is among the most versatile electron diffraction techniques of recent decades.

In this work, annular intensity images indicative of the structural ordering within the structures studied were generated offline through the flexibility in manipulation of any desired regions of the scanned diffraction data. Combining the real and reciprocal space imaging inspired by the VDF technique, it has been applied in novel ways to amorphous materials for the first time in this work. Furthermore, complementary annular variance images were generated for the first time, providing further novel insight into the nature of the amorphous structures studied, in terms of bond disorder, and the relative levels of heterogeneous ordering within regions of the partial structure reconstructions.

As can be imagined, any combination of offline mathematical manipulation may be carried out upon the 4D dataset. Correlations were calculated between the various images constructed, representative of specific aspects of the material structures, enabling visualisation and interpretation of amorphous structures in detail never seen before.

It is clear, however, that strict control over experimental parameters such as specimen thickness, probe size, current density, and linearity in $I(\boldsymbol{k})$ are essential for a quantitative analysis to be performed. Whilst significant results were obtained, the work constitutes a creative departure from formal approaches to structure investigations of amorphous materials, and much work remains to capitalise on the benefits offered by the methods.

For the un-doped Ta_2O_5 samples, a clear effect of thermal annealing was observed in the 600°C data; the normalised variance indicated a large and statistically significant increase in the heterogeneity of both the metal-metal, and the metal-oxygen nearest-neighbour distributions, with respect to the samples annealed at 300 and 400°C, and was due to increased structural ordering.

Furthermore, it has been demonstrated that the tantala structures investigated can be better described by a heterogeneous phase separated model in contrast to the continuous random network model of covalent glasses. Confirmed by the correlation analysis performed on the complementary intensity/variance images and the peak to peak image comparisons.

The relative extension of the 600°C variance peak to lower in *k*, correlated with the ePDF results of the same sample demonstrated in Chapter 3. The M-M distribution peak extended to higher in *r*, adding weight to those highly uncertain observations, and strengthened the initial assertion of its relative tensile stress characteristic. The tensile stress characteristic appears convincing, and suggests a modification to the long-standing theory of oxygen bond-flipping as the principal culprit in the generation of thermal noise in aLIGO.

In amorphous Ta_2O_5 under tensile stress, the Ta-O-Ta inter-polyhedral bonds between corner-shared polyhedra, extending towards their maximum 180° angle, shift from bending mode vibrations to increasingly stretching vibrational modes, which have shown to be ~ 2 orders of magnitude higher in frequency, and thus deposit thermal energy into the system at a much higher rate.

Although these vibrations are in the THz range, and aLIGO sensitivity is limited by thermal noise in the 100Hz region, the increased rate of energy transfer may impact larger ordered structures, such as those in the VDF images of this chapter, which very well may result in the low frequency noise limiting sensitivity in aLIGO.

The virtual dark-field imaging of the data elucidated the regions likely responsible for tensile stress immediately, in rich, visual context. The signals responsible for the increased variance signal of the 600°C data were spatially resolved in striking contrast to the average structure, convincingly explaining the tensile stress characteristic that appeared to increase with increasing heat-treatment temperatures.

It is believed that the highest intensity regions of the annular intensity images, those of highest relative structural ordering, through their densification pull upon the structure isotopically, inducing bond length extension through an equilibratory response, and doing so maximally where there is the greatest heterogeneity in the connectivity and contrast between similarly ordered regions shown in the images.

This is more so indicated when those trends are mirrored in the complementary angular variance images, where which the highest intensity regions reflect the highest relative levels of bond disorder.

The appearance of phase separated heterogeneity is apparent throughout, favouring of the crystallite theory of glass, in opposition to the continuous random network theory for these structures. Moreover, a complex energy landscape can be visualised through the reconstructed virtual images, in which a broad spectrum of Brownian thermal noise may arise; the nature of its frequency dependence is alluded to by the size, shape, density and connectivity of the sub-structures.

It is suggested that the observation of increased ordering, in conjunction with increased bond heterogeneity, increases the number and energetics of defects forming double well potentials at boundaries between high and low ordered regions, with a relatively low energy barrier between two metastable states, and scales with the number of boundaries. This is the mechanism presumed a precursor to the bond stretching proposed to result in the highest regions of tensile stress.

In the thermal annealing series of the 14% Ti-cation doped samples, similarly substantial increases in heterogeneous ordering was not observed to the same degree as in un-doped tantala. The M-O distribution peaked in variance magnitude equally for all samples except in the 300°C annealed structure, which did so significantly lower, corroborating this work and complementary studies that ascertained the addition of titanium homogenises the M-O distribution(190,208).

Longer range correlations at $k \approx 0.4$ Å^{-1}, were significantly different in their levels of variance with respect to the un-doped tantala structures; however, they were visible in the reduced intensity profiles of all structures investigated in the optically coupled setup, and are believed representative of the lower-*r* shell M-M correlations in the centre of edge-shared polyhedra.

In fact, the propensity of titanium in tantala to form equally as many edge-shared as corner-shared polyhedra may be the poignant factor in its reported reduction of internal friction. Un-doped tantala appears to increase its character of corner-shared polyhedra with respect to edge-shared polyhedra when thermally annealed, whereas the modest substitution of 14% titanium appears to increase the edge-shared polyhedral ratio with increased temperature thermal annealing.

Above the 400°C annealing temperature heterogeneity appeared to increase significantly, consistent with the notion discussed in Chapter 3 that activation energies were reached within this range that facilitated significant transformation of the structure.

Prior assertions that titanium doping attenuates significant structural reordering during relaxation, requiring greater thermal energy than their un-doped counterparts for an appreciable change in structure appeared to be confirmed. However, even with the increased heterogeneous ordering of the Ti-doped samples with increased annealing temperatures, the connectivity of the structures appeared to remain far superior than in the un-doped structures.

The longest-range correlations accessible, at $k \approx 0.22$ Å^{-1}, correlated with the position of the signature for 3D structural-crosslinking illustrated in Chapter 3, and were shown to be significant in the 400 and 300°C un-doped and 14% Ti-doped 300°C annealed specimens, and are likely to be highly significant regarding the mechanical stability of the structures.

The higher annealing temperature of 600°C appeared to prevent ordering in this region with preference for increased ordering of the main M-M distribution. Annealing the Ti-doped structures at temperatures greater than 300°C also appeared to attenuate this ordering.

The remainder of the FEM data, recorded on the Medipix detector, were not directly comparable with the previous results, as in addition to the different experimental setup, the structures were sampled with a probe 1.2 nm in diameter in contrast to the 2 nm probe used for the optically coupled setup.

However, parallels can be drawn; in sampling smaller volumes, a maximum in the structural variance is expected to coincide with the characteristic length scale of the MRO(263), and although different probe sizes have not been used for this determination, it was however determined through the PDF work in Chapter 3 that the extent of SRO consistently diminishes at ~4 Å.

This sets the lower limit for the MRO, with the upper limit residing in an unknown range above 2 nm, where the variance curves will flatten out to reveal the lower structural bounds of their homogeneity.

It was presumed that the peak heterogeneity of the structures probed at 2 nm would be found at shorter length scales, and indeed also for the structures probed at 1.2 nm; this is inferred from the angular variance images at both length scales probed, in which regions of equal intensity, ~6 nm in extent appear, that had not been visible through conventional TEM imaging or diffraction.

The structural variance computed across all samples were therefore thought to be roughly comparable, in consideration of the small difference in length scales probed in by two setups, and by considering the overall range of the parameter space left unexplored.

The highest degree of structural variance across all spatial frequencies in the Medipix setup was the 68% Ti as-deposited structure, by a large margin, followed by the 52% Ti structure annealed at 600°C, and finally the silica sample which was exceptionally low in comparison to all the structures investigated. The trends were corroborated by the intensity based approach.

The inclusion of silica in the study was for an indication of how tantala and tantala/titania mixtures compare in structural heterogeneity to this archetypal mechanically stable amorphous metal-oxide, which is due to its highly directional covalent bonding.

Whilst the Gaussian filter used to transform the tantala and tantala/titania diffraction patterns was chosen specifically in relation to those structures, most important for meaningful comparison of the data is consistency in the applied filter.

The choice of filter in fact does not need to be correlated with a specific structure; the choice of an effectual filter can be better ascertained by its performance in the simultaneous detection and separation of coherent diffraction events, from incoherent registered intensities, through the normalised cross-correlation.

The larger magnitude variance observed in the 68% Ti structure was expected in comparison to the 52% Ti structure, as it hadn't undergone a structural relaxation process, and also by the inference of a more mechanically stable structure that can be obtained with roughly equal concentrations of aliovalent transition-metal cations(225).

However, it was considerably more homogeneous than any of the other comparative structures studied, and likely stemmed from the predominant Ti composition which has a lower oxidation state than tantalum, and thus constrains the complexity of its compositional variety.

Incidentally, the 52% Ti structure annealed at 600°C was reported to have the lowest ever recorded mechanical loss for a coating with such high tantalum content, and conveniently had a SiN keying layer in lieu of silica, which meant its low temperature loss result was likely secure and uncorrupted by chemistry at the interface. This result, unfortunately, was not published, and is presumably due to poor optical performance.

The virtual dark-field images for both these structures told the same story as the normalised variance curves and more. The 52% Ti structure had very low variation in ordering for both the M-M and M-O distributions in its annular intensity images, however, the ordering did appear somewhat heterogeneously distributed in long connected structures, and is considered a reflection of well-connected phase separated Ti and Ta structures.

The same trend was apparent in its annular variance images, although the inferred levels of bond disorder were very low and homogeneous. The 68% Ti images, on the other hand displayed a completely heterogeneous distribution of structural ordering and in their relative magnitudes, also in terms of its bond disorder, as may be expected in an as-deposited structure.

Although a great deal of work is required to ascertain the relation between the various representations of the FEM data and internal friction within the structures, and thus the accuracy of the proposed mechanism, through proper correlative studies with loss measurements, much progress has been made in the investigation of these structures at length scales until now unexplored.

The VDF image representation of the FEM data adds new dimension to its analysis, literally and figuratively, and makes a significant contribution to the field through a novel extension of the technique.

5. General conclusions & future directions

The recent observation of gravitational waves by aLIGO(1) has borne a new astronomy, that in its infancy, is growing rapidly with a global network of interferometric detectors soon to join the search, and increase the accuracy of observations for follow-up by classical EM astronomical methods. Furthermore, experimentalists are working hard in the development of detector upgrades to improve detector sensitivity, and the mitigation of noise sources, expanding the cosmological reach of violent astrophysical events.

One of the principal routes to improved detector sensitivity is through the mitigation of thermal noise in the optics of aLIGO, which can be thought of fluctuations in phase coherence of the recombined laser beam at the interferometer photo-detector, caused by atomic scale displacements of the mirror surfaces. Brownian thermal noise arising from within the amorphous titania/tantala high-index mirror layers of the end test masses is one of the principal contributions(33).

Titania doping of tantala reduced its noise contribution by up to 40% of that in previous generation detectors, and post-deposition thermal annealing had significant effect on both thermal noise and optical absorption. Atomic structure investigation of these materials, however, were inconclusive in their attempts to ascertain significant structural changes resulting from doping and annealing that could explain the significant differences observed in the mechanical dissipation of their structures.

Whilst Brownian thermal noise is due to the inescapable motion of atoms at finite temperature, in tantala, it can in approximation be thought to predominantly arise from oxygen transitions in a stationary tantalum matrix (due to their extreme mass difference), these transitions are however generally inaccessible by experiment.

Titanium, much closer in mass to oxygen, and hence having non-negligible movement with respect to tantalum, may possibly reduce noise by inhibiting irreversible transitions of oxygen. More probable is its topological influence; titanium reduces the number of corner-shared polyhedra in favour of edge-shared polyhedra, thus reducing high frequency stretching character of Ta-O-Ta bonds.

In any case, a proxy measurement of macroscopically averaged internal friction, related to thermal noise through the fluctuation-dissipation theorem, is generally performed instead using mechanical spectroscopic methods, in which a mirror coated silicon cantilever is excited at some resonant frequency and its stress/strain amplitude is measured during ringdown as a function of time.

The mechanical loss measured for a coating, after substrate signal subtraction, is inferred to have a good thermal noise characteristic by its ability to store energy, i.e. by a long ringdown with a slow decay of amplitude; it is analogous to the sustained resonating note one hears when running a finger continuously over the circumference of a high-quality crystal wine glass.

How appropriate the cantilever ringdown method is as a proxy measurement for Brownian thermal noise is however debatable. The initial goal of this investigation was to determine significant changes in the atomic structures of mirror coatings due to doping and thermal annealing, using advances in electron diffraction hardware and techniques, and relate any observed differences to their measured mechanical losses.

This was however unfeasible during the investigation due to the problems discovered with the loss measurements as discussed at the end of Chapter 3. The electron diffraction investigations were far from ideal themselves, regardless of which, statistically significant changes of the structures were indeed discovered because of both thermal annealing and titanium doping, and whilst only qualitative arguments are currently presented, tentative mechanisms relating atomic structure to thermal noise have been proposed.

The first line of investigation was the pair distribution function analysis of Chapter 3. This directly followed on from previous electron diffraction PDF work, and was envisaged to enable much higher resolution studies of the structures using a new state of the art (S)TEM and detector.

It provided the ability to collect data to high-q, effectively diffraction collected at much higher scattering angles, with a much higher resolution sampling of reciprocal space that translates directly into higher resolution in the real space PDFs with finer discrimination of structural features.

This was performed in conjunction with high dynamic range diffraction imaging that improved the counting statistics at the higher scattering range. However, the ability to effectively utilise these advances in technique were significantly hampered by distortions and non-linearities in the diffraction patterns, making improvements upon previous work minimal without going to great lengths to extract useful data from the corrupted patterns.

The problem is considered to result from a slight misalignment of the microscope. A work-around was eventually implemented and enabled highly detailed PDFs to be generated with immense help from a newly released ePDF software, 'SUePDF'(264). Remaining uncertainties meant the statistical significance prevented conclusive statements to be made regarding the observed changes, however, some structural features appeared secure and corroborate with complementary studies.

Increased temperature thermal annealing appeared to affect an increased tensile stress characteristic, with significant changes in number density and stoichiometry. There also appeared to be indication of exceeding an ideal annealing temperature, in that stoichiometry got worse, decreasing at $T > 300°C$ with a commensurate reduction in number density and tensile stress characteristic.

The 14% Ti-cation doping seemed to have an attenuating effect upon oxygen diffusion, and a higher annealing temperature of 400°C was required to improve stoichiometry, but going higher in T again resulted in poorer quality films in terms of stoichiometry and number density.

Qualitative statements upon ideal stoichiometry were however predicated on the assumption of sole composition by TiO_2/Ta_2O_5 structures that is thought to be unlikely.

Higher Ti content films hinted at possible porosity in the as-deposited state, improved by thermal annealing. Signs of Ta-O-Ta primary structural units were also found as proposed in a complementary X-ray PDF study, that also predicted signatures of 3D-crosslinking of structural units not visible in their data, but signs of which were found in all the ePDFs in this work.

The main insights gained through the ePDFs were that thermal annealing temperatures have significantly misunderstood effects upon the structure; they are performed to relax the structures, improve stoichiometry and optical performance, but after a certain temperature benefits seem to be lost with degradation of stoichiometry, number density and increasing characteristics of tensile stress.

The technique may, with greater resolution, and greater control over experimental variables, enable quantification of changes that correlate with observed dissipation measurements, but then again, the inherent averaging of the technique may mask the poignant structural features responsible for large variation in the mechanical properties of the structures.

The PDFs do however clearly highlight an abrupt limit of the short-range order in the structures, at ~4 nm for all the samples, and gives an indication of the lower limit of their medium-range order.

The medium-range order was investigated using fluctuation electron microscopy in Chapter4; the length scale of the MRO studied is dictated by the size of electron probe used, and is essentially a dense sampling of the heterogeneity in the short-range order over that MRO length scale.

Initial experimental attempts were hampered with the same problems of non-linearity and distortion that affected the PDF work, and further experiments were put on hold until the problem was addressed. In the meanwhile, an opportunity arose to collect FEM scanning diffraction datasets in an optically coupled setup for a selection of samples at the University of Grenoble, sampled with a 2 nm probe.

Initially unworkable data due to poor SNR, resulted in the development of an alternative and unorthodox FEM method. Raw intensity values were rendered irrelevant through a normalised cross-correlation of the data with a Gaussian filter, that effectively filtered out noise and artefacts whilst retaining regions where coherent diffraction occurred.

The normalised cross-correlation coefficients replaced the intensity values in the computation of the structural variance, and proved to be a robust method with low uncertainties in the obtained results.

Good agreement was found between the new method and the classic intensity based method at low-*k*, its most statistically significant region, which was otherwise dominated by noise. The results also gave the most unambiguous evidence to date for structural change by increased temperature thermal annealing.

The 300 and 400°C annealed structures displayed almost equal levels of heterogeneity in their metal-metal and metal-oxygen distributions, whilst the 600°C annealed structure was significantly higher in both.

Furthermore, signs of tensile stress were apparent in the 600°C data which gave weight to the same signature found in its PDF data, as was the assertion of this higher annealing temperature affecting a more transformative change than relaxative corroborated.

The 14% Ti doped structures essentially followed the same trend, but with more modest changes, also supportive of assertions made from the PDF data that Ti has an attenuating affect upon significant structural changes by thermal annealing, likely due to its high affinity for oxygen over tantalum and simpler structural variety, in conjunction with its greater propensity for the formation of edge-shared polyhedra over un-doped tantala.

Possibly the most important aspect of the work has been adoption of the virtual dark-field imaging technique for a new representation and visualisation of the FEM scanned diffraction datasets.

Reconstructing the FEM data into annular integrated intensity and annular variance images, spatially resolves the features responsible for the FEM signal in what can be thought of as images of structural order distribution and images of bond disorder distribution.

The virtual images relay the same information as the standard FEM representation, but are much richer in content. Some structures whilst displaying some of the lowest variance in the standard FEM representation, show some the highest order in their annular intensity images, but they were homogeneously so, highlighting a shortcoming of the standard FEM method that makes no such differentiation.

Other specimens had shown elevated levels of variance in their 1D-functional representations with low level homogeneous order in their annular intensity images, whereas their higher variance is clearly relayed by heterogeneity in bond disorder, inferred from their angular variance images. Some require a combination of both images for interpretation of the standard variance.

Correlation analyses were conducted between the VDF annular intensity images and their complementary annular variance images, highlighting the increasing structural disorder with increasing thermal annealing temperatures. These correlations have also shown that 14% Ti-cation substitution indeed attenuates the relative levels of heterogeneous re-ordering found in the un-doped specimens when annealed at the same temperatures.

Correlation analyses between specific peak images were also conducted, highlighting the relative levels of structural ordering related to those peaks, which varied greatly with increasing annealing temperatures.

The VDF images and their correlation analysis demonstrate that tantala and Ti-doped tantala are better described by a heterogeneous phase separated model than the continuous random network model for covalent solids.

The extension of the FEM technique through VDF imaging may present a valuable step forward in the interpretation of structures utilising the wealth of hidden information within the FEM dataset.

The final data was collected on a Medipix direct electron counting detector, and was imagined to be more of a technological showcase, as it was in initial stages of implementation.

The data however was not free of the problems encountered in the PDF work, distortions were not as apparent, although non-linearity was significant in much of the data. It did however handle the intensity based approach of FEM much better than the optically coupled setup.

The new FEM method of variance calculation with normalised cross-correlation coefficients, on the other hand, overcame the sub-optimal conditions, cutting through noise and artefacts, producing trusted curves that agreed with the relative order in the magnitudes of the variance obtained by the formal approach.

The samples studied in this experiment were probed with a 1.2 nm beam, and consisted of a 52% Ti doped sample annealed at 600C, a 68% Ti as-deposited sample and an amorphous silica sample taken from the aLIGO multilayer mirror coating.

These coatings, despite the smaller volumes examined, all displayed lower variance than the previous structures. This is expected for the silica is was included for the others comparison to the archetypical stable amorphous structure.

However, the reason behind silicas low structural heterogeneity is believed to also partly explain the 52% and 68% Ti low levels in comparison to the other structures. The range of silica stoichiometry and its tetrahedral form constrains the variety of structures it can form; likewise, with the high Ti concentration samples, being lower in oxidation number than tantalum, it is constrained by its oxidation state in the complexity of structures it can form in comparison to tantalum oxide.

The VDF images for these structures share information as relayed before. A stable structure is inferred by low structural order and low bond disorder in their image representations. As is a structure high in order, if it is homogeneously distributed and connected with a low gradient of ordering between different regions.

A more consistent indicator of a relatively unstable structure may be one in which its angular variance images are highly heterogeneous in the size and contrast of connected regions.

Furthermore, a complex energy landscape may be visualised through the reconstructed images, in which a broad spectrum of Brownian thermal noise may arise, with clues given towards the nature of its frequency dependence, by the size, shape, density and connectivity of the distributed sub-structures.

In summary, the results presented herein, have unambiguously shown significant differences in the structures of these materials that have until now proved elusive.

Increased temperature thermal annealing relaxes and homogenises a structure through ordering up to a certain temperature, over which it becomes more heterogeneously transformative in its reordering, segregating substructures, likely through densification and stress redistribution.

Titanium doping homogenises a tantalum structure, likely through charge balancing of defect structures and increasing the connectivity of the structures through increased populations of edge-shared polyhedra; it follows the same trends with increased temperature thermal annealing as un-doped tantala, but apparently requires higher temperatures for equivalent heterogeneous ordering, a likely result of it greater affinity for oxygen, and denser networked structure of edge-shared polyhedra.

Furthermore, the suggestion is reiterated that the observation of increased ordering, similarly to the mechanical loss mechanism proposed for amorphous silica, in conjunction with the inference of increased bond heterogeneity, affects the number and energetics of defects forming double well potentials at boundaries between high and low ordered regions, with a relatively low energy barrier between two metastable states, scaling with the number of boundaries, and possibly free volume.

Further suggested is the greater losses suggested by an increased tensile stress characteristic, in which Ta-O-Ta bond angles approach their maximum 180° angle and develop stretching mode vibration character at the expense of bending modes. Stretching modes are almost two orders of magnitude higher in frequency than bending modes(208), and can thus dump energy into the system at a much greater rate.

If these assertions prove accurate, the data analysis methods shown can be used to enable faster and cheaper prototyping of new coating preparations for the LIGO collaboration, through a thorough exploration of the unwieldy parameter space of the IBS deposition process.

It is believed that the heterogeneities of these structures are to a large degree locked in at the deposition stage, through a heterogeneous spectrum of deposited sputter products. By using an iterative, high throughput, high volume method, as many different coating preparations as is practical should be deposited onto a single crystal substrate (to enable in-situ *q*-calibration), with a barrier layer between them, and thin enough for rapid production. Thereafter, the sample should be prepared for scanning diffraction study using FIB, and great care taken to ensure the cross sections are equal in dimension.

Using measures of the normalised variance, obtained with a variety of probe sizes starting at ~0.5 Å (determined through the PDF work to lay just above the upper limit of SRO), in conjunction with VDF image representations, the ideal sputtering parameters may be found that result in the most homogeneous and isotropic of structures in the as-deposited state. However, it may be simpler to investigate lower oxidation state materials that do not form such disparately complex structures.

In any case, steps to be taken in future efforts of quantitative analysis will involve a detailed study of the individual diffraction patterns from the current datasets that form regions of high and low order, and their boundaries in the VDF annular intensity images. Detailed study shall also be made of the differences in individual diffraction patterns responsible for the apparent heterogeneities in bond order observed in the annular variance images.

It is imagined that principal components will be found and quantified, enabling a more detailed correlative analysis with dissipation measurements when they are available.

Appendix A

Kirkland fitting parameters

In Chapter 2, Section 2.4, the Kirkland parameterised atomic scattering factors are referenced, $f_{Kirkland}$,

$$f_{Kirkland} = \sum_{i=1}^{N_L} \frac{a_i}{q^2 + b_i} + \sum_{i=1}^{N_G} c_i exp(-d_i q^2) \qquad (2\text{-}26)$$

where a_i, b_i, c_i, and d_i are the Kirkland fitting parameters. 12 fitting parameters are required, (a_1, a_2, a_3, b_1, b_2, b_3, c_1, c_2, c_3, d_1, d_2, d_3), and are given for the elements in the coatings studied (tantalum, titanium and oxygen), using the pair distribution function analysis of Chapter 3. The units for a_i, b_i, c_i, and d_i are, $Å^{-1}$, $Å^{-2}$, Å and $Å^2$, respectively, and are listed below in Table A.1

Element	Kirkland fitting parameters		
Tantalum	$a_1 = 0.747198223$	$a_2 = 3.22045387$	$a_3 = 2.93947802$
	$b_1 = 0.102352889$	$b_2 = 13.8766179$	$b_3 = 0.739861702$
	$c_1 = 0.0229176351$	$c_2 = 0.335663858$	$c_3 = 1.14728503$
	$d_1 = 0.035495002$	$d_2 = 0.205499378$	$d_3 = 0.135849981$
Titanium	$a_1 = 0.737291729$	$a_2 = 0.996300042$	$a_3 = 0.355417565$
	$b_1 = 8.32612403$	$b_2 = 0.496982599$	$b_3 = 0.072859585$
	$c_1 = 0.0163350335$	$c_2 = 0.360199179$	$c_3 = 1.42171303$
	$d_1 = 0.0731735660$	$d_2 = 0.957232308$	$d_3 = 15.8512114$
Oxygen	$a_1 = 0.368590229$	$a_2 = 0.13289645$	$a_3 = 2.77101233$
	$b_1 = 0.367542561$	$b_2 = 19.395483$	$b_3 = 0.367539567$
	$c_1 = 0.083909305$	$c_2 = 0.181631127$	$c_3 = 0.001052898$
	$d_1 = 0.758355003$	$d_2 = 2.04360334$	$d_3 = 0.031200946$

Appendix B

Matlab code referenced in Chapter 2, for computing the normalized structural variances and virtual dark-field images for the samples investigated in this thesis.

```
% Medipix data
% Make sure the current folder is correct
clear all
close all
% Read in diffraction patterns
data = h5read('default1.hdf5','/fpd_expt/fpd_data/data');
% Get dimensions of dataset
dims = size(data);
% 5D to 4D, remove singleton dimension
data = squeeze(data);
% dimensions of the 4D data stack
% 1st = ix, 2nd = iy, 3rd = rows, 4th = columns
dims = size(data);
% number of diffraction patterns
nimg = dims(3)*dims(4);
% Generate virtual bright-field image
BF = sum(data,1); BF = squeeze(BF);
BF = sum(BF,1); BF = squeeze(BF);
% Select coating data and reduce size of dataset
% Generate new BF image & get dimensions
r1 = input('Input 1st row: ');
r2=input('Input final row: ');
c1 = input('Input 1st column: ');
c2=input('Input final column: ');
data2 = data(:,:,r1:r2,c1:c2);
BF2 = sum(data2,1); BF2 = squeeze(BF2);
BF2 = sum(BF2,1); BF2 = squeeze(BF2);
dims = size(data2);
nimg = dims(3)*dims(4);
% reshape into 3D datacube
data3 = reshape(data2,256,256,[]);
```

```
% Test centre positions
% Get mean diffraction pattern and subtract 1st pattern
mdp = mean(data3,3);
TC = mdp - data3(:,:,1);
% If asymmetric intensity remains around direct beam
% diameter (12 px) after subtraction, find centres using
% centre finding and restacking script, otherwise
% set cx, cy to centre of mean diffraction pattern
% Patterns are centre of a square matrix
cx = input('Input x centre coordinate: ');
cy = input('Input y centre coordinate: ');
% Get azimuthal average using script
rmdp = radial (mdp);
% Free up memory
clear data
%%%%%%%%%%%%%%%%%%%%%%%%%%%%%%%%%%%%%%%%%%%%%%%%%%%%
% Formal intensity based variance calculations
%%%%%%%%%%%%%%%%%%%%%%%%%%%%%%%%%%%%%%%%%%%%%%%%%%%%

% Generate 5000 random numbers to get 5000 random DPs
% from the dataset and split into 100 subsets of 500
p = randperm(5000);
p = reshape(p,500,[]);
% Pre-allocate memory
A = zeros(size(data3,1),size(data3,2),size(p,1),size(p,2));
% populate diffraction pattern subsets
for ii = 1:size(p,2);
    A(:,:,:,ii) = data4(:,:,p(:,ii));
end
% Dead pixel data, set to NaN
A(A==0) = nan;
% Get mean DP arrays
M = mean(A,3,'omitnan');
M = squeeze(M);
% Get variance arrays, computed per
```

```
% pixel through the stacks
V = var(A,1,3,'omitnan');
V = squeeze(V);
% Normalise the variance arrays
V = bsxfun(@rdivide, V, M.^2);
% azimuthally average the 2D variance
Vp = zeros((size(V,1)/2)-1,size(V,3));
for ii = 1:size(V,3);
    Vp(:,ii) = radial(V(:,:,ii));
end
% plot results with error bars
stdVp = std(Vp,1,3,'omitnan');
meanV = mean(Vp,3,'omitnan');
figure
Var14600=errorbar(meanV,stdVp);
hold on
 %%%%%%%%%%%%%%%%%%%%%%%%%%%%%%%%%%%%%%%%%%%%
%% Prep for cross correlation matrices
%%%%%%%%%%%%%%%%%%%%%%%%%%%%%%%%%%%%%%%%%%%%

% 14x14 pixel Gaussian filter with 4 pixel std dev
GF = fspecial('Gaussian', 14, 4);
% correct for
cx = ceil((size(data4,1)+size(GF,1))/2);
cy = cx;
ix = (size(data4,1)+size(GF,1))-1;
iy = ix;
XcorPN = zeros(ix,iy,size(data4,3));
for ii = 1:size(data4,3);
CC = normxcorr2(GF,data4(:,:,ii));
XcorPN(:,:,ii) = CC;
end
% Get azimuthal average
mXcorPN = mean(XcorPN,3);
rmXcorPN = radial(mXcorPN);
```

```
%%%%%%%%%%%%%%%%%%%%%%%%%%%%%%
% NXcorr2 Variance calculation
%%%%%%%%%%%%%%%%%%%%%%%%%%%%%%

% Only use positive coefficients in calculations
XcorP = XcorPN;
XcorP(XcorP<0) = 0;
A = zeros(size(data4,1),size(data4,2),size(p,1),size(p,2));
for ii = 1:size(p,2);
    xA(:,:,:,ii) = XcorP(:,:,p(:,ii));
end
% Variance of pre-normalised data
xV = var(xA,1,3);
xV = squeeze(xV);
% Get variance profiles
xVp = zeros(floor(size(xV,1)/2),size(xV,3));
for ii = 1:size(V,3);
    xVp(:,ii) = radial(xV(:,:,ii));
end
% Plot with error bars
xstdVp = std(xVp,1,2);
xmeanV=mean(xVp,2);
figure
xVar=errorbar(xmeanV,xstdVp);
hold on
save('VarianceCalcs.mat', '-v7.3');
 %%%%%%%%%%%%%%%%%%%%%%%%%%%%%%
% VDF images azimuthal variance
%%%%%%%%%%%%%%%%%%%%%%%%%%%%%%

clear all
load('VarianceCalcs.mat', 'data2', 'BF2')
dims = size(data2);
nimg = dims(3)*dims(4);
```

```
GF = fspecial('Gaussian', 14, 4);
cx = ceil((size(data2,1)+size(GF,1))/2);
cy = cx;
ix = (size(data2,1)+size(GF,1))-1;
iy = ix;
data2 = reshape(data2,dims(1),dims(2),nimg);
XcorPN = zeros(ix,iy,nimg);
% Using positive & negative coefficients for images
for ii = 1:nimg;
CC = normxcorr2(GF,data2(:,:,ii));
XcorPN(:,:,ii) = CC;
end
% Use script to convert DPs from polar to cartesian coords
% Compute variance along rows equal in k
nrad = 134;
ntheta = 180;
Polar = zeros(nrad,ntheta,nimg);
PolarVarPN = zeros(nimg,nrad);
for ii = 1:nimg;
    img = polartrans(XcorPN(:,:,ii), nrad, ntheta,...
        cx, cy, 'linear', 'valid');
    Polar(:,:,ii) = img;
    PolarVarPN(ii,:) = var(img,1,2);
end
VarImPN = zeros(size(BF2,1),size(BF2,2),nrad);
% Reshape into image stack I(x,y,k)
for ii=1:nrad;
    img = reshape(PolarVar14600PN(:,ii),size(BF2,1),[]);
    VarImPN(:,:,ii) = img;
end
mPolarVarPN = mean(PolarVarPN,1);
varPolarVarPN = var(PolarVarPN,1,1);
save('PolarVAR.mat','-v7.3');
clear all
%%%%%%%%%%%%%%%%%%%%%%%%%%%%%
```

```
% VDF annular intensity images
%%%%%%%%%%%%%%%%%%%%%%%%%%%%%%
load('PolarVAR14600.mat','cx','cy','ix','iy',...
    'XcorPN','nimg','nrad','BF2')
% Initialise arrays for VDF annular masks
[x1,y1]=meshgrid(-(cx-1):(ix-cx),-(cy-1):(iy-cy));
[x2,y2]=meshgrid(-(cx-1):(ix-cx),-(cy-1):(iy-cy));
DFmask = zeros(ix,iy,nrad);
r2a = x1.^2+y1.^2;
r2b = x2.^2+y2.^2;
for ii = 1:nrad;
     % annular dark field masks
        c_mask2=(r2a<=ii^2);
        c_mask3=(r2b<=(ii-1)^2);
        DFmask(:,:,ii) = c_mask2 - c_mask3;
end
annDFCCPN = zeros(nrad,nimg);
% Annular dark field masks multiplied with DPs
% Very slow, needs optimised
for iii = 1:nrad;
    for ii = 1:nimg;
    img = XcorPN(:,:,ii);
        annDFCCPN(iii,ii) = sum(sum(img.*DFmask(:,:,iii)));
    end
end
VDF = zeros(size(BF2,1),size(BF2,2),nrad);
% Reshape into image stack I(x,y,k)
for ii = 1:nrad;
    img = reshape(annDFCCPN(ii,:), size(BF2,1), []); %
    VDF(:,:,ii) = img;
end
clear XcorPN
save('AnnularVDFi.mat','-v7.3');
clear all
```

Appendix C

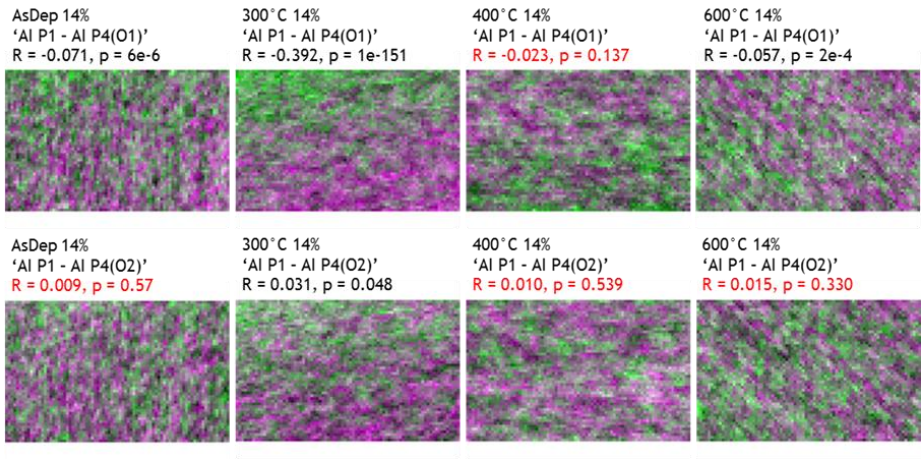

Appendix C 1 Composite VDF images of the 1st Peak MRO and the split oxygen distributions for the 14 % Ti-doped samples.

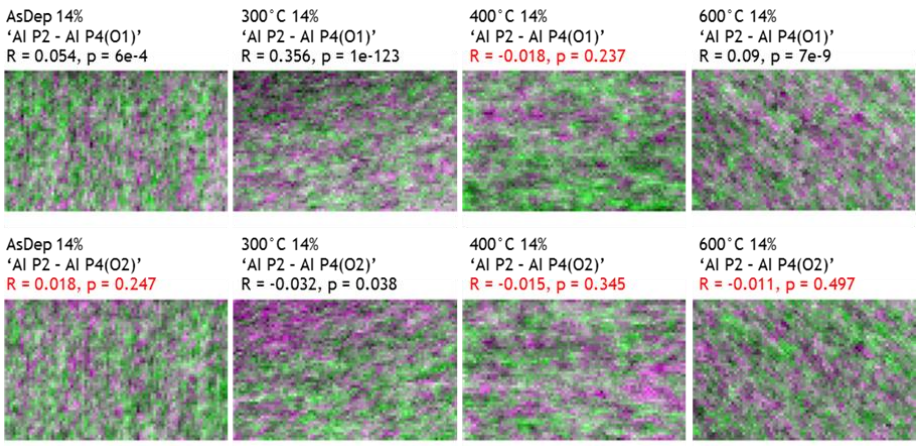

Appendix C 2 Composite VDF images of the 2nd peak and the split oxygen distributions for the 14 % Ti-doped samples.

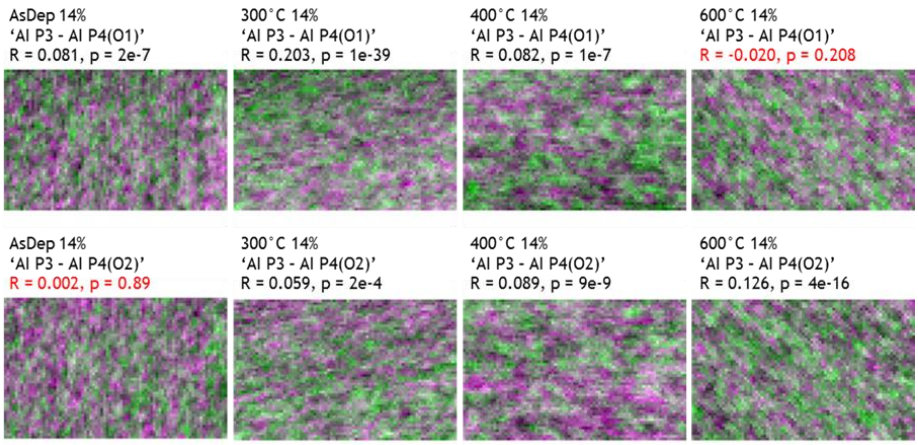

Appendix C 3 Composite VDF images of the 3rd peak and the split oxygen distributions for the 14 % Ti-doped samples.

1. Abbott BP, Abbott R, Abbott TD, Abernathy MR, Acernese F, Ackley K, et al. Observation of Gravitational Waves from a Binary Black Hole Merger. Phys Rev Lett. 2016 Feb 11;116(6):61102.

2. Einstein A. Die Grundlage der allgemeinen Relativitätstheorie. Ann Phys. 1916;354(7):769–822.

3. Einstein A. Über Gravitationswellen. In: Albert Einstein: Akademie-Vorträge. Weinheim, FRG: Wiley-VCH Verlag GmbH & Co. KGaA; 2006. p. 135–49.

4. Pitkin M, Reid S, Hough J. Gravitational Wave Detection by Interferometry. 2000;600:1–72.

5. Saulson PR. Physics of Gravitational Wave Detection: Resonant and Interferometric Detectors. XXVI SLAC Summer Inst Part Phys. 1998;9–11.

6. Cutler C, Thorne KS. An Overview of Gravitational-Wave Sources. In: General Relativity and Gravitation. World Scientific; 2002. p. 72–111.

7. Ott CD. Probing the core-collapse supernova mechanism with gravitational waves. Class Quantum Gravity. 2009 Oct 21;26(20).

8. Taylor JH. DISCOVERY OF A PULSAR IN A BINARY SYSTEM. Ann N Y Acad Sci. 1975 Oct;262(1 Seventh Texas):490–2.

9. Thorne KS. Gravitational Waves. Part Nucl Astrophys Cosmol Next Millenn. 1995 Jun 30;160–84.

10. Wagoner R V. Gravitational radiation from accreting neutron stars. Astrophys J. 1984 Mar;278:345.

11. Saulson PR. Fundamentals of Interferometric Gravitational Wave Detectors. World Scientific Publishing Co Pte Ltd; 1994. 316 p.

12. Weber J. Detection and Generation of Gravitational Waves. Phys Rev. 1960 Jan 1;117(1):306–13.

13. Ju L, Blair DG, Zhao C. Detection of gravitational waves. Reports Prog Phys. 2000 Sep 1;63(9):1317–427.

14. Menner. Simplified schematic of aLIGO [Internet]. Available from: https://commons.wikimedia.org/w/index.php?curid=46947503%0A

15. Shoemaker D. Advanced LIGO reference design v2. LIGO Document. 2011.

16. Aufmuth P, Danzmann K. Gravitational wave detectors. New J Phys. 2005 Sep 29;7:202–202.

17. Hough J, Rajantie A, Contaldi C, Dauncey P, Stoica H. The Search for Gravitational Waves. In: AIP Conference Proceedings. AIP; 2007. p. 93–8.

18. Lück H, Hewitson M, Ajith P, Allen B, Aufmuth P, Aulbert C, et al. Status of the GEO600 detector. Class Quantum Gravity. 2006 Apr 21;23(8):S71–8.

19. Fujimoto M. TAMA ground-based interferometer for the detection of gravitational waves. Adv Sp Res. 2000 Jan;25(6):1161–4.

20. Flaminio R, Bellachia F, Boget D, Buskulic D, Chollet F, David PY, et al. The gravitational wave detector VIRGO. In: Nanobeam 2002. 2003. p. 7–13.

21. Somiya K. Detector configuration of KAGRA–the Japanese cryogenic

gravitational-wave detector. Class Quantum Gravity. 2012 Jun 21;29(12):124007.

22. Unnikrishnan CS. IndIGO and LIGO-India: Scope and Plans for Gravitational Wave Research and Precision Metrology in India. Int J Mod Phys D. 2015 Oct 16;22(1):1341010.

23. Punturo M, Abernathy M, Acernese F, Allen B, Andersson N, Arun K, et al. The Einstein Telescope: a third-generation gravitational wave observatory. Class Quantum Gravity. 2010 Oct 7;27(19).

24. Armano M, Audley H, Auger G, Baird JT, Bassan M, Binetruy P, et al. Sub-Femto-g Free Fall for Space-Based Gravitational Wave Observatories: LISA Pathfinder Results. Phys Rev Lett. 2016 Jun 10;116(23):231101.

25. Harry GM. Advanced LIGO: the next generation of gravitational wave detectors. Class Quantum Gravity. 2010 Apr 21;27(8):84006.

26. Ballmer S, Mandic V. New Technologies in Gravitational-Wave Detection. Annu Rev Nucl Part Sci. 2015 Oct 19;65(1):555–77.

27. Hammond G, Hild S, Pitkin M. Advanced technologies for future ground-based, laser-interferometric gravitational wave detectors. J Mod Opt. 2014 Dec 12;61(sup1):S10–45.

28. Braginsky VB, Gorodetsky ML, Khalili FY, Matsko AB, Thorne KS, Vyatchanin SP. Noise in gravitational-wave detectors and other classical-force measurements is not influenced by test-mass quantization. Phys Rev D. 2003 Apr 7;67(8):82001.

29. Powles JG. Brownian motion- June 1827. Phys Educ. 1978 Aug;13(4):310.

30. Einstein A. Über die von der molekularkinetischen Theorie der Wärme geforderte Bewegung von in ruhenden Flüssigkeiten suspendierten Teilchen. Ann Phys. 1905;322(8):549–60.

31. Evans M, Ballmer S, Fejer M, Fritschel P, Harry G, Ogin G. Thermo-optic noise in coated mirrors for high-precision optical measurements. Phys Rev D. 2008 Nov 10;78(10):102003.

32. Penn SD, Sneddon PH, Armandula H, Betzwieser JC, Cagnoli G, Camp J, et al. Mechanical loss in tantala/silica dielectric mirror coatings. Class Quantum Gravity. 2003 Jul 7;20(13):2917–28.

33. Harry GM, Abernathy MR, Becerra-Toledo AE, Armandula H, Black E, Dooley K, et al. Titania-doped tantala/silica coatings for gravitational-wave detection. Class Quantum Gravity. 2007 Jan 21;24(2):405–15.

34. Nyquist H. Thermal agitation of electric charge in conductors. Phys Rev. 1928;32.

35. Callen HB, Greene RF. On a Theorem of Irreversible Thermodynamics. Phys Rev. 1952 Jun 1;86(5):702–10.

36. Harry G, Bodiya TP, DeSalvo R. Optical Coatings and Thermal Noise in Precision Measurement. Harry G, Bodiya TP, DeSalvo R, editors. Cambridge: Cambridge University Press; 2011. 328 p.

37. Zener C. Theory of Strain Interaction of Solute Atoms. Phys Rev. 1948 Sep

15;74(6):639–47.

38. Nowick AS, Berry BS. Anelastic relaxation in crystalline solids [by] A. S. Nowick and B. S. Berry. Vol. 11. 1972. 1972-1973 p.

39. Crooks DRM, Cagnoli G, Fejer MM, Gretarsson A, Harry G, Hough J, et al. Experimental measurements of coating mechanical loss factors. Class Quantum Gravity. 2004 Mar 7;21(5):S1059–65.

40. Fejer MM, Rowan S, Cagnoli G, Crooks DRM, Gretarsson A, Harry GM, et al. Thermoelastic dissipation in inhomogeneous media: loss measurements and displacement noise in coated test masses for interferometric gravitational wave detectors. Phys Rev D. 2004 Oct 22;70(8).

41. Granata M, Saracco E, Morgado N, Cajgfinger A, Cagnoli G, Degallaix J, et al. Mechanical loss in state-of-the-art amorphous optical coatings. Phys Rev D. 2016 Jan 27;93(1).

42. Hunklinger S. Phonons in Amorphous Materials. Le J Phys Colloq. 1982;43(C9):C9-461-C9-474.

43. Zallen R. The Physics of Amorphous Solids. Wiley-VCH Verlag GmbH & Co. KGaA; 1998. 318 p.

44. Zachariasen WH. The Atomic Arrangement in Glass. J Am Chem Soc. 1932 Oct 1;54(10):3841–51.

45. Houssa M. High k Gate Dielectrics. High k Gate Dielectrics. CRC Press; 2003. 614 p. (Series in Material Science and Engineering).

46. Lucovsky G. Electronic Structure, Amorphous Morphology and Thermal Stability of Transition Metal Oxide and Chalcogenide Alloys. J Optoelectron Adv Mater. 2001;3(2):155–66.

47. Pauling L. THE NATURE OF THE CHEMICAL BOND and the structure of molecules and crystals. An Introduction to Modern Structural Chemistry. Oxford University Press, London; 1952.

48. Messler Jr. RW. 1 - Introduction to Joining BT - Joining of Advanced Materials. In Boston: Butterworth-Heinemann; 1993. p. 3–24.

49. Popescu M, Leonovici M. Paracrystallinity or randomness: A challenge for non-crystalline structure. J Optoelectron Adv Mater. 2006;8(5):1831–7.

50. Seshan K. Hndbook of Thin-Film deposition processes and techniques. 2nd ed. William Andrew Publishing, Norwich, New Yourl, U.S.a.; 2002. 629 p.

51. Harry GM, Armandula H, Black E, Crooks DRM, Cagnoli G, Fejer MM, et al. Optical coatings for gravitational-wave detection. Spie. 2004;5578:0–7.

52. Graczyk JF. Defect structures in amorphous Germanium films. Phys status solidi. 1978;46(2):fmi–fmi, 411–733, K79–K173.

53. Oberlin A, Bonnamy S. A Realistic Approach to Disordered Carbons. In: Chemistry & Physics of Carbon. CRC Press; 2012. p. 1–84. (Chemistry and Physics of Carbon).

54. Lee M. Transmission electron microscopy (TEM) of earth and planetary materials: a review. Mineral Mag. 2010;74(1):1–27.

55. Herd SR, Chaudhari P. On the question of microcrystallites in some amorphous materials. An electron microscope investigation. Phys status solidi. 1974;26(2):627–42.

56. Buseck PR, Huang B, Keller LP. Electron microscope investigation of the structures of annealed carbons. Energy Fuels. 1987;1(1):DOI: 10.1021/ef00001a020.

57. Hirotsu Y, Ohkubo T, Bae I-T, Ishimaru M. Electron diffraction structure analysis for amorphous materials. Mater Chem Phys. 2003 Aug;81(2–3):360–3.

58. Campbell IM and MCC and GP and IA. Short-range order in FeV alloys as investigated by neutron scattering and NMR at 51 V nuclei. J Phys F Met Phys. 1982;12(1):25.

59. Hohlwein MP and WS and TS and RS and D. Diffuse neutron scattering to investigate the short range order for a single crystal of VD 0.781. Phys Scr. 1995;1995(T57):107.

60. Wright AC. Neutron scattering from vitreous silica. V. The structure of vitreous silica: What have we learned from 60 years of diffraction studies? J Non Cryst Solids. 1994 Nov;179:84–115.

61. Kohara S, Suzuya K. Intermediate-range order in vitreous SiO2 and GeO2. J Phys Condens Matter. 2005;17(5):S77–86.

62. Rodriguez JA, Moss SC, Robertson JL, Copley JRD, Neumann DA, Major J. Neutron scattering studies of short-range order, atomic displacements, and effective pair interactions in a null-matrix 62Ni0.52Pt0.48 crystal. Phys Rev B. 2006 Sep 28;74(10):104115.

63. Zaja W. Short Range Order in Polymers within Neutrons ' Eyeshot. 2009;115(2):594–8.

64. Paul F, Press W, Rabe P. Short range order of amorphous Mg70Zn30 investigated by means of anomalous X-ray scattering. J Non Cryst Solids. 1991;130(1):98–106.

65. Markova GS, Ovchinnikov JK, Bokhyan EB. A study of short-range order in amorphous polymers by diffraction methods. J Polym Sci Polym Symp. 1973 Jan 1;42(2):671–8.

66. Boucher PC and R de K and B. Determination of the atomic short-range order in a Tb-Cu amorphous alloy by X-ray and neutron diffraction. J Phys F Met Phys. 1984;14(10):2239.

67. Aleshina LA, Malinenko VP, Phouphanov AD, Jakovleva NM. The short-range order of anodic amorphous oxide films of Ta and Nb. J Non Cryst Solids. 1986;87(3):350–60.

68. Wignall CD, Longman GW. Studies of short-range order in amorphous polymers by radial distribution functions derived from X-ray diffraction. J Macromol Sci Part B. 1976 Jan 1;12(1):99–123.

69. Vishwanadh B, Sharma SK, Pujari PK, Kishore R, Dey GK, Tewari R. Influence of free volume and medium-range order on the deformation response of rapidly solidified and bulk Zr-based (Zr52Ti6Al10Cu18Ni14) metallic glass. Philos Mag. 2013 Sep 1;93(25):3442–71.

70. Xue X-Y, Bian X-F, Geng H-X, Sun M-H, Qin X-B. Relativity of medium range order in molten Cu–Sn alloys and phase diagram. Mater Sci Technol. 2003 May 1;19(5):557–60.

71. Hwang J, Voyles PM. Variable Resolution Fluctuation Electron Microscopy on Cu-Zr Metallic Glass Using a Wide Range of Coherent STEM Probe Size. Microsc Microanal. 2010/12/02. 2011;17(1):67–74.

72. Kalay YE, Kalay I, Hwang J, Voyles PM, Kramer MJ. Local chemical and topological order in Al–Tb and its role in controlling nanocrystal formation. Acta Mater. 2012 Feb;60(3):994–1003.

73. Quantitative Analysis of Nanoscale Order in Amorphous Materials By Stem-Mode Fluctuation Electron Microscopy. 2013;

74. Voyles PM, Muller DA. Fluctuation microscopy in the STEM. Ultramicroscopy. 2002 Nov;93(2):147–59.

75. Park JM, Na JH, Kim DH, Kim KB, Mattern N, Kühn U, et al. Medium range ordering and its effect on plasticity of Fe–Mn–B–Y–Nb bulk metallic glass. Philos Mag. 2010 Jul 7;90(19):2619–33.

76. Mu X, Neelamraju S, Sigle W, Koch CT, Totò N, Schön JC, et al. Evolution of order in amorphous-to-crystalline phase transformation of MgF2. J Appl Crystallogr. 2013;46(4):1105–16.

77. Tournarie BB and PC and PC and M. Small-angle neutron scattering determination of medium and long range order in the amorphous metallic alloy TbCu 3.54. J Phys F Met Phys. 1983;13(7):1339.

78. Al-Hasni BM, Mountjoy G, Barney E, Gismelseed A. A complete study of amorphous iron phosphate structure. J Non Cryst Solids. 2013;380:141–52.

79. Neov S, Gerasimova I, Skordeva E, Arsova D, Pamukchieva V, Mikula P, et al. Neutron diffraction study on the medium and short-range order of ternary chalcogenide glasses. J Mater Sci. 1999;34(15):3669–76.

80. Price DL, Susman S, Wright AC. Probing medium-range order in chalcogenide glasses by neutron scattering and optical spectroscopy. J Non Cryst Solids. 1987;97:167–70.

81. Cormier L, Gaskell PH, Calas G, Soper AK. Medium-range order around titanium in a silicate glass studied by neutron diffraction with isotopic substitution. Phys Rev B. 1998 Nov 1;58(17):11322–30.

82. Shyam B, Stone KH, Bassiri R, Fejer MM, Toney MF, Mehta A. Measurement and Modeling of Short and Medium Range Order in Amorphous Ta2O5 Thin Films. Sci Rep. 2016 Oct 26;6(1):32170.

83. Thomas MR, Hallett JE, Klein S, Mann S, Perriman AW, Richardson RM. Stability and Orientational Order of Gold Nanorods in Nematic Suspensions: A Small Angle X-ray Scattering Study. Mol Cryst Liq Cryst. 2015 Mar 24;610(1):44–50.

84. Hiraoka Y, Nakamura T, Hirata A, Escolar EG, Matsue K, Nishiura Y. Hierarchical structures of amorphous solids characterized by persistent homology. Proc Natl Acad Sci. 2016;113(26):201520877.

85. Youn Y, Kang Y, Han S. An efficient method to generate amorphous

structures based on local geometry. Comput Mater Sci. 2014;95:256–62.

86. Bogle SN, Voyles PM, Khare S V, Abelson JR. Quantifying nanoscale order in amorphous materials: simulating fluctuation electron microscopy of amorphous silicon. J Phys Condens Matter. 2007 Nov 14;19(45):455204.

87. Hamdan R, Trinastic JP, Cheng HP. Molecular dynamics study of the mechanical loss in amorphous pure and doped silica. J Chem Phys. 2014;141(5).

88. Bondi RJ, Fox BP, Marinella MJ. Role of atomistic structure in the stochastic nature of conductivity in substoichiometric tantalum pentoxide. J Appl Phys. 2016;119(12).

89. Rodney D, Tanguy A, Vandembroucq D. Modeling the mechanics of amorphous solids at different length scale and time scale. Model Simul Mater Sci Eng. 2011;19(8):83001.

90. Galvan-Colin J, Valladares AA, Valladares RM, Valladares A. Short-range order in ab initio computer generated amorphous and liquid Cu-Zr alloys: A new approach. Phys B Condens Matter. 2015;475:140–7.

91. Kim M, Khoo KH, Chelikowsky JR. Simulating liquid and amorphous silicon dioxide using real-space pseudopotentials. Phys Rev B - Condens Matter Mater Phys. 2012;86(5):1–8.

92. Bondi RJ, Desjarlais MP, Thompson AP, Brennecka GL, Marinella M. Electrical Conductivity in Oxygen- Deficient Phases of Transition Metal Oxides from First-Principles Calculations. 2013;(September).

93. Billman CR, Trinastic JP, Davis DJ, Hamdan R, Cheng H. Origin of the Second Peak in the Mechanical Loss Function of Amorphous Silica. 2001;

94. Borisenko KB, Haberl B, Liu ACY, Chen Y, Li G, Williams JS, et al. Medium-range order in amorphous silicon investigated by constrained structural relaxation of two-body and four-body electron diffraction data. Acta Mater. 2012;60(1):359–75.

95. Yi F, Voyles PM. Analytical and computational modeling of fluctuation electron microscopy from a nanocrystal/amorphous composite. Ultramicroscopy. 2012 Nov;122:37–47.

96. Trinastic JP, Hamdan R, Billman C, Cheng H-P. Molecular dynamics modeling of mechanical loss in amorphous tantala and titania-doped tantala. Phys Rev B. 2016 Jan 25;93(1):14105.

97. Keller JB. Geometrical Theory of Diffraction*. J Opt Soc Am. 1962 Feb 1;52(2):116.

98. Vaĭnshteĭn BK (Boris K. Structure analysis by electron diffraction. Structure Analysis by Electron Diffraction. Pergamon Press; 1964. 420 p.

99. Hubbell JH. Review and history of photon cross section calculations. Phys Med Biol. 2006 Jul 7;51(13):R245–62.

100. Tietz T. Electron Scattering Cross Section with Relativistic Correction Based on the Thomas-Fermi Theory. Phys Rev. 1959 Feb 15;113(4):1056–7.

101. D.J.H., R.B.S. Neutron cross sections. J Nucl Energy. 1958 Sep;7(3–4):228.

102. Römer H. Theoretical Optics: An Introduction. Theoretical Optics: An Introduction. 2005. 1-361 p.

103. Köhler H. On Abbe's Theory of Image Formation in the Microscope. Opt Acta Int J Opt. 1981 Dec 1;28(12):1691–701.

104. Yankovich AB, Berkels B, Dahmen W, Binev P, Sanchez SI, Bradley SA, et al. Picometre-precision analysis of scanning transmission electron microscopy images of platinum nanocatalysts. Nat Commun. 2014 Jun 11;5(May):4155.

105. Rong Y. Characterization of Microstructures by Analytical Electron Microscopy (AEM). Berlin, Heidelberg: Springer Berlin Heidelberg; 2012. 566 p.

106. Williams D, Carter C. Scattering and diffraction. Transm Electron Microsc A Textb Mater Sci. 2009;23–39.

107. Williams D, Carter C. Elastic Scattering. Transm electron Microsc a Textb Mater Sci. 2009;39–51.

108. Egerton RF. Electron energy-loss spectroscopy in the TEM. 2009;72.

109. Kirkland EJ. Advanced Computing in Electron Microscopy. Second Edi. Advanced Computing in Electron Microscopy: Second Edition. Boston, MA: Springer US; 2010. 47-50 p.

110. Holmqvist B, Wiedling T, Benzi V, Zuffi L. Analysis of fast neutron elastic scattering from tantalum using a non-spherical optical potential. Nucl Phys A. 1970;150(1):105–13.

111. Doyle PA, Turner PS. Relativistic Hartree–Fock X-ray and electron scattering factors. Acta Crystallogr Sect A. 1968 May 1;24(3):390–7.

112. Lobato I, Van Dyck D. An accurate parameterization for scattering factors, electron densities and electrostatic potentials for neutral atoms that obey all physical constraints. Acta Crystallogr Sect A Found Adv. 2014 Nov 1;70(6):636–49.

113. Peng L-M. Electron atomic scattering factors and scattering potentials of crystals. Micron. 1999 Dec;30(6):625–48.

114. DeepKling. Miller indices [Internet]. Wikipedia. Available from: http://creativecommons.org/licenses/by/3.0

115. Hetherington C. correction for TEM. Mater Today. 2004;7(12):50–5.

116. Bleloch A, Lupini A. Imaging at the picoscale. Mater Today. 2004;7(12):42–8.

117. Egerton RF. Limits to the spatial, energy and momentum resolution of electron energy-loss spectroscopy. Ultramicroscopy. 2007;107(8):575–86.

118. Egerton RF. Electron Energy- Loss Spectroscopy in the Electron Microscope. 1986;49–73.

119. Williams D, Carter C. Inelastic Scattering and Beam Damage. 2nd ed. Transmission electron microscopy: a textbook for materials science. Springer Science; 2009. 53-71 p.

120. Magnunor. Eels energy loss spectra [Internet]. Wikipedia. Available from:

https://commons.wikimedia.org/w/index.php?curid=60024900

121. Williams D, Carter C. The Instrument. Transm electron Microsc a Textb Mater Sci. 2009;(Chapter 5):141–71.

122. McMullan G, Faruqi AR, Henderson R, Guerrini N, Turchetta R, Jacobs A, et al. Experimental observation of the improvement in MTF from backthinning a CMOS direct electron detector. Ultramicroscopy. 2009 Aug;109(9):1144–7.

123. McMullan G, Cattermole DM, Chen S, Henderson R, Llopart X, Summerfield C, et al. Electron imaging with Medipix2 hybrid pixel detector. Ultramicroscopy. 2007 Apr;107(4–5):401–13.

124. Ballabriga R, Campbell M, Heijne E, Llopart X, Tlustos L, Wong W. Medipix3: A 64k pixel detector readout chip working in single photon counting mode with improved spectrometric performance. Nucl Instruments Methods Phys Res Sect A Accel Spectrometers, Detect Assoc Equip. 2011 May;633:S15–8.

125. J.A. Mir, R. Clough, R. MacInnes, C. Gough, R. Plackett, I. Shipsey, H. Sawada, I. MacLaren, R. Ballabriga, D. Maneuski, V. O'Shea, D. McGrouther AIK. Medipix3 Demonstration and understanding of near ideal detector performance for 60 & 80 keV electrons. :1–36.

126. Rauch EF, Véron M. Virtual dark-field images reconstructed from electron diffraction patterns. Eur Phys J Appl Phys. 2014 Apr 21;66(1):10701.

127. Hart MJ, Bassiri R, Borisenko KB, Véron M, Rauch EF, Martin IW, et al. Medium range structural order in amorphous tantala spatially resolved with changes to atomic structure by thermal annealing. J Non Cryst Solids. 2016 Apr;438:10–7.

128. Krajnak M, McGrouther D, Maneuski D, O'Shea V, McVitie S. Pixelated detectors and improved efficiency for magnetic imaging in STEM differential phase contrast. Ultramicroscopy. 2016;165:42–50.

129. Nord M, Ross A, Hallsteinsen I, Tybell T, MacLaren I. Towards Mapping Perovskite Oxide 3-D Structure Using Two-Dimensional Pixelated STEM Detector. Microsc Microanal. 2016/07/25. 2016;22(S3):476–7.

130. Yang H, Jones L, Ryll H, Simson M, Soltau H, Kondo Y, et al. 4D STEM: High efficiency phase contrast imaging using a fast pixelated detector. J Phys Conf Ser. 2015;644:12032.

131. Nanomegas. ASTAR - Application notes nanoscale TEM orientation imaging analysis [Internet]. 2016. p. 1–32. Available from: www.nanomegas.com

132. Nicolopoulos S, Rauch E, Véron M. Electron diffraction techniques and applications [Internet]. Available from: http://www.nanomegas.com/

133. Newcomb SB, Boothroyd CB, Stobbs WM. Specimen preparation methods for the examination of surfaces and interfaces in the transmission electron microscope. J Microsc. 1985 Nov;140(2):195–207.

134. Danh NC, Rajan K, Wallace W. A TEM study of microstructural changes during retrogression and reaging in 7075 aluminum. Metall Trans A. 1983 Sep;14(9):1843–50.

135. Mayer J, Giannuzzi L a, Kamino T, Michael J. TEM Sample Preparation and FIB-Induced Damage. MRS Bull. 2007 May 31;32(5):400–7.

136. Thompson K, Gorman B, Larson DJ, Leer B Van, Hong L. Minimization of Ga Induced FIB Damage Using Low Energy Clean-up. 2006;12(Supp 2):2006.

137. Simpson R, White RG, Watts JF, Baker MA. WITHDRAWN: XPS Investigation of Monatomic and Cluster Argon Ion Sputtering of Tantalum Pentoxide. Appl Surf Sci. 2017 Jan;405:79–87.

138. Keen DA. A comparison of various commonly used correlation functions for describing total scattering. J Appl Crystallogr. 2001 Apr 1;34(2):172–7.

139. Cockayne DJH. The Study of Nanovolumes of Amorphous Materials Using Electron Scattering. Annu Rev Mater Res. 2007 Aug;37(1):159–87.

140. Warren B. X-ray Diffraction. Dover Publications; 1969. 381 p.

141. Cusack NE, Stein DL. The Physics of Structurally Disordered Matter: An Introduction. Phys Today. 1988 Dec;41(12):110–2.

142. Debye P. Interferenz von Röntgenstrahlen und Wärmebewegung. Ann Phys. 1913;348(1):49–92.

143. Debye P. Note on the Scattering of X-rays. J Math Phys. 1925 Jan;4(1–4):133–47.

144. Egerton RF. Electron Energy-Loss Spectroscopy in the Electron Microscope. Boston, MA: Springer US; 2011. 29-109 p.

145. Cockayne DJH, Chen Y, Li G, Borisenko KB. The technique of RDF of nanovolumes using electron diffraction. J Phys Conf Ser. 2010 Jul 1;241:12006.

146. Ishimaru M, Hirata A, Naito M. Electron diffraction study on chemical short-range order in covalent amorphous solids. Nucl Instruments Methods Phys Res Sect B Beam Interact with Mater Atoms. 2012 Apr;277:70–6.

147. Hirata A, Hirotsu Y, Kuboya S, Nieh TG. Local structural fluctuation in Pd-Ni-P bulk metallic glasses examined using nanobeam electron diffraction. J Alloys Compd. 2009;483(1–2):64–9.

148. Hirata A, Hirotsu Y, Ohkubo T, Tanaka N, Nieh TG. Local atomic structure of Pd-Ni-P bulk metallic glass examined by high-resolution electron microscopy and electron diffraction. Intermetallics. 2006;14(8–9):903–7.

149. Chen YM, Ohkubo T, Mukai T, Hono K. Structure of shear bands in Pd40Ni40P20 bulk metallic glass. J Mater Res. 2009 Jan 31;24(1):1–9.

150. Guoqiang L, Borisenko KB, Chena Y, Duc N-M, Mac E, Cockayne DJH. Local structure variations in Al89La6Ni5 metallic glass. Acta Mater. 2009 Feb;57(3):804–11.

151. Hirata A, Hirotsu Y, Ohkubo T, Hanada T, Bengus VZ. Compositional dependence of local atomic structures in amorphous Fe100−xBx „x=14,17,20… alloys studied by electron diffraction and high-resolution electron microscopy Akihiko. Phys Rev B. 2006 Dec 29;74(21):214206.

152. Ankele J, Mayer J, Lamparter P, Steeb S. Quantitative Electron Diffraction Data of Amorphous Materials. Zeitschrift für Naturforsch A. 2005 Jan 1;60(6):459–68.

153. Chen Y. Electron diffraction analysis of amorphous Ge2Sb2Te5. University of

Oxford; 2010.

154. Hirata A, Morino T, Hirotsu Y, Itoh K, Fukunaga T. Local Atomic Structure Analysis of Zr-Ni and Zr-Cu Metallic Glasses Using Electron Diffraction. Mater Trans. 2007;48(6):1299–303.

155. McBride W, Cockayne DJH, Tsuda K. Deconvolution of electron diffraction patterns of amorphous materials formed with convergent beam. Ultramicroscopy. 2003 Apr;94(3–4):305–8.

156. McBride W, Cockayne DJH, Nguyen-Manh D. Electron diffraction from nanovolumes of amorphous material using coherent convergent illumination. Ultramicroscopy. 2003 Aug;96(2):191–200.

157. Tran DT, Svensson G, Tai C-W. SUePDF: a program to obtain quantitative pair distribution function from electron diffraction data. 2016 Feb 29;13.

158. Treacy MMJ, Gibson JM. Variable Coherence Microscopy: a Rich Source of Structural Information from Disordered Materials. Acta Crystallogr Sect A Found Crystallogr. 1996 Mar 1;52(2):212–20.

159. Gibson JM, Treacy MMJ, Voyles PM, Jin H-C, Abelson JR. Structural disorder induced in hydrogenated amorphous silicon by light soaking. Appl Phys Lett. 1998;73(21):3093–5.

160. Cheng J-Y, Gibson JM, Jacobson DC. Observations of structural order in ion-implanted amorphous silicon. J Mater Res. 2001 Nov;16(11):3030–3.

161. Voyles PM, Gerbi JE, Treacy MMJ, Gibson JM, Abelson JR. Increased medium-range order in amorphous silicon with increased substrate temperature. J Non Cryst Solids. 2001 Nov;293–295(1):45–52.

162. Nittala LN, Jayaraman S, Sperling BA, Abelson JR. Hydrogen-induced modification of the medium-range structural order in amorphous silicon films. Appl Phys Lett. 2005 Dec 12;87(24):241915.

163. Bogle SN, Nittala LN, Twesten RD, Voyles PM, Abelson JR. Size analysis of nanoscale order in amorphous materials by variable-resolution fluctuation electron microscopy. Ultramicroscopy. 2010 Sep;110(10):1273–8.

164. Voyles PM, Gerbi JE, Treacy MMJ, Gibson JM, Abelson JR. Absence of an Abrupt Phase Change from Polycrystalline to Amorphous in Silicon with Deposition Temperature. Phys Rev Lett. 2001 Jun 11;86(24):5514–7.

165. Gibson J., Treacy MM., Voyles P. Atom pair persistence in disordered materials from fluctuation microscopy. Ultramicroscopy. 2000 Jun;83(3–4):169–78.

166. Gibson JM, Treacy MMJ. Diminished Medium-Range Order Observed in Annealed Amorphous Germanium. Phys Rev Lett. 1997 Feb 10;78(6):1074–7.

167. Kwon M-H, Lee B-S, Bogle SN, Nittala LN, Bishop SG, Abelson JR, et al. Nanometer-scale order in amorphous Ge2Sb2Te5 analyzed by fluctuation electron microscopy. Appl Phys Lett. 2007 Jan 8;90(2):21923.

168. Lee B-S, Burr GW, Shelby RM, Raoux S, Rettner CT, Bogle SN, et al. Observation of the Role of Subcritical Nuclei in Crystallization of a Glassy Solid. Science (80-). 2009 Nov 13;326(5955):980–4.

169. Darmawikarta K, Lee B-S, Shelby RM, Raoux S, Bishop SG, Abelson JR. Quasi-equilibrium size distribution of subcritical nuclei in amorphous phase change AgIn-Sb2Te. J Appl Phys. 2013 Jul 21;114(3):34904.

170. Stratton WG, Hamann J, Perepezko JH, Voyles PM, Mao X, Khare S V. Aluminum nanoscale order in amorphous Al92Sm8 measured by fluctuation electron microscopy. Appl Phys Lett. 2005 Apr 4;86(14).

171. Darmawikarta K, Raoux S, Tchoulfian P, Li T, Abelson JR, Bishop SG. Evolution of subcritical nuclei in nitrogen-alloyed Ge2Sb2Te5. J Appl Phys. 2012 Dec 15;112(12).

172. Yan A, Sun T, Borisenko KB, Buchholz DB, Chang RPH, Kirkland AI, et al. Multi-scale order in amorphous transparent oxide thin films. J Appl Phys. 2012 Sep;112(5):54907.

173. Gibson JM, Treacy MMJ, Sun T, Zaluzec NJ. Substantial Crystalline Topology in Amorphous Silicon. Phys Rev Lett. 2010 Sep 17;105(12).

174. Li TT, Darmawikarta K, Abelson JR. Quantifying nanoscale order in amorphous materials via scattering covariance in fluctuation electron microscopy. Ultramicroscopy. 2013 Oct;133:95–100.

175. Bassiri R, Hart M, Byer RL, Borisenko KB, Evans K, Fejer MM, et al. Investigating the medium range order in amorphous Ta2O5 coatings. J Phys Conf Ser. 2014 Jun 11;522(1):12043.

176. Wei S-D, Lai S-H. Fast template matching based on normalized cross correlation with adaptive multilevel winner update. IEEE Trans Image Process. 2008 Nov;17(11):2227–35.

177. Li TT, Bogle SN, Abelson JR. Quantitative Fluctuation Electron Microscopy in the STEM: Methods to Identify, Avoid, and Correct for Artifacts. Microsc Microanal. 2014 Oct 17;20(5):1605–18.

178. Kumerički K. Feynman Diagrams for Beginners. Adriat Sch Part Phys Phys Informatics. 2001;11–21.

179. Kwan-Liu Ma, Liao I, Frazier J, Hauser H, Kostis H-N. Scientific Storytelling Using Visualization. IEEE Comput Graph Appl. 2012 Jan;32(1):12–9.

180. Lum PY, Singh G, Lehman A, Ishkanov T, Vejdemo-Johansson M, Alagappan M, et al. Extracting insights from the shape of complex data using topology. Sci Rep. 2013 Dec 7;3(1):1236.

181. Smith C. Imperial student shows how diagrams can be used to make buildings energy smart [Internet]. Imperial College London News. 2016 [cited 2017 Apr 14]. Available from: http://www3.imperial.ac.uk/newsandeventspggrp/imperialcollege/newssummary/news_21-7-2016-11-36-28

182. Rauch EF, Veron M. Coupled microstructural observations and local texture measurements with an automated crystallographic orientation mapping tool attached to a tem. Materwiss Werksttech. 2005 Oct 1;36(10):552–6.

183. Garner A, Gholinia A, Frankel P, Gass M, MacLaren I, Preuss M. The microstructure and microtexture of zirconium oxide films studied by transmission electron backscatter diffraction and automated crystal orientation mapping with transmission electron microscopy. Acta Mater.

2014 Nov;80:159–71.

184. Stratton WG, Voyles PM. Comparison of fluctuation electron microscopy theories and experimental methods. J Phys Condens Matter. 2007 Nov 14;19(45).

185. Bassiri R, Borisenko KB, Cockayne DJH, Hough J, MacLaren I, Rowan S. Probing the atomic structure of amorphous Ta2 O5 coatings. Appl Phys Lett. 2011;98(3):2009–12.

186. Bassiri R, Evans K, Borisenko KB, Fejer MM, Hough J, MacLaren I, et al. Correlations between the mechanical loss and atomic structure of amorphous TiO2-doped Ta2O5 coatings. Acta Mater. 2013 Feb;61(4):1070–7.

187. Martin IW, Chalkley E, Nawrodt R, Armandula H, Bassiri R, Comtet C, et al. Comparison of the temperature dependence of the mechanical dissipation in thin films of Ta 2 O 5 and Ta 2 O 5 doped with TiO 2. Class Quantum Gravity. 2009;26(15):155012.

188. Martin IW, Bassiri R, Nawrodt R, Fejer MM, Gretarsson A, Gustafson E, et al. Effect of heat treatment on mechanical dissipation in Ta2O5 coatings. Class Quantum Gravity. 2010 Nov 21;27(22):225020.

189. Bassiri R, Liou F, Abernathy MR, Lin AC, Kim N, Mehta A, et al. Order within disorder: The atomic structure of ion-beam sputtered amorphous tantala (a-Ta2O5). APL Mater. 2015 Mar;3(3):36103.

190. Bassiri R, Abernathy MRMR, Liou F, Mehta A, Gustafson EKEK, Hart MJMJ, et al. Order, disorder and mixing: The atomic structure of amorphous mixtures of titania and tantala. J Non Cryst Solids. 2016;438:59–66.

191. Hirotsu Y, Ishimaru M, Ohkubo T, Hanada T, Sugiyama M. Application of nano-diffraction to local atomic distribution function analysis of amorphous materials. J Electron Microsc (Tokyo). 2001;50(6):435–42.

192. Bhattacharyya S, Madel O, Schulze S, Häussler P, Hietschold M, Richter F. Structure of nitrogenated carbon films by electron diffraction and imaging. Phys Rev B. 2000 Feb 1;61(6):3927–35.

193. Li G, Borisenko KB, Cockayne DJH. Local structures of two metallic glasses with good plasticity. J Phys Conf Ser. 2010 Jul 1;241:12066.

194. Bassiri R, Borisenko KB, Cockayne DJH, Hough J, MacLaren I, Rowan S. Probing the atomic structure of amorphous Ta2 O5 coatings. Appl Phys Lett. 2011;98(3):1–3.

195. Juhás P, Cherba DM, Duxbury PM, Punch WF, Billinge SJL. Ab initio determination of solid-state nanostructure. Nature. 2006 Mar 30;440(7084):655–8.

196. Netterfield RP, Gross M, Baynes FN, Green KL, Harry GM, Armandula H, et al. Low mechanical loss coatings for LIGO optics: progress report. In: Fulton ML, Kruschwitz JDT, editors. ProcSPIE. 2005. p. 58700H.

197. Farhan MS, Zalnezhad E, Bushroa AR. Properties of Ta2O5 thin films prepared by ion-assisted deposition. Mater Res Bull. 2013 Oct;48(10):4206–9.

198. Martin PJ, Bendavid A, Swain M, Netterfield RP, Kinder TJ, Sainty WG, et al.

Properties of thin films of tantalum oxide deposited by ion-assisted deposition. Thin Solid Films. 1994 Mar;239(2):181–5.

199. Gaboriaud R., Pailloux F, Guerin P, Paumier F. Yttrium sesquioxide, Y2O3, thin films deposited on Si by ion beam sputtering: microstructure and dielectric properties. Thin Solid Films. 2001 Dec;400(1–2):106–10.

200. Manova D, Gerlach JW, Mändl S. Thin Film Deposition Using Energetic Ions. Materials (Basel). 2010 Jul 29;3(8):4109–41.

201. Langston PF. A study of the influence of process parameter variations on the material properties and laser damage performance of ion beam sputtered Sc2O3 and HfO2 thin films. Colorado State University; 2016.

202. Kim N, Stebbins JF. Effects of annealing on the structure of ion beam sputtered amorphous tantalum oxide: Oxygen-17 NMR spectra and relaxation times. J Non Cryst Solids. 2013 Oct;378:158–62.

203. Chin H-S, Chao L-S. The Effect of Thermal Annealing Processes on Structural and Photoluminescence of Zinc Oxide Thin Film. J Nanomater. 2013;2013:1–8.

204. Conference I, Engineering PS. Effect of the rapid thermal annealing on the structural properties of TaO. In: 13th International Conference on Plasma Surface Engineering. 2012. p. 443–6.

205. Quinn DJ, Wardle B, Spearing SM. Residual stress and microstructure of as-deposited and annealed, sputtered yttria-stabilized zirconia thin films. J Mater Res. 2011/01/01. 2008 Mar 31;23(3):609–18.

206. Brown JT. Center wavelength shift dependence on substrate coefficient of thermal expansion for optical thin-film interference filters deposited by ion-beam sputtering. Appl Opt. 2004 Aug 10;43(23):4506.

207. Grigoriev FV, Katkova EV, Sulimov AV, Sulimov VB, Tikhonravov AV. Annealing of deposited SiO2 thin films: full-atomistic simulation results. Opt Mater Express. 2016 Dec 1;6(12):3960.

208. Damart T, Coillet E, Tanguy A, Rodney D. Numerical study of the structural and vibrational properties of amorphous Ta2O5 and TiO2 -doped Ta2O5. J Appl Phys. 2016 May 7;119(17):175106.

209. Takeshi E, Billinge SJL. The Method of Total Scattering and Atomic Pair Distribution Function Analysis. In: Underneath the Bragg Peaks Structural Analysis of Complex Materials. 2012. p. 55–111.

210. Chaneliere C, Autran JL, Devine R a. B, Balland B. Tantalum pentoxide (Ta2O5) thin films for advanced dielectric applications. Mater Sci Eng R Reports. 1998 May;22(6):269–322.

211. Joseph C, Bourson P, Fontana MD. Amorphous to crystalline transformation in Ta2O5 studied by Raman spectroscopy. J Raman Spectrosc. 2012 Aug;43(8):1146–50.

212. Fukumoto A, Miwa K. Prediction of hexagonal Ta2O5 structure by first-principles calculations. Phys Rev B. 1997 May 1;55(17):11155–60.

213. Denny YR, Firmansyah T, Oh SK, Kang HJ, Yang D-S, Heo S, et al. Effect of oxygen deficiency on electronic properties and local structure of amorphous

tantalum oxide thin films. Mater Res Bull. 2016 Oct;82:1–6.

214. Prato M, Chincarini A, Gemme G, Canepa M. Gravitational waves detector mirrors: Spectroscopic ellipsometry study of Ta2O5 films on SiO2 substrates. Thin Solid Films. 2011 Feb;519(9):2877–80.

215. Voronkov V V. Agglomeration of Vacancies into Voids and Oxide Particles in Silicon Crystals. ECS Trans. 2009;18(1):945–57.

216. Takeshi E, Billinge SJL. UNDERNEATH THE BRAGG PEAKS Structural Analysis of Complex Materials. Vol. 7, Pergamon Materials Series. 2012. 424 p.

217. Triana C. Atomic short-range order , optical and electronic properties of amorphous transition metal oxides. Uppsala University; 2017.

218. Kim Y-M, He J, Biegalski MD, Ambaye H, Lauter V, Christen HM, et al. Probing oxygen vacancy concentration and homogeneity in solid-oxide fuel-cell cathode materials on the subunit-cell level. Nat Mater. 2012 Oct;11(10):888–94.

219. Lü X, Hu Q, Yang W, Bai L, Sheng H, Wang L, et al. Pressure-Induced Amorphization in Single-Crystal Ta2O5 Nanowires: A Kinetic Mechanism and Improved Electrical Conductivity. J Am Chem Soc. 2013 Sep 18;135(37):13947–53.

220. Sun CQ. Relaxation of the Chemical Bond. Relaxation of the Chemical Bond. Singapore: Springer Singapore; 2014. 345-370 p. (Springer Series in Chemical Physics; vol. 108).

221. Evans K. Computational Modelling of Amorphous mirror coatings for use in Advanced Gravitational wave detectors. University of Glasgow; 2012.

222. Zhang RZ, Wang CL, Li JC, Zhang JL, Yang K, Zhang C, et al. Dopant position in Ti-doped high-temperature phase Ta2O5: First principles study. Appl Phys Lett. 2007;91(9):92909.

223. Pozio A. Effect of Tantalum Doping on TiO2 Nanotube Arrays for Water-Splitting. Mod Res Catal. 2015;4(1):1–12.

224. Chang JP, Steigerwald ML, Fleming RM, Opila RL, Alers GB. Thermal stability of Ta2O5 in metal–oxide–metal capacitor structures. Appl Phys Lett. 1999 Jun 14;74(24):3705–7.

225. Lee JH, Lee HJ, Lim SY, Chae KH, Park SH, Chung KY, et al. Stabilized Octahedral Frameworks in Layered Double Hydroxides by Solid-Solution Mixing of Transition Metals. Adv Funct Mater. 2017 Feb;27(7):1605225.

226. Lee HJ, Lee JH, Chung S-Y, Choi JW. Enhanced Pseudocapacitance in Multicomponent Transition-Metal Oxides by Local Distortion of Oxygen Octahedra. Angew Chemie Int Ed. 2016 Mar 14;55(12):3958–62.

227. Park SW, Baek YK, Lee JY, Park CO, Im HB. Effects of annealing conditions on the properties of tantalum oxide films on silicon substrates. J Electron Mater. 1992;21(6):635–9.

228. Kim J-W, Kim D-O, Hahn Y-B. Effect of rapid thermal annealing on the structural and electrical properties of TiO2 thin films prepared by plasma enhanced CVD. Korean J Chem Eng. 1998 Mar;15(2):217–22.

229. Fang Q, Zhang J-Y, Wang ZM, Wu JX, O'Sullivan BJ, Hurley PK, et al. Interface of tantalum oxide films on silicon by UV annealing at low temperature. Thin Solid Films. 2003 Mar;428(1–2):248–52.

230. Ono H, Koyanagi K. Formation of silicon–oxide layers at the interface between tantalum oxide and silicon substrate. Appl Phys Lett. 1999 Nov 29;75(22):3521–3.

231. Kamiyama S. Ultrathin Tantalum Oxide Capacitor Process Using Oxygen-Plasma Annealing. J Electrochem Soc. 1994;141(5):1246.

232. Kim S-O, Byun JS, Kim HJ. The effect of substrate temperature on the composition and growth of tantalum oxide thin films deposited by plasma-enhanced chemical vapour deposition. Thin Solid Films. 1991 Dec;206(1–2):102–6.

233. Alers GB, Werder DJ, Chabal Y, Lu HC, Gusev EP, Garfunkel E, et al. Intermixing at the tantalum oxide/silicon interface in gate dielectric structures. Appl Phys Lett. 1998 Sep 14;73(11):1517–9.

234. Rauch EF, Véron M, Portillo J, Bultreys D, Maniette Y, Nicolopoulos S. Automatic Crystal Orientation and Phase Mapping in TEM by Precession Diffraction. Microscopy and Analysis. 2013;22(6):S5–8.

235. Rauch EF, Portillo J, Nicolopoulos S, Bultreys D, Rouvimov S, Moeck P. Automated nanocrystal orientation and phase mapping in the transmission electron microscope on the basis of precession electron diffraction. Zeitschrift für Krist. 2010 Jan;225(2–3):103–9.

236. Lupini AR. The Electron Ronchigram BT - Scanning Transmission Electron Microscopy: Imaging and Analysis. In: Pennycook SJ, Nellist PD, editors. New York, NY: Springer New York; 2011. p. 117–61.

237. Daulton TL, Bondi KS, Kelton KF. Nanobeam diffraction fluctuation electron microscopy technique for structural characterization of disordered materials-Application to Al88-xY7Fe5Tix metallic glasses. Ultramicroscopy. 2010;110(10):1279–89.

238. Yi F, Voyles PM. Effect of sample thickness, energy filtering, and probe coherence on fluctuation electron microscopy experiments. Ultramicroscopy. 2011;111(8):1375–80.

239. Egerton RF, Li P, Malac M. Radiation damage in the TEM and SEM. Micron. 2004 Aug;35(6):399–409.

240. Rees a. LG, Spink J a. The shape transform in electron diffraction by small crystals. Acta Crystallogr. 1950 Jul 1;3(4):316–7.

241. Burgers WG. Optical demonstration of electron-diffraction effects due to small particle size. Acta Crystallogr. 1951 Nov 1;4(6):502–3.

242. Darmawikarta K. Role of nanoscale order in the nucleation of amorphous chalcogenide alloys. University of Illinois at Urbana-Champaign; 2013.

243. Xu C, Dong H, Yuan L, He H, Shao J, Fan Z. Investigation of annealing effects on the laser-induced damage threshold of amorphous Ta2O5 films. Opt Laser Technol. 2009 Apr;41(3):258–63.

244. Wang W-H, Wei Q, Friedrich S, Macht MP, Wanderka N, Wollenberger H.

Microstructure studies of Zr41Ti14Cu12.5Ni10Be22.5 bulk amorphous alloy by electron diffraction intensity analysis. Appl Phys Lett. 1997 Aug 25;71(8):1053–5.

245. Hwang J. Nanometer Scale Atomic Structure of Zirconium Based Bulk Metallic Glass. University of Wisconsin--Madison; 2011.

246. Zhao G, Treacy MMJ, Buseck PR. Fluctuation electron microscopy of medium-range order in ion-irradiated zircon. Philos Mag. 2010 Dec 14;90(35–36):4661–77.

247. Gelin S, Tanaka H, Lemaître A. Anomalous phonon scattering and elastic correlations in amorphous solids. Nat Mater. 2016 Aug 29;15(11):1177–81.

248. Ebeid MR, Abdelraheem SK. Verification of Crystallite Theory of Glass Modeling Using Rietveld Method. Egypt J Sol. 2000;23(1):1–12.

249. Eder FR, Kotakoski J, Kaiser U, Meyer JC. A journey from order to disorder — Atom by atom transformation from graphene to a 2D carbon glass. Sci Rep. 2015 May 11;4(1):4060.

250. Lichtenstein L, Heyde M, Freund H-J. Atomic Arrangement in Two-Dimensional Silica: From Crystalline to Vitreous Structures. J Phys Chem C. 2012 Sep 27;116(38):20426–32.

251. Hunklinger S, v. Schickfus M. Acoustic and Dielectric Properties of Glasses at Low Temperatures. In: Phillips WA, editor. Berlin, Heidelberg: Springer Berlin Heidelberg; 1981. p. 81–105.

252. Burleigh Cooper C, Woodyard JR. Low energy sputtering of neutral Cu2 molecules. Phys Lett A. 1980;79(1):124–6.

253. Wucher A, Wahl M. Cluster Emission in Sputtering. In: Proceedings of the Tenth International Conference on Secondary Ion Mass Spectrometry (SIMS X). 1995.

254. Gnaser H, Hofer WO. The emission of neutral clusters in sputtering. Appl Phys A. 1989;48(3):261–71.

255. Karetta F, Urbassek HM. The dimer sputtering mechanism of Cu(001) at low bombarding energy. Appl Phys A. 1992;55(4):364–71.

256. Schmidt B, Wetzig K. Ion Beams in Materials Processing and Analysis. 1st ed. Vienna: Springer Vienna; 2013. IX, 418.

257. Sosale G, Almecija D, Das K, Vengallatore S. Mechanical spectroscopy of nanocrystalline aluminum films: effects of frequency and grain size on internal friction. Nanotechnology. 2012 Apr 20;23(15):155701.

258. PENN RL, BANFIELD JF. Oriented attachment and growth , twinning , polytypism , and formation of metastable phases : Insights from nanocrystalline TiO2. Am Mineral. 2000;83:1077–82.

259. Tu Y, Tersoff J. Structure and Energetics of the Si- ${\mathrm{SiO}}_{2}$ Interface. Phys Rev Lett. 2000 May;84(19):4393–6.

260. Owen AE, Firth AP, Ewen PJS. Photo-induced structural and physico-chemical changes in amorphous chalcogenide semiconductors. Philos Mag Part B. 1985 Sep 1;52(3):347–62.

261. Payne MC, Bristowe PD, Joannopoulos JD. Ab initio determination of the structure of a grain boundary by simulated quenching. Phys Rev Lett. 1987 Mar 30;58(13):1348–51.

262. Voyles PM, Gibson JM, Treacy MMJ. Fluctuation microscopy: a probe of atomic correlations in disordered materials. J Electron Microsc (Tokyo). 2000 Jan 1;49(2):259–66.

263. Voyles PM, Abelson JR. Medium-range order in amorphous silicon measured by fluctuation electron microscopy. Sol Energy Mater Sol Cells. 2003;78(1–4):85–113.

264. Tran DT, Svensson G, Tai C-W. SUePDF : a program to obtain quantitative pair distribution functions from electron diffraction data. J Appl Crystallogr. 2017 Feb 1;50(1):304–12.